Title
Green Chemistry - From Potential Boron Cluster Based Cathodes to Clumped Isotopes

Author
Parvez, Zeeshan Anjum

Publication Date
2022

Peer reviewed|Thesis/dissertation

UNIVERSITY OF CALIFORNIA

Los Angeles

Green Chemistry – From Potential Boron Cluster Based Cathodes to Clumped Isotopes

A dissertation submitted in partial satisfaction of the

requirements for the degree Doctor of Philosophy

in Chemistry

by

Zeeshan Parvez

2022

ABSTRACT OF THE DISSERTATION

Green Chemistry – From Potential Boron Cluster Based Cathodes to Clumped Isotopes

by

Zeeshan Parvez

Doctor of Philosophy in Chemistry

University of California, Los Angeles, 2022

Professor Aradhna K. Tripati, Co-Chair

Professor Alexander Michael Spokoyny, Co-Chair

Green chemistry encompasses a broad range of topics that enable us to understand and address major environmental issues. This dissertation advances multiple green chemistry topics through three independent projects: 1) Development of boron cluster-based cathode materials for use in developing a new approach to lithium-ion based energy storage. 2) Application of a quantitative probing technique for kinetic isotope effects, using the dual-clumped isotope proxy, to evaluate dissolved inorganic carbon transformation at geological sites being considered for use as CO_2 storage sinks. 3) Advancing dual clumped isotopes as a next-generation probing technique to determine if terrestrial cave carbonate samples can be used to study climate through palaeothermometry and study kinetic isotope effects in speleothems.

Novel boron-cluster based molecules were synthesized for use as cathodes in lithium-ion batteries. The $B_{12}(OC_7H_6COOH)_{12}$ cluster exhibited the greatest potential for use as a cathode material in lithium-ion batteries. This novel molecule served as a scaffold for post-modification to enhance cyclability in the solid state. $B_{12}(OC_7H_6COOLi)_{12}$, a derivative of $B_{12}(OC_7H_6COOH)_{12}$, was deemed compatible with cell design and reversibly cycled for one redox event at an $E_{1/2}$ of 3.4 V vs Li/Li^+ in an *in situ* swagelock cell setup. However, this cluster suffered from specific capacity issues associated with only one (out of 2) reversible redox event and a high molecular weight relative to traditional metal oxides used in current generation cells.

$CaCO_3$ samples recovered from The Cedars, peridotite-associated springs located in Northern California, were analyzed using the novel dual clumped isotope proxy to evaluate CO_2 transformation processes and kinetic isotope effects and biases. Surface floe samples begin to precipitate out of solution within the first hour of CO_2 absorption, and the DIC pool requires a residence time of approximately 100 hours to achieve isotopic equilibria. The Δ_{47}/Δ_{48} slope of samples from the Cedars (-2.803±0.500; 1.s.e.) agrees with published values from lab experiments designed to constrain CO_2 hydrolysis-related kinetic fractionation (-2.911±0.200). Ancient travertine samples that are close to equilibrium in the Δ_{47}-Δ_{48} space yield an average temperature of 8.3±1.1 °C, suggesting that the conditions during that time were approximately 10°C colder than present day temperature. The consistency of slopes in the multi-isotope space suggests the Δ_{47}-Δ_{48} dual carbonate clumped isotope framework can be applied to study CO_2-absorption processes in applied systems including sites of interest for geological sequestration.

$CaCO_3$ samples from terrestrial cave sites at 13 localities from around the world were analyzed using dual clumped isotope (Δ_{47}-Δ_{48}) system. Data showed that 27 samples exhibited isotopic equilibrium with the majority having Δ_{47}-T predicted temperatures matching measured

temperatures. 17 samples exhibited isotopic disequilibria in the Δ_{47}-Δ_{48} space. Of the latter suite of samples, 15 fell within quadrant 3, 1 within quadrant 2, and 1 within quadrant 1 in the $\Delta\Delta_{47}$-$\Delta\Delta_{48}$ space. Samples that fell within quadrant 2 exhibited traditional degassing disequilibria consistent with previous speleothem studies. Samples which fell within quadrants 1 and 3 were identified to have oxygen and carbon isotope exchange within the Rayleigh distillation model approach, however the specific type of exchange could only be resolved in the $\Delta\Delta_{47}$-$\Delta\Delta_{48}$ space. Samples within quadrant 1 were identified to have oxygen isotope exchange while samples within quadrant 3 had carbon isotope exchange. Cave raft samples collected from Mexico exhibited the largest carbon isotope exchange phenomenon with magnitudes of disequilibria into quadrant 3 correlating to the relative ventilation from caves that they were recovered from. This study suggests the Δ_{47}-Δ_{48} dual carbonate clumped isotope framework can be applied to varying types of cave carbonate samples enabling quick identification of (dis)equilibria for use in paleoclimate reconstruction applications.

The dissertation of Zeeshan Parvez is approved.

Richard B. Kaner

Rubin F. Yves

Chong Liu

Alexander Michael Spokoyny, Committee Co-Chair

Aradhna K. Tripati, Committee Co-Chair

University of California, Los Angeles

2022

Table of Contents

Table of Figures/Tables

Chapter 1

Chapter 2

Chapter 3

Biographical Sketch

Zeeshan Parvez is a Marine Corps veteran who served with the Marine Special Operations Command as a critical skills operator, now known as the Marine Raiders. He conducted foreign internal defense and unconventional warfare operations in support of Operation Enduring Freedom from 2007 to 2011. For his service, he was awarded the Joint Service Achievement Medal, Navy and Marine Corps Achievement Medal, Marine Corps Good Conduct Medal, and two meritorious promotions to Corporal and Sergeant.

He completed a Bachelor of Science (B.Sc.) in Chemical Engineering from The Pennsylvania State University in 2015. He concurrently completed his studies in Master of Business Administration (M.B.A.) and a Master of Science (M.Sc.) in Chemistry from the University of Rhode Island in 2017. At UCLA he was awarded the Tillman Foundation scholarship, Sentinels of Freedom scholarship, and Center for Diverse Leadership in Science fellowship. He is the founder of the Veterans in STEM initiative which was awarded a $300,000 National Science Foundation grant to support veterans in STEM fields and establish a methodology for increasing veteran representation in STEM fields in higher education. He has authorship on 5 peer-reviewed publication ranging from inorganic synthesis to probing techniques for carbon dioxide transformation and storage application. As a Ph.D. candidate he concurrently consulted for various companies in Southern California, developing business strategies for incorporating technology into their company portfolios. In addition to this, he worked as a business development manager for a recreational organization and competed in wingsuit piloting at the professional level.

Thesis Overview

Chapter 1 – Synthesis of novel dodecaborate clusters for potential lithium-ion battery applications

Background: The dodecaborate cluster is a unique three-dimensional aromatic molecule which can undergo functionalization at its vertices, analogous to classic aromatic compounds, such as benzene. These clusters are chemically and thermally stable; possess reversible redox activity in a tunable manner via per substitution of vertices; and can undergo perfunctionalization which enables the augmentation and exploitation of unique terminal functional groups, such as, halogens, ethers, esters, carbonates, and carbamates.

The goal of this research is to exploit the unique nature of these clusters and evaluate the possibility of using it for the development of next generation energy storage systems. Most clusters worked on in this research have three sequentially accessible redox states (-2, -1, and neutral) that are tuned based on the ligands attached to the vertices. The research in this dissertation can be broken down into three distinct sections: (1) synthesis of $B_{12}(OR)_{12}$ molecular clusters (Perfunctionalized), (2) synthesis of $B_{12}(OR)_{11}(R')$ clusters (monovertex differentiated), and (3) synthesis of metal-linked perfunctionalized clusters. These three different approaches to cluster synthesis were used to synthesize molecules and materials with an aim to integrate into lithium ion battery systems.

Chapter 2 - Paired dual carbonate clumped isotopes (Δ_{47}-Δ_{48}) constrains kinetic effects and timescales in peridotite-associated springs at The Cedars, Northern California

Background: The study of kinetic effects with respect to clumped isotopes is the foundation of chapters 2 and 3 of this dissertation. Carbonates such as calcite, magnesite, and dolomite represent a class of minerals that are ubiquitous in nature and have been studied by physical chemists and geoscientists since the pioneering work of Harold Urey on thermodynamic controls

on their equilibrium isotope fractionations. Clumped isotope geochemistry is the study of multiply substituted isotopologues, which are used to trace kinetic isotope effects, and at equilibrium, are thermodynamically favored to form at lower temperatures. Unlocking this chemical information requires the transformation of mineral carbonates to gaseous CO_2 for analysis on gas-source isotope ratio mass spectrometers. The Δ_{47} clumped isotope signature measures the relative abundance of [$^{13}C^{18}O^{16}O$]. Applications for geothermometry assume that sufficient shuffling of isotopes has occurred achieve isotopic equilibrium. Violation of this assumption leads to inaccurate paleoclimate reconstruction and kinetic biases in Δ_{47}. Only recently has instrumentation technology progressed to the point where the second most abundant multiply substituted isotopologue, [$^{12}C^{18}O^{18}O$], reported as Δ_{48}, can be reliably measured. Pairing these two clumped isotope signatures [Δ_{47}-Δ_{48}] enables for the evaluation the magnitude and origin of kinetic biases.

In chapter 2 of this dissertation, paired clumped isotope signatures, Δ_{47} and Δ_{48}, of $CaCO_3$ samples recovered from highly alkaline springs, located in Northern California at the Cedars, are analyzed. The Cedars are of interest as a natural laboratory for isotopic fractionation, and because of the potential use of peridotites for geological carbon sequestration. The springs have a pH range of approximately 11-12, due to their interactions with an ultramafic, peridotite body, which readily undergoes serpentinization. These highly alkaline conditions result in large kinetic biases due to the precipitation of mineral carbonates outside of isotopic equilibria. In this research, we evaluate disequilibria within the dual clumped isotope (Δ_{47}-Δ_{48}) space and compare isotopic data with modeling.

Chapter 3 Paired Δ_{47}-Δ_{48} constrains kinetic effects associated with cave carbonates

Background: Terrestrial cave carbonates are used for paleoclimate reconstructions in inland environments. Clumped isotope palaeothermometry is a tool being explored for application to cave carbonates because it only relies on the preferential clumping of heavy isotopes due to temperature and does not require explicit information on the isotopic composition of the parent fluid media, which can vary substantially both spatially and temporally in such settings. However, the underlying assumption for clumped isotope thermometry is that the samples have achieved isotopic equilibria – a condition that is not always met in the cave environment.

In chapter 3 of this dissertation, we evaluate cave rafts, speleothems (natural and synthetic), and farmed calcite plate samples from 17 localities around the world. We use the dual clumped isotope (Δ_{47}-Δ_{48}) system to evaluate kinetic biases and draw correlations between these novel measurements and the traditionally used Rayleigh distillation model. The goal of our research is to evaluate the type and extent of kinetic biases associated with a variety of cave carbonate samples and develop a probing framework which can evaluate samples for isotopic equilibria and screen for potential use in paleoclimate reconstruction.

Chapter 1 : Synthesis of Novel Dodecaborate Clusters for Potential Lithium-Ion Battery Applications

Abstract

Efficient energy storage is one of the largest hurdles when scaling up renewable energy production to combat climate change. Herein, we explore the potential application of boron clusters within a modern lithium-ion battery. Novel boron-cluster based molecules were synthesized for their potential use as cathodes due to their chemical stability, $2e^-$ redox activity, and tunable nature. The $B_{12}(OC_7H_6COOH)_{12}$ cluster exhibited the greatest potential for use as a cathode material in lithium-ion batteries due to its insolubility in common electrolyte solvents. This novel molecule served as a scaffold for post-modification to enhance cyclability in the solid state. $B_{12}(OC_7H_6COOLi)_{12}$, a derivative of $B_{12}(OC_7H_6COOH)_{12}$, was deemed compatible with cell design and reversibly cycled for one redox event at an $E_{1/2}$ of 3.4 V vs Li/Li^+ in an *in situ* swagelock cell setup. However, this cluster suffered from specific capacity issues associated with only one (out of 2) reversible redox event and a high molecular weight relative to traditional metal oxides used in current generation cells.

1.1 Introduction

Climate change is an ever-growing concern that threatens our collective future. To combat this, a multiple pronged approach must be adopted where CO_2 emissions are not only reduced, but greenhouse gases are actively removed from the atmosphere (IPCC, 2014, 2018). Speculations indicate that the primary source of global-zero carbon energy will be derived from electricity generation from renewable sources (IRENA, 2018). However, the ability to store this energy for use will be a critical piece of the overall strategy (Smith, 2021). Wind and solar sources are feasible renewable solutions, however both sources are restricted by the intermittence of energy sources, among other factors (Lewis, 2016). Battery-based energy storage could partly ensure consistent

and reliable energy supply when coupled with these renewable sources. Lithium-ion batteries (LIBs) can be coupled with photovoltaics (PV)s with promising applications in PV-based communal grids. Compared to other batteries, LIBs have the fastest charging and discharging cycles with efficiencies of up to 99% (Opiyo, 2016). This makes research in expanding the potential for LIBs a critical piece in developing a long-term strategy to combat climate change.

LIBs offer a wide range of benefits over other battery systems such as no memory, high specific capacity and voltage, excellent cycling performance, little self-discharge, and a wide temperature threshold for operation (Wang *et al*., 2017; Chen *et al*., 2021). This opens the need to expand research in further developing this technology to meet future energy storage demands. The LIB consists of four major parts: cathode, anode, separator, and electrolyte (Dunn *et al*., 2011). All four of these components must work in sync for proper charge and discharge. The cathode generally consists of transition metal oxides such as $LiCoO_2$, which have dominated the LIB industry for portable and grid storage applications (Mizushima *et al*., 1981; Ozawa, 1994; Whittingham, 2004). However, due to the high cost of Co and ethical issues related to sourcing other alloy mixtures including Ni, Mn, and Al are being explored. Lower cost and capacity increases associated with Ni put it at the forefront of research, however lower thermal stability, greater reactivity with electrolyte, sensitivity to the environment, and the formation of surface films (Faenza *et al*., 2017) result in limitations. To overcome some of these limitations it is important to expand our understanding of cathodes which deviate from the traditional metal oxide combination.

Icosahedral dodecaborate clusters represent a unique class of molecules which exhibit great thermal and chemical stability; undergo electrochemically tunable and reversible redox events; have great functionalization potential; and can have their solubilities modified through cation

exchange or ligand functionalization (Hawthorne and Pitochelli, 1960; Knoth *et al*., 1962; Hawthorne, 2003, 2009; Wixtrom *et al*., 2016; Axtell *et al*., 2018). The adjustable nature of these clusters enables them to be modified to adhere to different electrolyte and anode combinations. The tunable nature forwards the potential to adjust voltage windows with respect to other LIB components. By integrating modified clusters into cathode mixtures, we can determine their potential use as cathode material substitutes to the current transitional metal oxides.

Background

1.1.1 The Icosahedral Boron Cluster

The icosahedral borane cluster $[B_{12}H_{12}]^{2-}$ was theoretically predicted by Libscomb *et al.* (1954), followed by subsequent studies by Longuet-Higgens *et al.* (1955) who proposed the stable form existed in a di-anionic state. The first icosahedron dodecaborane $[B_{12}H_{12}]^{2-}$ cluster was first successfully isolated and characterized by Pitochelli and Hawthorne (1960). This dodecaborane cluster was further persubstituted by Knoth and Muettereties (1962, 1964). Within the past two decades this per substitution was further expanded to include hydroxyl functional groups $[B_{12}(OH)_{12}]^{2-}$ (Peymann *et al*., 1999; Saylik *et al*., 1999; Hawthorne, 2003; Ivanov *et al*., 2003; Peryshkov *et al*., 2009; Gu and Ozerov, 2011). Among all the perfunctionalized derivatives the *closo*-$[B_{12}(OH)_{12}]^{2-}$ allowed for a favorable pathway for further functionalization by forming carbonate, carbamate, ester, and ether linkages (Peymann *et al*., 1999; Maderna *et al*., 2001; Farha *et al*., 2005; Jalisatgi, Satish; Kulkarni, Vikas; Tang, Betty; Houston, Zachary; Lee, Mark; Hawthorne, 2011).

Under controlled oxidation conditions, the $[B_{12}H_{12}]^{-2}$ anion leads to an irreversible cluster degradation which forms a B-B dimer (Wiersema and Middaugh, 1969). With the perfunctionalization of this cluster, Hawthorne and coworkers reported that the $B_{12}(OCH_2Ph)_{12}$

cluster can exist in three distinct charge states which are accessible via two sequential and quasi-reversible one-electron oxidation reactions of the parent di-anionic parent species. Additional perfunctionalizations have been performed which indicate similar patterns of redox activity and the ability to modify the voltage windows via ligand modification or substitution (Farha *et al*., 2005; Lee *et al*., 2007; Wixtrom *et al*., 2016, 2018; Axtell *et al*., 2018; Barton *et al*., 2019).

While it has been well established that the dodecaborate cluster shows reversible cyclability in the solution phase, its' cyclability in the solid state has yet to be explored. By understanding its' behavior in the solid state and the properties that allow the cluster to remain insoluble in common electrolyte solvents, we can begin to explore the possibilities of this cluster being used in ion battery applications.

1.2 Methods and Materials

Various boron cluster molecules were screened for use as cathodes, however only those that Parvez *et al.* worked on are explicitly described below.

1.2.1 Synthesis of $B_{12}(OR)_{12}$ Molecular Clusters (Perfunctionalized)

$B_{12}(OC_7H_6COOCH_3)_{12}$

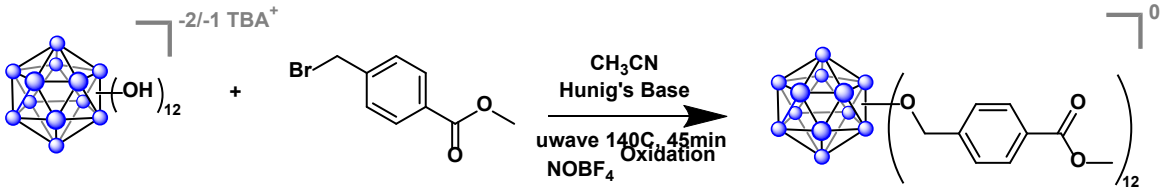

150 mg (0.183 mmol) of $TBA_2B_{12}(OH)_{12}$, 0.6 mL (3.00 mmol) of N,N-Diisopropylethylamine, and 1.26 g (5.50 mmol) of Methyl 4-(bromomethyl)benzoate was dissolved in 2 mL (40 mmol) of

acetonitrile. This reaction mixture was subjected to a microwave assisted reaction at 140 ºC for 45 minutes. The acetonitrile was then removed through rotary-evaporation, and then subjected to silica gel separation using 100% ethyl acetate to remove residual Methyl 4-(bromomethyl)benzoate and N,N-Diisopropylethylamine. 100% acetone was then used to elute the cluster from the column. Upon removal of the acetone, this yielded a solid mixture of $TBAB_{12}(OC_7H_6COOCH_3)_{12}$ and $TBA_2B_{12}(OC_7H_6COOCH_3)_{12}$ weighing 0.399 g (88% yield) in total. This solid mixture of oxidation states was then chemically oxidized to the neutral form dissolving it with 0.064 g (0.544 mmol) of $NOBF_4$ in acetonitrile. This reaction was allowed to proceed for 12 hours. A reddish-brown solid precipitated out of the solution, which was filtered and washed with additional acetonitrile to remove any borates and additional $NOBF_4$. This solid was dried under heat and vacuum to give 0.197 g (60% yield).

$TBA_xB_{12}(OC_7H_6COOH)_{12}$

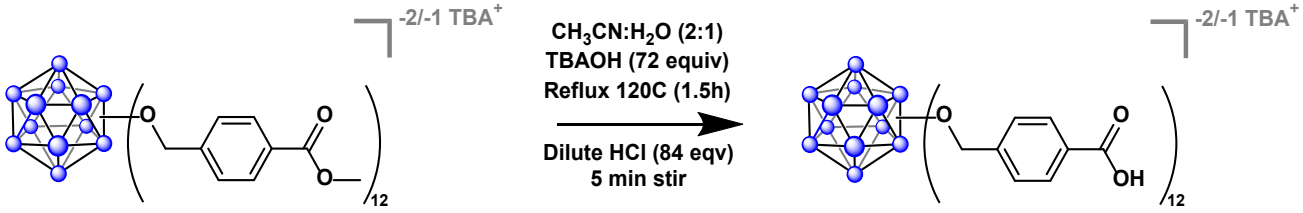

30 mg (0.012 mmol) of the precursor material, $B_{12}(OC_7H_6COOCH_3)_{12}$, was dissolved into a 2:1 solution of $MeCN:H_2O$. 55 equivalence (0.78 mmol), relative to $B_{12}(OC_7H_6COOCH_3)_{12}$ of tetrabutyl ammonium hydroxide (TBAOH) was added to the mixture and allowed to reflux at 120 ºC for 1.5 hours. During the reflux process, the product goes from a mixture of redox states to the -2 redox state, denoted from the color change from purple to clear. Following reflux, the acetonitrile was removed through rotary evaporation. 84 equivalence (12.07 mmol) of HCl, relative to $B_{12}(OC_7H_6COOCH_3)_{12}$, at a concentration of 1 mM, was added dropwise to the stirring

solution. The solution turns pink as more HCl is added with the product precipitating out of solution, indicating a completion of the reaction. This mixture is allowed to stir for no longer than 1 minute after precipitate has formed (or 5 minutes from introduction of HCl), and thoroughly washed with H_2O to remove any residual HCl.

$TBA_2B_{12}(OC_7H_6SCH_3)_{12}$

25 mg (0.03 mmol) of $TBA_2B_{12}(OH)_{12}$ was added to a microwave vessel with 60 equivalence (35 mL, 0.57 mmol) of 4-(methylthio)benzyl chloride, 0.10 mL (0.57 mmol) of N,N-Diisopropylethylamine. The previously mentioned reagents were dissolved into 1 mL of acetonitrile and microwaved for 20 minutes at 140 ˚C. The mixture was then subjected to rotary evaporation to remove excess acetonitrile and any unreacted 4-(methylthio)benzyl chloride. The resulting product was tested for purity through GC/MS and TLC.

1.2.2 Synthesis of $B_{12}(OR)_{11}(R')$ Clusters (Monovertex Differentiated)

$B_{12}NO_2(OC_7F_5)_{11}$

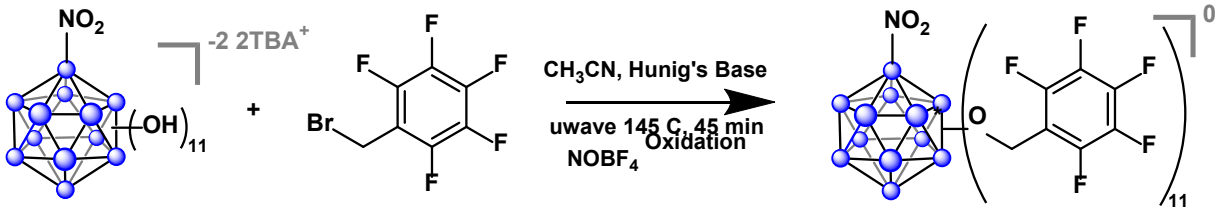

100.40 mg of $TBA_2B_{12}(OH)_{11}NO_2$ was dissolved into 1 mL of acetonitrile with 0.47 mL N,N-Diisopropylethylamine (Hunig's Base) and 1.96 mL (12.98 mmol) of 2,3,4,5,6-Pentafluorobenzyl bromide in a 10 mL microwave vial. This solution was subjected to heated (140 ˚C), microwave assisted synthesis. The yellow-orange solution was then subjected to rotary evaporation to remove all remaining acetonitrile. The product was then subjected to a slurry-

packed silica gel column with a 35:65 (EtOAc:Hexane) mobile phase solvent. This was used to remove any remaining 2,3,4,5,6-Pentafluorobenzyl bromide which had not reacted. Upon discharge of the 2,3,4,5,6-Pentafluorobenzyl bromide, the target cluster was eluted using 100% acetone. The acetone was then removed by rotary evaporation. The remaining product, a mixture of multiple redox states ($TBA_2B_{12}NO_2(OC_7F_5)_{11}$ and $TBAB_{12}NO_2(OC_7F_5)_{11}$, was then subjected the heated high vacuum overnight to remove any residual acetone. This product was then dissolved into 2 mL of acetonitrile with 31 mg (0.27 mmol) of $NOBF_4$ under inert atmosphere and then subjected to stirring at room temperature overnight. The oxidized product, $B_{12}NO_2(OC_7F_5)_{11}$ was washed with minimal, cold acetonitrile to remove any residual $NOBF_4$, and then subjected to heated (120 ˚C) high vacuum overnight. This cluster was synthesized by Wixtrom *et al.* (2018).

1.2.3 Synthesis of Metal-linked Clusters

$B_{12}(OC_7H_6COOZn)_{12}$

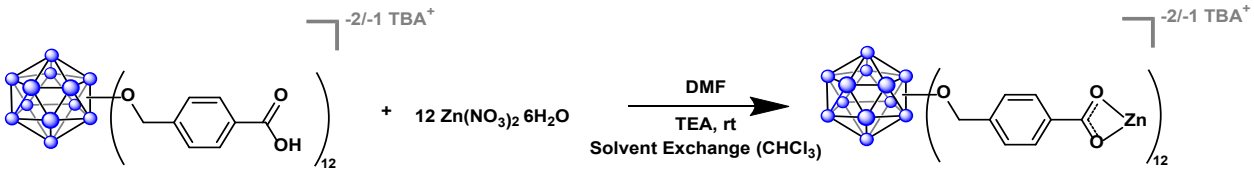

50 mg (0.02 mmol) of $B_{12}(OC_7H_6COOH)_{12}$ was dissolved into 5 mL of N,N-dimethylformamide using sonicated agitation. 75 mg (0.25 mmol) of $Zn(NO_3)_2 \cdot 6H_2O$ was then subsequently added to the previous mixture and thoroughly dissolved through sonicated agitation. The mixture was subjected to solvothermal heating at 120 ºC for approximately 5 days. During this time, the solution goes from a dark purple color to completely white. Upon completion of the solvothermal synthesis the resulting material was thoroughly washed with DMF, and subjected to a solvent exchange using $CHCl_3$ over the course of 5 days. The $CHCl_3$ was swapped out every day

during this 5-day period. Upon completion of this, the resulting material was heated to 100 ºC to remove any residual $CHCl_3$.

$B_{12}(OC_7H_6COOTi)_{12}$

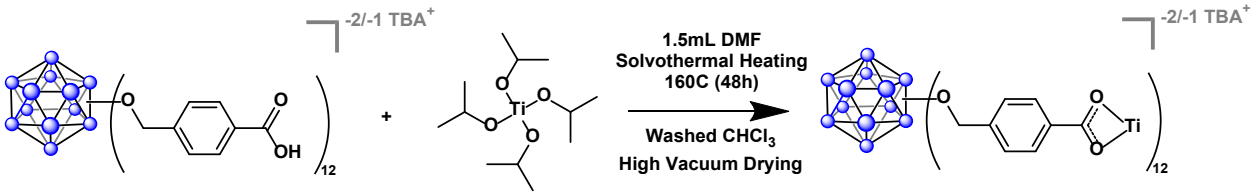

20 mg (0.01 mmol) of $B_{12}(OC_7H_6COOH)_{12}$ and 12 equivalence, 30 µL (0.12 mmol), of titanium (IV) isopropoxide was dissolved in 1 mL of N,N-dimethylformamide using sonicate assisted agitation. The mixture was subjected to solvothermal heating at 160 ºC for 2 days. Upon completion of the solvothermal synthesis, the gel-like material was isolated and thoroughly washed with N,N-dimethylformamide. This material was then subjected to a solvent change using $CHCl_3$ for 5 days. The $CHCl_3$ was swapped out daily for the 5-day duration. Upon completion of this the product was subjected to 100 ºC heating overnight to remove any residual $CHCl_3$.

$B_{12}(OC_7H_6COOLi)_{12}$

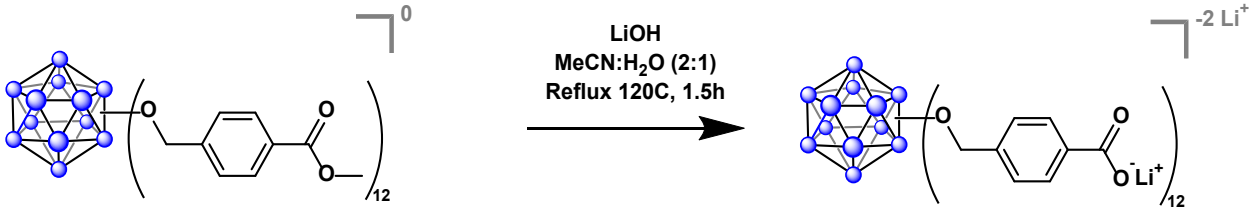

150 mg of the previous precursor, $B_{12}(OC_7H_6COOCH_3)_{12}$, was dissolved in 150 mL of a 2:1 mixture of H_2O and acetonitrile. 60 mg (1.5 mmol) LiOH was subsequently added to this mixture and allowed to reflux at 120 ºC for 2.5 hours. The cluster undergoes two reduction events which is indicated by a color change from reddish-brown to purple (neutral to monoanionic), and

purple to clear (monoanionic to dianionic). The solvent from the reaction mixture was evaporated and the solid recovered. The crude solid material recovered was then subjected to separation using a G-50 medium grade Sephadex size exclusion column and water as the effluent solvent. Fractions were collected in 15 mL test tubes, and the first 3 fractions were collected. The other fractions were subjected to subsequent size exclusion columns to separate. The water was thoroughly evaporated using heat and vacuum and the solid was collected, yielding 45 mg (30% yield) of purified product. This product was then subjected to a thorough sonication and filtration cycle using dry THF. The material was then subjected to high vacuum at 60 ºC.

The resulting material, $B_{12}(OC_7H_6COOLi)_{12}$ showed no solubility in commonly used organic electrolyte battery solvents, including various carbonate solvents and THF. It did however show particularly good solubility in H_2O.

This material was structurally characterized through nuclear magnetic resonance spectroscopy (NMR), infrared spectroscopy (IR), scanning electron spectroscopy (SEM), and powder x-ray spectroscopy (PXRD).

Electrochemical testing of the $Li_2B_{12}(OC_7H_6COOLi)_{12}$ cluster was performed in Swagelok style cells assembled in an argon-filled glovebox, using a Li metal combined counter and reference electrode and a Whatman GF/D borosilicate glass fiber sheet as a separator. 1M $LiPF_6$ in ethylene carbonate and dimethyl carbonate (1:1 w/w) was used as the electrolyte (LP30). The as prepared $Li_2B_{12}(OC_7H_6COOLi)_{12}$ cluster was dried under vacuum and introduced into the glovebox. The material was then carbon coated $Li_2B_{12}(OC_7H_6COOLi)_{12}$ cluster was subsequently cycled as a loose powder with a typical electrode mass of 5 mg. Cyclic voltammetry was performed using a sweep rate of 0.1 mV/s with a typical voltage window of 3.0-4.0 V (vs Li/Li^+).

1.2.3 Electrochemical Testing in the Solid State

Electrochemical testing was conducted using a common swagelock cell. The anode consisted of lithium metal and the electrolyte solution consisted of common carbonate solvents or tetrahydrofuran with 1M of $LiPF_6$. The cathode was a loose powder electrode with approximately 20% Super P carbon and 80% target cluster. The loose powder was ball milled for 10 minutes to facilitate homogenous mixing of the two components. A standard 0.1 mV/s sweep rate was used on cycling unless otherwise stated. All electrochemical testing was performed by Bashian *et al.*

1.3 Results

Only clusters synthesized for cathode related applications are characterized and analyzed. Clusters created by collogues for other applications are mentioned, however structural characterization and testing is not provided. Structural characterization of the $B_{12}(OC_7F_5)_{11}NO_2$ was performed by Wixtrom *et al.* (2018)

1.3.1 $B_{12}(OR)_{12}$ Molecular Clusters (Perfunctionalized)

Structural characterization through BNMR and HNMR was performed as a standard on all perfunctionalized clusters that were soluble in standard deuterated solvents. Additional characterization (i.e. PXRD, IR, etc.) was performed on clusters that showed promising characteristics for use in LIB cathodes.

$TBA_xB_{12}(OC_7H_6COOH)_{12}$

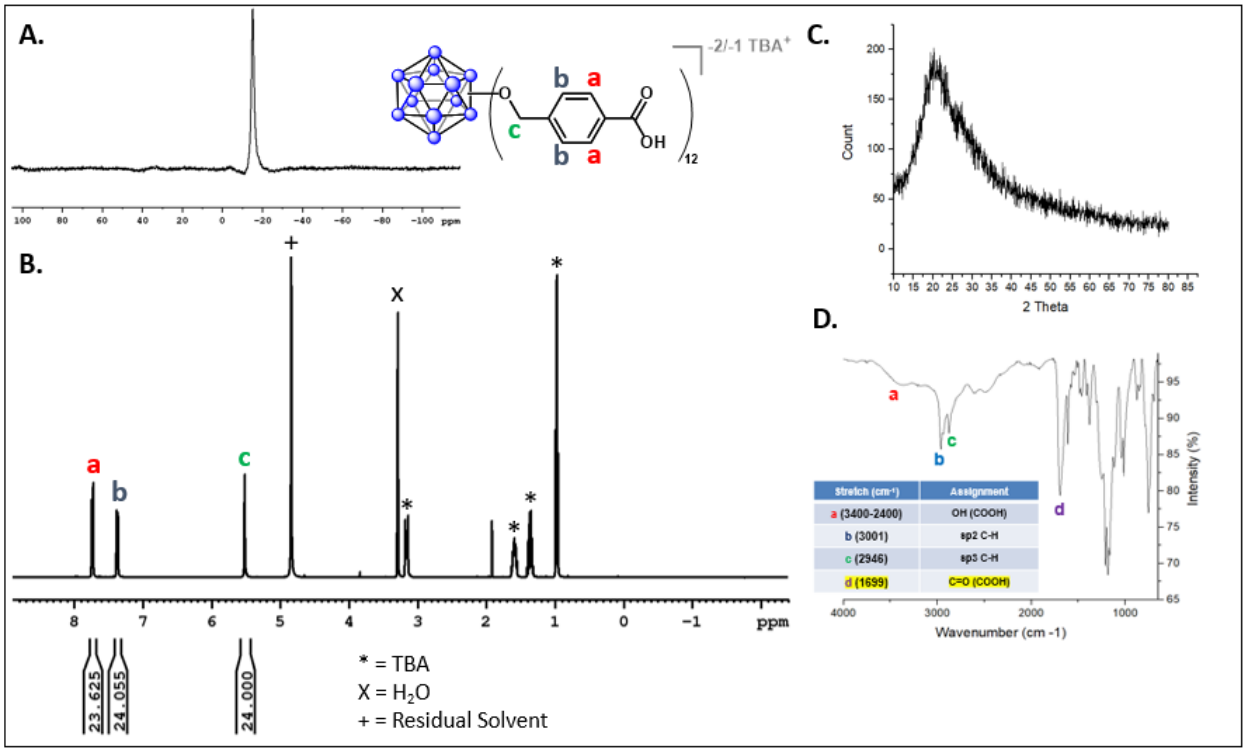

Figure 1.1 Structural characterization of $B_{12}(OC_7H_6COOH)_{12}$. HNMR and BNMR indicate a perfunctionalized cluster with carboxylic acid functionalized arene ring. The proton on the carboxylic acid is not present in the HNMR spectra due to potential deuterium exchange. PXRD indicates a material which does not have long range order. IR spectra indicates the presence of appropriate functional groups. **A)** BNMR spectra **B)** HNMR spectra w/ labeling on figure. Carboxylic acid proton is not visible due to deuterium exchange. **C)** PXRD spectra **D)** IR spectra w/ functional groups labeled.

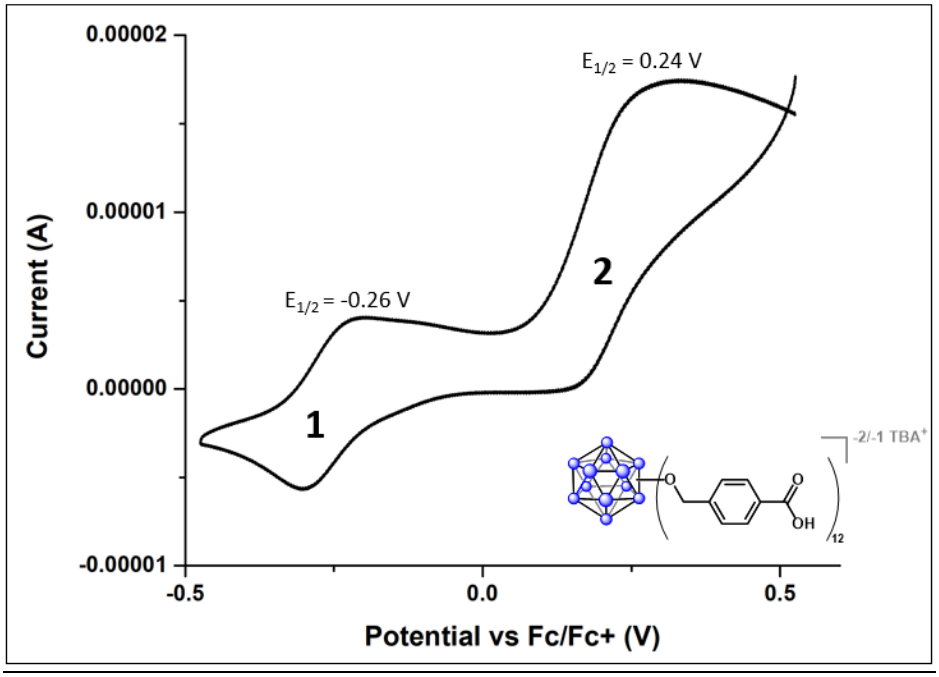

Figure 1.2 Cyclic voltammetry of $B_{12}(OC_7H_6COOH)_{12}$ in MeOH. Cluster shows two distinct, reversible redox states with $E_{1/2}$ = -0.26 V and 0.24 V vs Fe/Fe^{+}.

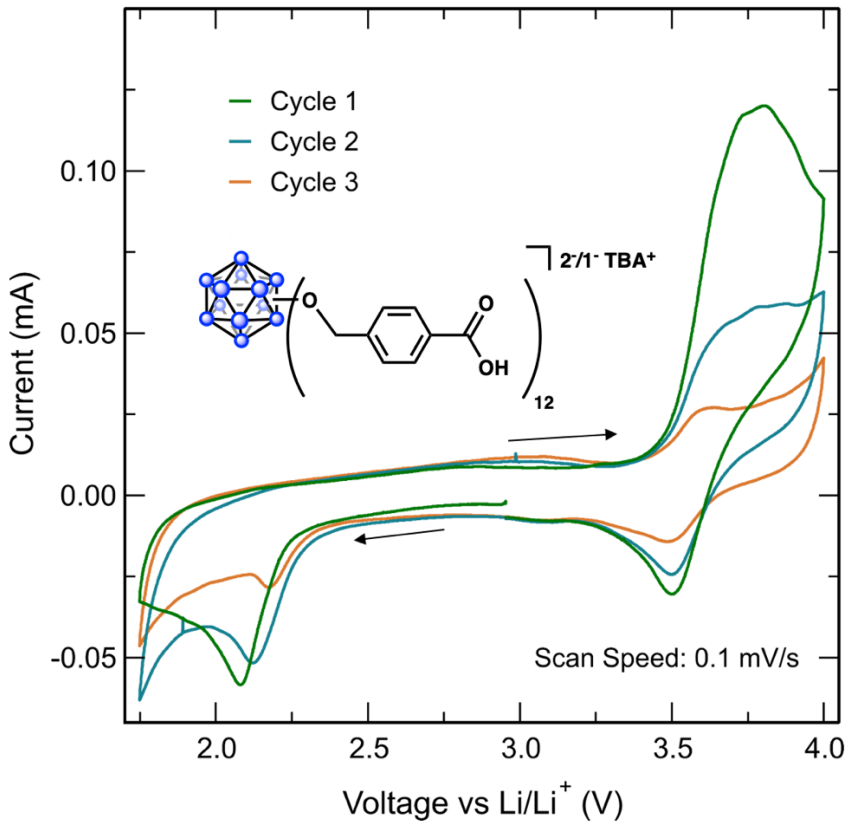

Figure 1.3 In-situ cyclic voltammetry of $B_{12}(OC_7H_6COOH)_{12}$ in standard swagelock cell. Cathode was made by mixing carbon and $B_{12}(OC_7H_6COOH)_{12}$ together. Common carbonate-based electrolyte solution with 1M $LiPF_6$ was used. CV was terminated after 3 cycles due to degradation of the signal.

$TBA_2B_{12}(OC_7H_6SCH_3)_{12}$

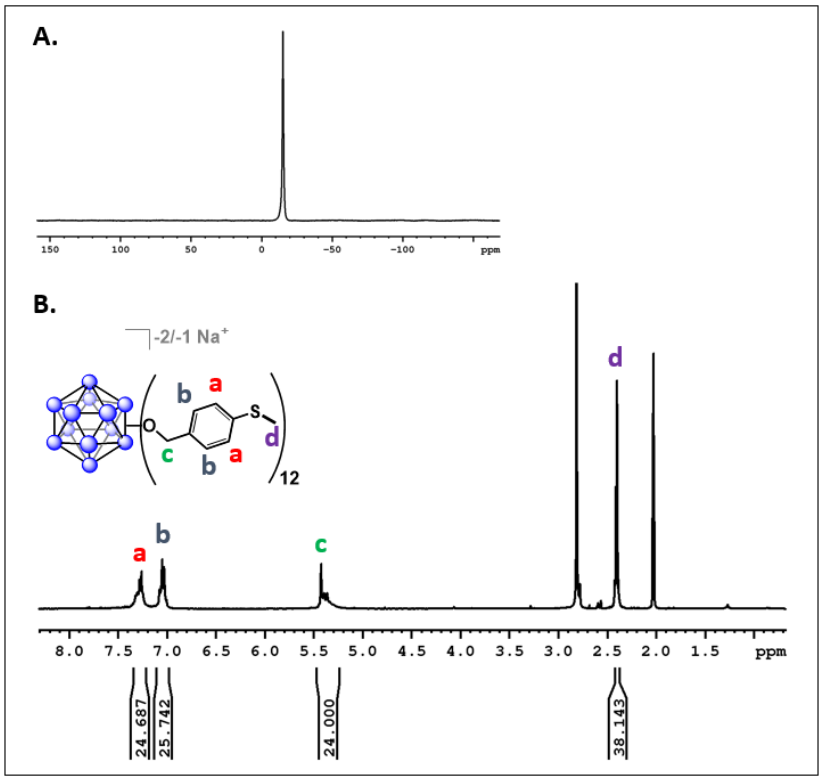

Figure 1.4 Structural characterization of $B_{12}(OC_7H_6SCH_3)_{12}$. Both BNMR and HNMR indicate a perfunctionalized cluster with protons labeled. **A)** BNMR spectra **B)** HNMR spectra with respective protons labeled peaks. Unlabeled peaks are H_2O and residual solvent.

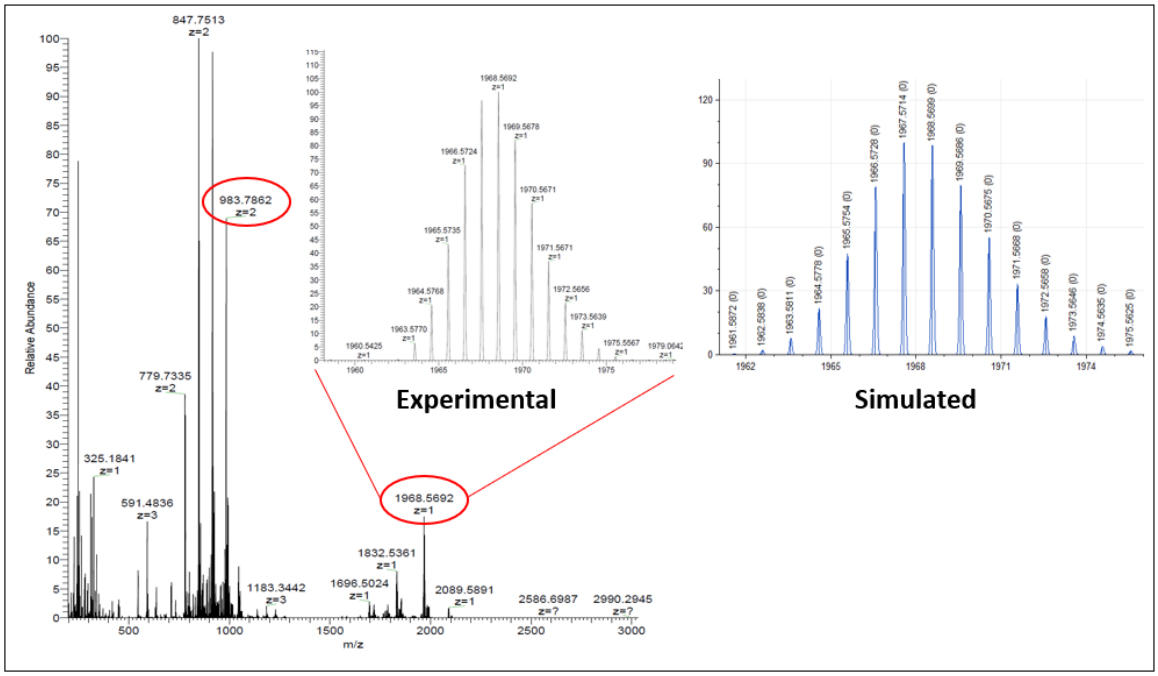

Figure 1.5 Mass spectrometry of $B_{12}(OC_7H_6SCH_3)_{12}$. Experimental values were compared against simulated values and yielded good agreement.

$TBA_2B_{12}(OC_7H_6COOCH_3)_{12}$

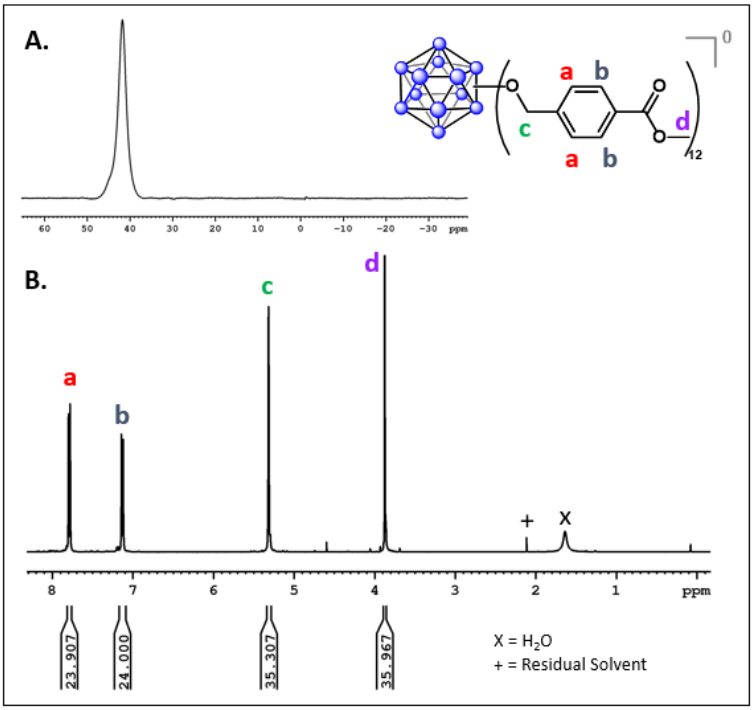

Figure 1.6 Structural characterization of $B_{12}(OC_7H_6COOCH_3)_{12}$. Both BNMR and HNMR indicate a perfunctionalized cluster with protons labeled. **A)** BNMR spectra **B)** HNMR spectra with respective protons labeled peaks. Unlabeled peaks are H_2O and residual solvent.

1.3.2 Metal Linked Clusters

$B_{12}(OC_7H_6COOLi)_{12}$

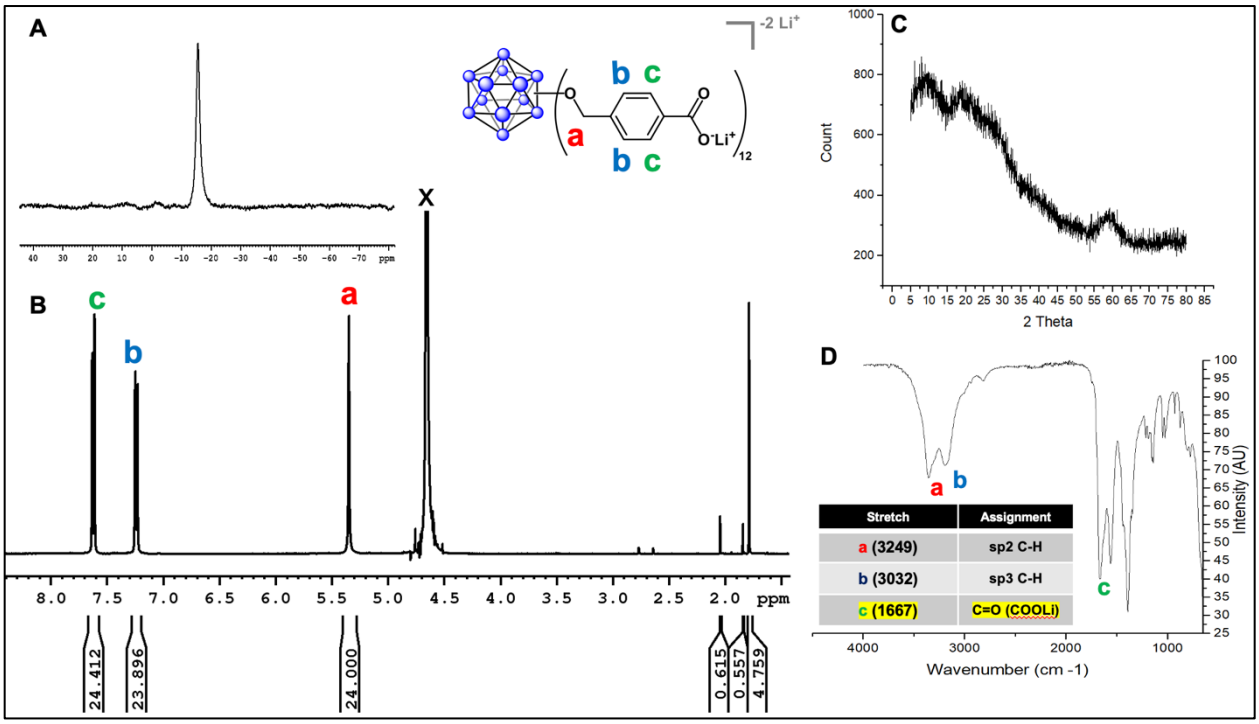

Figure 1.7 Structural characterization of $B_{12}(OC_7H_6COOLi)_{12}$. BNMR and HNMR indicate a perfunctionalized borane cluster with ligand protons identified. IR spectra indicates a slightly shifted carbonyl group relative to $B_{12}(OC_7H_6COOH)_{12}$. PXRD indicates no long-range order of the molecule. **A)** BNMR spectra **B)** HNMR spectra **C)** PXRD spectra **D)** IR spectra

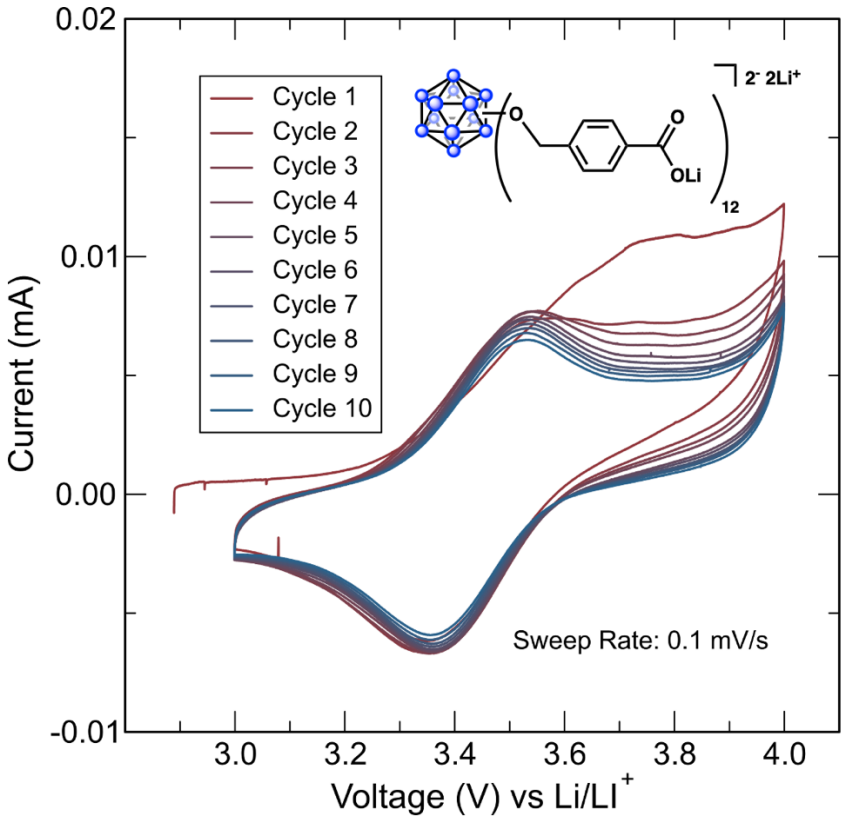

Figure 1.8 In-situ cyclic voltammetry of $B_{12}(OC_7H_6COOLi)_{12}$ in standard swagelock cell. 10 cycles were performed at a sweep rate of 0.1 mV/s.

$B_{12}(OC_7H_6COOTi)_{12}$

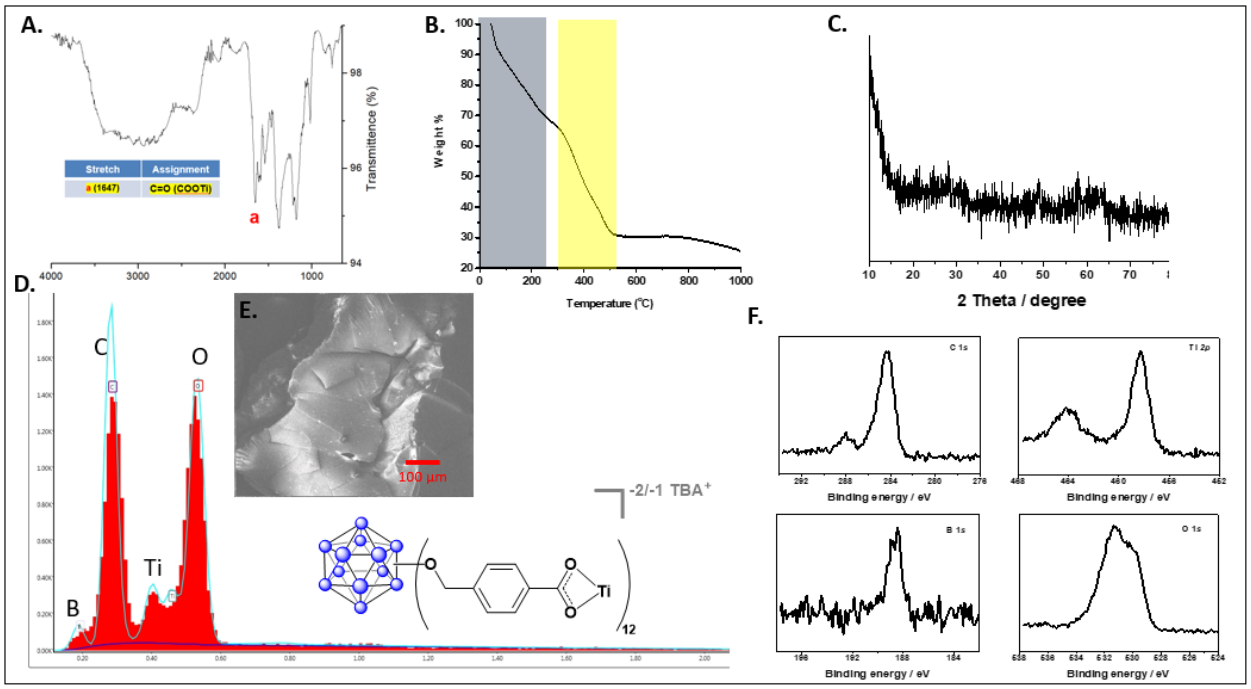

Figure 1.9 Structural characterization of $B_{12}(OC_7H_6COOTi)_{12}$. NMR characterization could not be performed as this material was insoluble in common deuterated solvents. Characterization was performed through IR, TGA, PXRD, EDS, SEM, and XPS. PXRD spectra indicates no long-range order. TGA indicates two distinct events associated with solvent removal (shaded gray) and organic material degradation (shaded yellow). EDS and XPS indicate the presence of boron, carbon, titanium, and oxygen. **A)** IR spectra **B)** TGA **C)** PXRD spectra **D)** EDS of structure **E)** SEM w/ 100 µm of resolution **F)** XPS spectra.

$B_{12}(OC_7H_6COOZn)_{12}$

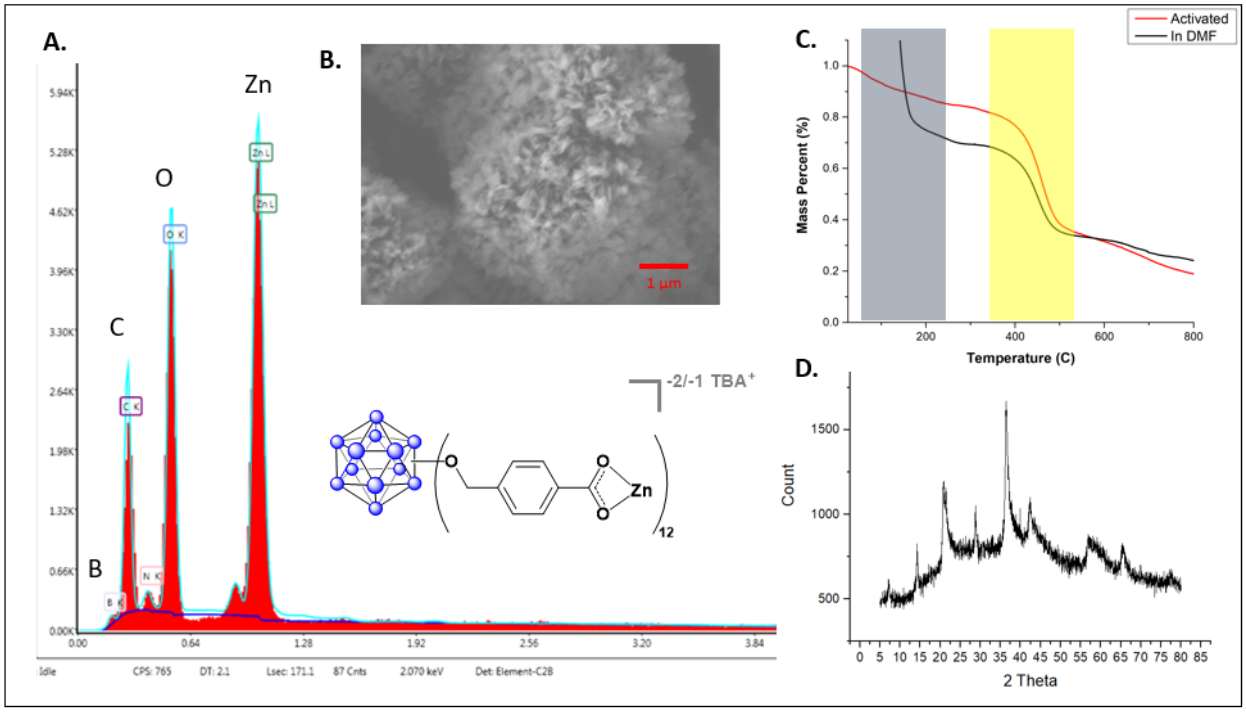

Figure 1.10 Structural characterization of $B_{12}(OC_7H_6COOZn)_{12}$. NMR characterization could not be performed as this material was insoluble in common deuterated solvents. Characterization was performed through TGA, PXRD, EDS, and SEM. PXRD spectra indicates crystalline structure with long-range order. TGA indicates two distinct events associated with solvent removal (shaded gray) and organic material degradation (shaded yellow). EDS and XPS indicate the presence of boron, carbon, titanium, and oxygen. **A)** EDS spectra **B)** SEM image w/ 1 µm of resolution **C)** TGA **D)** PXRD

1.3.3 Solubility

Table 1.1 shows the solubility of synthesized clusters in common electrolyte media. Table 1.1 reflects only a handful of clusters that were tested. Clusters with similar variations of ligands and terminal functional groups had similar solubilities in target solvents.

	Ethylene Carbonate	**Diethyl Carbonate**	**Dimethyl Carbonate**	**Propylene Carbonate**	**Tetrahydrofuran**
Metal-linked Clusters					
$B_{12}(OC_7H_6COOLi)_{12}$	Insoluble	Insoluble	Insoluble	Insoluble	Insoluble
$B_{12}(OC_7H_6COOTi)_{12}$	Insoluble	Insoluble	Insoluble	Insoluble	Insoluble
$B_{12}(OC_7H_6COOZn)_{12}$	Insoluble	Insoluble	Insoluble	Insoluble	Insoluble
Molecular $B_{12}(OR)_{12}$ Clusters					
$B_{12}(OC7H_6COOCH_3)_{12}$	Soluble	Soluble	Soluble	Soluble	Soluble
$B_{12}(OC_7H_2F_5)_{12}$	Soluble	Soluble	Soluble	Soluble	Soluble
$B_{12}(OC_2H_5)_{12}$	Soluble	Insoluble	Soluble	Soluble	Insoluble
$B_{12}(OC_7H_6COOH)_{12}$	Insoluble	Insoluble	Insoluble	Insoluble	Insoluble
$B_{12}(OC_7H_3(CF_3)_2)_{12}$	Soluble	Soluble	Soluble	Soluble	Soluble
$B_{12}(OC_7H_6SCH_3)_{12}$	Soluble	Soluble	Soluble	Soluble	Soluble
Molecular $B_{12}(OR)_{11}(R')$					
$B_{12}(OC_7F_5)_{11}(NO_2)$	Soluble	Soluble	Soluble	Soluble	Soluble

Table 1.1 Solubility screening of various boron clusters in common electrolyte solvents. If the cluster showed any solubility at any redox state, it was listed as soluble.

1.4 Discussion

1.4.1 Clusters Insoluble in Common LIB Electrolyte Solvents

The first major hurdle when applying these boron clusters to LIB cathode applications was to determine solubility in common electrolyte solvents. Even a partial bit of solubility at any redox state would lead to degradation of the cathode and reduced cyclability of the cell after subsequent charge/discharge cycles. The solubilities of the various clusters in common electrolyte solvents can be seen on Table 1.1. A large proportion of the tested molecular $B_{12}(OR)_{12}$ clusters show some degree of solubility in common electrolyte media at one or more charge states. This was consistent with most alkyl or arene perfunctionalized clusters that were ionically balanced by tetrabutyl ammonium or tetryethyl ammonium. This was the same case for the mono-vertex differentiated cluster, which had similar solubility properties as the perfunctionalized clusters. $B_{12}(OC_7H_6COOH)_{12}$ was the only $B_{12}(OR)_{12}$ molecular cluster to show insolubility in the target electrolyte solvents. This cluster was further analyzed through in-situ cyclic voltammetry to determine feasibility for use in an LIB.

Metal linked clusters showed the most promise in terms of solubility. The $B_{12}(OC_7H_6COOH)_{12}$ cluster was used as a base scaffold for linking the clusters through a metal intermediary by exploiting the reactive, terminal, carboxylic acid functional groups. Zn, Ti, and Li were successfully coordinated to the terminal functional groups. All three of these clusters were insoluble in common electrolyte solvents.

1.4.2 The First Cluster to Cycle in Solid State

The $B_{12}(OC_7H_6COOH)_{12}$ cluster was electrochemically analyzed through solution phase and in-situ cyclic voltammetry. The solution-based approach, conducted in MeOH, identified two

distinct redox events with half-wave values ($E_{1/2}$) of -0.26 V and 0.24 V (Figure 1.2) vs Fc/Fc^+. This was consistent with the electrochemical activity of other arene functionalized clusters, in that three charge states exist resulting in two distinct redox events. This would allow for a $2e^-$ transfer during cell cycling. However, when this cluster was subjected to in-situ cyclic voltammetry using the swagelock cell, there was only one redox event with an approximate $E_{1/2}$ value of 3.4 V vs Li/Li^+ (Figure 1.3). Subsequent cycling of this cluster around the redox event voltage results in a major degradation of the current intensity. This was hypothesized to have been due to the solubility changes associated with the cluster in different redox states. Because this cluster was never isolated in any state other than a mixture of -2 and -1 redox states, it was possible that when the cluster goes to the neutral state, it becomes soluble in carbonate-based electrolytes.

This prompted us to modify our approach and explore different options for meeting the (in)solubility requirements as well as electrochemical activity in the solid state. Due to the reactivity of the carboxylic acid terminal functional groups, we opted to react with metal atoms to reduce solubility while retaining electrochemical activity. $B_{12}(OC_7H_6COOTi)_{12}$ and $B_{12}(OC_7H_6COOZn)_{12}$ were tested through in-situ cyclic voltammetry using the swagelock setup. However, these specific clusters did not show any significant sign of redox activity during in-situ cyclic voltammetry in the swagelock cells. Our hypothesis for this was that the metal centers terminal functional groups and the metal centers prevented redox activity of the cluster. In light of this, we began exploring Li^+ variations of the $B_{12}(OC_7H_6COOH)_{12}$ cluster. The $B_{12}(OC_7H_6COOLi)_{12}$ was a derivative of this cluster and showed the greatest promise in the solid state. The cyclic voltammetry spectra (Figure 1.8) show reversible cycling at an $E_{1/2}$ of 3.4 vs Li/Li^+. Through the 10 cycles performed, there is notable degradation of the current that stabilizes after cycle 8-10. This was promising in the regards that this was the first cluster to show redox

activity in solid state. However, because this cluster only had one redox event, the theoretical capacity of the cell during a $2e^-$ transfer (Q: 28 mAh g^{-1}) was cut in half.

1.4.3 Theoretical Specific Capacity Issues

The tunable nature of these clusters coupled with the potential for a reversible $3e^-$ transfer, make these clusters very appealing for energy storage applications. However, the tunability of these clusters generally requires the addition of ligands which increase the molecular weight, lowering the theoretical specific capacity of the cluster. The theoretical capacity of $LiCoO_2$, a standard metal oxide cathode, is 274 mAh g^{-1} with a practical capacity of around 140 mAh g^{-1} (Deng, 2015) The theoretical capacity of the lightest target cluster $Li_2B_{12}(OH)_{12}$ is 77 mAh g^{-1}. The $B_{12}(OC_7H_6COOLi)_{12}$ cluster which was able to cycle in the solid state had a theoretical specific capacity of 28 mAh g^{-1}, which was reduced to 14 mAh g^{-1} after the discovery of only one reversible redox event during in-situ cyclic voltammetry. This could be addressed in the future with the addition of electrochemically active metal centers which could contribute to the electrons transferred, or exploring clusters that exhibit 3 redox events, correlating to a potential $3e^-$ transfer. Stauber *et al.* (2020) discovered that a third redox event of $B_{12}(OC_5H_{11})_{12}$ from the neutral form resulted in a super-oxidized cationic variation of the cluster. This enables the potential transfer for $3e^-$ which could be used to adjust the theoretical specific capacity to higher values. This is promising in the regards that other clusters may also possess this capability and have yet to be explored.

1.5 Conclusion

Exploring additional avenues for energy storage is an important endeavor which must be explored at every level to develop new technology which can help address future energy storage demands. The icosahedral boron cluster platform opens the opportunity to explore different pathways for energy storage, by designing a new style of tunable cathode. Our research explored the first application of the icosahedral boron cluster for use as a cathode in a lithium-ion cell. It was able to reliably cycle with $1e^-$ transfer in the solid state. Notably, the current shows signs of degradation in the oxidative direction. Theoretical specific capacity concerns relating to overall molecular weight exist as it relates to overall performance relative to current metal oxide standards. These concerns are something that can be addressed by exploring clusters with additional redox events and/or reducing the weight of the ligands attached.

Chapter 2 : Paired dual carbonate clumped isotopes (Δ_{47}-Δ_{48}) constrains kinetic effects and timescales in peridotite-associated springs at The Cedars, Northern California

Abstract

The Cedars, located in Northern California, represents a class of sites where large-scale geological CO_2 sequestration can take place. The area is characterized by a chain of highly alkaline springs resulting from CO_2-charged meteorological water interacting with a peridotite body. Serpentinization resulting from this interaction at depth leads to the sequestration of various mineral carbonates into veins accompanied by a release of Ca^{2+} and OH^- enriched water to the surface, creating an environment which promotes rapid precipitation of $CaCO_3$ at surface springs. This unique environment enables us to apply the recently developed Δ_{47}-Δ_{48} dual clumped isotope analysis to probe kinetic isotope effects and timescales of CO_2 transformation. We analyze $CaCO_3$ recovered from various localities and identify significant kinetic fractionations associated with CO_2 absorption in a majority of samples, with Δ_{47} enrichment and Δ_{48} depletion relative to equilibrium. Surface floes exhibited the largest kinetic isotope effects ($\Delta\Delta_{47}$: 0.157‰, $\Delta\Delta_{48}$: -0.708‰). Surface floe samples begin to precipitate out of solution within the first hour of CO_2 absorption, and the DIC pool requires a residence time of approximately 100 hours to achieve isotopic equilibria. The Δ_{47}/Δ_{48} slope of samples from the Cedars (-2.803±0.500; 1.s.e.) agrees with published values from lab experiments designed to constrain CO_2 hydrolysis-related kinetic fractionation (-2.911±0.200). The $\Delta_{47}/\delta^{18}O$ slope (-0.008±0.001), and $\Delta_{47}/\delta^{13}C$ slope (0.008±0.001) agree with literature values reported from lab experiments and from a peridotite in Oman. The average modern samples that are close to equilibrium in the Δ_{47}-Δ_{48} space yield an average temperature of 17.9±2.4 °C and is in good agreement with the modern temperature of the Cedar springs (17.0±1.0 °C). Ancient travertine samples that are close to equilibrium in the Δ_{47}-Δ_{48} space yield an average temperature of 8.3±1.1 °C, suggesting that the conditions during that time were approximately 10°C colder than what they are now. The consistency of slopes between in the multi-isotope space suggests the Δ_{47}-Δ_{48} dual carbonate clumped isotope framework can be applied to study CO_2-absorption processes in applied systems including sites of interest for geological sequestration.

2.1 Introduction

Climate change is an ever-growing concern that threatens our collective future. With the rapid input of greenhouse gases into the atmosphere, we have reached a point where the reduction of greenhouse gas emissions needs to be coupled with active removal to prevent the global average temperature increase from exceeding model projections of 1.5 to 2 ºC (IPCC, 2014, 2018). This need has brought negative emission technologies and strategies to the forefront of research efforts. Carbon dioxide removal from the air has been proposed in various forms, including, but not limited to, direct air capture with subsequent geologic sequestration, carbon mineralization via enhanced weathering, and increasing carbon storage in soils and biomass. While each of these approaches has its strengths and weaknesses, it is likely that multiple strategies will need to be used in parallel to reach global carbon dioxide reduction goals, which are 10 Gt/yr by 2050 and 20 Gt/yr by 2100 (UNEP, 2017; Pacala *et al*., 2019). Because the CO_2 captured during this time must be stored such that it remains permanently removed from the atmosphere carbon mineralization and underground sequestration into natural geological formations (Pacala *et al*., 2019) offer a distinct advantage. While underground sequestration in geological formations is promising (Kelemen *et al*., 2019), and one of the most cost-effective prospective options (McCollum *et al*., 2018), in-situ sequestration through carbon mineralization can be achieved at similar storage cost of around $7-$30 per ton of CO_2 sequestered (McCollum *et al*., 2018; Pacala *et al*., 2019). In particular, carbon mineralization involves the long-term and non-toxic sequestration of CO_2 through its chemical transformation into a solid form, such as carbonates (W Seifritz, 1990; Lackner *et al*., 1995; Pacala *et al*., 2019).

Because CO_2 transformation associated with carbon mineralization is into carbonate minerals, sites with an abundance of divalent cations, such as Mg^{2+} and Ca^{2+}, commonly found in

peridotite bodies (Bruni *et al*., 2002; Vinet and Zhedanov, 2011; Paukert *et al*., 2012; Zhang and DePaolo, 2017) are of interest as they can ionically bind and facilitate mineral precipitation. It is hypothesized that serpentinization, a process that involves the hydration of ultramafic minerals, facilitates the carbon mineralization process, which leads to the formation of serpentine and various carbonates (Bruni *et al*., 2002; Vinet and Zhedanov, 2011; Falk *et al*., 2016; García del Real *et al*., 2016; Kelemen *et al*., 2017; Suzuki *et al*., 2017; de Obeso and Kelemen, 2018). Peridotites that could be targeted for sequestration exist worldwide (e.g., Figure 2.1), and thus, research into the dynamics of CO_2 transformation at these sites using isotopic tracers and other approaches is of interest (Cipolli *et al*., 2004; Marques *et al*., 2008; Morrill *et al*., 2013; Falk *et al*., 2016; Christensen *et al*., 2021). At these sites, highly alkaline, high-pH, NaCl, and CaOH charged fluids occur (Figure 2.2; Cipolli *et al*., 2004; Marques *et al*., 2008). These fluids are typically supersaturated with serpentine, indicating that they have interacted with ultramafic rock which has undergone serpentinization (Kelemen and Matter, 2008; Paukert *et al*., 2012; de Obeso *et al*., 2017; Kelemen *et al*., 2017, 2018; Fones *et al*., 2019).

Clumped isotope analysis measures the relative abundance of multiply substituted isotopologues, which have a temperature-dependent preference of aggregation based on relative zero-point energies (Ghosh *et al*., 2006; Schauble *et al*., 2006). The measurement of carbonate clumped isotopes in minerals precipitated from alkaline fluids has a potential to constrain kinetic isotope effects (Tripati *et al*., 2015; Bajnai *et al*., 2020; Guo *et al*., 2020; Lucarelli *et al*., 2022). One prior study has examined clumped isotopes in carbonate veins from the Oman ophiolite (Falk *et al.*, 2016) with a focus on the most abundant multiply-substituted isotopologue of CO_3, m/z 63 ($^{13}C^{18}O^{16}O_2$), measured via gas source isotope ratio mass spectrometry of CO_2 with m/z 47 ($^{13}C^{18}O^{16}O - \Delta_{47}$) , referring to parts per thousand excess of this isotopologue in a sample relative

to a stochastic value) (Eiler and Schauble, 2004; Upadhyay *et al*., 2021). Their findings showed that that carbonate veins from these highly alkaline systems exhibit significant enrichments in the Δ_{47} signature, accompanying a depletion in the $\delta^{18}O$ and $\delta^{13}C$ signatures, consistent with kinetic isotope effects (KIEs) associated with CO_2 absorption-driven disequilibria processes related to the CO_2 hydroxylation reaction being expressed (Falk *et al.,* 2016).

Here, we build on their work using the novel dual carbonate clumped isotope approach that combines Δ_{47} with a second clumped isotope signature ($^{12}C^{18}O_2$ - Δ_{48}) and measure carbonate minerals from alkaline springs at The Cedars, a coastal mountain range with associated peridotite located in Northern California. Our goal is to mechanistically evaluate disequilibria, timescales associated with mineral precipitation, and test a framework established with theory (Tripati *et al.,* 2015; Guo, 2020; Watkins and Devriendt; 2022); experiments (Lucarelli *et al*. 2022); and field-collected samples (Bajnai *et al.,* 2020; Lucarelli *et al*., 2021). The dual measurement of Δ_{47} and Δ_{48} has been theoretically and experimentally shown to have a characteristic equilibrium relationship, and thus the measurement of Δ_{47}-Δ_{48} can be used to identify disequilibrium, examine the origin of KIEs in dissolved inorganic carbon (DIC) and carbonate minerals, and can be used to study the timescales associated with carbonate and mineral evolution through modeling (Hill *et al*., 2014; Tripati *et al*., 2015; Fiebig *et al*., 2019, 2021; Guo, 2020; Bajnai *et al*., 2020; Lucarelli *et al*., 2021).

Herein, we investigate how the isotopic composition of the precipitated carbonate minerals are affected by the highly alkaline spring environment of The Cedars. We examine the measured departures from equilibrium values of clumped (Δ_{47} and Δ_{48}) and bulk ($\delta^{13}C$ and $\delta^{18}O$) and compare measured values to modeled values from simulations to study the origin of KIEs and

timescales associated with DIC pool equilibration and mineral evolution. Finally, we compare our results to published work from other peridotites bodies and evaluate our approach for its potential use in geological CO_2 sequestration applications.

Background

2.1.1 The Cedars

The Cedars is part of the Northern California coastal mountain range, located at N38º37'14.84"/W123º08'02.13, and consist of peridotites in contact with part of the Franciscan Subduction Complex (FSC) (Figure 2.1). The FSC consists of primarily greywacke-type sandstone, greenstone, radiolarian chert, and minor foraminiferal limestone (Blake *et al*., 2012). The peridotite body has an approximate surface area of 22.4 km^2 (3.5 km width / 6.4 km length) and extends 1-2 km below the surface (Coleman, 2000). The peridotite body consists primarily of olivine, orthopyroxene, and clinopyroxene in varying proportions as harzburgite (75% olivine and 25% orthopyroxene/clinopyroxene) and dunite (100% olivine) (Coleman, 2000). Interactions between the peridotite body and groundwaters derived from multiple sources has resulted in serpentinization of 5-20% of the ultramafic body, particularly around the perimeter that is in contact with the FSC, which is predominantly composed of sheared serpentine (R.G. Coleman, 2000; Blake *et al*., 2012). Groundwater discharge from the ultramafic body is highly alkaline, enriched in Ca^{2+} and OH^-, and is brought to the surface through various springs in the area (Coleman, 2004; Sleep *et al*., 2004) where it mixes with relatively neutral pH surface waters charged with atmospheric CO_2 at an elevation between ~275 m and 335 m ASL (Barnes and O'Neil, 1969; Morrill *et al*., 2013).

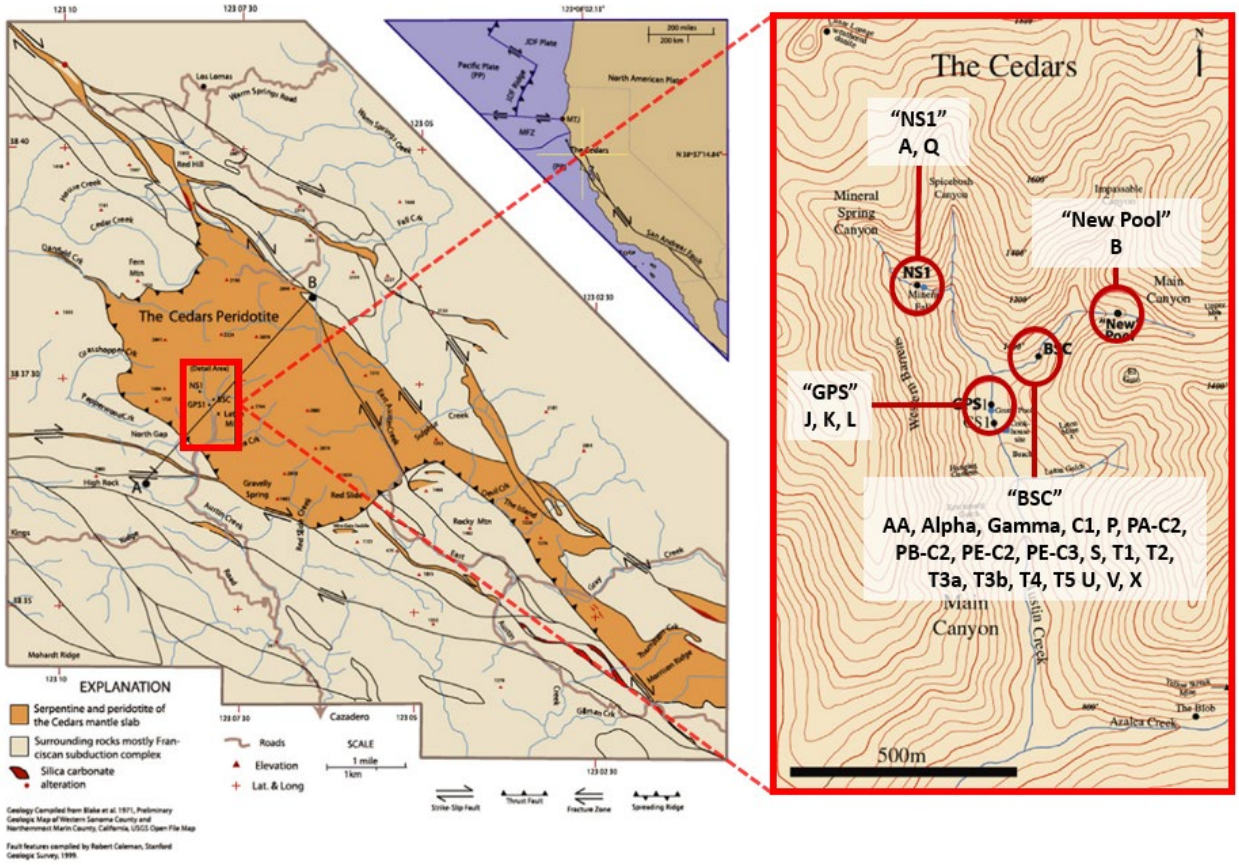

Figure 2.1 Map of the Cedars site showing the location of samples. Sample groups shown in right panel re: NS1 (Samples: A, Q,), Grotto Pool Springs (GPS)(Samples: J, K, L), Barnes Spring Complex (BSC) (Samples: AA, Alpha, Gamma C1, P, PA-C2, PB-C2, PE-C2, PE-C3, S, T1, T2, T3a, T3b, T4, T5, U, V, X), and New Pool (Samples: B). The "Wedding Cake" is located at the NS1 location above the Mineral Falls. Modified from Christensen *et al.* (2021)

2.1.2 Serpentinization

Serpentinization can be described by Equations 1-3 listed below. Olivine {$(Mg, Fe)_2SiO_4$} and pyroxene {$(Ca, Mg, Fe)_2Si_2O_6$)} react with CO_2-charged water to form serpentine, magnetite, and carbonates. These carbonate minerals, $MgCO_3$ (magnesite), $CaMg(CO_3)_2$ (dolomite), and $CaCO_3$ (calcite) are sequestered as solids into veins within the peridotite body. Ongoing serpentinization of mantle peridotite bodies by meteoric waters can be identified by highly alkaline water in proximate springs, stable isotope ratios of precipitated carbonate minerals, the formation of travertines in the carbonate precipitant mix and carbonate veins in the hosting peridotite body (Bruni *et al*., 2002; Cipolli *et al*., 2004). Barnes and O'Neil *et al.* (1969) conducted early research on ultramafic formations undergoing serpentinization and developed a conceptual model for the process that is illustrated in Figure 2.2. Meteoric groundwater charged with atmospheric CO_2 reacts with the peridotite body near the surface and forms water that is rich in Mg^{2+}-HCO_3^- - Type 1 waters (Barnes and O'Neil *et al.*, 1969). As this water moves underground and comes in contact with the peridotite body, the serpentinization process is catalyzed by CO_2-charged H_2O, leading to the precipitation of $MgCO_3$ (magnesite) and small amounts of $CaMg(CO_3)_2$ (dolomite) and $CaCO_3$ (calcite) into veins in the peridotite. A sharp elevation in pH accompanies the mineral precipitation due to the enrichment of the water solution with OH^- anions. This Type 2 water also exhibits significant enrichment in Ca^{2+} cations and DIC depletion. Type 2 water is brought up to the surface which then interacts with Type 1 waters, instantly supersaturating the fluids with respect to carbonates and leading to the precipitation of calcite, aragonite, and travertine in surface springs.

$$2Mg_2SiO_4 + Mg_2Si_2O_6 + 4H_2O \rightarrow 2Mg_3Si_2O_5(OH)_4 \quad (1)$$

$$Mg_2SiO_4 + 2CO_2 \rightarrow 2MgCO_3 + SiO_2 \quad (2)$$

$$Mg_2SiO_4 + CaMgSi_2O_6 + 2CO_2 + 2H_2O \rightarrow 2Mg_3Si_2O_5(OH)_4 + CaCO_3 + MgCO_3 \quad (3)$$

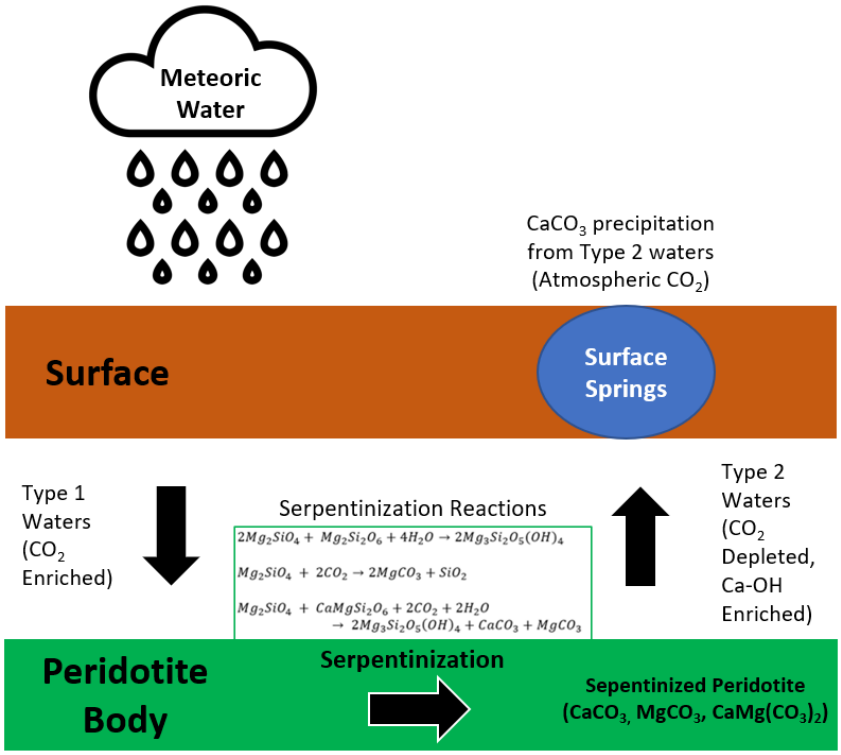

Figure 2.2 Processes associated with CO_2 absorption and transformation at the Cedars. Surface waters from meteoric sources are enriched with CO_2 from the atmosphere ("Type 1" waters) and then seep into the ground and interact with ultramafic peridotite. Through a series of serpentinization reactions, various carbonate minerals precipitate (calcite, magnesite, and dolomite) and are sequestered in pores and fractures resulting in veins in the peridotite body. Reaction by-products are ejected into pore waters ("Type 2" waters) which are enriched in Ca^{2+} and OH^- ions and depleted in CO_2, are shuttled to the surface. Type 1 and Type 2 interact at the surface in the presence of atmospheric CO_2, resulting in rapid precipitation of $CaCO_3$. Terminology from Barnes *et al.* (1969).

2.1.3 Dissolved Inorganic Carbon (DIC) Transformation in H_2O

CO_2 dissolution and transformation in aqueous media follow reactions 4-8. Due to the high alkalinity (pH = 11.5) of the Cedars system, CO_2 uptake into the water is increased (Lívanský, 1982; Devriendt *et al*., 2017). Once the CO_2 is dissolved in an aqueous solution, it undergoes hydration or hydroxylation reactions leading to the formation of HCO_3^-, as seen in reactions 4 and 6. These two reactions are the most important in understanding $^{18}O/^{16}O$ isotopic equilibration as they provide the only route for the direct exchange of O atoms between H_2O and DIC (Zeebe and Wolf-Gladrow, 2001). Reactions 6-8 show the pathway from HCO_3^- to CO_3^{2-} and splitting of water molecules. These reactions also contribute to clumped and oxygen isotope equilibration of DIC in an aqueous solution.

$$CO_2 + H_2O \leftrightarrow HCO_3^- + H^+ \quad (4)$$

$$CO_2 + OH^- \leftrightarrow HCO_3^- \quad (5)$$

$$HCO_3^- + OH^- \leftrightarrow H_2O + CO_3^{2-} \quad (6)$$

$$HCO_3^- \leftrightarrow H^+ + CO_3^{2-} \quad (7)$$

$$H_2O \leftrightarrow H^+ + OH^- \quad (8)$$

The amount of time required for isotopic equilibrium to be achieved is governed by the temperature-dependent forward and reverse rate constants for the hydration and hydroxylation reaction pathways (Zeebe and Wolf-Gladrow, 2001; Tripati *et al*., 2015; Guo, 2020), as well as DIC speciation. DIC speciation is a function of temperature and pH (Uchikawa and Zeebe, 2012; Tripati *et al*., 2015). Reactions 1-3 proceed more slowly at elevated pH and reduced temperature such that oxygen and clumped isotope disequilibrium can occur unless there is sufficient time to

reach equilibrium (Beck *et al*., 2005; Zeebe and Wolf-Gladrow, 2001; Tripati *et al*., 2015; Guo, 2020). At pH > 10, similar to what is observed in Type 1 and Type 2 waters in massive peridotite bodies like the Cedars, the time to reach equilibration is significantly increased due to DIC speciation being dominated by CO_3^{2-}, resulting in low concentrations of CO_2 remaining for isotopic exchange reactions 1 and 2 (Beck *et al*., 2005; Hill *et al*., 2014; Tripati *et al*., 2015; Weise and Kluge, 2020). If the DIC pool does not have sufficient time to achieve isotopic equilibrium, disequilibrium isotopic compositions may be recorded in the mineral.

2.1.4 Carbonate "Clumped" Isotope Geochemistry and Notation

There are 20 different isotopologues of CO_2, with four that are singly-substituted and contain either a heavy isotope of carbon or oxygen. The singly substituted variants are the most abundant and makeup about 99.99% of carbonate ions in minerals (Eiler and Schauble, 2004; Eiler, 2007). The remaining 16 are multiply substituted "clumped" variations that contain heavy isotopes of carbon and/or oxygen (Ghosh *et al*., 2006). Below are examples of two isotopic disproportionation reactions (Polyakov *et al*., 2005) of interest as they generate isotopologues of carbonates that have relative abundances within the detection limits of modern instrumentation.

$$[^{12}C^{16}O^{18}O^{16}O]^{2-} + [^{13}C^{16}O^{16}O^{16}O]^{2-} \leftrightarrow [^{12}C^{16}O^{16}O^{16}O]^{2-} + \mathbf{[^{13}C^{16}O^{18}O^{16}O]^{2-}} \quad (9)$$

$$[^{12}C^{16}O^{18}O^{16}O]^{2-} + [^{12}C^{18}O^{16}O^{16}O]^{2-} \leftrightarrow [^{12}C^{16}O^{16}O^{16}O]^{2-} + \mathbf{[^{12}C^{18}O^{18}O^{16}O]^{2-}} \quad (10)$$

While there are many versions of the isotopic disproportionation reactions, like the ones above, reactions 9 and 10, respectively, yield the most abundant m/z 63 (67 ppm) and m/z 64 isotopologues (12 ppm) (Ghosh *et al*., 2006). The temperature dependency of these disproportionation reactions and the preference of heavy isotope aggregation as a function of mineral precipitation temperature is the basis of the carbonate clumped isotope thermometer

(Ghosh *et al*., 2006; Schauble *et al*., 2006) However, one critical caveat to this correlation is that the carbonate isotopologues must be at isotopic equilibrium. This means that the preferential aggregation of heavy isotopes must not be inhibited and that it must achieve equilibrium conditions at the respective temperature. (Ghosh *et al*., 2006)

No current technique allows for the direct measurement of clumped isotopes in carbonate minerals. Thus, m/z 63 and m/z 64 carbonate ions within the mineral are converted to gaseous m/z 47 and m/z 48 CO_2, respectively, by phosphoric acid digestion and measured in a gas-source isotope-ratio mass spectrometer (Ghosh *et al*., 2006).

The Δ_{47} and Δ_{48} quantities refer to the abundance of m/z 47 [$^{18}O^{13}C^{16}O$] and m/z 48 [$^{18}O^{12}C^{18}O$] CO_2 isotopologues relative to a stochastic or random distribution, described by equations 11 and 12,

$$\Delta_{47} = \left[\left(\frac{R_{47}}{R_{47}^*} - 1\right) - \left(\frac{R_{46}}{R_{46}^*} - 1\right) - \left(\frac{R_{45}}{R_{45}^*} - 1\right)\right] * 1000 \quad (11)$$

$$\Delta_{48} = \left[\left(\frac{R_{48}}{R_{48}^*} - 1\right) - 2 * \left(\frac{R_{46}}{R_{46}^*} - 1\right)\right] * 1000 \quad (12)$$

where R_i and R_i^* represent the measured and stochastic ratios of i/44 isotopologue (Eiler and Schauble, 2004; Z. Wang *et al*., 2004; Affek and Eiler, 2006). We report all values of Δ_{47} on the Intercarb-Carbon Dioxide Equilibrium Scale (I-CDES) (Bernasconi *et al*., 2021), which adjusted to an acid digestion temperature of 90 ºC. Δ_{48} values are reported in the Carbon Dioxide Equilibrium Scale at 90 ºC, CDES90 (Lucarelli *et al*., 2021).

The conversion of carbonate minerals into gaseous CO_2 has a temperature dependent preferential removal of O^{16} relative to O^{18} and is corrected by an acid fractionation factor (AFF), denoted by *y* in Equations 13 and 14.

$$\Delta_{47} = \Delta_{63} + y \quad (13)$$

$$\Delta_{48} = \Delta_{64} + y \quad (14)$$

No AFF is applied to measured values but was used for the comparison of measured Δ_{47} and Δ_{48} values to theoretical Δ_{63} and Δ_{64} values. The reference frame and temperature to which the value is being converted also dictates the value of *y*. In the I-CDES reference frame, for the conversion of Δ_{63} to Δ_{47}, the AFF varies from 0.188 to 0.197 from calcite precipitation temperatures ranging from 1000 ºC to 0 ºC, respectively (Hill *et al*., 2014; Tripati *et al*., 2015; Bernasconi *et al*., 2021; Lucarelli *et al*., 2021). For the temperature ranges of the samples collected from The Cedars, we use the AFF *y*=0.196 for the conversion of Δ_{63} to Δ_{47} (Lucarelli *et al*., 2021). For the conversion of Δ_{64} to $\Delta_{48,}$ in the CDES90 reference frame (Hill *et al*., 2014; Tripati *et al*., 2015), we use 0.131 (Lucarelli *et al*., 2021) as the AFF.

2.1.5 Kinetic Fractionation in Clumped Isotope Signatures

Various mechanisms have been proposed to explain isotopic disequilibria in clumped and stable isotope signatures. Tang *et al.* (2014) hypothesized that kinetic fractionation observed in inorganic calcite precipitation experiments at pH ≥ 10 occurred due to the DIC pool not having sufficient time to achieve isotopic equilibrium prior to mineral precipitation and DIC speciation favoring CO_3^{2-} at higher pH (Beck *et al*., 2005; Hill *et al*., 2014, 2020; Tripati *et al*., 2015). CO_2 (de)hydration and (de)hydroxylation reactions have also been hypothesized to give rise to isotopic

disequilibrium through CO_2 absorption or degassing pathways (Guo, 2020; Boettger and Kubicki, 2021). CO_2 absorption dominant disequilibria processes, arising from (de)hydration and (de)hydroxylation reactions, have been seen in many hyperalkaline springs, and in the Oman ophiolite, due to the favorable increase in CO_2 absorption in H_2O at elevated pH (Falk *et al*., 2016).

Kinetic isotope effects have been reported for Δ_{47} in most Earth-surface carbonate mineral species (Daeron *et al*., 2019). KIEs in biotic and abiotic systems associated with (de)hydration and (de)hydroxylation reactions can drive deviations from clumped isotope equilibrium (Ghosh *et al*., 2006; Guo, 2009; Saenger *et al*., 2012; Falk *et al*., 2016; Spooner *et al*., 2016), as can CO_2 degassing, as exhibited kinetic fractionation in the carbonate mineral-clumped isotope signatures of speleothems (Affek *et al*., 2008; Guo *et al*., 2011). Biotic carbonate minerals such as brachiopod shells (Bajnai *et al*., 2018) and coral skeletons (Thiagarajan *et al*., 2011; Saenger *et al*., 2012; Tripati *et al*., 2015; Kimball *et al*., 2016; Spooner *et al*., 2016) are known to have biological effects that lead to kinetic departures in clumped isotope signatures.

Kinetic biases should also be expressed in the novel dual clumped isotopes system of Δ_{47}-Δ_{48} (Tripati *et al*., 2015; Hill *et al*., 2020; Fiebig *et al*., 2019; Guo and Zhou, 2019; Guo, 2020; Bajnai *et al*., 2020; Lucarelli *et al*., 2021, 2022). It is important to note that KIE trajectories are not well constrained due to the limited number of studies that have been conducted. Guo *et al.* (2020) aimed to constrain KIEs in Δ_{47}, Δ_{48}, and $\delta^{18}O$ in the HCO_3^- endmember in (de)hydration and (de)hydroxylation reactions occurring in CO_2 absorption, CO_2 degassing, and DIC-H_2O exchange driven disequilibria pathways. Bajnai *et al.* (2020) provided regressions relative to equilibrium values to correct kinetic biases of carbonate mineral samples from warm and cold-

water coral, belemnite, stalagmite, speleothems, and brachiopod in Δ_{47}-Δ_{48} dual clumped isotope space (Fiebig *et al*., 2019; Bajnai *et al*., 2020a). These studies did not, however, explore the possible magnitude of the KIEs especially in the CO_2 absorption regime operating at the kinetic limit. Lucarelli *et al.* (2022) conducted lab experiments where $CaCO_3$ was precipitated at high pH in the presence and absence of carbonic anhydrase, and measured samples in the Δ_{47}-Δ_{48} dual clumped isotope space. They found significant KIEs arising from CO_2 hydroxylation and DIC speciation, and their hypothesis was that they were operating at the kinetic limit due to the associated rapid precipitation in their experiments.

2.2 Materials and Methods

2.2.1 Sampling

Cedars Samples

The $CaCO_3$ samples used for this study were collected from The Cedars by Christensen *et al.* (2021), spanning eight visits in 2013, 2014, 2016, and 2018. Four major sites, seen in Figure 2.1, were sampled: (1) NS1 "Wedding Cake" (Samples: A, Q), The Barnes Spring Complex (BSC) (Samples: AA, Alpha, Gamma, C1, P, PA-C2, PB-C2, PE-C2, PE-C3, S, T1, T2, T3a, T3b, T4, T5, U, V, X), Grotto Pool Springs (GPS) (Samples: J, K, L), and the "New Pool" (Sample: B). The "Wedding Cake," where some of the samples were taken, is at the NS1 location above the Mineral Falls. Water samples from the high pH springs were taken using a 0.22 μm Millipore filter unit, acidified to a pH of 2 using HNO_3, and collected in high-density polyethylene (HDPE) bottles. The pH of the water was measured onsite using a Thermo-Scientific, Orion hand-held pH meter. Other $CaCO_3$ samples were collected from several different localities within the circled regions adjacent to the springs seen in Figure 2.1: (1) partially consolidated materials from rims of pools;

(2) precipitates from the surface of pools, also known as floes; (3) dendritic forms and encrustations from sites of creek-spring mixing; (4) unconsolidated material, also known as snow, from the bottom of the pools; and (5) solid, old travertine deposits, taken as a hand sample, representing different layers, collected from the BSC. Any consolidated, or partially consolidated surface materials were skimmed from the surface or captured on screens based on the location they were collected from. Specific sample information including composition and location of recovery is listed in Table 2.1. Temperature measurements were taken of the water source at the time of $CaCO_3$ recovery. All terminology used to describe samples in this paper are after Christensen *et al.* (2021).

Sample Name	Sample Composition	Location	Notes
A	Travertine	NS1	Wedding Cake - Rim Formation
AA	Arag 91%; Calc 1%; Brucite 8%	BSC	Mixed Water (BSC + Creek)
Alpha	Travertine	BSC	Wedding Cake - Rim Formation
B	Unspecified (Non-Travertine)	New Pool	Mixed Water (New Pool Spring + Creek)
C1	Arag 86%; Calc 7%; Brucite 7% bottom	BSC	Snow - Bottom of Pool
Gamma	Travertine	BSC	Rim of Wedding Cake Formation
J	Unspecified (Non-Travertine)	GPS	Unspecified
K	Arag 25%; Calc 20%; Hydromagnesite 50%; Nitromagnesite 2%; Nesquehonite 3%	GPS	Snow - Bottom of Pool
L	Unspecified (Non-Travertine)	GPS	Pool Floe
P	Arag 78%; Calc 18%; Brucite 4%	BSC	Pool Floe
PA-C2	Unspecified (Non-Travertine)	BSC	Snow - Bottom of Pool
PB-C1	Arag 86%; Calc 7%; Brucite 7%	BSC	Snow - Bottom of Pool
PB-C2	Arag 46%; Calc 49%; Brucite 5%	BSC	Outer Edge Surface
PE-C2	Arag 78%; Calc 18%; Brucite 4%	BSC	Outer Edge Surface
PE-C3	Unspecified (Non-Travertine)	BSC	Snow - Bottom of Pool
Q	Unspecified (Non-Travertine)	NS1	Wedding Cake - Floe
S	Unspecified (Non-Travertine)	BSC	Mixed Water (BSC + Creek)
T1	Travertine	BSC	Hand Sample - Multiple Layers
T2	Travertine	BSC	Hand Sample - Multiple Layers
T3a	Travertine	BSC	Hand Sample - Multiple Layers
T3b	Travertine	BSC	Hand Sample - Multiple Layers
T4	Travertine	BSC	Hand Sample - Multiple Layers
T5	Travertine	BSC	Hand Sample - Multiple Layers

U	Unspecified (Non-Travertine)	BSC	Pool Floe
V	Unspecified (Non-Travertine)	BSC	Pool Floe
X	Unspecified (Non-Travertine)	BSC	Pool Floe

Table 2.1 Cedars sample information. Sample name, locations, and notes were provided by Christensen *et al.* (2021).

2.2.2 Analysis and Instrumentation

All isotopic measurements were made using two Nu Instruments Perspective isotope ratio mass spectrometers (IRMS) over the time frame 2019 to 2021. Both Nu Instruments Perspective IRMS systems produce statistically indistinguishable Δ_{47} (Lucarelli *et al*., 2021; Upadhyay *et al*., 2021) and Δ_{48} data (Lucarelli *et al*., 2021) with standards that agree with published values from other labs for Δ_{47} (Bernasconi *et al*., 2021) and Δ_{48} (Bajnai *et al*., 2020; Swart *et al*., 2021). The general configuration for sample processing on these two instruments is (1) phosphoric acid digestion and conversion of $CaCO_3$ to CO_2 gas, (2) CO_2 gas purification, and (3) Nu Instruments Perspective IRMS system. For descriptive purposes, these instruments will be labeled NuIP IRMS 1 and NuIP IRMS 2. Clumped isotopic measurements were performed on evolved CO_2 produced using a common acid bath (CAB) approach. In this approach, 0.4-0.6 mg $CaCO_3$ samples were subjected to phosphoric acid digestion at 90 ºC for approximately 20 minutes, leading to the evolution of CO_2 gas, which is then subjected to intensive purification. NuIP IRMS 1 used an in-house built, automated system commonly referred to as the "Autoline," a modified version of the Passey style system (Passey *et al*., 2010), further described below. The "system consists of (1) a Costech Zero Blank autosampler or custom-built Fairbanks device made of stainless steel that is capable of pulling high vacuum, (2) a CAB for phosphoric acid digestion of samples that are reacted for 20 minutes at 90 ºC, (3) cryogenic traps (dry ice and ethanol, and liquid nitrogen) for CO_2 purification through removal of water and other gases with low vapor pressures, and collection of CO_2, (4) a Gas Chromatograph (GC) column (UHP Helium carrier gas, Porapak Type-Q TM 50/80 mesh column packing material) held at -20 ºC during the gas transit to separate CO_2 from the remaining components of the produced gas mixture, (5) an in-line elemental-silver wool (Sigma-Aldrich) column before the GC column to remove sulfur compounds from the gas

mixture, and (6) a final cryogenic purification stage before transfer of CO_2 into the bellows of the mass spectrometer. The use of a GC column packed with Porapak-Q and helium as a carrier gas enables this system to handle larger samples with significant organic content and small amounts of pure carbonate compared to other systems (Upadhyay *et al*., 2021). Upon leaving the Autoline, CO_2 gas was further purified through an Adsorption Trap (AdTrap), an-inline, short GC column packed with Porapak Type-Q^{TM} 50/80. On the NuIP IRMS 2 system, the gas was sent directly to the AdTrap. Upon purification, the gas is transferred to the IRMS system, which continuously references a standard CO_2 gas against the sample gas through a changeover block system. All samples, except for sample Gamma (Table 2.1), had a minimum of three replicates run and analyzed, regardless of which instrument they were run on. The number of replicates run was dictated by the amount of sample provided, how precise the data was, and robustness of standards. One sample (Gamma) had insufficient material for three replicate analyses and is denoted with an open shape in figures.

Description of Nu Instruments Perspective IRMS

The Nu Perspective IRMS is a mass spectrometer that is optimized for clumped isotope analysis with secondary electron suppression, which reduces the signal-to-noise ratio. Energy filters and quadratic lenses fitted in front of the Faraday collector array drives the suppression. Both NuIP IRMS 1 and NuIP IRMS 2 have identical mass spectrometer configurations. The detectors for masses 44, 45, and 46 are registered through $3x10^8$, $3x10^{10}$, and $3x10^{11}$ Ω resistors, respectively. The detectors for masses 47, 48, and 49 are registered with $3x10^{12}$ Ω resistors. Detectors for masses 47, 48, and 49 are shielded by secondary electron suppressors. A dual-inlet system allows for the input of the sample gas and a reference gas controlled by a bellows system that inputs both gasses through a changeover block, so the sample and reference gases can be

compared in real-time. This bellow system has four blocks of 15 cycles for a total of 60 cycles of sample to standard comparison with an 8-second changeover delay and 20 seconds of integration per cycle for a total integration time of 1200 seconds. There are continuous pressure adjustments using a Newtonian zeroing technique, with balancing to achieve 80 nA (or 16 V) on mass 44 at every acquisition, compared to just at the beginning of the block (Lucarelli *et al*., 2021; Upadhyay *et al*., 2021).

Standardization and data processing

The CO_2 reference gas used to establish real-time comparison to unknown sample compositions was sourced from Oztech and has an isotopic composition as follows: $\delta^{18}O_{V\text{-}SMOW}$ = 24.9 ‰; $\delta^{13}C_{V\text{-}PDB}$ = -3.56 ‰. $CaCO_3$ standards, for which all Δ_{47} and Δ_{48} are presented relative to, include Carmel Chalk, CMTile, ETH-1, ETH-2, ETH-3, ETH-4, and Veinstrom (Lucarelli *et al*., 2021; Upadhyay *et al*., 2021). International standards ETH-1 and ETH-2 were the primary standards used to make non-linearity corrections associated with both Δ_{47} and Δ_{48} raw data. Mean values for Δ_{47}, Δ_{48}, $\delta^{18}O$, and $\delta^{13}O$ of the $CaCO_3$ standards are given in Table 2.2 and raw and standardized data for all standards and samples will be archived on EarthChem upon publication.

	$\Delta_{47\ (I\text{-}CDES)}$ (‰)	$\Delta_{48\ (CDES90)}$ (‰)	$\delta^{18}O_{V\text{-}PDB}$ (‰)	$\delta^{13}C_{V\text{-}PDB}$ (‰)
CMTile	0.313	0.145	-1.524	2.031
Carmel Chalk	0.592	0.237	-3.948	-2.183
Veinstrom	0.713	0.272	-12.612	-6.166
ETH-1	0.205	0.132	-2.187	2.028
ETH-2	0.209	0.132	-18.671	-10.162
ETH-3	0.613	0.247	-1.741	1.706
ETH-4	0.451	0.201	-18.81	-10.2

Table 2.2 Clumped and stable isotope data for all carbonate standards. All Δ_{47} data is presented in the I-CDES reference frame and the Δ_{48} data is presented in the CDES90 reference frame. ETH-1 and ETH-2 are used to make non-linearity corrections to the raw data.

Data was processed and corrected using Easotope 64-bit, release version 20201231 (Cédric M. John and Bowen, 2016) with IUPAC parameters (Brand *et al*., 2010; Daëron *et al*., 2016). The Δ_{47} and Δ_{48} clumped isotope signatures are in the I-CDES and CDES90 reference frames, respectively. The I-CDES reference frame is also in the 90 ºC temperature, so no additional corrections have to be applied to compare $\Delta_{47\ (\text{I-CDES})}$ and $\Delta_{48\ (\text{CDES90})}$ (Bernasconi *et al*., 2021; Lucarelli *et al*., 2021; Upadhyay *et al*., 2021).

Equilibrium Values

Oxygen isotope equilibrium is calculated for calcite samples at The Cedars using a temperature of 17.5 ºC and water $\delta^{18}O_{\text{V-PDB}}$ of -35.5 ‰ (Christensen *et al*., 2021) and the equation of Kim and O'Neil (1997). Δ_{47} and Δ_{48} equilibrium is calculated using a temperature of 17.5 ºC and the reported relationships from Lucarelli *et al.* (2021).

(15)
$$\begin{aligned}\Delta_{47\ I-CDES\ EQ} &= [0.6646 \pm 0.0009] - [0.0032 \pm (3.033 \times 10^{-5})]T \\ &+ [(1.012 \times 10^{-5}) \pm (2.449 \times 10^{-7})]T^2 \\ &- [(1.559 \times 10^{-8}) \pm (6.717 \times 10^{-10})]T^3 \\ &+ [(9.251 \times 10^{-12}) \pm (5.802 \times 10^{-13})]T^4\end{aligned}$$

(16) $$\Delta_{48\ CDES90\ EQ} = [0.2842 \pm 0.0009] - [0.0014 \pm (3.048 \times 10^{-5})]T + [(5.741 \times 10^{-6}) \pm (2.437 \times 10^{-7})]T^2 - [(1.017 \times 10^{-8}) \pm (6.749 \times 10^{-10})]T^3 + [(6.570 \times 10^{-12}) \pm (5.830 \times 10^{-13})]T^4$$

An equilibrium Δ_{48}/Δ_{47} relationship, Equation 17, was determined experimentally by Lucarelli *et al.* (2021) and is used here to provide a reference for equilibrium conditions.

(17) $$\Delta_{48(CDES90)} = (0.1132 \pm 0.010) + (0.008 \pm 0.055)\Delta_{47(CDES90)} + (0.3692 \pm 0.065)\Delta^2_{47(CDES90)}$$

2.2.3 Modeling of DIC-H_2O-CO_2 System Using IsoDIC

To study the evolution of the CO_3^{2-} endmember in a CO_2 absorption driven pathway that simulated the conditions of The Cedar's springs, we used the IsoDIC modeling software developed by Guo *et al.* (2019, 2020). This modeling software predicts kinetic isotope fractionation in clumped isotopes in a DIC-H_2O-CO_2 system. It simulates (de)hydration and (de)hydroxylation reactions 1-5, for the evolution of CO_2 to CO_3^{2-}, and the isotopologue reactions involving all major isotopes of C and O. This equates to a total of 155 reactions. The forward and reverse rate constants were estimated using Equation 18 below,

$$k^* = a_{KIE} * k \qquad (18)$$

where k is the rate constant of the isotopically non-substituted reactions, and a_{KIE} is the kinetic isotope fractionation factor for the isotopically substituted reaction. The product of these variables yields k^*, the modified rate constant for the isotopically substituted reaction. (De)hydration and (de)hydroxylation reactions, Equation 1 and 2, are the only reactions that contribute to isotopic fractionation where Equations 3-5 are assumed to be at equilibrium due to their relative rates of reaction when compared to Equations 1 and 2 (Guo, 2019, 2020a).

Parameters measured *in-situ* from The Cedars were used to simulate conditions associated with The Cedars Springs (Morrill *et al*., 2013). The following parameters were input into the IsoDIC software to perform modeling in the CO_2 absorption regime: (1) solution temperature: 17.5 ºC, (2) solution pH: 11.5, (3) air pCO_2: 400 ppm, (4) $\delta^{13}C$ air: -8.431 ‰, (5) $\delta^{18}O$ air: 0.144 ‰. The system evolution time parameter was set to 1, 10, 50, 100, and 1000 hours to simulate different timescales for the evolution of the HCO_3^- and CO_3^{2-} DIC species. The equations used by this model are described in greater detail in the Supplementary Materials, S.2.1.

2.2.4 Modeling of $CaCO_3$-DIC-H_2O System Using COAD

To model the KIEs in both the clumped isotope and stable isotope data, of the mineral carbonates with respect to the conditions at The Cedars, we used the COAD (carbon, oxygen, α, Δ) model adapted from the ExClump38 model (Chen *et al*., 2018; Uchikawa *et al*., 2021). The COAD model uses two MATLAB scripts to simulate KIEs associated with exchange reactions with the DIC-H_2O system and crystal growth reactions in the $CaCO_3$-DIC system (Watkins and Devriendt, 2022). We used this in conjunction with the IsoDIC model because it takes mineral growth rate into account, which has been hypothesized to influence the clumped isotope composition (Tripati *et al*., 2015). It takes an ion-ion approach first developed by Chen *et al.* (2018) for calculations associated with C and O isotopes. This ion-ion model was then expanded by

Uchikawa *et al.* (2021) to include Δ_{47}, and was subsequently labeled ExClump38. It was further expanded to include Δ_{48} by Watkins *et al.* (2022). The isotope kinetic fractionation factors (KFFs) used in the IsoDIC software (Guo, 2020a) were used in the COAD model. Eight differential equations model the chemical and isotopic evolution of DIC species in solution. Nine additional differential equations are used to calculate the $\delta^{18}O$, $\delta^{13}C$, Δ_{47}, and Δ_{48} of the $CaCO_3$ (Watkins and Hunt, 2015; Watkins and Devriendt, 2022). In addition to modeling the five major reactions, Equations 1-5, that IsoDIC uses, it also considers mineral growth rate reactions in the mineral precipitation script of the COAD model. The equations used for this can be seen in Equations 19 and 20 below.

$$Ca^{2+} + HCO_3^- \leftrightarrow CaCO_3 + H^+ \qquad (19)$$

$$Ca^{2+} + CO_3^{2-} \leftrightarrow CaCO_3 \qquad (20)$$

The rate constants associated with Equations 17 and 18 are mass-dependent (Watkins and Hunt, 2015), and the flux of precipitated $CaCO_3$ is controlled by the concentrations of $[Ca^{2+}]$ and $[CO_3^{2-}]$. In contrast to the IsoDIC model, this model only describes the most abundant isotopolouges for the respective masses, while IsoDIC describes all isotopolouges in the DIC-H_2O system. A more thorough description of the equations used can be viewed in Supplemental Materials, S.2.

For our purposes, this model was used to simulate $\delta^{18}O$, $\delta^{13}C$, Δ_{47}, Δ_{48}, and molar precipitation rate of $CaCO_3$ (R_p) using modified parameters from Christensen *et al.* (2021) for The Cedars, which were updated due to an error in the code originally used in the study. Those parameters are in Supplemental Materials, S.2. Code is available on the Tripati Lab Github at (https://github.com/Tripati-Lab/Parvez-et-al.-2022-Cedars-)

2.3 Results

All clumped isotope and stable isotope data are reported in Table 2.3. The equilibrium regions shown on all figures are from Lucarelli *et al* (2021).

Sample Name	Number of Replicates	$\delta^{13}C_{V\text{-}PDB}$ (‰)	1 s.d.	$\delta^{18}O_{V\text{-}PDB}$ (‰)	1 s.d.	$\Delta\delta^{18}O$	$\Delta_{47\ I\text{-}CDES}$ (‰)	1 s.e.	$\Delta\Delta_{47}$	$\Delta_{48\ CDES90}$ (‰)	1 s.e.	$\Delta\Delta_{48}$	End Member
A	4	-14.053	0.035	-3.593	0.061	-2.060	0.644	0.005	0.032	0.256	0.017	-0.006	Equilibrium
AA	4	-12.417	0.006	-2.897	0.150	-1.364	0.654	0.014	0.042	0.193	0.086	-0.069	Equilibrium
Alpha	4	-9.580	0.061	-2.793	0.012	-1.260	0.651	0.003	0.039	0.173	0.029	-0.088	Equilibrium
B	3	-11.977	0.021	-3.700	0.010	-2.167	0.637	0.008	0.025	0.237	0.009	-0.024	Equilibrium
C1	5	-16.157	0.040	-7.900	0.122	-6.367	0.762	0.036	0.150	0.141	0.031	-0.121	Mixed
Gamma	2	-18.255	0.205	-13.395	0.035	-11.862	0.665	0.103	0.053	-0.093	0.104	-0.354	Mixed
J	4	-13.227	0.046	-0.073	0.139	1.460	0.600	0.004	-0.011	0.000	0.000	-0.261	Equilibrium
K	10	-15.625	0.135	-7.203	0.183	-5.669	0.728	0.011	0.116	0.140	0.032	-0.122	Mixed
L	5	-23.447	0.047	-15.170	0.036	-13.637	0.787	0.006	0.176	-0.221	0.015	-0.483	Disequilibrium
P	5	-27.302	0.008	-19.272	0.040	-17.739	0.786	0.012	0.174	-0.274	0.032	-0.536	Disequilibrium
PA-C2	3	-20.053	0.150	-10.557	0.127	-9.024	0.714	0.014	0.102	-0.036	0.064	-0.298	Mixed
PB-C1	3	-17.417	0.031	-8.573	0.064	-7.040	0.715	0.026	0.103	-0.019	0.038	-0.280	Mixed
PB-C2	3	-20.160	0.099	-12.340	0.014	-10.807	0.733	0.012	0.121	-0.416	0.180	-0.677	Disequilibrium
PE-C2	6	-21.978	0.182	-14.595	0.320	-13.062	0.768	0.008	0.157	-0.299	0.081	-0.561	Disequilibrium
PE-C3	4	-16.135	0.148	-7.965	0.219	-6.432	0.689	0.012	0.077	0.007	0.094	-0.254	Mixed
Q	5	-17.617	0.029	-6.743	0.051	-5.210	0.695	0.016	0.083	0.168	0.011	-0.093	Equilibrium
S	3	-11.690	0.014	-2.640	0.057	-1.107	0.612	0.011	0.000	0.174	0.029	-0.088	Equilibrium

T1	8	-9.806	0.076	-3.279	0.115	-1.745	0.623	0.015	0.012	0.162	0.024	-0.100	Equilibrium
T2	9	-14.660	0.034	-9.733	0.070	-8.199	0.705	0.015	0.094	0.015	0.058	-0.246	Mixed
T3a	9	-14.775	0.060	-9.113	0.209	-7.579	0.737	0.031	0.125	-0.019	0.033	-0.280	Mixed
T3b	3	-13.795	0.049	-7.875	0.177	-6.342	0.702	0.023	0.090	0.013	0.046	-0.249	Mixed
T4	3	-9.980	0.079	-3.537	0.075	-2.004	0.662	0.023	0.050	0.171	0.018	-0.090	Equilibrium
T5	3	-9.243	0.025	-3.057	0.040	-1.524	0.661	0.020	0.049	0.175	0.030	-0.086	Equilibrium
U	8	-26.603	0.049	-18.671	0.064	-17.138	0.769	0.009	0.157	-0.446	0.077	-0.708	Disequilibrium
V	8	-23.780	0.082	-14.802	0.094	-13.269	0.794	0.013	0.182	-0.206	0.031	-0.468	Disequilibrium
X	8	-22.430	0.081	-15.504	0.083	-13.971	0.678	0.014	0.066	-0.158	0.050	-0.420	Disequilibrium

Table 2.3 Clumped and stable isotope data for all samples collected from the Cedars. All Δ_{47} data is presented in the I-CDES reference frame and the Δ_{48} data is presented in the CDES90 reference frame. Calculations to determine $\Delta\Delta_{47}$ and $\Delta\Delta_{48}$ values were performed using Equations 15 and 16 from Lucarelli *et al*. (2021). Calculations to determine $\Delta\delta^{18}O$ values were performed using the temperature dependent relationship determined by Kim and O'Neil (1997).

2.3.1 Clumped and Stable Isotope Analysis

Δ_{47} of modern (triangles) and Holocene (squares) calcite samples from The Cedars are plotted against $\delta^{18}O$ and $\delta^{13}C$ in Figure 2.3 and compared to calcite samples from alkaline springs in the Oman ophiolite (Falk *et al*., 2016) and inorganic calcite precipitated experimentally at high pH (Lucarelli *et al.*, 2022). The $\Delta_{47(I\text{-}CDES)}$, $\delta^{18}O_{V\text{-}PDB}$, and $\delta^{13}O_{V\text{-}PDB}$ range for The Cedars calcites (this study) are 0.600‰ to 0.794‰, -19.3‰ to -0.1‰, and -27.3‰ to -9.2‰ respectively. These values broadly overlap with the Oman calcite $\Delta_{47(CDES90)}$, $\delta^{18}O_{V\text{-}PDB}$, $\delta^{13}O_{V\text{-}PDB}$ which are 0.583‰ to 0.791‰, -16.7‰ to 0.6‰, and -27.2‰ to -3.8‰ respectively, and with the inorganic calcite samples grown at 5, 10, 15, and 25 ºC at pH greater than 10, with values of 0.686‰ to 0.849‰, -26.1‰ to -9.8‰, and -31.6‰ to -12.2‰ respectively. A subset of the Lucarelli *et al.* (2022) experiments incorporated carbonic anhydrase (CA), an enzyme known to accelerate isotopic equilibration (Berg *et al*., 2002).

Linear regressions through each of these three sample sets are in strong agreement. The $\Delta_{47}/\delta^{18}O$ and $\Delta_{47}/\delta^{13}C$ data of the Cedars calcites exhibit slopes of -0.008±0.001 and -0.008±0.001, respectively. $\Delta_{47}/\delta^{18}O$ and $\Delta_{47}/\delta^{13}C$ data from the Oman data (Falk *et al*., 2016) exhibit slopes of -0.006±0.002 and -0.005±0.002, respectively, and the experimental calcite precipitates (Lucarelli *et al*., 2022) have slopes of -0.008±0.001 and -0.008±0.002, respectively.

Figure 2.4 compares Δ_{48} to $\delta^{18}O$ and $\delta^{13}C$ for the Cedars samples compared to data from high pH inorganic calcite precipitation experiments (Lucarelli *et al.*, 2022). The $\Delta_{48(CDES90)}$ range for The Cedars is -0.446‰ to 0.290‰, while the $\Delta_{48(CDES90)}$ ranges for the high pH inorganic calcite precipitation experiments is -0.356‰ to 0.265. $\Delta_{48}/\delta^{18}O$ and $\Delta_{48}/\delta^{13}C$ regression slopes from both datasets are in agreement, with the Cedars calcites data exhibiting values of 0.036±0.003 and

0.034±0.004, respectively, and experimental calcite data slopes of 0.039±0.003 and 0.038±0.009, respectively.

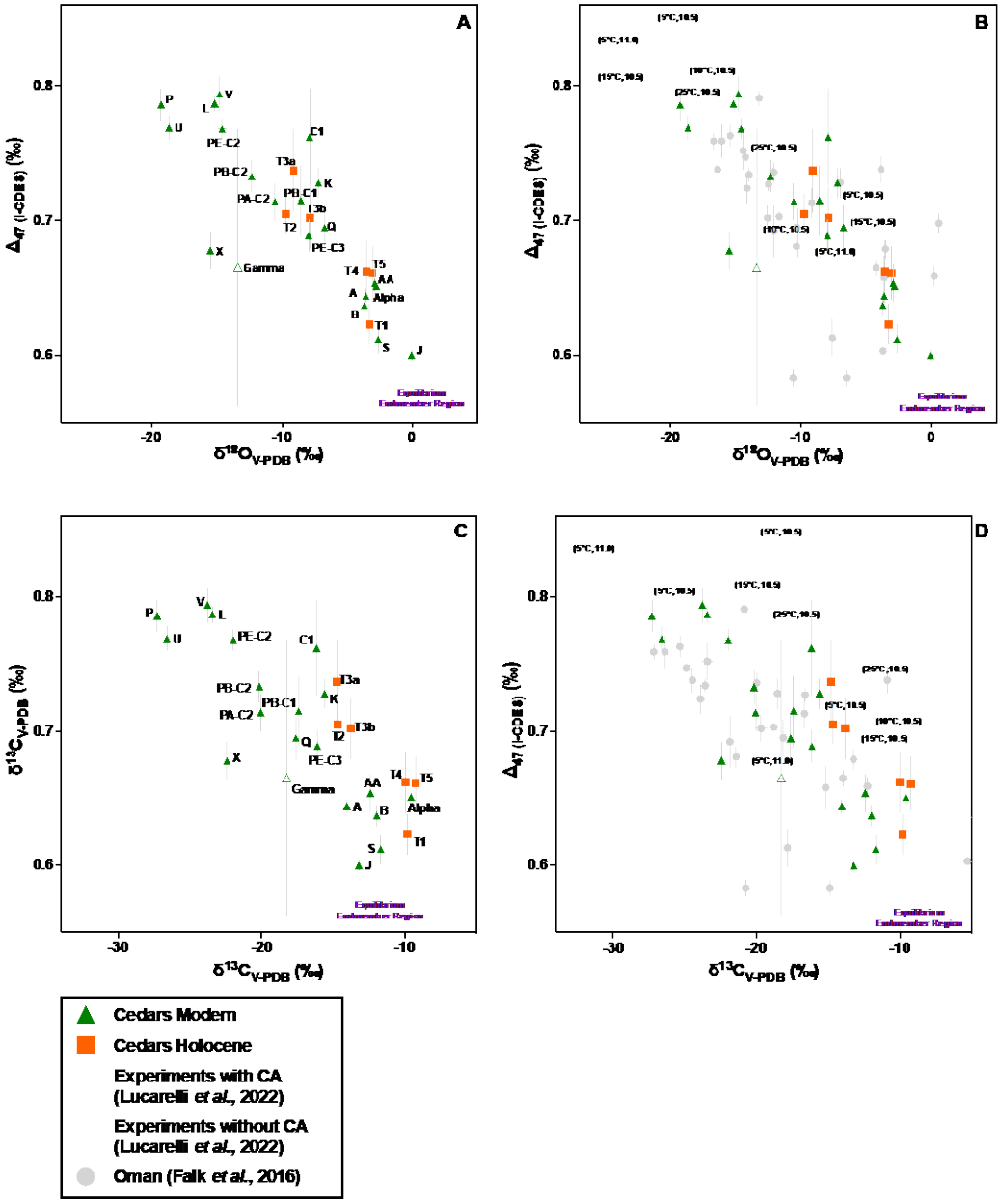

Figure 2.3 Clumped (Δ_{47}) and bulk stable isotope ($\delta^{18}O$ and $\delta^{13}C$) composition of modern and Holocene surface spring carbonate samples at the Cedars. Results are compared to equilibrium values (Lucarelli *et al.*, 2021). Panels B and D also show similarity of these results to inorganic calcite experimental values grown at variable temperature and pH (indicated by sample labels) and with and without carbonic anhydrase (CA), an enzyme known to accelerate isotopic equilibration (Berg *et al.*, 2002; Lucarelli *et al.*, 2022), and data from carbonate veins precipitated from Type 1 waters at a peridotite in Oman (Falk *et al.*, 2016). The Oman sample data was published in the CDES25 reference frame and was converted to the CDES90 reference frame using an adjustment factor of 0.092‰ (Henkes *et al.*, 2013). All other Δ_{47} data is presented in the I-CDES reference frame (Bernasconi *et al.*, 2021) **A)** Δ_{47} and $\delta^{18}O$ for the Cedars. A linear regression indicates a slope of -0.008±0.001, with a $\delta^{18}O_{PDB}$ range of -19.3‰ to -0.1‰ and a $\Delta_{47(I\text{-}CDES)}$ range of 0.600‰ to 0.794‰. **B)** Δ_{47} and $\delta^{18}O$ for the Cedars compared to other samples. The Oman

data exhibit a slope of -0.006±0.002 with a $\delta^{18}O_{PDB}$ range of -16.7‰ to 0.6‰ and a $\Delta_{47(CDES90)}$ range of 0.583‰ to 0.791‰. The experimental data exhibit a slope of -0.009±0.001 with a $\delta^{18}O_{PDB}$ range of -26.1‰ to -9.8‰ and a $\Delta_{47\ (CDES90)}$ range of 0.686‰ to 0.849‰. **C)** Δ_{47} and $\delta^{13}C$ for the Cedars. The slope is -0.008±0.001 with a $\delta^{13}C_{PDB}$ range of -27.3 ‰ to -9.2 ‰ and a $\Delta_{47\ (I\text{-}CDES)}$ range of 0.600‰ to 0.794‰. **D)** Δ_{47} and $\delta^{13}C$ for the Cedars compared to other samples. The Oman data exhibit a slope of -0.005±0.002 with a $\delta^{13}C_{PDB}$ range of -27.2‰ to -3.8‰ and a $\Delta_{47\ (CDES90)}$ range of 0.600‰ to 0.794‰. The experimental data exhibit a slope of -0.008±0.002 with a $\delta^{13}C_{PDB}$ range of -31.6‰ to -12.2‰ and a $\Delta_{47(CDES90)}$ range of 0.686‰ to 0.849‰.

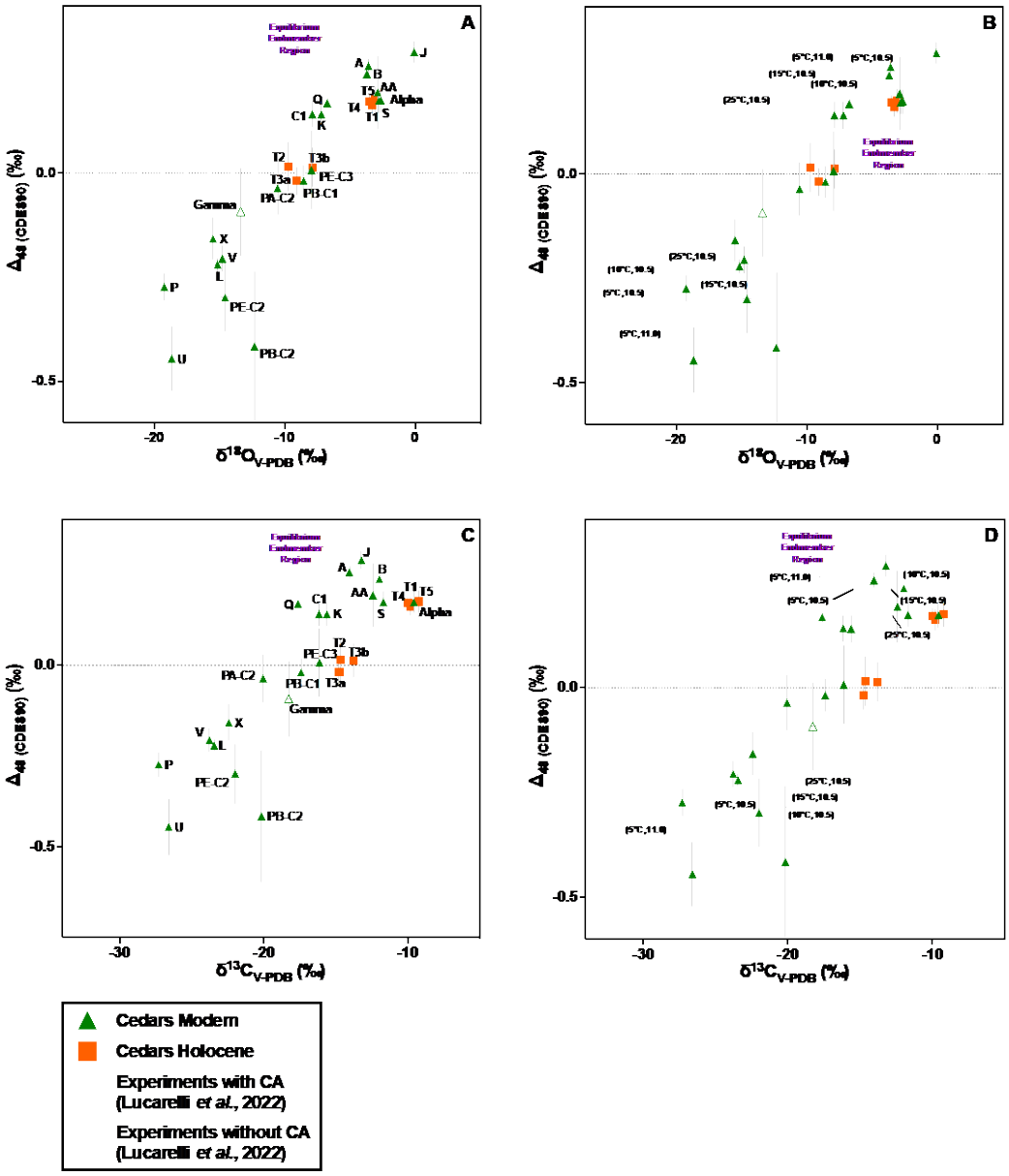

Figure 2.4. Clumped (Δ_{48}) and bulk stable isotope ($\delta^{18}O$ and $\delta^{13}C$) composition of modern and Holocene surface spring carbonate samples at the Cedars. Results are compared to equilibrium values (Lucarelli *et al.*, 2021). Panels B and D also show similarity of these results to inorganic calcite experimental values grown at variable temperature and pH (indicated by sample labels) and with and without carbonic anhydrase (CA), an enzyme known to accelerate isotopic equilibration (Berg *et al.*, 2002). (Lucarelli *et al.*, 2022). **A)** Δ_{48} and $\delta^{18}O$ for the Cedars. A linear regression indicates a slope of 0.036±0.003 with a $\delta^{18}O_{PDB}$ range of -19.3‰ to -0.1‰ and a $\Delta_{48(CDES90)}$ range of -0.446‰ to 0.290‰. **B)** Δ_{48} and $\delta^{18}O$ for the Cedars compared to other samples. The experimental data exhibit a slope of 0.039±0.003 with a $\delta^{18}O_{PDB}$ range of -26.1‰ to -9.8‰ and a $\Delta_{48(CDES90)}$ range of -0.356‰ to 0.265‰. **C)** Δ_{48} and $\delta^{13}C$ for the Cedars. The slope is is 0.034±0.004 with a $\delta^{13}C_{PDB}$ range of -27.3‰ to -9.2‰ and a $\Delta_{48\,(CDES90)}$ range of -0.446‰ to 0.290‰. **D)** Δ_{48} and $\delta^{13}C$ for the Cedars compared to other samples. The experimental data exhibit a

slope of 0.038±0.009 with a $\delta^{18}O_{PDB}$ range of -31.6‰ to -12.2‰ and a $\Delta_{48(CDES90)}$ range of -0.356‰ to 0.265‰.

2.3.2 Δ_{48}-Δ_{47} Paired Clumped Isotope Analysis

Dual clumped isotope (Δ_{47} and Δ_{48}) values for The Cedars samples from this work are shown in Figure 2.5, along with a comparison to synthetic calcites (Lucarelli *et al.*, 2022). Samples fall in three regions corresponding to an equilibrium endmember, mixed endmember, and disequilibrium endmember. The equilibrium endmember includes samples A, AA, Alpha, B, S, T1, T4, and T5, and are within error of nominal equilibrium values (Lucarelli *et al.*, 2021). The mixed endmember region includes samples C1, Gamma, K, Q, PA-C2, PB-C1, PE-C3, T2, T3a, T3b, and X. The disequilibrium endmember, also referred to as the kinetic endmember region, includes samples L, P, PB-C2, PE-C2, V, and U, and exhibits the greatest departure from the equilibrium calibration curve. Sample U exhibits the greatest KIEs amongst the entire sample set ($\delta^{18}O_{V\text{-}PDB}$ = -18.7‰, $\delta^{13}C_{V\text{-}PDB}$ = -26.6‰, $\Delta_{47(I\text{-}CDES)}$ = 0.769‰, $\Delta_{48(CDES90)}$ = -0.446‰), seen in Table 3.3. The sampling location of each sample can be seen in Figure 2.1. Linear regression of the data set from the Cedars yields -2.803±0.500. The slope from Lucarelli's study is -2.911±0.200 and was constructed using all samples precipitated at 15 ºC to better match the measured temperatures of the Cedars, at 17 ºC.

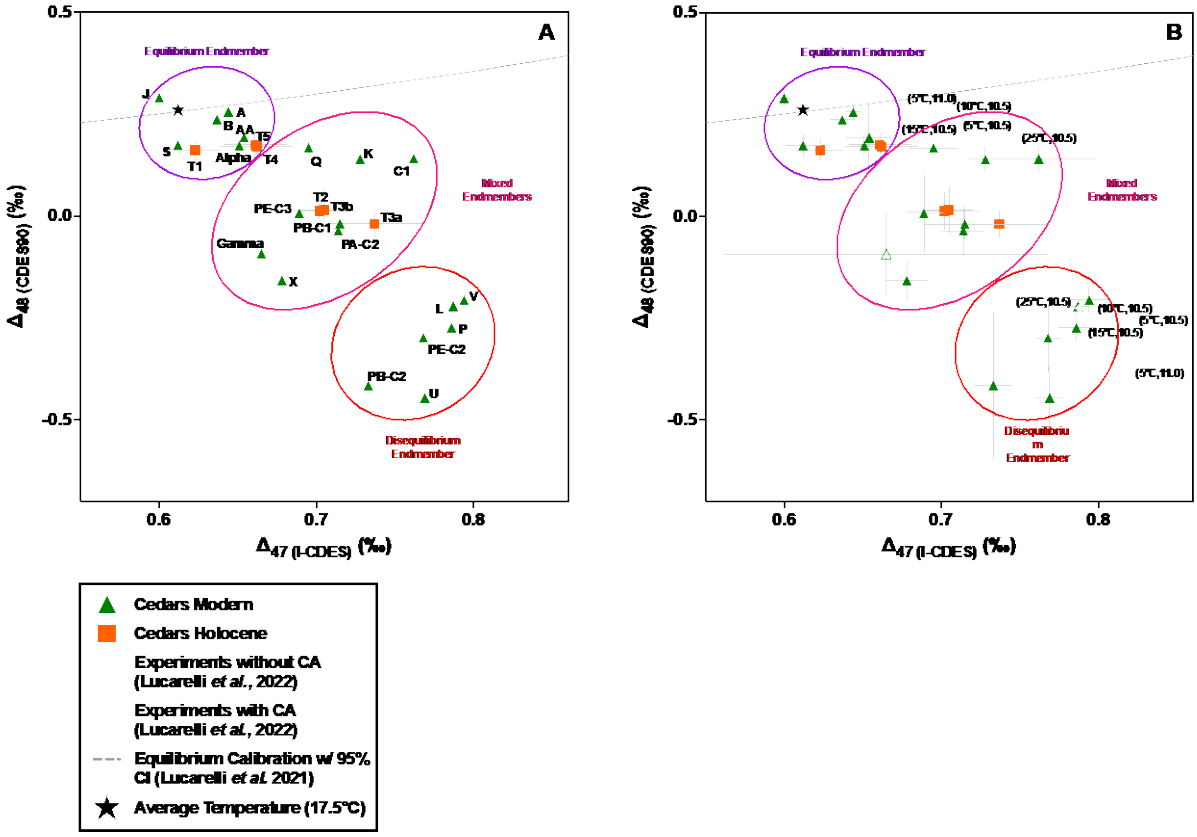

Figure 2.5 Dual clumped isotope (Δ_{47} and Δ_{48}) comparison for modern and Holocene surface spring carbonate samples at the Cedars. Results are compared to equilibrium values. Panel B also shows the similarity of these results to inorganic calcite experimental values grown at variable temperature and pH (indicated by sample labels) and with and without carbonic anhydrase (CA), an enzyme known to accelerate isotopic equilibration (Berg *et al*., 2002; Lucarelli *et al*., 2022b). Data falls into three regions corresponding to different endmembers: Equilibrium, disequilibrium, and mixed. The disequilibrium endmember region includes samples that exhibit the largest kinetic isotope effects and includes samples primarily recovered from surface floes. The equilibrium region was defined using values from Lucarelli *et al*. (2021), and overlaps with samples that are within error of equilibrium that are from areas at the Cedars where surface and spring waters mix, and Holocene-age travertine samples. The mixed region includes "snow" samples recovered from the bottom of the highly alkaline springs, a small portion of surface floes, and Holocene-era travertine samples. Panel C compares the extent of disequilibria with temperature-dependent equilibrium, based on Lucarelli *et al.* (2021), and using 17.5 ºC as the average temperature of the Cedars for calculations. Panel D compares data from the Cedars to experimentally determined disequilibria departure vectors by Lucarelli *et al.* (2022). **A)** Δ_{47} and Δ_{48} for the Cedars. A linear regression indicates a slope of -2.803±0.500 with a $\Delta_{47(\text{I-CDES})}$ range of 0.600‰ to 0.794‰ and a $\Delta_{48(\text{CDES90})}$ of -0.446‰ to 0.290‰. **B)** Δ_{47} and Δ_{48} for the Cedars compared with high pH inorganic calcite precipitation experiment data (Lucarelli *et al.*, 2022), with temperature and pH by each experimental sample. The experimental data for 15 ºC samples exhibit a slope of -2.976±0.034 (Lucarelli *et al*., 2022) and is shown because it is from samples grown under conditions that are the closest to site temperatures of 17.5 ºC.

2.3.3 Isotopic disequilibrium analysis

Isotopic disequilibrium values were calculated using mean sample values and the equation for oxygen isotope equilibrium from Kim and O'Neil *et al.* (1997) and for Δ_{47} and Δ_{48} equilibrium from Lucarelli *et al.* (2022). These values are shown in Figure 2.6 and Table 3.3. $\Delta\delta^{18}O$ values range from -17.739‰ to 1.460‰, while $\Delta\Delta_{47}$ and $\Delta\Delta_{48}$ values are -0.011‰ to 0.182‰ and -0.708 to -0.006 respectively. The slopes of the $\Delta\delta^{18}O$-$\Delta\Delta_{47}$, $\Delta\delta^{18}O$-$\Delta\Delta_{48}$, and $\Delta\Delta_{47}$- $\Delta\Delta_{48}$ are -0.008±0.001, 0.037±0.004, and -2.803±0.216 respectively. For comparison, values from calcites grown at variable temperature and pH are -0.008±0.001, 0.039±0.003, and -3.791±0.652 respectively. The $\Delta\Delta_{47}$-$\Delta\Delta_{48}$ slope for the calcite precipitation experiments is reflective of only high pH grown samples at varying temperatures. The slope reported in this study for samples at 15 ºC is -2.911±0.200. These values and theoretical vectors/trajectories are shown in Figure 2.6.

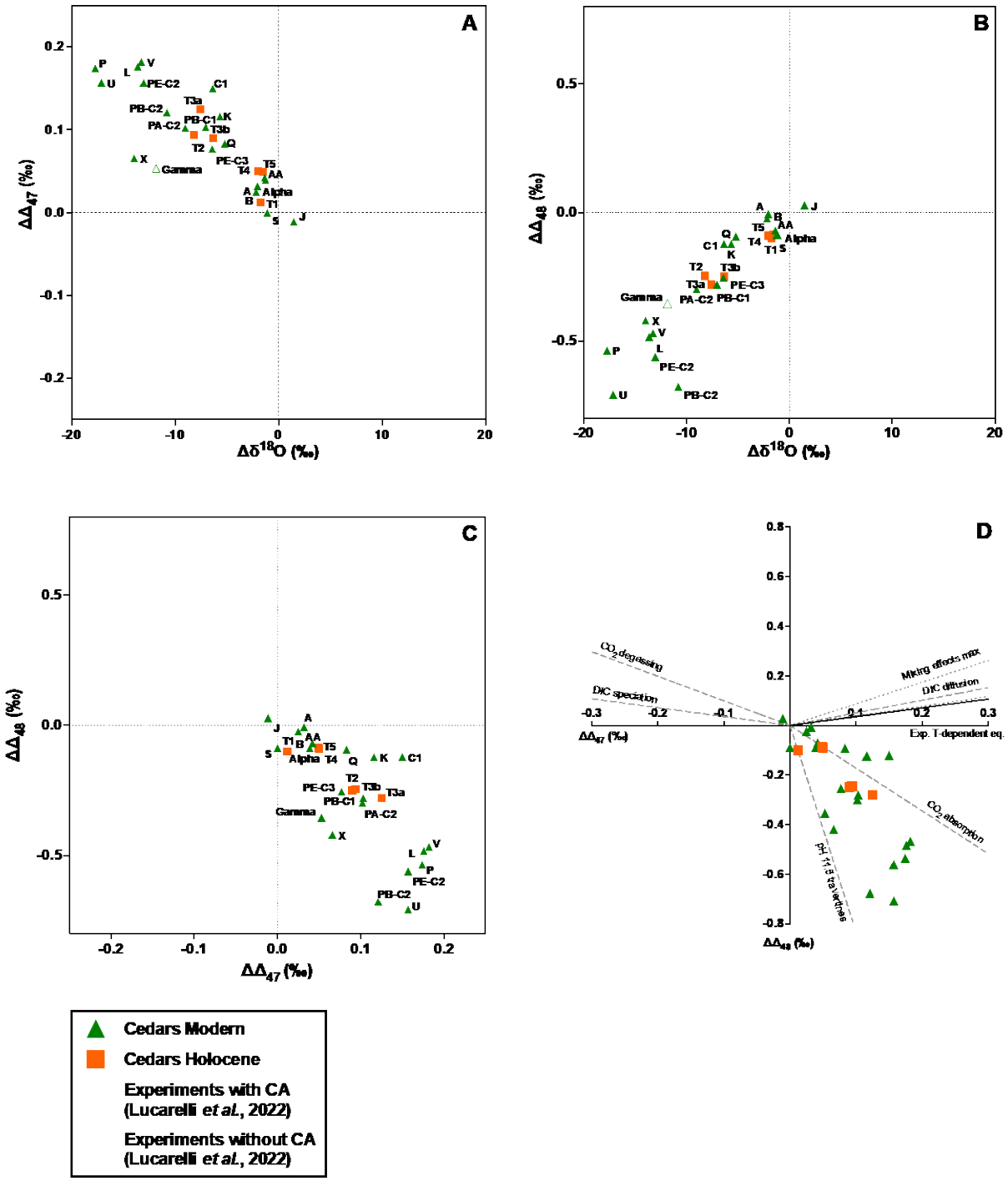

Figure 2.6 Extent of disequilibria associated with clumped (Δ_{47} and Δ_{48}) and stable oxygen isotope ($\delta^{18}O$). $\Delta\Delta_{47}$ and $\Delta\Delta_{48}$ were calculated by measuring the difference between the measured clumped isotope signal versus the equilibrium clumped isotope signature. Equilibrium values were calculated by using the temperature dependent clumped isotope equations for equilibrium, determined experimentally by Lucarelli *et al.* (2021). $\Delta\delta^{18}O$ was determined using the temperature-dependent relationship from Kim and O'Neil *et al.* (1997). The temperature used for all calculations was set to 17.5 ºC. Inorganic calcite precipitation values are presented (blue diamonds) and were grown at variable temperature and pH, with

and without carbonic anhydrase (Lucarelli *et al*., 2022b). **A)** $\Delta\Delta_{47}$ and $\Delta\delta^{18}O$ of the Cedars and inorganic calcite precipitation values. Independent linear regressions of the Cedars data and inorganic calcite precipitation values both indicate a slope of -0.008±0.001. **B)** $\Delta\Delta_{47}$ and $\Delta\delta^{18}O$ of the Cedars and inorganic calcite precipitation values. Independent linear regressions of the Cedars data and inorganic calcite precipitation experiments indicate slopes of 0.037±0.004 and 0.039±0.003 respectively. **C)** $\Delta\Delta_{47}$ and $\Delta\Delta_{48}$ for the Cedars and inorganic calcite precipitation values. Independent linear regressions indicate a slope of -2.803±0.216 and -3.791±0.652. The slope from Lucarelli *et al.* (2022) for samples precipitated at 15 ºC at variable pH was reported as -2.911±0.200. The linear regression conducted in this study comprises of samples varying from 5, 10, 15, and 25 ºC w/ and w/o carbonic anhydrase. **D)** $\Delta\Delta_{47}$ and $\Delta\Delta_{48}$ for the Cedars with disequilibria departure vectors overlayed.

2.3.4 Modelling calculations

We used the IsoDIC model (Guo and Zhou, 2019; Guo, 2020) to study the evolution of DIC as function of system evolution time in the Cedars (Figure 2.7A). The model simulates the predicted disequilibrium pathway of Δ_{47} and Δ_{48} in DIC species and in the composite DIC pool. For these calculations, we assume a CO2-absorption dominated setting, and predict the isotopic composition of HCO_3^- and CO_3^{2-} after 0, 1, 10, 50, 100, and 1000 hours.

Conditions for surface floe samples (Samples: L, P, U, V, PE-C2, PB-C2, and X), presented in bold green, were measured and are used for model input parameters. The calculations for the remaining samples assume modern values for the composition of fluids. We note that equilibrium endmember modern samples are collected from locations where surface creek (pH = 8.7) and spring waters (pH = 11.5) are mixing, resulting in a potential drop in pH to an intermediate value (pH = 8.7 to 11.5) that would reduce equilibration times from the longer values associated with highly alkaline solutions. Holocene sample calculations use assumed values and yield plausible numbers that are similar to modern values.

The COAD model was used to predict the isotopic compositions of calcite, and factors in mineral precipitation rate (Watkins and Devriendt, 2022). Figure 2.7 and 2.8 overlays the COAD model simulations of HCO_3^-, CO_3^{2-}, equilibrated inorganic carbon (EIC), and $CaCO_3$ in Δ_{48}-Δ_{47}, $\Delta_{47}/\delta^{18}O$, and $\Delta_{48}/\delta^{18}O$ plots. Similar plots including HCO_3^- and CO_3^{2-} generated from IsoDIC are included in the Supplementary Materials, S.3. All parameters and equations used by these models can be seen in the Supplementary Materials, S.1 and S.2. The box model takes mineral growth into account so that the $CaCO_3$ species can be compared directly with the samples collected from The Cedars.

Figure 2.9 compares the IsoDIC model and COAD box model predictions for the evolution of CO_3^{2-} and $CaCO_3$ respectively. Figures 10A and 10B show Δ_{47} and Δ_{48} with respect to $Log_{10}(R_p)$, where R_p is the molar growth rate of $CaCO_3$ in mol m^{-2} s^{-1}. The BSC average point is the averaged growth rate and respective clumped isotope signature associated. This is an estimated growth rate measured by Christensen *et al.* (2021) of floes collected from the BSC springs location. Samples U, V, and X were used for this averaging as they were collected from the point where these growth measurements were taken.

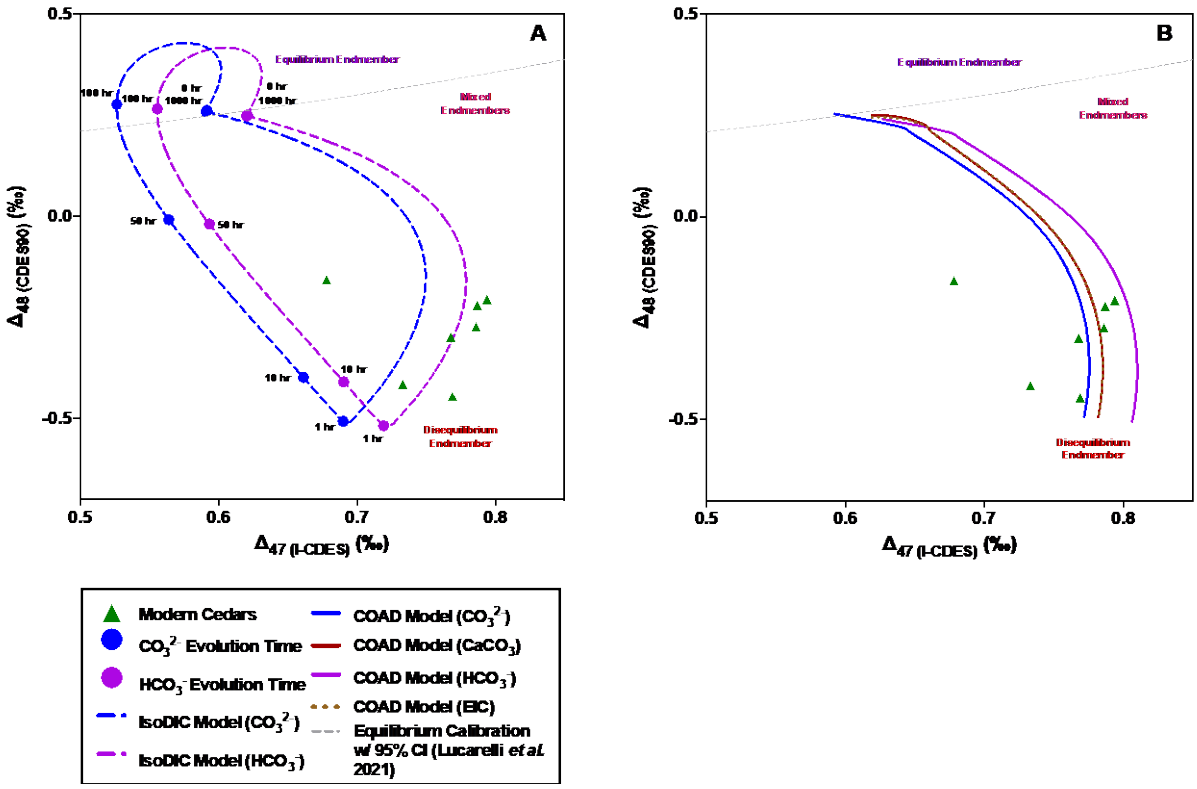

Figure 2.7 Dual clumped isotope (Δ_{47} and Δ_{48}) comparison for modern surface spring carbonate samples at the Cedars compared using IsoDIC (Guo *et al*., 2021) and COAD model (Watkins and Devriendt, 2021). Panel A shows the evolution of clumped isotope signatures (Δ_{47} and Δ_{48}) of HCO_3^- and CO_3^{-2} with respect to time intervals using IsoDIC. IsoDIC evaluates the disequilibria associated with the DIC pool. Panel B shows the evolution of clumped isotope signatures (Δ_{47} and Δ_{48}) of HCO_3^-, CO_3^{-2}, $CaCO_3$, and equilibrated inorganic carbon (EIC) using the COAD model that also examines fractionation due to variable growth rate. Modern samples highlighted in bold green reflect those collected from the surface of springs and are consistent with the input parameters for each model. Results are compared to equilibrium values (Lucarelli *et al.*, 2021). **A)** Δ_{47} and Δ_{48} with IsoDIC modeling overlayed, for the Cedars. IsoDIC model calculations used the following parameters: solution temperature – 17.5ºC, solution pH - 11.5, air pCO_2 - 400ppm, air $\delta^{13}C_{V\text{-}PDB}$ -8.431‰, air $\delta^{18}O_{V\text{-}PDB}$: 0.144‰. **B)** Δ_{47} and Δ_{48} with COAD model overlayed, for the Cedars. Model parameters are the same as those used in IsoDIC. Information on model calculations can be found in the SI.

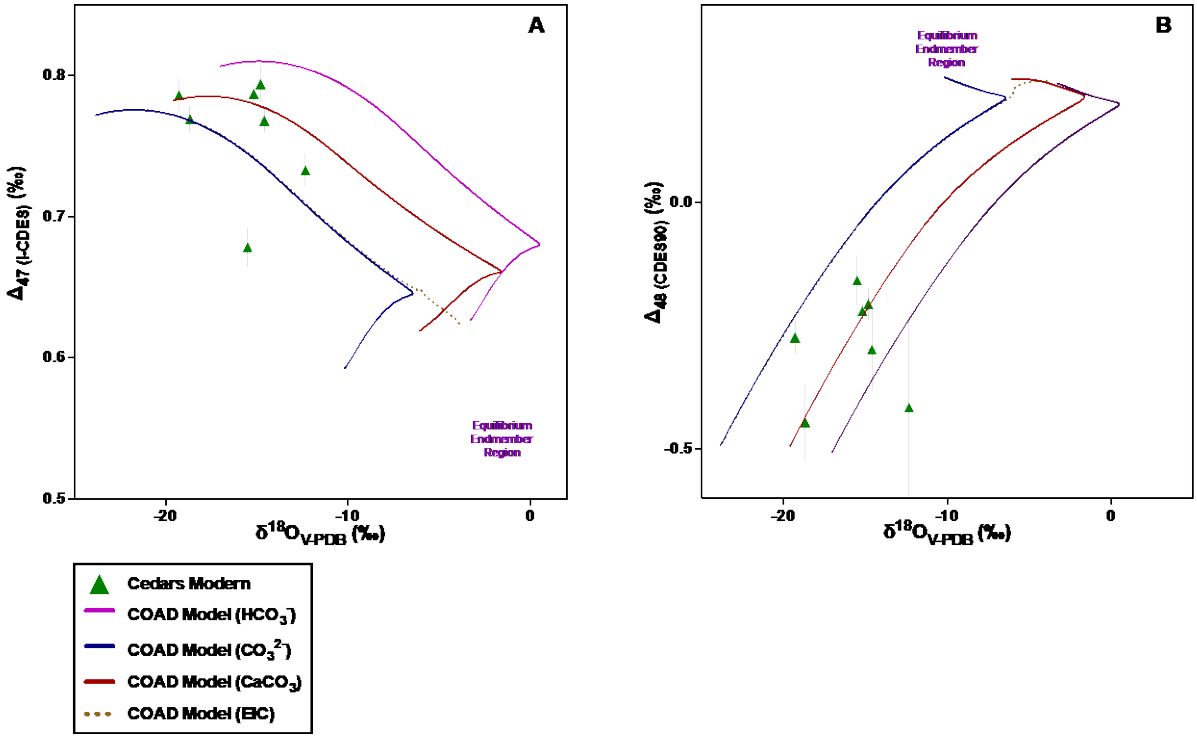

Figure 2.8 Clumped (Δ_{47} and Δ_{48}) and bulk oxygen ($\delta^{18}O$) isotope analysis of the Cedars with COAD model overlayed. The box-model simulates the evolution of the clumped isotope signature (Δ_{47} and Δ_{48}) of HCO_3^-, CO_3^{2-}, $CaCO_3$, and equilibrated inorganic carbon (EIC) using parameters consistent with the modern surface floe conditions. The modern surface floe samples are seen in bold green. Parameters for this box model can be seen in SI. The approximate equilibrium regions were determined by calibration data, from Lucarelli *et al.* (2021), in the dual clumped isotope space. **A)** Graph of $\Delta_{47}/\delta^{18}O$ with box model simulation overlayed using COAD model (Watkins and Devriendt, 2021). **B)** Graph of $\Delta_{48}/\delta^{18}O$ with box model simulation using COAD model (Watkins and Devriendt, 2021). Information on model calculations can be found in the SI.

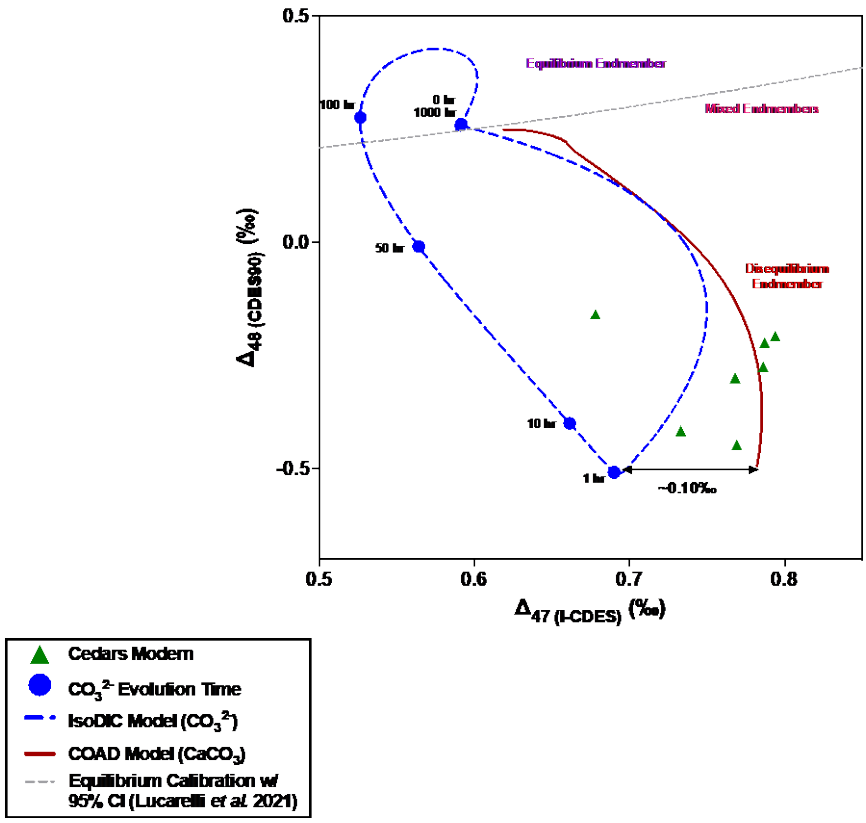

Figure 2.9 Dual clumped (Δ_{47} and Δ_{48}) isotope comparison of surface carbonates at the Cedars coupled with IsoDIC and COAD modeling. The IsoDIC model only simulates the disequilibria associated with the DIC pool, where the COAD model takes mineral precipitation into account. The measured difference at the disequilibria endmember region is approximately 0.10‰, accounting for the mineral precipitation effects associated with the precipitation of $CaCO_3$ from solution. IsoDIC parameters from Figure 2.6A were used to create the IsoDIC curve for the CO_3^{2-} species. Parameters from Figure 2.6B were used to create the box-model curve for $CaCO_3$. The equilibrium relationship shown is from Lucarelli *et al.* (2021). Information on model calculations can be found in the SI.

2.4 Discussion

2.4.1 Broad Patterns in Multi-Isotope Space: Comparison of Sample Sets

The similarity in $\Delta_{47}/\delta^{18}O$ and $\Delta_{47}/\delta^{13}C$ regression slopes for the Cedars data, high pH precipitation experiments (Lucarelli *et al.*, 2022), and data from surface springs and veins in the Samail ophiolite of Oman (Falk *et al*., 2016) (Figure 2.3) point to the same processes driving disequilibrium in each system. However, regional, and possible local and temporal, variations in the $\delta^{18}O$ of waters, and $\delta^{13}C$ of DIC, also are reflected in these data (Figure 2.3). For example, the Oman dataset (Falk *et al*., 2016) may have larger fluctuations in $\delta^{13}C$ and $\delta^{18}O$ due to the amount and type of samples analyzed, and greater fluctuations in DIC $\delta^{13}C$ and meteoric water $\delta^{18}O$, due to the significantly larger area, 200 x 50 km, of the Oman site (Christensen *et al.* 2021). The experiments (Lucarelli *et al*., 2022) sourced DIC from $NaHCO_3$ dissolved in lab-purified water, and used a sealed permeable membrane apparatus adapted from Tang *et al.* (2014). This approach yields isotopically lighter $\delta^{13}C$ and $\delta^{18}O$ values compared with naturally precipitated samples that derive their DIC pool from atmospheric CO_2 that dissolves in meteoric waters.

In contrast, the Δ_{47}-Δ_{48} dual clumped isotope approach (Figure 2.5) allows for mechanistic fingerprinting of the processes associated with disequilibria, and a rough estimation of timescales for equilibration. This dual clumped space represents a major advancement in the clumped isotope field as data from different localities, natural and synthetic, can be directly compared without knowledge of additional parameters such as the isotopic composition of the parent fluid or DIC source. The Cedars data has some samples that exhibit an enrichment in Δ_{47} accompanied by a depletion in Δ_{48}, similar to what was observed in high pH samples without CA in calcite precipitation experiments (Lucarelli *et al.*, 2022) (Figure 2.5B). The range in slope in their

precipitation experiments was produced by varying pH from 8.3 to 11.0, and temperatures from 5, 10, 15, and 25ºC to study kinetic effects associated with CO_2 hydrolysis and were between -2.455±0.024 and -3.071±0.011 (Lucarelli *et al*., 2022). The Δ_{47}-Δ_{48} slope observed with our data set, -2.803±0.500, is statistically indistinguishable from their results. Thus, the comparable Δ_{47}-Δ_{48} slopes, and the $\Delta\Delta_{47}$-$\Delta\Delta_{48}$ values (Figure 2.6C), for The Cedars samples and experimentally precipitated carbonates robustly confirm that disequilibria is occurring through a similar pathway that is largely associated with CO_2 hydroxylation. We note a similar trend was also observed by Bajnai *et al.* (2020) during their dual-clumped evaluation of cold-water coral, warm-water coral, and brachiopods, and in coral data reported by Lucarelli *et al*. (2021), which both studies concluded exhibited CO_2-absorption related kinetic biases in the dual-clumped isotope space.

2.4.2 Patterns in (Dis)Equilibrium Within the Cedars

Modern and Ancient Samples

Modern samples fall within each of three (equilibrium, mixed, and disequilibria) endmembers. Modern samples L, P, U, V, and X collected from pool floes, primarily from the BSC location, exhibited the greatest KIEs. Modern samples PA-C2 and PE-C2 were collected from the outer edge surface of the BSC, where similar conditions to the pool floe samples led to high KIEs. The modern "snow" samples C1, K, PA-C2, and PB-C1 exhibited moderate KIEs and fell between equilibrium and disequilibrium endmembers. Modern samples A, AA, B, and S that were collected from rim formations and areas where fresh creek water mixed with spring water fell within the equilibrium endmember region. All modern samples collected from mixing waters, floes from the surface of springs, and pool snow are predominantly composed of a mixture of aragonite, calcite, and other isomorphs of $CaCO_3$.

Ancient travertine samples T2, T3a, and T3b display intermediate disequilibrium (Figure 2.5A), where travertine samples T1, T4, and T5 fell within the equilibrium endmember region. This distinction between the two populations could be due to post-depositional events such as recrystallization in the presence of surface and groundwater mixing, which could have shifted disequilibrium isotopic values towards equilibrium. This would be analogous to what Falk *et al.* (2016) hypothesized occurred in Oman, where the absence of aragonite in travertine samples may have indicated post-depositional events had taken place, thereby influenced isotopic values.

Locational differences

Sample location within The Cedars was a major factor influencing whether bulk and clumped isotopic data exhibited departures from equilibria, likely linked to variations in DIC sources (i.e., Type 1 and Type waters) and equilibration time. Samples exhibiting the greatest KIEs (disequilibrium endmember region in Figure 2.5A) were collected from floes at the surface pools, and in two cases (PE-C2 and PB-C2), along the outer edge surface of the pool at the BSC locality. Those showing the smallest KIEs (equilibrium endmember region), were travertine samples collected from rim formation at the NS1 locality and modern $CaCO_3$ samples collected from points where mixing water sources converged at the New Pool and BSC localities. Below we discuss the processes that are causing (dis)equilibrium effects on isotope signals in more detail. We discuss this within the context of a published "thin-film model" and "box-model" which was used to described bulk carbon and oxygen stable isotope disequilibria at different locations at The Cedars (Christensen *et al.*, 2021) developed. The thin film model was used to describe processes associated $CaCO_3$ precipitation and DIC evolution at a depth of 100μm from the surface of the springs. The box-model was used to describe the same processes associated with the bulk volume of the pool below 100μm from the surface.

Disequilibrium Endmember Region

Samples U, P, L, V, PE-C2, and PB-C2 lie at the kinetic endmember region in the Δ_{47}-Δ_{48} space, with sample U exhibiting the greatest KIEs. These samples are floes collected from the surface of pools located at the BSC and GPS locations (Figure 2.1). At these two localities, KIEs could be related to the rapid uptake of CO_2 at the surface, leading to similarly rapid carbonate mineral precipitation at the air and water interface. These results would be consistent with the interpretations of bulk stable isotopic data by Christensen *et al.* (2021), who investigated the dynamics associated with $CaCO_3$ precipitation and stable isotope fractionation associated with surface floes, and argued that at the Cedars, KIEs may be the largest when $CaCO_3$ precipitates at the surface of the springs. The BSC location had a high saturation state (Ω) value of ~13, while the GPS location had an Ω value of ~5. The rate of CO_2 uptake at the surface layer, at the BSC location, was calculated at 1.6×10^{-5} mol kg-soln^{-1}, several orders of magnitude higher than the concentration of the bulk pool. The rate of Ca^{2+} replenishment from the springs at the BSC was determined to be 1.5×10^{-6} mol s^{-1}, which is comparable to the DIC flux from the atmosphere. The CO_2 taken from the atmosphere is converted to HCO_3^-, via hydroxylation reaction (Equation 2), with rapid and near-quantitative conversion to CO_3^{2-}. With this higher influx of CO_2 and precipitation of $CaCO_3$, the surface pH is reduced slightly from 11.5, in the bulk pool springs, to 11.0 at the surface (Christensen *et al*., 2021a). However, the pH is still high enough to favor CO_3^{2-} DIC speciation (Uchikawa and Zeebe, 2012b; Tripati *et al*., 2015) preventing isotopic equilibrium through exchange reactions associated with the other DIC species. In addition to this, because the concentration of the DIC is so high at the surface due to the large CO_2 gradient between the water and atmosphere, the supersaturation state of $CaCO_3$ is also considerably high further promoting

rapid precipitation of $CaCO_3$ outside of isotopic equilibrium, as indicated by the thin film model (Christensen *et al.*, 2021).

Equilibrium Endmember Region

As seen in Figure 2.5A, most equilibrium endmembers include modern and old travertine samples. A, Alpha, T1, T4, and T5, which were collected at BSC. Modern $CaCO_3$ samples AA, B, and S, recovered from mixing water sources (spring and creek) also fell within the equilibrium endmember region. The compositions of both the modern and ancient samples reflect the composition of isotopically equilibrated DIC from the creek or surface water (7.8-8.7 pH) that occasionally mixes with the high-pH springs (Christensen *et al*., 2021a). Samples AA, B, and S, were recovered from waters mixed from the springs and creek where the pH and the influx of Ca^{2+} are reduced, leading to potentially more favorable conditions for isotopic equilibration in the DIC-H_2O-CO_2 system. In the case of modern and ancient travertine samples A, Alpha, T1, T4, and T5, their proximity to the equilibrium line suggests that the isotopic composition closely reflects isotopically equilibrated creek water rather than atmospheric CO_2 (Beck *et al*., 2005; Christensen *et al*., 2021), indicating that mixing of water sources had taken place, resulting in the sharp disparity in clumped and stable isotope signatures relative samples in the disequilibrium endmember region. Christensen *et al.* (2021) hypothesized that because ancient travertine samples would have surface DIC as the primary carbon source, they could be used to provide paleoenvironmental data on past precipitation and surface/creek water temperatures. Given these samples exhibit Δ_{47} and Δ_{48} values consistent with equilibrium, we suggest they can be in fact used for the study of paleoclimate.

We applied a published calibration equation (Anderson *et al*., 2021a) to modern samples that precipitate from intermediate pH waters, which the dual clumped isotope measurements

indicate form at equilibrium ($\Delta\Delta_{47}$-$\Delta\Delta_{48}$; green symbols near the origin in Figure 2.6C). This calculation yields temperatures that are similar to modern mean annual values of 17.0±1.0 ºC (Christensen *et al*., 2021). Sample S, J, B yield temperatures of 19.3±3.4 ºC, 22.8±1.3 ºC, and 11.5±2.5 ºC respectively. The average modern temperature, of samples close to equilibrium, was 17.9±2.4 ºC, and is in good agreement with modern temperature conditions. The ancient sample that formed at equilibrium as determined from the dual clumped isotope measurements ($\Delta\Delta_{47}$-$\Delta\Delta_{48}$; orange symbols near the origin in Figure 2.6C). The estimated temperatures of the ancient samples Alpha, T1, T4, and T5 are 6.3±1.6 ºC, 16.2±4.4 ºC, 4.7±6.3 ºC, and 4.9±5.6 ºC. The average temperature of the ancient travertine samples close to equilibrium was 8.3±1.1 ºC. This suggests that the temperatures where approximately 10 °C cooler when they formed, and this is corroborated by literature values (Malamud-Roam *et al*., 2006).

Mixed Endmember

Samples in this region are from multiple sites at The Cedars, with the majority being from "snow" that was recovered from the bottom of the pools. The term snow is used to describe the physical appearance of fine particulates of $CaCO_3$ aggregating at the bottom of the pools. However, their texture is similar to surface floe samples (Christensen *et al.*, 2021). The thin-film model for surface dynamics suggests that as the surface floes thicken or are perturbed by falling debris, $CaCO_3$ aggregates detach and sink deeper into the springs (Christensen *et al*., 2021). The floes would carry some surface waters with the particles (Christensen *et al*., 2021), and thus could mix in a pool of DIC that is not in isotopic equilibrium to particles that comprise snow, driving KIEs in the clumped and bulk stable isotope signatures. Even though these detached layers, composed of a mixture of particle aggregates and solution, have moved away from the surface, where the majority of rapid precipitation is occurring, isotopic equilibration of DIC within the

detached layer is still hindered by the high pH (11.5), which favors hydroxylation, and CO_3^{2-} as the most abundant DIC species. Given water temperatures, DIC in this fragmented layer can retain its kinetic signature for tens of days at a pH of 11.5 (Usdowski *et al*., 1991; Beck *et al*., 2005) which can contribute to the KIEs in dual clumped isotopes and bulk stable isotopes. DIC mixing can also drive deviations from equilibrium in Δ_{47} and Δ_{48} (Lucarelli *et al.,* 2022). Thus, our hypothesis for why these samples are in an intermediate location relative to equilibrium and disequilibrium endmembers is due to location-specific conditions associated with the mixing of creek and spring waters.

2.4.3 Examination of Kinetic Isotope Effects in Calcite at The Cedars

Several factors control the expression of KIEs in carbonate minerals at the springs samples from The Cedars. These include the hydroxylation favored pathway, DIC speciation, increased rate of CO_2 uptake into the system, and mineral precipitation prior to isotopic equilibria. Because Type 1 and 2 waters are readily mixing at the surface, a hyperalkaline environment (pH > 11) is created due to excess OH^- anions present in Type 2 fluids. At a pH greater than 10, the hydroxylation pathway represents 95% of reactions transforming CO_2 to HCO_3^- (McConnaughey, 1989). This high pH also creates an environment that facilitates a more rapid uptake of CO_2 into the aqueous media (Lerman and Stumm, 1989) due to the concentration gradient created by the DIC speciation preference of CO_3^{2-} at pH above 10 (Hill *et al*., 2014; Tripati *et al*., 2015). This condition coupled with the rapid precipitation of $CaCO_3$ due to the high saturation state (Christensen *et al*., 2021) creates a stronger gradient, further facilitating the uptake of CO_2 from the atmosphere. Because the forward reaction associated with Reaction 2 is >1000 times the reverse reaction (Christensen *et al*., 2021), it creates a pathway that is essentially unidirectional. We hypothesize this is preventing backwards conversion which is essential for O isotope exchange

that would facilitate $\delta^{18}O$, Δ_{47}, and Δ_{48} equilibrium. The high pH results in a much greater equilibration time, >100 hours (Figure 2.6A), being required for the DIC pool to achieve clumped and oxygen stable isotopic equilibria prior to mineral precipitation. As the system moves into the deeper parts of the spring pool (below 100 μm), there are additional fluxes including advection and diffusion of Type 2 waters, $CaCO_3$ precipitation, and EIC contribution from the surface. Most samples forming in the deeper parts of the springs at the Cedars (samples Q, X, etc.) are in the mixed or equilibrium endmember regions that suggests they achieved an equilibrium, or were progressing towards equilibrium, relative to the surface floes.

2.4.4 Examination of Kinetic Isotope Effects Using Modeling

IsoDIC modeling of disequilibria in the DIC that uses input parameters taken from the surface floe conditions of the Cedars predicted the range of Δ_{47} and Δ_{48} signatures in DIC at The Cedars. The model was used to generate the predicted pathway of disequilibria associated with HCO_3^- (purple dashed line) and CO_3^{2-} (blue dashed line) with respect to residence time (purple and blue nodes) in the system, seen in Figure 2.6A. In this figure, there is a rapid departure away from equilibria with a disequilibria maxima achieved at the 1-hour mark of DIC introduction into the system. This initial departure rebounds back to equilibria as the system has more time equilibrate, which is eventually achieved prior to the 100-hour mark. Due to the hydroxylation dominating pathway and pH dependent DIC speciation, the migration back to equilibria at these conditions is very slow. Thus, in the CO_3^{2-} prediction it underestimates the kinetic departure in the Δ_{47} direction correlating to a rebound back to equilibria prior to 1-hour. We suggest this DIC species to be the more appropriate simulation due to the pH-dependent speciation that would favor CO_3^{2-}. This approach can be used to predict the approximate timeframe associated with precipitation at the surface, which we hypothesize to be within the first hour of CO_2 introduction into the surface

spring system. A caveat is that this model only considers the KIEs associated with the DIC pool and does not factor those associated with mineral precipitation.

Because the IsoDIC model did not consider KIEs associated with mineral precipitation, modeling through COAD model was performed with the same parameters used for the IsoDIC model. This box-model seen in Figure 2.6B shows a very similar trend as the IsoDIC model in terms of migration from equilibrium to disequilibrium endmember region. Because the box-model takes mineral precipitation into account, there is a very small difference between the $CaCO_3$ and CO_3^{2-} simulated curves (~0.01‰). We hypothesize there should be a minimal difference between the two as the COAD model accounts for CO_3^{2-} removal from a system that already is at an elevated pH where CO_3^{2-} is the favored DIC species. However, a difference of ~0.10‰ exists between the simulated CO_3^{2-} disequilibria from IsoDIC to the predicted calcite disequilibria from the box-model (Figure 2.8). This difference can be explained by KIEs associated with mineral precipitation that is not factored into IsoDIC. Each model provides different sets of tools, where the IsoDIC model provides greater insights into the timescales associated with achieving (dis)equilibrium within a DIC pool, while when mineral growth is moderately rapid, mineral compositions, which can differ from the DIC pool, are slightly more (~0.10‰) accurately predicted by the COAD model.

Differences Between Box-Model Predicted Values and Observations

Comparison of The Cedars data with box model calculations shows that most samples fall in line with predicted calcite values and within the bounds of simulated HCO_3^- and CO_3^{2-} values, except for sample U ($\delta^{18}O_{V\text{-}PDB}$ = -18.7‰, $\Delta_{47\ (I\text{-}CDES)}$ = 0.769‰), X ($\delta^{18}O_{V\text{-}PDB}$ = -15.5 ‰, $\Delta_{47\ (I\text{-}CDES)}$ = 0.678 ‰) and Gamma ($\delta^{18}O_{V\text{-}PDB}$ = -13.4‰, $\Delta_{47\ (I\text{-}CDES)}$ = 0.665‰) (Figure 2.7A). The model accurately simulates the $\Delta_{47\ (I\text{-}CDES)}$ of samples falling in the disequilibrium endmember

region. For $\Delta_{48\ (CDES90}$, the box model accurately simulates the data with only one sample, PB-C2 ($\delta^{18}O_{V\text{-}PDB}$ = -12.3‰, $\Delta_{48\ (CDES90)}$ = -0.416‰), outside of the HCO_3^- and CO_3^{2-} simulated bounds. (Figure 2.7B). Values of samples falling in the disequilibrium region is well simulated, with the model accurately predicting the isotopic composition of sample U ($\delta^{18}O_{V\text{-}PDB}$ = -18.7‰, $\Delta_{48(CDES90)}$ = -0.446‰), which exhibits the greatest KIEs. However, the model underestimates Δ_{47} and Δ_{48} values of samples in the equilibrium endmember. This underestimation could be due to heterogeneity in natural conditions where isotopic equilibrium is occurring, such as pH alteration from mixing of waters, which was not simulated by the model, but would impact Δ_{47} and Δ_{48} values (Lucarelli *et al*., 2022).

2.4.5 Potential CO_2 Sequestration Application

The primary motivation of this study was to apply the dual clumped isotope framework (Δ_{47}-Δ_{48}) to study processes associated with CO_2 absorption and transformation in waters, of broad relevance to a number of systems, including application to sites that are of interest for possible carbon sequestration. There is interest in peridotites for the potential to sequester CO_2 through carbon mineralization. While the Cedars represents an area for potential CO_2 sequestration applications, its relative size, approximately 44 km^3 (R.G. Coleman, 2000), is small compared to analogous sites, such as that in the Samail ophiolite, Sultanate of Oman, at approximately 21000 km^3 (Kelemen and Matter, 2008). This would equate to a CO_2 sequestration potential of $7.7x10^{13}$ tons (Kelemen and Matter, 2008) at the site in Oman, compared to an extrapolated, based on volume, $1.6x10^{11}$ tons of CO_2 at the Cedars site.

Our work on carbonates forming in surface springs provides insight on the potential use of these springs as secondary or auxiliary sequestration points for CO_2. Due to highly alkaline water conditions, which are known to increase the uptake of CO_2 (Lerman and Stumm, 1989), and the

rate of calcite precipitation (Korchef and Touaibi, 2008), these sites would be able to sequester additional CO_2 through carbon transformation and sequestration into the springs themselves. This, of course, would not be the primary point of CO_2 sequestration due to their limited size relative to the peridotite of interest, but an auxiliary location to increase the overall efficiency of sequestration for the entire system. COAD modeling enables us to determine and predict the rates of precipitation associated with the respective system through the dual clumped framework. Because the COAD model adheres to the Cedar's dataset, it was accurately used to predict the Δ_{47} and Δ_{48} signatures of the surface floe calcite with respect to molar precipitation rate (R_p) (Figure 10). By expanding this analysis to analogous sites, we can use the same modeling framework to predict the rates associated with mineral precipitation, enabling us to evaluate them for use as secondary auxiliary sequestration points.

Additionally, the robustness of the paired Δ_{47}-Δ_{48} framework (including $\Delta\Delta_{47}$-$\Delta\Delta_{48}$) when comparing results from The Cedars to experiments, and similarity in $\delta^{18}O$-Δ_{47} (and $\Delta\delta^{18}O$-$\Delta\Delta_{47}$) (Figure 2.3A and 2.6A) of Cedars calcites to both Samail carbonates and experiments, suggests this will be a useful tool to combine with disequilibria modeling to evaluate processes that affect carbon absorption, equilibration, mixing, and mineralization, including in cases where there is not without prior knowledge of the bulk stable isotope composition of fluids and dissolved inorganic carbon. This becomes a powerful tool when evaluating multiple sites and may be beneficial for the development of methodologies that can be used to predict isotopic compositions to compare to data from sequestration sites.

2.5 Conclusions

Through our research, we have analyzed calcite samples collected from springs at The Cedars, located in a peridotite body in Northern California, through a Δ_{47}-Δ_{48} dual clumped isotope lens. This work brings together data from a geological site with lab experiments and with theory. Our work suggests kinetic biases in dual clumped and bulk stable isotope values arise due to carbonate minerals precipitating out of highly alkaline parent media through a CO_2 absorption-driven disequilibrium pathway. Results are comparable to inorganic lab calcite precipitated at high pH (Lucarelli *et al.*, 2022), with significant KIEs including Δ_{47} enrichments and Δ_{48} depletions relative to equilibrium. Our analysis indicates that the largest KIEs are from samples recovered from surface floes where there is sufficient contact with the spring waters and the atmosphere where CO_2 absorption and rapid precipitation conditions are favored. Modern samples that were close to equilibrium occur in locations where significant mixing of surface and spring waters occurs, and as well as in ancient travertine samples. Samples in a mixed endmember region include one surface floe sample, "snow" samples recovered from the bottom of springs, and an ancient travertine sample. We successfully modeled the KIEs associated with a CO_2 absorption-driven disequilibrium process through two different modeling frameworks.

This work builds on prior work on bulk stable isotopes and Δ_{47} at the Samail ophiolite and sets up the potential use of the Δ_{47}-Δ_{48} dual clumped isotope system in potential sites of interest for geological sequestration, as a universal approach for determining (dis)equilibria. It also adds to an emerging body of work that uses the dual clumped isotope measurement to evaluate if samples can be used for Δ_{47} palaeothermometry. Future research at analogous sites can evaluate if the Δ_{47}-Δ_{48} dual clumped isotope space technique can be used to probe for and locate potential on-land CO_2 sequestration sites, through a relatively non-invasive technique. We recommend

expansion of research into carbonate minerals precipitating from peridotite veins to compare surface and subsurface processes and better understand the feasibility of these sites for CO_2 sequestration.

Chapter 3 Paired Δ_{47}-Δ_{48} constrains kinetic effects associated with cave carbonates

Abstract

Cave carbonates are an important archive of terrestrial paleoclimate and have been analyzed using different proxies to develop climate reconstructions. A few studies have explored the potential for carbonate clumped isotope thermometry as a tool for constraining past temperatures at a small number of localities. To date, most papers have reported that isotopic equilibrium is rarely observed in such systems, and that kinetic isotope effects associated with CO_2 degassing impact the mass-47 clumped isotope signature (Δ_{47}). Here, we examined 44 cave carbonate samples of various types from 13 localities for (dis)equilibrium using paired dual clumped isotope ratios (Δ_{47} and Δ_{48}), in concert with light stable carbon and oxygen isotope ratios. Using a Raleigh distillation model, we confirm carbon isotope exchange and oxygen isotope exchange trajectories, and examine the relationship with dual clumped isotope disequilibria ($\Delta\Delta_{47}$ and $\Delta\Delta_{48}$). Data showed that 27 samples exhibited isotopic equilibrium in $\Delta\Delta_{47}$-$\Delta\Delta_{48}$, and thus the majority of samples yield Δ_{47}-T predicted temperatures within error of measured modern temperatures. However, 17 samples exhibited isotopic disequilibria in the Δ_{47}-Δ_{48} space. We find that while traditional degassing effects are present in some stalagmite samples, most exhibit kinetic effects associated with different processes, which we hypothesize reflects isotopic buffering effects on clumped isotopes that can be considerable and cannot be overlooked, and could be studied using proxy data and modeling based approaches in the future. Carbon isotope exchange is associated with depletion of both Δ_{47} and Δ_{48} relative to equilibrium, while oxygen isotope exchange is associated with enrichment of both Δ_{47} and Δ_{48} relative to equilibrium. Cave rafts collected from proximate locations in Mexico exhibit the largest negative departures in $\Delta\Delta_{47}$-$\Delta\Delta_{48}$, with relative cave ventilation impacting the magnitude of isotopic disequilibria. This study suggests the Δ_{47}-Δ_{48} dual carbonate clumped isotope framework can be applied to varying types

of cave carbonate samples enabling identification of (dis)equilibria for use in paleoclimate reconstruction and the probing of kinetic isotope effects.

3.1 Introduction

Cave carbonates (speleothems) have been widely used as terrestrial paleoclimate archives (Bar-Matthews *et al*., 1997; Wang *et al*., 2001; Burns *et al*., 2003; Fleitmann *et al*., 2003; X. Wang *et al*., 2004). Speleothems can be dated accurately through U-series disequilibrium dating methods (Richards and Dorale, 2003; Scholz and Hoffmann, 2008). Because cave temperatures typically reflect mean annual surface temperatures (Poulson and White, 1969; McDermott *et al*., 2006), temperature proxies have been targeted for palaeothermometry. Oxygen isotopes ratios are the most commonly studied temperature proxy applied to speleothems used for paleoclimatology, and are based on a temperature-dependent relationship of the oxygen isotope fractionation factor between calcium carbonate and water (Kim and O'Neil, 1997). However, quantitative interpretation of oxygen isotopic ratios in terrestrial carbonates is hampered by the lack of constraints on the isotopic composition of waters, and on the magnitude of isotope disequilibria effects. The complex isotopic evolution of meteoric water as it passes through the surface atmosphere, soil, karst zones, and adjusted cave atmospheric zone poses a challenge for accurate application of this paleothermometer (Dreybrodt, 1988; McDermott, 2004; Matthew S. Lachniet, 2009). In addition, fractionation associated with prior calcite precipitation and isotopic exchange between CO_2 in the cave atmosphere further complicate the use of this proxy (Mickler *et al*., 2006; Dreybrodt *et al*., 2016; Hansen *et al*., 2017, 2022). While in modern samples this can be circumvented by controlled studies where the bulk isotopic composition of cave drip waters are

monitored at the approximate time and location of precipitation, the potential for variation further back in time, with older speleothems, complicate reconstructions.

Alternate temperature proxies have also been used in speleothems to varying degrees of success. They include Mg/Ca and alkenone unsaturation indexes as indirect proxies (Bar-Matthews *et al*., 2003; Almogi-Labin *et al*., 2009), analyzing isoprenoid tetraether (TEX_{86}) found in speleothems (Powers *et al*., 2004; Tierney *et al*., 2008), fluid inclusion micro thermometry (Krüger *et al*., 2011; Meckler *et al*., 2015), fluid inclusion stable isotope analysis (Van Breukelen *et al*., 2008; Dennis *et al*., 2011; Affolter *et al*., 2014), noble gas thermometry (Kluge *et al*., 2008; Scheidegger *et al*., 2011; Ghadiri *et al*., 2018), nontraditional Ca-isotope analysis (Owen *et al*., 2016), and clumped isotope palaeothermometry (Ghosh *et al*., 2006; Schauble *et al*., 2006; Affek *et al*., 2008; Meckler *et al*., 2015; Kluge *et al*., 2014; Daeron *et al*., 2019).

Here, we examine factors influencing dual carbonate clumped isotopes in speleothems. Clumped isotope palaeothermometry evaluates the thermodynamically driven preference of heavy isotope aggregation based on zero-point energies, from which a temperature dependent relationship is derived (Wang *et al*., 2004; Ghosh *et al*., 2006; Schauble *et al*., 2006; Eiler, 2007, 2011; Tripati et al., 2015). By measuring the relative abundance of the multiply substituted isotopologue of CO_2, m/z 47 ($^{13}C^{18}O^{16}O$ – Δ_{47}), correlating to the Δ_{47} clumped isotope signature, accurate paleotemperature information can be extracted. This approach has been used to successfully evaluate glacial-interglacial temperature changes (Affek *et al*., 2008; Meckler *et al*., 2015) and the slow growing speleothems of the Devil's Hole and Corchia Caves (Kluge *et al*., 2014; Daeron *et al*., 2019). However, one of the major caveats of this system is the underlying assumption that the mineral has achieved isotopic equilibrium prior to precipitation (Ghosh *et al*., 2006). Empirical observations suggest CO_2 degassing disequilibria effects cause enrichments in

$\delta^{18}O$ and a depletion in the Δ_{47} signatures (Daëron *et al*., 2011; Kluge and Affek, 2012; Affek and Zaarur, 2014). In such cases, speleothems exhibit a temperature bias of 10ºC or more when compared to mineral formation temperatures (Kluge *et al*., 2013). Isotopic disequilibria is observed in cave monitoring studies as well as synthetic precipitation experiments which have reported speleothem fractionation factors, that are between kinetic and equilibrium endmember values (Tremaine *et al*., 2011; Day and Henderson, 2011; Johnston *et al*., 2013; Hansen *et al*., 2019, El-Shenawy *et al*., 2020). One of the oldest and most used tests for probing disequilibria is the Hendy's test used for speleothems (Hendy, 1971). However, this test is not universal for all cave carbonates (Dorale and Liu, 2009).

The novel paired dual clumped isotope (Δ_{47} and Δ_{48}) system can provide another method for probing disequilibria (Tripati *et al*., 2015) including in cave carbonates (Bajnai *et al.,* 2021). Recent advancements in mass spectrometry have enabled the measurement of the less abundant m/z 48 isotopologue ($^{12}C^{18}O^{18}O$ - Δ_{48}) at sufficient precision for such applications (Fiebig *et al*., 2019; Bajnai *et al*., 2020; Lucarelli *et al.*, 2021). Dual clumped isotope measurements of Δ_{47} and Δ_{48} have been theoretically and experimentally shown to have an equilibrium relationship, and constrained boundaries for disequilibrium trajectories in dissolved inorganic carbon (DIC) pools and carbonate minerals, which can be used to identify the origin of kinetic isotope effects (KIEs), the extent of deviation from equilibrium, and timescales associated with carbonate and mineral evolution (Hill *et al*., 2014; Tripati *et al*., 2015; Fiebig *et al*., 2019, 2021; Guo, 2020; Bajnai *et al*., 2020; Lucarelli *et al*., 2021). Bajnai *et al.* (2021) and Lucarelli *et al.* (2021) successfully used this paired dual clumped isotope (Δ_{47} and Δ_{48}) space to assess equilibrium conditions associated with modern and Pleistocene Devil's Hole cave carbonate samples, and confirmed consistent temperature over the past 570 ka.

Herein we analyze different types of cave carbonate samples from 13 localities around the world, formed under natural and synthetic conditions, through a bulk stable isotope ($\delta^{13}C$ and $\delta^{18}O$) paired clumped isotope (Δ_{47} and Δ_{48}) lens. We evaluate equilibrium, study the extent and type of kinetic isotope effects (KIEs) associated with our samples, explore complexities associated with different sample groups, and discuss future applications.

Background

3.1.1 DIC Transformation in H_2O

CO_2 dissolution and transformation in aqueous media follow the reactions 1-5 below. Once the CO_2 is dissolved in an aqueous solution, it undergoes (de)hydration or (de)hydroxylation reactions leading to the formation of HCO_3^-, as seen in reactions 1 and 2. These two reactions are the most important in $^{18}O/^{16}O$ isotopic equilibration as they provide the only route for the direct exchange of O atoms between H_2O and DIC (Zeebe and Wolf-Gladrow, 2001). Reactions 3-5 show the pathway from HCO_3^- to CO_3^{2-} via (de)hydration and (de)hydroxylation, and also contribute to the clumped and oxygen isotope equilibration of DIC in an aqueous solution (Guo, 2020).

$$CO_2 + H_2O \leftrightarrow HCO_3^- + H^+ \quad (1)$$

$$CO_2 + OH^- \leftrightarrow HCO_3^- \quad (2)$$

$$HCO_3^- + OH \leftrightarrow H_2O + CO_3^{2-} \quad (3)$$

$$HCO_3^- \leftrightarrow H^+ + CO_3^{2-} \quad (4)$$

$$H_2O \leftrightarrow H^+ + OH^- \quad (5)$$

For clumped isotope analysis, it is crucial that isotopic equilibrium is achieved in the DIC pools prior to carbonate mineral precipitation (Ghosh *et al*., 2006). Isotopic equilibrium is achieved when the DIC and H_2O have had sufficient time to isotopically equilibrate through the previously listed set of reactions. The (de)hydration reactions dominate in cave environments because of the neutral pH in the cave water. The amount of time required for isotopic equilibrium to be achieved is governed by the temperature-dependent forward and reverse rate constants for the hydration and hydroxylation reaction pathways (Zeebe and Wolf-Gladrow, 2001). If the DIC pool does not have sufficient time to achieve isotopic equilibrium, KIEs and disequilibrium isotopic compositions may be recorded in the mineral.

3.1.2 Migration of Meteoric Water from Surface Atmosphere to Subsurface Caves

Meteoric water seeps through various subsurface zones prior to introduction into cave systems. Its interactions along the way dictate its bulk isotopic composition of $\delta^{18}O$ and $\delta^{13}C$ as it enters the cave environment. These zones normally include surface atmosphere, soil, karst, and cave atmosphere environments. In the surface environment, the bulk isotopic composition of meteoric water is modified and adjusted per the hydrological cycle (Dansgaard, 1964; Craig and Gordon, 1965). Upon entry into soil the meteoric water is introduced to an environment which generally has a high pCO_2 that forces an equilibration of pCO_2 dissolved in the water (Dreybrodt and Scholz, 2011). In this environment, the bulk isotopic composition of carbon is dictated by environmental factors. An example of which is the shift in $\delta^{13}C$ based on the type of vegetative decay. C3 plants generally induce a -26‰ average adjustment, where C4 plants induce a -13‰ (McDermott, 2004; McDermott *et al*., 2006). The oxygen isotopic composition, $\delta^{18}O$, is derived from the meteoric water, but generally fractionates due to evaporation, transpiration, canopy interception, or runoff (Fetter, 2018). This results in a $\delta^{18}O$ that is the amount-weighted mean of

infiltrating waters that can be further modified by evaporation (Tang and Feng, 2001; Clark and Fritz, 2013).

Following the soil zone is the epikarst and karst zone, which is the upper surface of bedrock and is characterized by solutional features along the joint and bedding planes where water is stored or mixed (Yonge *et al*., 1985; Klimchouk, 2000; Williams, 2008). The timing and amount of recharge that occurs in this zone dictates the resulting cave drip $\delta^{18}O$ value (Lachniet, 2009). This zone can also cause the saturation state of the drip water to vary over time, thus influencing timing of calcite deposition (Treble *et al*., 2005; Baldini *et al*., 2006). Seasonal variations greatly influence the recharge of this zone thus directly influencing the cave drip and cave air pCO_2 that imparts seasonal bias on the cave carbonate records (Baldini *et al*., 2008; Mattey *et al*., 2008). Partial calcite precipitation in these karst aquifers is also known to occur and only recharge waters that are saturated with $CaCO_3$ will participate in the deposition of speleothem $CaCO_3$ in the caves (Lachniet, 2009)

The final zone that is encountered is the actual cave system. In this zone the partial pressure gradient of the pCO_2 from the cave atmosphere and the cave drip water influences the degree of degassing that occurs, defined by reaction 6 below. In this zone degassing leads to the removal of CO_2 from the cave drip waters resulting in an increase in pH from around 5.0 to between 6.8 to 8.9, based on if the cave is an open or closed system (Dreybrodt, 1988). This leads to the DIC speciation to favor HCO_3^- with approximately 96% abundance, and through Rayleigh distillation it begins to enrich the solution with heavy isotopes (Lachniet, 2009). In addition to this, isotopic exchange with the cave atmosphere can also influence the final isotopic composition of the mineral precipitant. The pCO_2 from the cave atmosphere is influenced by the CO_2 degassing from the

carbonate solutions, vadose CO_2 originating from biological decay (Benavente *et al*., 2010), and atmospheric CO_2 that enters through cave ventilation (Spötl *et al*., 2005).

$$H_2O + CO_2 + CaCO_3 \leftrightarrow Ca^{2+} + 2HCO_3 \qquad (6)$$

Interactions with all these zones, and seasonal variations can greatly affect the bulk isotopic composition along with the degree of kinetic fractionation which is imparted on the final mineral precipitant. Because of this, it is very difficult to extrapolate historical isotopic conditions without explicitly monitoring the respective site.

3.1.3 Carbonate "Clumped" Isotope Geochemistry and Notation

There are 20 different isotopologues of CO_2, with four that are singly-substituted and contain either a heavy isotope of carbon or oxygen. The singly substituted variants are the most abundant and makeup about 99.99% of carbonate ions in minerals (Eiler and Schauble, 2004; Eiler, 2007). The remaining 16 are multiply substituted "clumped" variations that contain heavy isotopes of carbon and/or oxygen (Ghosh *et al*., 2006). Below are examples of two isotopic disproportionation reactions (Polyakov *et al*., 2005) of interest as they generate isotopologues of carbonates that have relative abundances within the detection limits of modern instrumentation.

$$[^{12}C^{16}O^{18}O^{16}O]^{2-} + [^{13}C^{16}O^{16}O^{16}O]^{2-} \leftrightarrow [^{12}C^{16}O^{16}O^{16}O]^{2-} + \mathbf{[^{13}C^{16}O^{18}O^{16}O]^{2-}} \qquad (9)$$

$$[^{12}C^{16}O^{18}O^{16}O]^{2-} + [^{12}C^{18}O^{16}O^{16}O]^{2-} \leftrightarrow [^{12}C^{16}O^{16}O^{16}O]^{2-} + \mathbf{[^{12}C^{18}O^{18}O^{16}O]^{2-}} \qquad (10)$$

While there are many versions of the isotopic disproportionation reactions, like the ones above, reactions 9 and 10, respectively, yield the most abundant *m/z* 63 (67 ppm) and *m/z* 64 isotopologues (12 ppm) (Ghosh *et al*., 2006). The temperature dependency of these

disproportionation reactions and the preference of heavy isotope aggregation as a function of mineral precipitation temperature is the basis of the carbonate clumped isotope thermometer (Ghosh *et al*., 2006; Schauble *et al*., 2006) However, one critical caveat to this correlation is that the carbonate isotopologues must be at isotopic equilibrium. This means that the preferential aggregation of heavy isotopes must not be inhibited and that it must achieve equilibrium conditions at the respective temperature (Ghosh *et al*., 2006)

No current technique allows for the direct measurement of clumped isotopes in carbonate minerals. Thus, *m/z* 63 and *m/z* 64 carbonate ions within the mineral are converted to gaseous *m/z* 47 and *m/z* 48 CO_2, respectively, by phosphoric acid digestion and measured in a gas-source isotope-ratio mass spectrometer (Ghosh *et al*., 2006).

The Δ_{47} and Δ_{48} quantities refer to the abundance of *m/z* 47 [$^{18}O^{13}C^{16}O$] and *m/z* 48 [$^{18}O^{12}C^{18}O$] CO_2 isotopologues relative to a stochastic or random distribution, described by equations 11 and 12,

$$\Delta_{47} = \left[\left(\frac{R_{47}}{R_{47}^*} - 1\right) - \left(\frac{R_{46}}{R_{46}^*} - 1\right) - \left(\frac{R_{45}}{R_{45}^*} - 1\right)\right] * 1000 \quad (11)$$

$$\Delta_{48} = \left[\left(\frac{R_{48}}{R_{48}^*} - 1\right) - 2 * \left(\frac{R_{46}}{R_{46}^*} - 1\right)\right] * 1000 \quad (12)$$

where R_i and R_i^* represent the measured and stochastic ratios of i/44 isotopologue (Eiler and Schauble, 2004; Z. Wang *et al*., 2004; Affek and Eiler, 2006). (Bernasconi *et al*., 2021)

The conversion of carbonate minerals into gaseous CO_2 has a temperature dependent removal of O^{16} versus O^{18} and is corrected by an acid fractionation factor (AFF), denoted by *y* in Equations 13 and 14.

$$\Delta_{47} = \Delta_{63} + y \quad (13)$$

$$\Delta_{48} = \Delta_{64} + y \quad (14)$$

No AFF is applied to measured values but was used for the comparison of measured Δ_{47} and Δ_{48} values to theoretical Δ_{63} and Δ_{64} values. The reference frame and temperature to which the value is being converted also dictates the value of *y*. In the I-CDES reference frame, for the conversion of Δ_{63} to Δ_{47}, the AFF varies from 0.188 to 0.197 from calcite precipitation temperatures ranging from 1000 ºC to 0 ºC, respectively (Hill *et al*., 2014; Tripati *et al*., 2015; Bernasconi *et al*., 2021; Lucarelli *et al*., 2021). For the temperature ranges of the samples collected from the Cedars, we use the AFF *y*=0.196 for the conversion of Δ_{63} to Δ_{47} (Lucarelli *et al*., 2022). For the conversion of Δ_{64} (Hill *et al*., 2014) to Δ_{48}, in the CDES90 reference frame (Hill *et al*., 2014; Tripati *et al*., 2015), we use 0.131 (Lucarelli *et al*., 2021) as the AFF.

3.1.5 Kinetic Fractionation Clumped Isotope (Δ_{47} and Δ_{48}) Signatures

One of the key underlying assumptions is that the carbonate species is within isotopic equilibrium prior to mineral precipitation (Ghosh *et al*., 2006). When this condition is not met, it can affect the heavy isotope distribution and give clumped isotope signatures that do not agree to the equilibrium calibration values. Kinetic departures such as this exist in most Earth-surface carbonate minerals (Daeron *et al*., 2019) in both the biotic and abiotic sphere. On the biotic side, brachiopod shells (Lowenstam, 1961; Carpenter and Lohmann, 1995; Bajnai *et al*., 2018; Rollion-Bard *et al*., 2019) and coral skeletons (McConnaughey, 1988; Cohen and McConnaughey, 2003; Rollion-bard *et al*., 2010; Thiagarajan *et al*., 2011; Saenger *et al*., 2012b; Kimball *et al*., 2016; Spooner *et al*., 2016) are all known to have biotic effects that influence mineral precipitation and can lead to kinetic fractionation. On the abiotic side of the spectrum KIEs associated with

(de)hydration and (de)hydroxylation reactions can cause departures from equilibrium (Ghosh *et al*., 2006; Guo, 2009; Saenger *et al*., 2012; Falk *et al*., 2016; Spooner *et al*., 2016). In the abiotic spectrum speleothems are also known to exhibit kinetic fractionation in their carbonate mineral clumped isotope signatures due to CO_2 degassing effects which are facilitated by the environment from which they precipitate from (C. H. Hendy, 1971; Affek *et al*., 2008; Guo *et al*., 2011; Mcdermott *et al*., 2011; Wainer *et al*., 2011).

Various mechanisms have been proposed to explain isotopic disequilibria in clumped and stable isotope signatures. In lab experiments, Lucarelli *et al.* (2022) observed kinetic fractionation in calcite precipitated from elevated pH solutions. This phenomenon has been hypothesized to have occurred due to the DIC pool not achieving isotopic equilibrium prior to mineral precipitation due to the system not having sufficient time to achieve isotopic equilibria and DIC speciation preference as a function of pH (Beck *et al*., 2005; Hill *et al*., 2014, 2020; Tripati *et al*., 2015). In cave settings, it is known that upon the exposure of the seepage water to cave atmosphere, CO_2 degassing out of the water occurs because of the pCO_2 gradient between the cave water and the cave atmosphere (Dreybrodt, 1988; McDermott *et al*., 2006; Lachniet, 2009). This CO_2 degassing leads to an enrichment of $\delta^{18}O$, accompanied by a depletion in the Δ_{47} clumped isotope signature (Daëron *et al*., 2011; Kluge and Affek, 2012; Affek and Zaarur, 2014). Kinetic biases, during the early stages of degassing, result in an enrichment of the Δ_{48} clumped isotope signature (Fiebig *et al*., 2019; Guo and Zhou, 2019; Guo, 2020; Bajnai *et al*., 2020).

3.2 Materials and Methods

3.2.1 Sample Collection and Information

Samples were collected from 13 localities shown in Figure 3.2 and tabulated in Table 3.1. A brief description of each respective site and recovered samples is provided below. Additional details on collection method, recovery protocols, and processing are in listed citations.

3.2.1.1 Cenote Rainbow, Feno, and Monkey Dust, Mexico Cave Samples (Kovacs et al. 2018)

These cave raft samples, collected by Kovacs *et al.* (2018), were from three cave systems located in the Yucatan Peninsula. The cave systems from where they were collected are referred to as Cenote Rainbow, Feno, and Monkey Dust. Each cave had a different profile exposed to the atmosphere and water levels which fluctuated following seasonal trends. Samples R1, R2, R3, and R5 were collected from Cenote Rainbow. The Cenote Rainbow cave system is 2.2 km inland (20º29'52.44"N,87º15'29.65"W) from the Caribbean Sea coast, and is situated in between the townships of Puerto Aventuras and Akumal. This cenote is an extension of the X'tabay cave system that is 1394 m in length and 13.7 m in depth is considered semi-enclosed. The water level of the cave fluctuated from 0.34 m and 0.94 m. Samples F1, F2, F3, F4, and F5 were collected from Cenote Feno. The Cenote Feno cave is located north of Tulum (20º19'17.34"N, 87º25'43.91"W) and is part of the Sistema Fenomeno cave system and is considered a closed system, with only a small opening to outside atmosphere. The water level of this cave fluctuated from 0.31 m to 0.98 m. Samples B1, B3, and B5 were collected from Cenote Monkey Dust, also known as Cenote Borge. The Cenote Monkey Dust is the located south of Tulum (20º11'19.81"N, 87º33'4.66"W) and is part of the Sistema Dos Pisos cave system and is considered completely open to atmosphere. The water level of this cave fluctuated from 0.41 m to 1.15 m. An additional map with locations of the respective cenotes can be seen in S.3.2 of the Supplemental Information.

3.2.1.2 Cueva Bonita, Mexico Cave Samples (Wright et al. 2022)

Farmed calcite plates and naturally occurring speleothem samples were collected by Wright *et al.* (2022) from the Cueva Bonita (23ºN, 99ºW; 1071m above sea level) caves located in the northern-most tropical rainforest of Sierra Madre Oriental in the Northeast state of Tamaulipas. The farmed calcite plates include samples CB-D6, CB-D62, CB3, CB4-Scar, and CB4-Scar2. The speleothem (stalagmite) samples include samples CB4-12-Wet, CB4-48-Dry, CB4-82-Wet, CB4-99-Dry, and CB4-Top. Farmed calcite plates were collected using frosted glass plates that were placed under cave drip water. Speleothem samples were collected via core sampling.

3.2.1.3 Cueva de la Puente, Mexico Cave Samples (Serrato, 2020)

Farmed calcite plates were recovered from Cueva de la Puente in San Luis Potosi, Mexico (21.98°N, 100.57°W) by Serrato *et al.* (2020). The cave is located at an elevation of 2109 m above sea level and the local geology is dominated by upper Cretaceous limestone fluorite deposits with thin soil cover.

3.2.1.4 Lilburn Cave, California, United States (Wortham et al. 2021)

Farmed calcite samples GLR and CPY were recovered by Wortham *et al.* (2021) from the Lilburn Caves in Sequoia and Kings Canyon National Park located in Central California. GLR was recovered from a site located 30m away from the surface entrance to the cave system. CPY was recovered further away from the surface entrance at 61m. Cave drip from stalactites were subjected to collection under sanded watch glasses of approximately 10cm in diameter were used to initiate calcite growth.

3.2.1.5 Moaning Cave, California, United States (Oster et al. 2009)

Speleothems were collected by Oster *et al.* (2009) from the Moaning Cave (38.06ºN, 120.46ºW) located in California Sierra Nevada mountain range. The samples were collected through core sampling of stalagmite where the drip center was well defined. U-series dating indicates an age of approximately 10.37±0.25 ka putting it in the early Holocene era.

3.2.1.6 Tham Doun Mai Cave, Laos (Wang et al., 2019; Griffiths et al., 2020)

Samples were collected from the Tham Doun Mai Cave (20°45'N, 102°38'E) (Wang *et al*., 2019; Griffiths *et al*., 2020), labeled TM-D10 in our paper. This cave is ~3,745 m-long and located 352 m above sea level in Luang Prabang Province, Laos. Core samples of the stalagmites were taken for analysis about 200 m from the entrance of the cave.

3.2.1.7 Tham Nguen Mai Cave, Laos (Unpublished)

Samples labeled TNM were collected from the Tham Nguen Mai cave located in Khammouane Province Laos. The cave is 2189 m long and located upstream from the Xe Bang Fai sink, and is likely part of an ancient underground route of the Xe Bang Fai river. Farmed calcite plates were collected from under an active drip approximately 300 m from the cave entrance. These calcite plates were farmed between Jan 2019 and Mar 2020. Site information was provided by Kathleen Johnson (UC Irvine).

3.2.1.8 McMaster Artificial Cave Samples (El-Shenawy et al., 2020)

Synthetic speleothem samples were grown in an artificial cave that simulated cave drip and stalagmite growth. A pure $CaCO_3$ saturated solution with a pCO_2 level of 14000-18000 ppmv was distributed to a 35 cm long Pyrex tube channel (e.g., stalactite) that allowed for CO_2 degassing to occur before the water impinges the upper watch glass (e.g., stalagmite) at a distance of 85 cm and then flow into the lower watch glass (e.g., pool). The solution was injected into the long tube at

three different flow rates (Fast, Intermediate and Slow). The environment in this cave system was controlled with temperature being modulated between 15, 25, and 32ºC; relative humidity at 95%; and a pCO_2 of approximately 550 ppmv. Samples MIE-15-95-9-FL-Cent, MIE-15-95-9-FU-Edge, MIE-15-95-9-SL-Cent, MIE-25-95-8-FL-Cent, MIE-25-95-8-FU-Edge, MIE-32-95-3-FL-Cent, and MIE-32-95-3-FU-Cent were precipitated from this artificial cave.

3.2.1.9 Mechara and Tigray Caves, Ethiopian Highlands (Asrat et al., 2008)

Sample ASFA was collected by Asrat *et al.* (2008) from the Rukiessa cave in the Mechara cave system, that is located in the Southeastern part of the Ethiopian highlands. The Rukiessa cave's entrance is located 1 km east of the eastern bank of the Mechara river (09°51'N, 37°65'E, elevation: 1618 m ASL). The cave is regularly flushed by seasonal floods which contain allogenic sediments. The entrance is a 2 m deep vertical hole in a sandy limestone layer that opens to a few chambers in a vertical series. The third chamber, known as the Asfa Chamber, approximately 30 m below the surface is where stalagmite sample ASFA was collected. This chamber is described as very wet, with pool waters fed by drips from active stalacites, and percolation fed streams (Asrat *et al*., 2008).

Sample MM1 was collected from May Mekden cave (13°34'58"N, 39°34'5"E). It is a small 3 m long cave at the side of a cliff with the stalagmite collected near the entrance of the cave. The ZA-3 sample is collected from Zayei cave (13.5586°N, 39.1454°E) and has similar conditions and collection location as the May Mekden cave. Both caves are part of the Tigray Cave system. These two samples are not from dripping caves, so no drip water stable isotope information is available.

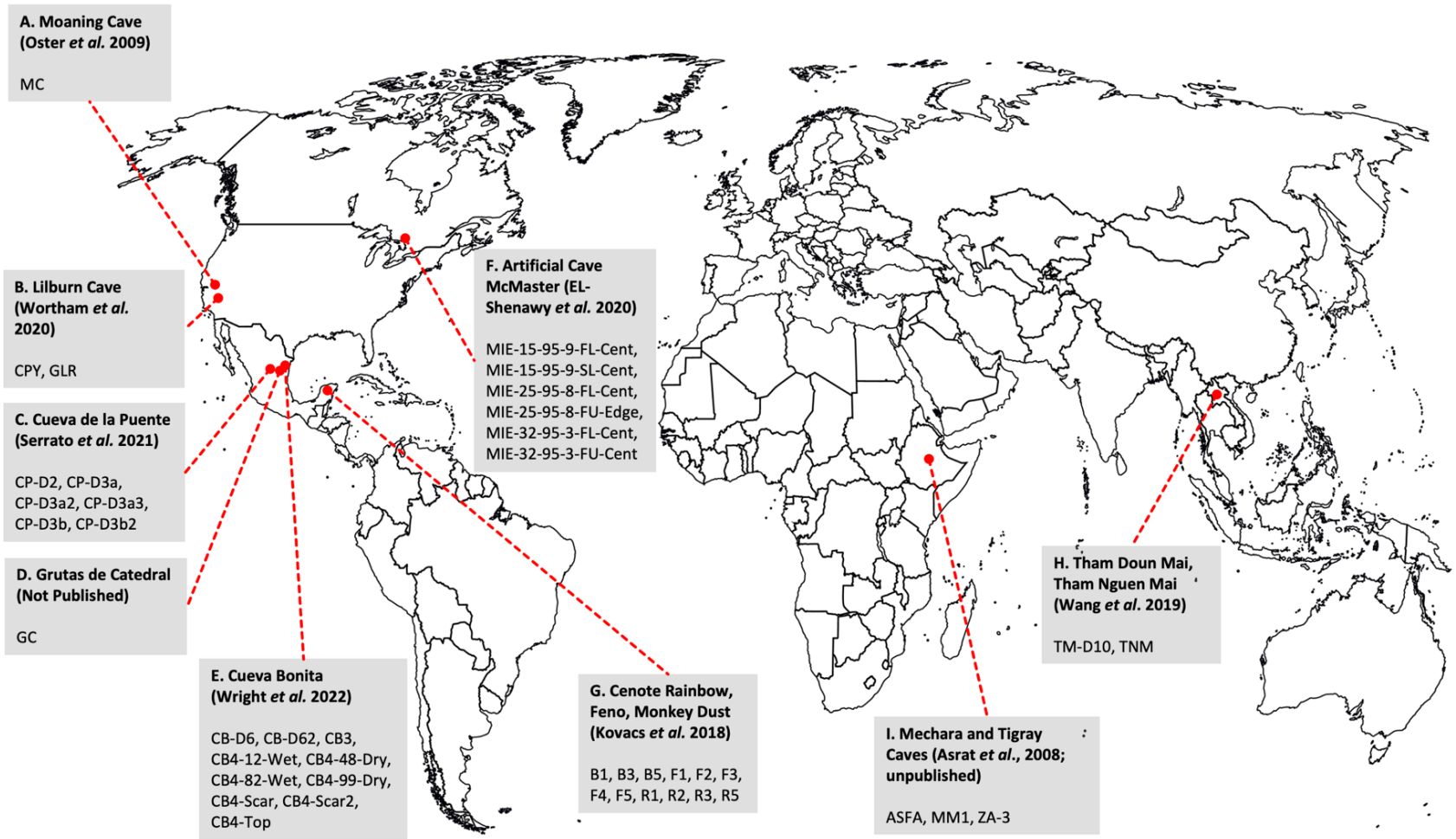

Figure 3.2 Map of the world showing the location of sample groups and individual samples recovered. **A)** Moaning Cave, USA, California samples: MC (Oster *et al.* 2009) **B)** Liliburn Cave, USA, California samples: CPY and GLR (Wortham *et al.* 2021) **C)** Cueva de la Puente, Mexico samples: CP-D2, CP-D3a, CP-D3a2, CP-D3a3, CP-D3b, and CP-D3b2 (Serrato *et al.* 2021) **D)** Grutas de Catedral, Mexico samples: GC (Not Published) **E)** Cueva Bonita, Mexico samples: CB-D6, CB-D62, CB3, CB4-12-Wet, CB4-48-Dry, CB4-82-Wet, CB4-99-Dry, CB4-Scar, CB4-

Scar2, and CB4-Top (Wright *et al.* 2022) **F)** Artificial Cave, McMaster, Canada samples: MIE-15-95-9-FL-Cent, MIE-15-95-9-SL-Cent, MIE-25-95-8-FL-Cent, MIE-25-95-8-FU-Edge, MIE-32-95-3-FL-Cent, and MIE-32-95-3-FU-Cent (EL-Shenawy *et al.* 2020) **G)** Cenote (Rainbow, Feno, Monkey Dust), Mexico samples: B1, B3, B5, F1, F2, F3, F4, F5, R1, R2, R3, and R5 (Kovacs *et al.* 2018) **H)** Tham Doun Mai and Tham Nguen Mai, Laos samples: TM-D10 and TNM (Wang *et al.* 2019)

Sample Name	Sample Type	Location	Recovery Dates	Source Citation
B1	Cave Raft	Monkey Dust (Borge) Cenote, Mexico	May 2014 - May 2016	Kovacs *et al.,* (2018)
B3	Cave Raft	Monkey Dust (Borge) Cenote, Mexico	May 2014 - May 2016	
B5	Cave Raft	Monkey Dust (Borge) Cenote, Mexico	May 2014 - May 2016	
F1	Cave Raft	Feno Cenote, Mexico	May 2014 - May 2016	
F2	Cave Raft	Feno Cenote, Mexico	May 2014 - May 2016	
F3	Cave Raft	Feno Cenote, Mexico	May 2014 - May 2016	
F4	Cave Raft	Feno Cenote, Mexico	May 2014 - May 2016	
F5	Cave Raft	Feno Cenote, Mexico	May 2014 - May 2016	
R1	Cave Raft	Rainbow Cenote, Mexico	May 2014 - May 2016	
R2	Cave Raft	Rainbow Cenote, Mexico	May 2014 - May 2016	
R3	Cave Raft	Rainbow Cenote, Mexico	May 2014 - May 2016	
R5	Cave Raft	Rainbow Cenote, Mexico	May 2014 - May 2016	
CB-D6	Farmed Calcite Plate	Cueva Bonita, Mexico	May 2018 - May 2020	Wright *et al.,* (2022)
CB-D62	Farmed Calcite Plate	Cueva Bonita, Mexico	May 2019 - Feb 2020	
CB3	Farmed Calcite Plate	Cueva Bonita, Mexico	Jan 2017 - Jan 2018	
CB4-12-Wet	Speleothem	Cueva Bonita, Mexico	June 2018 - May 2019	
CB4-48-Dry	Speleothem	Cueva Bonita, Mexico	June 2018 - May 2019	
CB4-82-Wet	Speleothem	Cueva Bonita, Mexico	June 2018 - May 2019	
CB4-99-Dry	Speleothem	Cueva Bonita, Mexico	June 2018 - May 2019	
CB4-Scar	Farmed Calcite Plate	Cueva Bonita, Mexico	May 2018 - May 2019	
CB4-Scar2	Farmed Calcite Plate	Cueva Bonita, Mexico	May 2019 - Feb 2020	
CB4-Top	Speleothem	Cueva Bonita, Mexico	June 2018 - May 2019	
CP-D2	Farmed Calcite Plate	Cueva de la Puenta, Mexico	Apr 2017 - May 2018	Serrato, (2020)
CP-D3a	Farmed Calcite Plate	Cueva de la Puenta, Mexico	May 2018 - May 2019	
CP-D3a2	Farmed Calcite Plate	Cueva de la Puenta, Mexico	May 2019 - Nov 2019	
CP-D3a3	Farmed Calcite Plate	Cueva de la Puenta, Mexico	Nov 2019 - Feb 2020	
CP-D3b	Farmed Calcite Plate	Cueva de la Puenta, Mexico	May 2018 - May 2019	
CP-D3b2	Farmed Calcite Plate	Cueva de la Puenta, Mexico	May 2019 - Nov 2019	
GC	Farmed Calcite Plate	Grutas de Catedral, Mexico	Apr 2017 - May 2018	unpublished

TM-D10	Farmed Calcite Plate	Tham Doun Mai, Laos	Feb 2015 - Feb 2017	Wang *et al.,* (2019); Griffith *et al.,* (2020)
TNM	Farmed Calcite Plate	Tham Nguen Mai, Laos	Jan 2019 - Feb 2020	unpublished
CPY	Farmed Calcite Plate	Liburn Cave, California, United States	May 2018 - Feb 2020	Wortham *et al.,* (2021)
GLR	Farmed Calcite Plate	Liburn Cave, California, United States	May 2018 - Feb 2020	
MC	Speleothem	Moaning Cave, California, United States	Mar 2006 - Jul 2009	Oster *et al.,* (2009)
MIE-15-95-9-FL-Center	Artificial Speleothem	McMaster-Carr University, Ontario, Canada	N/A	EL-Shenawy *et al.,* (2020)
MIE-15-95-9-FU-Edge	Artificial Speleothem	McMaster-Carr University, Ontario, Canada	N/A	
MIE-15-95-9-SL-Center	Artificial Speleothem	McMaster-Carr University, Ontario, Canada	N/A	
MIE-25-95-8-FL-Center	Artificial Speleothem	McMaster-Carr University, Ontario, Canada	N/A	
MIE-25-95-8-FU-Edge	Artificial Speleothem	McMaster-Carr University, Ontario, Canada	N/A	
MIE-32-95-3-FL-Center	Artificial Speleothem	McMaster-Carr University, Ontario, Canada	N/A	
MIE-32-95-3-FU-Center	Artificial Speleothem	McMaster-Carr University, Ontario, Canada	N/A	
ASFA	Speleothem	Machara Caves, Ethiopia, Africa	Apr 2004 - Sep 2007	Asrat *et al.,* (2008)
MM1	Speleothem	Tigray Caves, Ethiopia, Africa	N/A	unpublished
ZA-3	Speleothem	Tigra Caves, Ethiopia Africa	N/A	

Table 3.1 Sample information. Sample names, type, recovery location, recovery dates, and citation source are provided. Information associated with samples GC and TNM was provided by co-author Kathleen Johnson (UC Irvine); and ASFA was provided by co-author Daniel Gebregiorgis (Georgia State University).

3.2.2 Analysis and Instrumentation

All isotopic measurements were made using Nu Instruments Perspective IS isotope ratio mass spectrometers (IRMS) over the time frame ranging from 2020 to 2022. The Nu Instruments Perspective IRMS system produces statistically indistinguishable Δ_{47} (Lucarelli *et al*., 2021; Upadhyay *et al*., 2021) and Δ_{48} data (Lucarelli *et al*., 2021; Upadhyay *et al*., 2021) with standards that agree with published values from other labs for Δ_{47} (Bernasconi *et al.,* 2021) and Δ_{48} (Bajnai *et al*., 2020; Swart *et al*., 2021). The general configuration for sample processing on these two instruments is (1) phosphoric acid digestion for the conversion of $CaCO_3$ (s) to CO_2 (g), (2) CO_2 (g) purification, (3) IRMS system for quantitative detection of isotopes, and (4) a data processing station which uses Easotope (Cédric M John and Bowen, 2016) for processing and applying data corrections. Clumped isotopic measurements were performed on evolved CO_2 produced using a common acid bath (CAB) approach. In this approach, ~0.5 mg $CaCO_3$ samples were subjected to phosphoric acid digestion at 90 ºC for approximately 20 minutes, leading to the evolution of CO_2 gas, which is then subjected to intensive purification. This purification is accomplished using an Adsorption Trap (AdTrap), an–inline, short GC column packed with Porapak Type-Q^{TM} 50/80. Upon purification, the gas is transferred to the IRMS system, which continuously references a standard CO_2 gas against the sample gas through an automated changeover block system. All samples, except for sample CB4-12-Wet, had a minimum of three replicates run and analyzed, regardless of which instrument they were run on. The number of replicates run was dictated by the amount of sample provided, how precise the data was, and robustness of standards. One sample (CB4-12-Wet) had insufficient material for three replicate analyses and is denoted with an open symbol in all of the figures.

Description of Nu Instruments Perspective IRMS

The Nu Perspective IRMS is a mass spectrometer that is optimized for clumped isotope analysis with secondary electron suppression, which reduces the signal-to-noise ratio. Energy filters and quadratic lenses fitted in front of the Faraday collector array drives the suppression. The detectors for masses 44, 45, and 46 are registered through $3x10^8$, $3x10^{10}$, and $3x10^{11}$ Ω resistors, respectively. The detectors for masses 47, 48, and 49 are registered with $3x10^{12}$ Ω resistors. Detectors for masses 47, 48, and 49 are shielded by secondary electron suppressors, tuned to screen out secondary electrons. A dual-inlet system allows for the input of the sample gas and a reference gas controlled by a bellows system that inputs both gasses through a changeover block, so the sample and reference gases can be compared in real-time. This bellow system has four blocks of 15 cycles for a total of 60 cycles of sample to standard comparison with an 8-second changeover delay and 20 seconds of integration per cycle for a total integration time of 1200 seconds. There are continuous pressure adjustments using a Newtonian zeroing technique, with balancing to achieve 80 nA (or 16 V) on mass 44 at every acquisition, compared to just at the beginning of the block (Lucarelli *et al*., 2021; Upadhyay *et al*., 2021).

Standardization and data processing

The CO_2 reference gas used to establish real-time comparison to unknown sample composition was sourced from Oztech with an isotopic composition as follows: $\delta^{18}O_{V\text{-}SMOW}$ = 24.9 ‰; $\delta^{13}C_{V\text{-}PDB}$ = -3.56 ‰. $CaCO_3$ standards, for which all Δ_{47} and Δ_{48} are presented relative to, include Carmel Chalk, CMTile, ETH-1, ETH-2, ETH-3, ETH-4, and Veinstrom (Lucarelli *et al*., 2021; Upadhyay *et al*., 2021). International standards ETH-1 and ETH-2 were the primary standards used to make non-linearity corrections associated with both Δ_{47} and Δ_{48} raw data. Mean values for Δ_{47}, Δ_{48}, $\delta^{18}O$, and $\delta^{13}O$ of the $CaCO_3$ standards are given in Table 3.2 and raw and standardized data for all standards and samples will be archived on EarthChem upon publication.

Data was processed and corrected using Easotope 64-bit, release version 20201231 (Cédric M. John and Bowen, 2016) with IUPAC parameters (Brand *et al*., 2010; Daëron *et al*., 2016). We report all values of Δ_{47} on the Intercarb-Carbon Dioxide Equilibrium Scale (I-CDES) (Bernasconi *et al*., 2021), at an acid digestion temperature of 90 ºC. The Δ_{48} values are reported in the Carbon Dioxide Equilibrium Scale at 90 ºC, CDES90 (Fiebig *et al*., 2019; Lucarelli *et al*., 2022).

	$\Delta_{47\ (I\text{-}CDES)}$ (‰)	$\Delta_{48\ (CDES90)}$ (‰)	$\delta^{18}O_{V\text{-}SMOW}$ (‰)	$\delta^{13}C_{V\text{-}PDB}$ (‰)
CMTile	0.313	0.145	29.349	2.031
Carmel Chalk	0.592	0.237	26.850	-2.183
Veinstrom	0.713	0.272	17.918	-6.166
ETH-1	0.205	0.132	28.665	2.028
ETH-2	0.209	0.132	11.672	-10.162
ETH-3	0.613	0.247	29.125	1.706
ETH-4	0.451	0.201	11.528	-10.2

Table 3.2 Mean clumped and stable isotope values determined for all carbonate standards used in this study. All Δ_{47} data is presented in the I-CDES reference frame and the Δ_{48} data is presented in the CDES90 reference frame. ETH-1 and ETH-2 are used to make non-linearity corrections to the raw data.

Equilibrium Values

Oxygen isotope equilibrium is calculated for calcite samples at the varying caves using the reported temperature and water $\delta^{18}O_{V\text{-}PDB}$ that was measured, or reported, in conjunction with the relationship determined by Kim and O'Neil (1997). The Δ_{47} and Δ_{48} equilibrium is calculated with respect to reported temperature conditions using relationships from Lucarelli *et al.* (2022)

$$\Delta_{47\ I-CDES\ EQ} = (0.037 \pm 0.002) \times 10^6 T^{-2} + (0.178 \pm 0.009) \quad (15)$$

$$\Delta_{48\ CDES90\ EQ} = (0.015 \pm 0.0005) \times 10^6 T^{-2} + (0.078 \pm 0.006) \quad (16)$$

An equilibrium Δ_{48}/Δ_{47} relationship, Equation 17, was determined experimentally by Lucarelli *et al.* (2022) and is used here to provide a reference for equilibrium conditions.

$$\Delta_{48(CDES90)} = (0.429 \pm 0.010)\Delta_{47\ (I-CDES)} - (0.006 \pm 0.006) \quad (17)$$

3.2.3 Qualitative Modeling of DIC-H2O-CO2 System Using IsoDIC

To qualitatively illustrate the evolution disequilibria in the DIC pool, specifically CO_3^{2-}, we used the IsoDIC modeling software developed by Guo *et al.* (Guo, 2019; Guo, 2020). This modeling software predicts kinetic isotope fractionation in clumped isotopes in a DIC-H_2O-CO_2 system. It simulates (de)hydration and (de)hydroxylation reactions 1-5, for the evolution of CO_2 to CO_3^{2-}, and the isotopologue reactions involving all major isotopes of C and O, equating to a total of 155 reactions. The forward and reverse rate constants were estimated using Equation 18 below,

$$k^* = a_{KIE} * k \qquad (18)$$

where k is the rate constant of the isotopically non-substituted reactions, and a_{KIE} is the kinetic isotope fractionation factor for the isotopically substituted reaction. The product of these variables yields k^*, the modified rate constant for the isotopically substituted reaction. (De)hydration and (de)hydroxylation reactions, Equation 1 and 2, are the only reactions that contribute to isotopic fractionation where Equations 3-5 are assumed to be at equilibrium due to their relative rates of reaction when compared to Equations 1 and 2 (Guo, 2019, 2020).

The following parameters were input into IsoDIC to perform modeling in the absorption and degassing regimes: Degassing (1) solution temperature: 25.0 ºC, (2) solution pH: 8, (3) air pCO_2: 300 ppm, (4) $\delta^{13}C_{V\text{-}PDB}$ air: -10.00 ‰, (5) $\delta^{18}O_{V\text{-}SMOW}$ air: 41.46 ‰ (6) system evolution time: 12h (7) clumped T: 25.0 ºC; Absorption 1) solution temperature: 25.0 ºC, (2) solution pH: 9, (3) air pCO_2: 3000 ppm, (4) $\delta^{13}C_{V\text{-}PDB}$ air: -10.00 ‰, (5) $\delta^{18}O_{V\text{-}SMOW}$ air: 41.46 ‰ (6) system evolution time: 12h (7) clumped T: 25.0 ºC. These values do not correlate to a specific cave or environment, and are default parameters used by Guo *et al.*, (2020) when he explained the model. Conversions from D_{63} and D_{64} were conducted using the AFFs previously listed. $\Delta\Delta_{47}$ and $\Delta\Delta_{48}$ plots were created using the same temperature equilibrium equations used by Guo *et al*., (2020). The equations used by this model are described in greater detail in the Supplementary Materials, S.3.1.

3.3 Results

All clumped and stable isotope data are reported in Table 3.3. The three different variations of cave carbonates include speleothems (diamonds), farmed calcite plates (circles), and cave rafts (triangles). Temperature predictions, seen in Table 3.4, were made using the Δ_{47}-T calibration

curve reported by Anderson *et al.*, (2021). Temperatures were listed as agreeing if the reported and predicted values fell within 1 s.e. of each other.

3.3.1 Clumped (Δ_{47} and Δ_{48}) and Stable ($\delta^{13}C$ and $\delta^{18}O$) Isotope Analysis

Plots of clumped isotope (Δ_{47} and Δ_{48}) and stable isotope ($\delta^{13}C$ and $\delta^{18}O$), with respect to sample type, can be seen in Figures 3.3 and 3.4. Plots of clumped isotope (Δ_{47} and Δ_{48}) and stable isotope ($\delta^{13}C$ and $\delta^{18}O$) with all samples aggregated can be viewed in the Supplementary Information (SI) (S.3). Plots of paired (Δ_{47}-Δ_{48}) clumped isotope and aggregated extent of disequilibria ($\Delta\Delta_{47}$-$\Delta\Delta_{48}$) can be viewed in the SI (S.3).

3.3.1.1 Cave Rafts

The $\Delta_{47\ (I\text{-}CDES)}$, $\Delta_{47\ (CDES90)}$, $\delta^{18}O_{V\text{-}SMOW}$, and $\delta^{13}C_{V\text{-}PDB}$ range for the cave rafts from three proximate cenotes, Rainbow, Feno, and Monkey Dust, (samples: B1, B3, B5, F1, F2, F3, F4, F5, R1, R2, R3, R5), collected by Kovacs *et al.* (2018), are 0.550‰ to 0.610‰, 0.119‰ to 0.275‰, 24.616‰ to 25.502‰, and -6.115‰ to –5.432‰ respectively.

3.3.1.2 Calcite Plates

The $\Delta_{47\ (I\text{-}CDES)}$, $\Delta_{48\ (CDES90)}$, $\delta^{18}O_{V\text{-}SMOW}$, and $\delta^{13}C_{V\text{-}PDB}$ range for the calcite plates from Cueva Bonita (CB-D6, CB-D62, CB3, CB4-Scar, CB4-Scar2) collected by Wright *et al.* (2022) are 0.601‰ to 0.634‰, 0.234‰ to 0.274‰, 25.722‰ to 26.802‰, and -12.866‰ to –5.328‰ respectively. The $\Delta_{47\ (I\text{-}CDES)}$, $\Delta_{48\ (CDES90)}$, $\delta^{18}O_{V\text{-}SMOW}$, and $\delta^{13}C_{V\text{-}PDB}$ range for the calcite plates from Cueva de la Puenta (CP-D2, CP-D3a, CP-D3a2, CP-D3a3, CP-D3b, CP-D3b2) collected by Serrato (2020) are 0.579‰ to 0.639‰, 0.171‰ to 0.271‰, 21.464 ‰ to 22.215‰, and -10.798‰ to –8.508‰ respectively. The $\Delta_{47\ (I\text{-}CDES)}$, $\Delta_{48\ (CDES90)}$, $\delta^{18}O_{V\text{-}SMOW}$, and $\delta^{13}C_{V\text{-}PDB}$ range for calcite

plates from Liburn Cave (CPY, GLR) collected by Wortham *et al.* (2021) are 0.640‰ to 0.645‰, 0.236‰ to 0.239‰, 22.087‰ to 22.474‰, and -8.675‰ to –9.720‰ respectively. The $\Delta_{47\,(I\text{-}CDES)}$, $\Delta_{48\,(CDES90)}$, $\delta^{18}O_{V\text{-}SMOW}$, and $\delta^{13}C_{V\text{-}PDB}$ for individual calcite plate samples collected from Grutas de Catedral (GC), Tham Doun Mai (TM-D10), and Tham Nguen Mai (TNM) can be found in Table 3.3.

3.3.1.3 Speleothems

The $\Delta_{47\,(I\text{-}CDES)}$, $\Delta_{48\,(CDES90)}$, $\delta^{18}O_{V\text{-}SMOW}$, and $\delta^{13}C_{V\text{-}PDB}$ range for the speleothem samples from Cueva Bonita (CB4-12-Wet, CB4-48-Dry, CB4-82-Wet, CB4-99-Dry, CB4-Top) collected by Wright *et al.* (2022) are 0.606‰ to 0.617‰, 0.265‰ to 0.305‰, 25.513‰ to 26.896‰, and -11.065‰ to –7.406‰ respectively. The $\Delta_{47\,(I\text{-}CDES)}$, $\Delta_{48\,(CDES90)}$, $\delta^{18}O_{V\text{-}SMOW}$, and $\delta^{13}C_{V\text{-}PDB}$ range for the synthetic speleothem samples (MIE-15-95-9-FL-Center, MIE-15-95-9-FU-Edge, MIE-15-95-9-SL-Center, MIE-25-95-8-FL-Center, MIE-25-95-8-FU-Edge, MIE-32-95-3-FL-Center, MIE-32-95-3-FU-Center) synthesized by EL-Shenawy *et al* are 0.564‰ to 0.629‰, 0.169‰ to 0.315‰, 20.069‰ to 24.324‰, and -29.041‰ to –15.428‰ respectively. Information on the individual cave sample collected from Moaning Cave, California, USA (sample: MC) (Wortham *et al.*, 2021); Mechara Caves, Ethiopia, Africa (ASFA); and Tigray Caves, Ethiopia, Africa (MM1 and ZA-3) can be found in Table 3.3.

Sample Name	Replicates (n)	$\delta^{13}C_{V\text{-}PDB}$ (‰)	1 s.d.	$\delta^{18}O_{V\text{-}SMOW}$ (‰)	1 s.d.	$\Delta_{47\ (I\text{-}CDES)}$ (‰)	1 s.e.	$\Delta_{48\ (CDES90)}$ (‰)	1 s.e.
B1	3	-10.977	0.021	25.027	0.197	0.550	0.007	0.119	0.026
B3	5	-10.710	0.007	24.976	0.049	0.566	0.013	0.163	0.034
B5	5	-11.038	0.056	24.724	0.145	0.573	0.005	0.194	0.014
F1	4	-11.433	0.040	25.023	0.067	0.570	0.004	0.149	0.022
F2	5	-11.510	0.138	25.042	0.043	0.610	0.018	0.204	0.019
F3	5	-11.660	0.086	25.011	0.107	0.589	0.007	0.172	0.018
F4	5	-11.010	0.055	24.697	0.246	0.574	0.010	0.182	0.014
F5	5	-11.428	0.160	24.761	0.165	0.602	0.018	0.275	0.069
R1	3	-10.347	0.136	25.257	0.072	0.587	0.020	0.123	0.016
R2	4	-11.790	0.079	24.616	0.034	0.579	0.010	0.197	0.017
R3	5	-9.530	0.131	25.320	0.189	0.564	0.012	0.147	0.029
R5	5	-10.084	0.094	25.502	0.181	0.565	0.012	0.144	0.018
CB-D6	5	-9.916	0.054	25.747	0.089	0.634	0.017	0.267	0.016
CB-D62	4	-9.920	0.034	25.722	0.034	0.601	0.010	0.263	0.010
CB3	4	-5.328	0.005	26.802	0.047	0.602	0.015	0.264	0.030
CB4-12-Wet	2	-10.310	0.057	25.513	0.007	0.607	0.002	0.265	0.054
CB4-48-Dry	13	-9.499	0.067	26.776	0.088	0.615	0.009	0.304	0.046
CB4-82-Wet	5	-9.834	0.064	25.984	0.123	0.617	0.013	0.265	0.053
CB4-99-Dry	5	-7.406	0.140	26.896	0.145	0.606	0.013	0.305	0.026
CB4-Scar	5	-12.866	0.061	25.945	0.057	0.627	0.015	0.274	0.024
CB4-Scar2	5	-12.224	0.051	25.747	0.105	0.623	0.023	0.234	0.012
CB4-Top	6	-11.065	0.102	25.847	0.148	0.607	0.011	0.267	0.050
CP-D2	6	-10.798	0.357	21.464	0.106	0.623	0.029	0.264	0.034
CP-D3a	5	-8.796	0.388	22.166	0.238	0.595	0.022	0.171	0.027
CP-D3a2	5	-8.654	0.202	22.043	0.148	0.610	0.024	0.211	0.024
CP-D3a3	5	-10.376	0.438	21.537	0.187	0.639	0.008	0.271	0.030
CP-D3b	4	-8.508	0.041	22.215	0.081	0.579	0.008	0.247	0.039

CP-D3b2	5	-9.848	0.294	21.659	0.224	0.618	0.018	0.201	0.030
GC	5	-10.542	0.244	23.601	0.189	0.641	0.014	0.263	0.021
TM-D10	5	-14.446	0.071	21.818	0.098	0.603	0.008	0.324	0.035
TNM	5	-14.754	0.103	21.168	0.122	0.632	0.021	0.266	0.024
CPY	7	-9.720	0.040	22.087	0.044	0.645	0.008	0.236	0.010
GLR	7	-8.675	0.093	22.474	0.056	0.640	0.012	0.239	0.029
MC	7	-8.228	0.081	22.753	0.051	0.600	0.006	0.235	0.028
MIE-15-95-9-FL-Center	4	-24.298	0.057	23.889	0.014	0.612	0.005	0.215	0.037
MIE-15-95-9-FU-Edge	4	-27.795	0.103	23.768	0.049	0.616	0.009	0.315	0.004
MIE-15-95-9-SL-Center	5	-15.428	0.228	24.324	0.025	0.629	0.005	0.282	0.024
MIE-25-95-8-FL-Center	5	-23.306	0.050	21.636	0.022	0.596	0.005	0.233	0.016
MIE-25-95-8-FU-Edge	8	-28.804	0.097	22.064	0.058	0.569	0.011	0.280	0.027
MIE-32-95-3-FL-Center	5	-20.734	0.040	20.069	0.024	0.564	0.012	0.169	0.014
MIE-32-95-3-FU-Center	7	-29.041	0.070	20.874	0.059	0.578	0.005	0.237	0.021
ASFA	6	-7.405	0.019	29.745	0.037	0.610	0.008	0.181	0.022
MM1	7	-4.640	1.217	28.026	0.732	0.590	0.003	0.185	0.018
ZA-3	7	-1.013	1.401	24.550	1.376	0.614	0.006	0.183	0.016

Table 3.3 Clumped and stable isotope data for all samples. All Δ_{47} data is presented in the I-CDES reference frame and the Δ_{48} data is presented in the CDES90 reference frame. Calulations to determine $\Delta\Delta_{47}$ and $\Delta\Delta_{48}$ values were performed using Equations 15 and 16 from Lucarelli *et al*. (2022). Calculations to determine $\Delta\delta^{18}O$ values were performed using the temperature dependent relationship determined by Kim and O'Neil (1997).

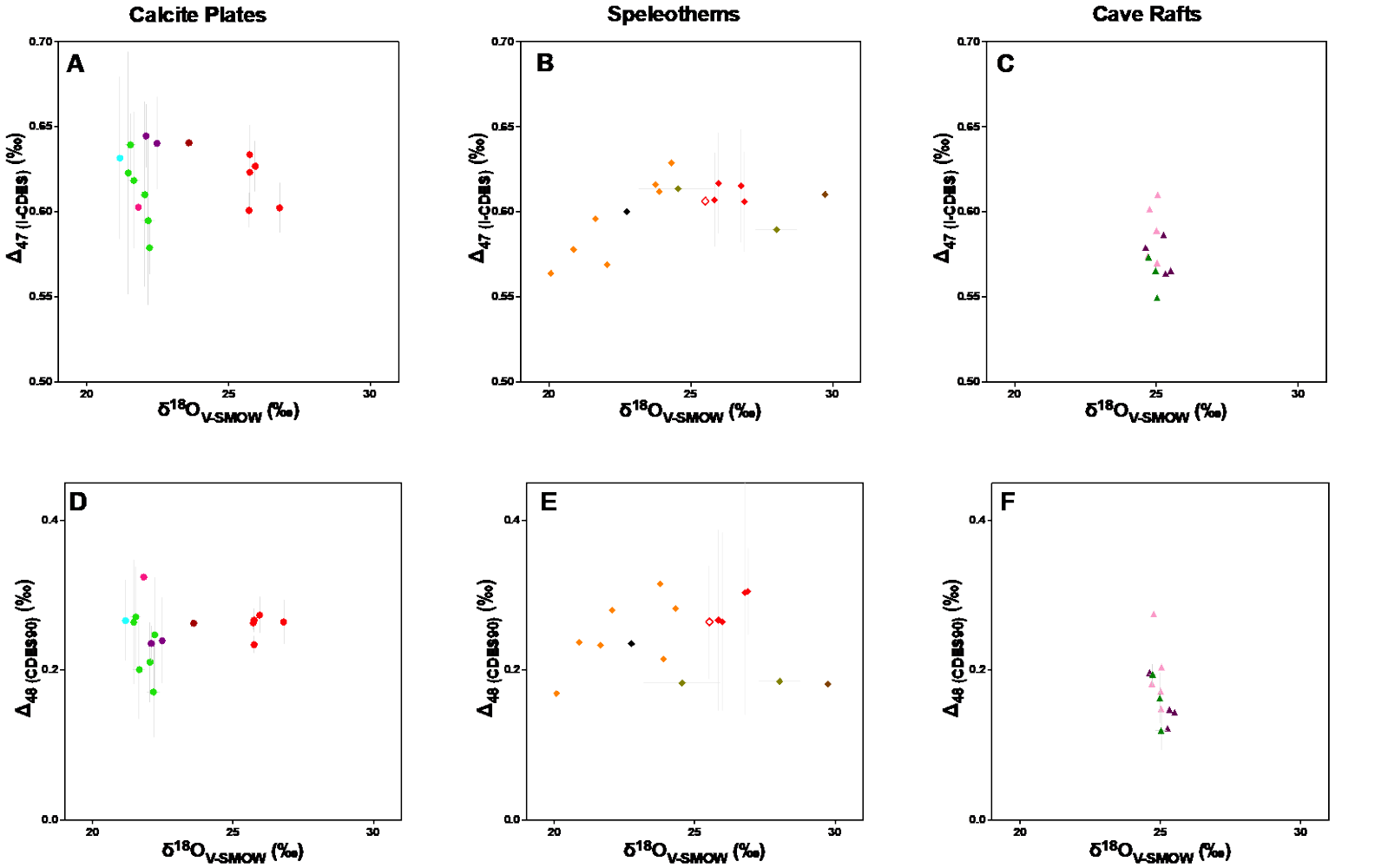

Calcite Plates

- Mexico, Cueva Bonita (Wright *et al.* 2021)
- Mexico, Cueva de la Puenta (Serrato, unpublished)
- USA, California (Wortham *et al.* 2021)
- Mexico, Grutas de Catedral (unpublished)
- Laos, Tham Doun Mai (Wang *et al.*, 2019)
- Laos, Tham Nguen Mai (unpublished)

Speleothems

- USA, California (Oster *et al.* 2009)
- Mexico, Cueva Bonita (Wright *et al.* 2021)
- Artificial Cave (EL-Shenawy *et al.* 2020)
- Ethiopia, Mechara Caves (Asrat *et al.*, 2008)
- Ethiopia, Tigray Caves (unpublished)

Cave Rafts

- Mexico, Cenote Feno (Kovacs *et al.* 2018)
- Mexico, Cenote Rainbow (Kovacs *et al.* 2018)
- Mexico, Cenote Monkey Dust (Kovacs *et al.* 2018)

Figure 3.3 Clumped (Δ_{47} and Δ_{48}) and $\delta^{18}O$ composition of calcite plates, speleothems (natural and synthetic), and cave rafts from various locations around the world. **A)** Δ_{47} and $\delta^{18}O$ of farmed calcite plates. **B)** Δ_{47} and $\delta^{18}O$ of speleothems. **C)** Δ_{47} and $\delta^{18}O$ of cave rafts **D)** Δ_{48} and $\delta^{18}O$ of farmed calcite plates **E)** Δ_{48} and $\delta^{18}O$ of speleothems **F)** Δ_{48} and $\delta^{18}O$ of cave rafts

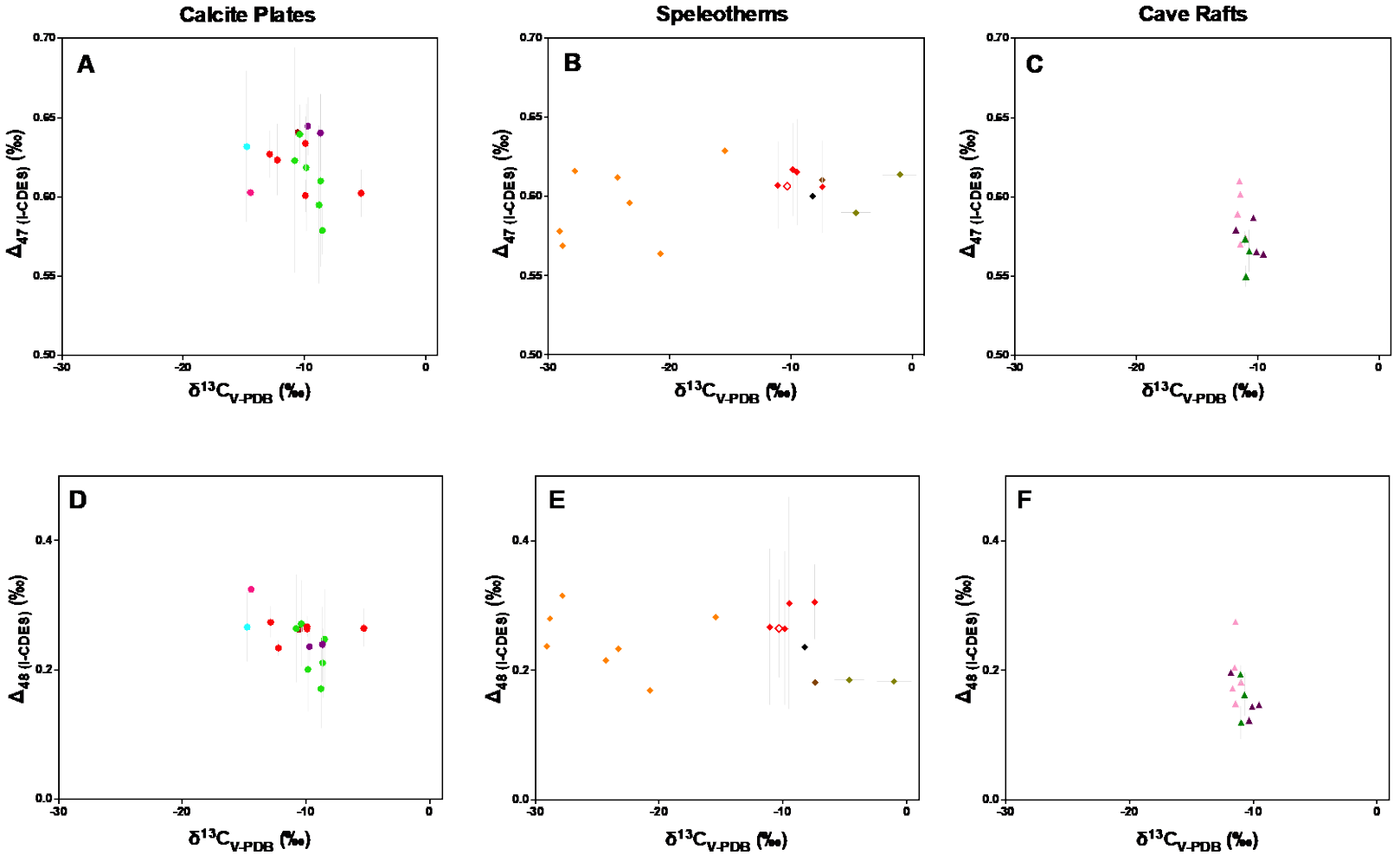

Calcite Plates

- Mexico, Cueva Bonita (Wright *et al.* 2021)
- Mexico, Cueva de la Puenta (Serrato, unpublished)
- USA, California (Wortham *et al.* 2021)
- Mexico, Grutas de Catedral (unpublished)
- Laos, Tham Doun Mai (Wang *et al.*, 2019)
- Laos, Tham Nguen Mai (unpublished)

Speleothems

- USA, California (Oster *et al.* 2009)
- Mexico, Cueva Bonita (Wright *et al.* 2021)
- Artificial Cave (EL-Shenawy *et al.* 2020)
- Ethiopia, Mechara Caves (Asrat *et al.*, 2008)
- Ethiopia, Tigray Caves (unpublished)

Cave Rafts

- Mexico, Cenote Feno (Kovacs *et al.* 2018)
- Mexico, Cenote Rainbow (Kovacs *et al.* 2018)
- Mexico, Cenote Monkey Dust (Kovacs *et al.* 2018)

Figure 3.4 Clumped (Δ_{47} and Δ_{48}) and $\delta^{18}O$ composition of calcite plates, speleothems (natural and synthetic), and cave rafts from various locations around the world. **A)** Δ_{47} and $\delta^{13}C$ of farmed calcite plates. **B)** Δ_{47} and $\delta^{13}C$ of speleothems. **C)** Δ_{47} and $\delta^{13}C$ of cave rafts **D)** Δ_{48} and $\delta^{13}C$ of farmed calcite plates **E)** Δ_{48} and $\delta^{13}C$ of speleothems **F)** Δ_{48} and $\delta^{13}C$ of cave rafts

3.3.2 Isotopic Disequilibrium Analysis ($\Delta\Delta_{47}$, $\Delta\Delta_{48}$, and $\Delta\delta^{18}O$)

Isotopic disequilibrium values were calculated using the mean sample values against oxygen isotope equilibrium (Kim and O'Neil, 1997) and clumped isotope (Δ_{47} and Δ_{48}) equilibrium equation values (Lucarelli *et al.*, 2022). These values are shown in Figure 3.7, 3.8, and 3.9; and Table 3.4. Samples were designated at equilibrium if the standard error of $\Delta\Delta_{47}$ and $\Delta\Delta_{48}$ fell within range of the origin of Figure 3.9.

3.3.2.1 Cave Rafts

The $\Delta\Delta_{47}$, $\Delta\Delta_{48}$, and $\Delta\delta^{18}O$ range of the cave rafts collected from Cenote Feno, Rainbow, and Monkey Dust, in Mexico (Kovacs *et al.*, 2018) are -0.046‰ to 0.013‰, -0.128‰ to 0.028‰, and -0.914‰ to 1.201‰ respectively.

3.3.2.2 Calcite Plates

The $\Delta\Delta_{47}$, $\Delta\Delta_{48}$, and $\Delta\delta^{18}O$ range of the calcite plates farmed by Wright *et al.* (2022) from Cueva Bonita, Mexico are -0.013‰ to 0.019‰, -0.021‰ to 0.019‰, and -0.127‰ to 1.247‰ respectively. The $\Delta\Delta_{47}$, $\Delta\Delta_{48}$, and $\Delta\delta^{18}O$ range of the calcite plates farmed by Serrato (2022) from Cueva de la Puente, Mexico are -0.033‰ to 0.032‰, -0.083‰ to 0.019‰, and -0.246‰ to 0.786‰ respectively. The $\Delta\Delta_{47}$, $\Delta\Delta_{48}$, and $\Delta\delta^{18}O$ range of the calcite plates farmed by Wortham *et al.* (2021) from Liburn Cave, California, USA are –0.008‰ to -0.003‰, -0.033‰ to -0.029‰, and 1.290‰ to 1.677‰ respectively. The $\Delta\Delta_{47}$, $\Delta\Delta_{48}$, and $\Delta\delta^{18}O$ for individual calcite plate samples collected from Grutas de Catedral (unpublished), Tham Doun Mai (Wang *et al.*, 2019; Griffiths *et al.*, 2020), and Tham Nguen Mai (unpublished) can be found in Table 3.4.

3.3.2.3 Speleothems

The $\Delta\Delta_{47}$, $\Delta\Delta_{48}$, and $\Delta\delta^{18}O$ range for the speleothem samples from Cueva Bonita, Mexico, collected by Wright *et al.* (2022) are -0.008‰ to 0.003‰, 0.010‰ to 0.051‰, and -0.042‰ to 1.340‰ respectively. The $\Delta\Delta_{47}$, $\Delta\Delta_{48}$, and $\Delta\delta^{18}O$ range for the artificial speleothem samples synthesized by EL-Shenawy *et al.* (2020) are -0.025‰ to 0.005‰, -0.070 ‰ to 0.057‰, and -0.061‰ to 1.773‰ respectively. Information on the individual cave sample collected from the Moaning Cave, USA (Wortham *et al.*, 2021); Mechara Caves, Ethiopia (Asrat *et al.*, 2008); and Tigray Caves, Ethiopia (unpublished) can be seen in Table 3.4.

Sample Name	$\Delta\delta^{18}O$ (‰)	$\Delta\delta^{18}O$ s.d.	$\Delta\Delta_{47}$ (‰)	$\Delta\Delta_{47}$ s.e.	$\Delta\Delta_{48}$ (‰)	$\Delta\Delta_{48}$ s.e.	Dual Clumped Isotope Equilibrium (Y/N)	Reported Temperature (°C)	Δ_{47}-T Predicted Temperature (°C)	s.e.	Agreement (Y/N)
F2	-0.914	0.150	0.013	0.038	-0.044	0.031	Y	24	20	6	Y
F5	0.040	0.170	0.005	0.038	0.028	0.081	Y	24	23	6	Y
CB-D6	0.127	0.092	0.019	0.038	0.012	0.164	Y	18	13	5	Y
CB-D62	0.145	0.035	-0.013	0.031	0.009	0.084	Y	18	23	3	Y
CB3	1.247	0.048	-0.011	0.036	0.010	0.095	Y	18	23	5	Y
CB4-48-Dry	1.221	0.090	0.002	0.030	0.049	0.180	Y	18	18	3	Y
CB4-82-Wet	0.429	0.127	0.003	0.034	0.010	0.124	Y	18	18	4	Y
CB4-99-Dry	1.340	0.150	-0.008	0.034	0.051	0.085	Y	18	21	4	Y
CB4-Scar	0.455	0.059	0.014	0.036	0.019	0.074	Y	19	15	4	Y
CB4-Scar2	0.192	0.108	0.010	0.043	-0.021	0.024	Y	18	17	7	Y
CB4-Top	0.291	0.152	-0.007	0.032	0.012	0.061	Y	18	21	4	Y
CP-D2	-0.246	0.109	0.007	0.050	0.009	0.150	Y	18	17	8	Y
CP-D3a2	0.775	0.152	0.001	0.045	-0.042	0.115	Y	20	21	9	Y
CP-D3b2	0.392	0.231	0.009	0.039	-0.052	0.229	Y	20	18	5	Y
GC	0.542	0.194	0.014	0.036	0.003	0.096	Y	14	11	4	Y
TM-D10	0.454	0.101	0.000	0.029	0.074	0.249	Y	22	22	3	Y
CPY	1.290	0.046	-0.003	0.030	-0.033	0.037	Y	7	9	2	Y
GLR	1.677	0.058	-0.008	0.034	-0.029	0.160	Y	7	11	4	Y
MIE-15-95-9-FL-Center	0.452	0.015	-0.011	0.026	-0.043	0.049	Y	15	19	1	Y
MIE-15-95-9-SL-Center	-0.061	0.026	0.005	0.026	0.024	0.036	Y	15	14	1	Y

MIE-25-95-8-FL-Center	0.436	0.023	0.002	0.026	-0.013	0.028	Y	25	24	2	Y
MIE-32-95-3-FL-Center	0.217	0.025	-0.011	0.032	-0.070	0.026	Y	32	36	5	Y
MIE-32-95-3-FU-Center	1.773	0.061	0.002	0.025	-0.002	0.032	Y	32	31	2	Y
CB4-12-Wet	-0.042	0.007	-0.007	0.022	0.010	0.022	Y	18	21	0	N
TNM	-0.069	0.126	0.031	0.042	0.017	0.042	Y	23	14	6	N
MC	-0.093	0.053	-0.016	0.026	-0.020	0.176	Y	18	23	2	N
MIE-25-95-8-FU-Edge	1.441	0.060	-0.025	0.031	0.034	0.038	Y	25	34	4	N
R1	1.201	0.090	-0.009	0.040	-0.125	0.028	N	25	28	7	Y
MIE-15-95-9-FU-Edge	1.063	0.051	-0.008	0.030	0.057	0.016	N	15	18	3	Y
ASFA	1.298	0.039	-0.004	0.029	-0.074	0.034	N	18	20	3	Y
B1	0.775	0.090	-0.046	0.027	-0.128	0.038	N	25	41	3	N
B3	0.591	0.150	-0.030	0.034	-0.085	0.045	N	25	36	5	N
B5	0.411	0.100	-0.022	0.025	-0.053	0.026	N	25	32	2	N
F1	0.961	0.070	-0.027	0.024	-0.099	0.033	N	24	33	1	N
F3	0.835	0.190	-0.008	0.028	-0.076	0.029	N	24	27	2	N
F4	-0.908	0.060	-0.023	0.030	-0.066	0.025	N	24	32	4	N
R2	0.499	0.220	-0.016	0.030	-0.051	0.028	N	25	30	4	N
R3	1.028	0.110	-0.031	0.032	-0.100	0.040	N	25	36	4	N
R5	N/A	N/A	-0.030	0.032	-0.104	0.030	N	25	36	4	N
CP-D3a	0.738	0.246	-0.017	0.043	-0.083	0.043	N	19	26	7	N
CP-D3a3	0.409	0.193	0.032	0.029	0.019	0.029	N	20	11	2	N

CP-D3b	0.786	0.084	-0.033	0.028	-0.006	0.028	N	19	30	3	N
MM1	N/A	N/A	-0.009	0.024	-0.06	0.02943132	N	24	26	1	N
ZA-3	N/A	N/A	0.015	0.026	-0.07	0.02782649	N	24	19	2	N

Table 3.4 Extent of disequilibria and comparison of reported and predicted temperatures using Anderson *et al.*, (2021) calibration curve. Agreement criteria is if extent of disequilibria is within 1 s.e. of origin and predicted temperature is within 1 s.e. of reported temperature.

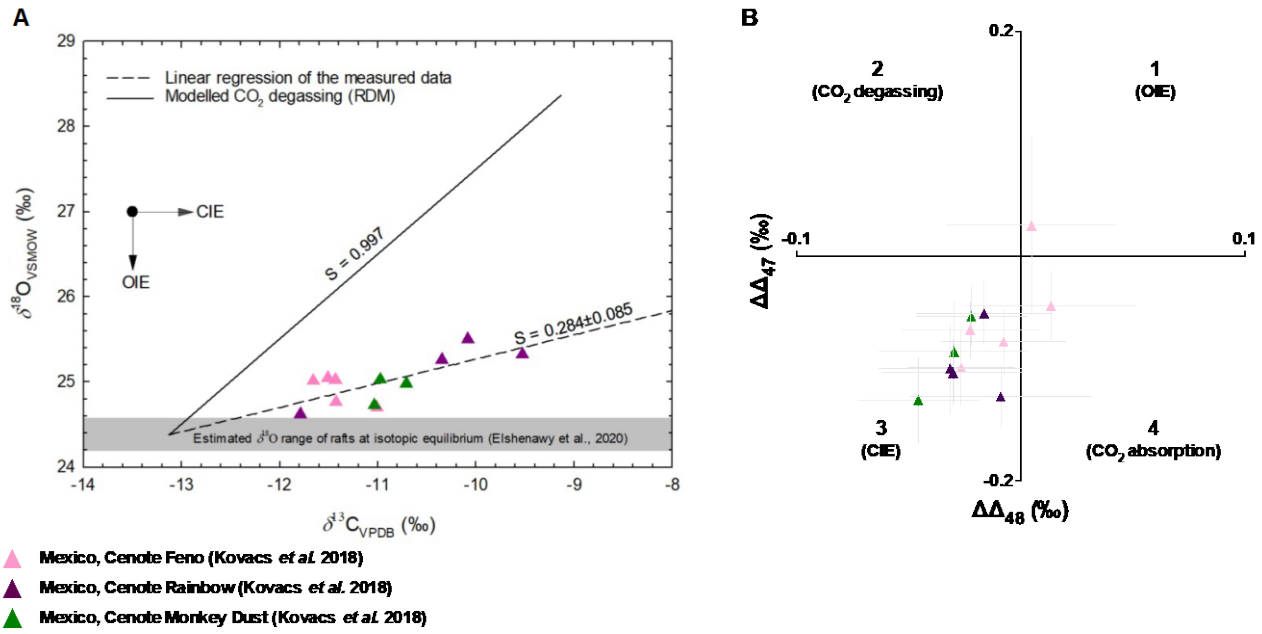

Figure 3.5 Disequilibria analysis of cave rafts from Mexico (Kovacs *et al.*, 2018). Panel A analyzes the variation of $\delta^{13}C$ and $\delta^{18}O$ using the Rayleigh distillation model (RDM) method. Panel B uses the extent of disequilibria ($\Delta\Delta_{47}$ and $\Delta\Delta_{48}$) in the dual clumped isotope space. In both plots cave raft samples were not separated during analysis as they would yield similar results. **A)** $\delta^{18}O$ and $\delta^{13}C$ covariation plot with linear regression analysis of cave rafts. Slope of aggregate cave raft samples is 0.284±0.085. **B)** $\Delta\Delta_{47}$ and $\Delta\Delta_{48}$ plot of all cave raft samples. Slope of all samples from the origin is -3.06±0.512.

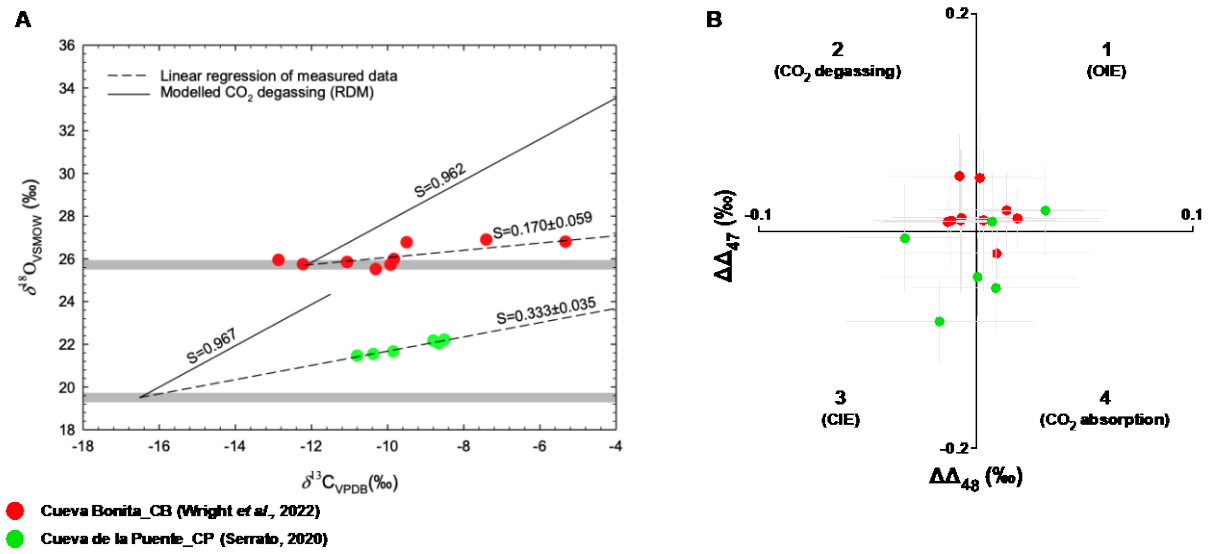

Figure 3.6 Disequilibria analysis of calcite plates and speleothems from Cueva Bonita, Mexico (Wright *et al.*, 2022) and calcite plates from Cueva de la Puente (Serrato, 2020). Panel A analyzes the variation of $\delta^{13}C$ and $\delta^{18}O$ using the Rayleigh distillation model (RDM) method. Panel B uses the extent of disequilibria ($\Delta\Delta_{47}$ and $\Delta\Delta_{48}$) in the dual clumped isotope space. In the case of samples from Cueva Bonita, samples were not separated based on sample type in this analysis for accurate comparison of RDM and $\Delta\Delta_{47}$-$\Delta\Delta_{48}$ method **A)** $\delta^{18}O$ and $\delta^{13}C$ covariation plot with linear regression analysis. Slopes of sample set from Cueva Bonita and Cueva de la Puente are 0.170±0.058 and 0.333±0.035 respectively. **B)** $\Delta\Delta_{47}$ and $\Delta\Delta_{48}$ analysis.

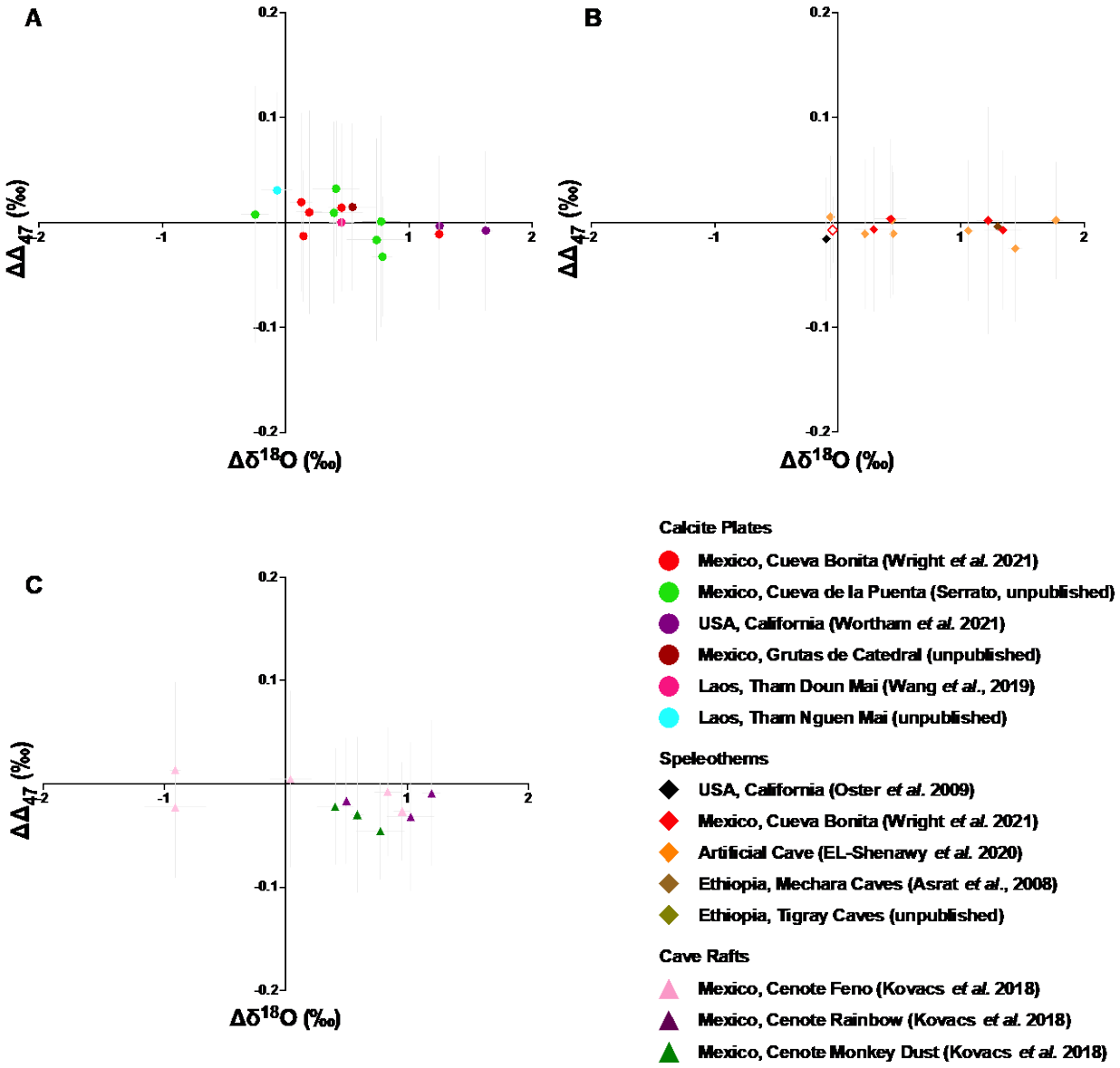

Figure 3.7 Extent of disequilibria associated with clumped (Δ_{47}) and stable oxygen isotope ($\delta^{18}O$). $\Delta\Delta_{47}$ was calculated by measuring the difference between the measured clumped isotope signal versus the equilibrium clumped isotope signature, using the temperature-dependent relationship developed by Lucarelli (2022) $\Delta\delta^{18}O$ was determined using the temperature-dependent relationship established by Kim and O'Neil *et al.* (1997). Temperatures varied by the location of recovery and were explicitly measured by collaborators. **A)** $\Delta\Delta_{47}$ and $\Delta\delta^{18}O$ of farmed calcite plates. **B)** $\Delta\Delta_{47}$ and $\Delta\delta^{18}O$ of speleothems. **C)** $\Delta\Delta_{47}$ and $\Delta\delta^{18}O$ of cave rafts.

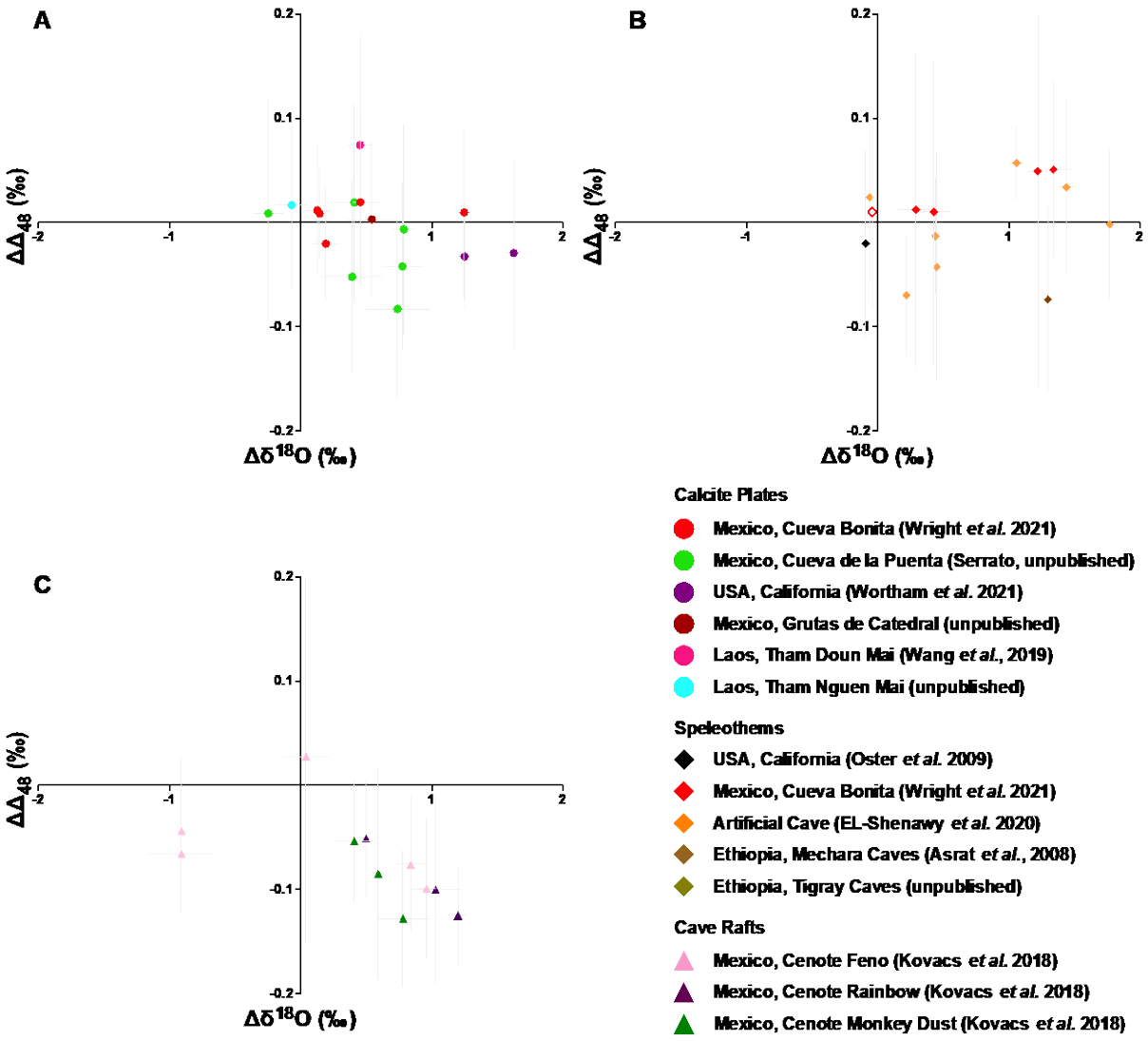

Figure 3.8 Extent of disequilibria associated with clumped (Δ_{47}) and stable oxygen isotope ($\delta^{18}O$). $\Delta\Delta_{47}$ was calculated by measuring the difference between the measured clumped isotope signal versus the equilibrium clumped isotope signature, using the temperature-dependent relationship developed by Lucarelli (2022) $\Delta\delta^{18}O$ was determined using the temperature-dependent relationship established by Kim and O'Neil *et al.* (1997). Temperatures varied by the location of recovery and were explicitly measured by collaborators. **A)** $\Delta\Delta_{48}$ and $\Delta\delta^{18}O$ of farmed calcite plates. **B)** $\Delta\Delta_{48}$ and $\Delta\delta^{18}O$ of speleothems. **C)** $\Delta\Delta_{48}$ and $\Delta\delta^{18}O$ of cave rafts.

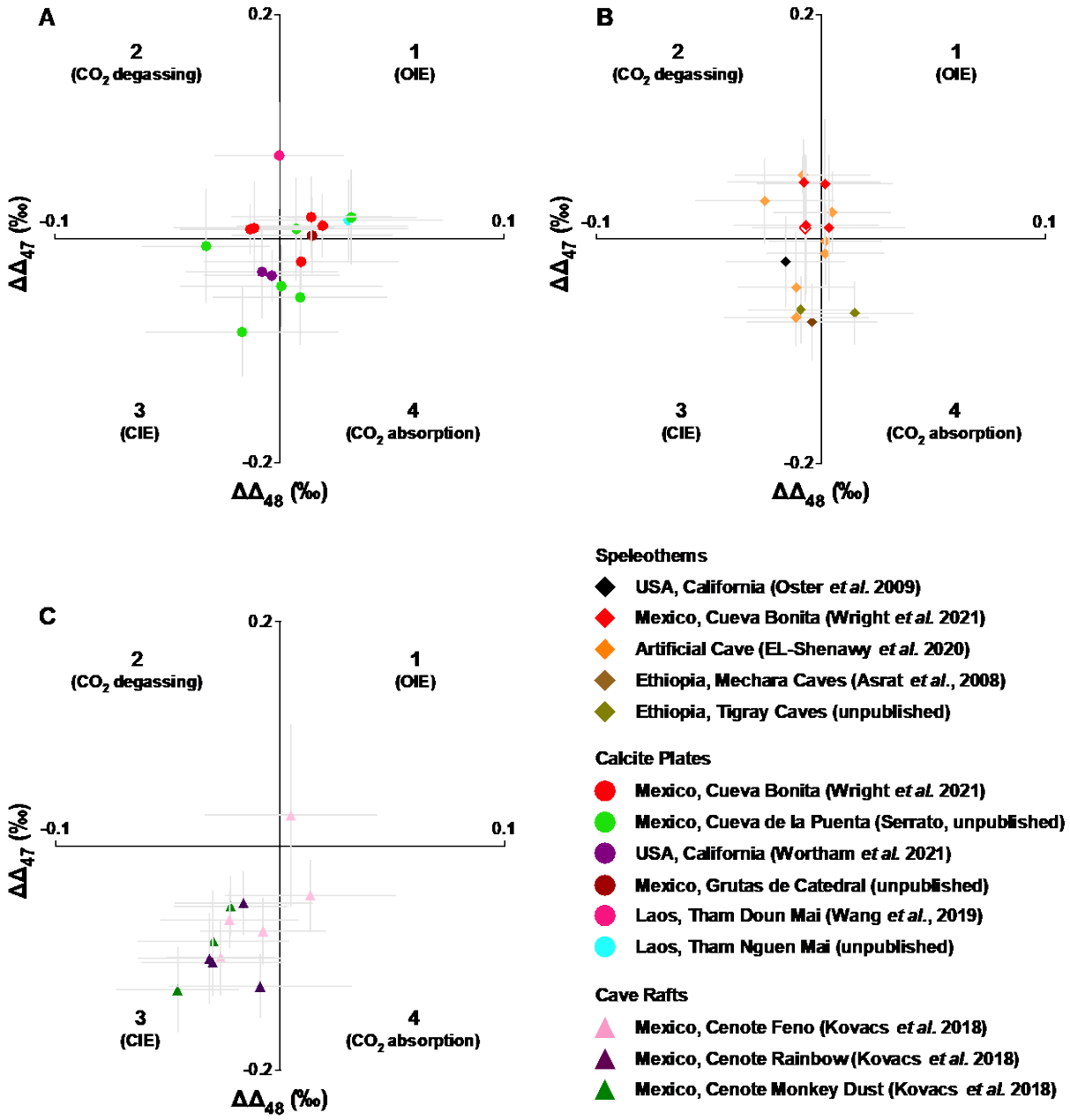

Figure 3.9 Extent of disequilibria ($\Delta\Delta_{47}$ and $\Delta\Delta_{48}$) plots for calcite plates (panel A), speleothems (panel B), and cave carbonates (panel C). $\Delta\Delta_{47}$ and $\Delta\Delta_{48}$ were calculated by measuring the difference between the measured clumped isotope signal versus the equilibrium clumped isotope signature, using the temperature-dependent relationship developed by Lucarelli *et al.* (2022). The temperatures varied by the location of recovery and were explicitly measured by collaborators. **A)** $\Delta\Delta_{47}$ and $\Delta\Delta_{48}$ extent of disequilibria plot of farmed calcite plates. **B)** $\Delta\Delta_{47}$ and $\Delta\Delta_{48}$ extent of disequilibria plot of farmed speleothems. **C)** $\Delta\Delta_{47}$ and $\Delta\Delta_{48}$ extent of disequilibria plot of cave rafts.

3.4 Discussion

Analysis was performed using two separate approaches; one that focused on the traditional stable isotope ($\delta^{13}C$ and $\delta^{18}O$) approach, and the second focusing on a clumped isotope (Δ_{47} and Δ_{48}) approach.

3.4.1 Assessing Disequilibria of Cave Carbonates using Traditional Stable Isotopes ($\delta^{13}C$ and $\delta^{18}O$)

Carbonates in cave environments are mainly formed via CO_2 degassing out of calcite ($CaCO_3$) saturated water that is triggered by the pCO_2 gradient between this calcite saturated water and cave atmosphere (Dreybrodt, 1988; Hansen *et al*., 2013). Fast CO_2 degassing tends to result in a coherent increase (i.e., covariation) in $\delta^{18}O$ and $\delta^{13}C$ values of the dissolved bicarbonates and consequently in those of the precipitating carbonates due to the preferential loss of ^{12}C and ^{16}O (Mickler *et al*., 2004; Scholz *et al*., 2009; Day and Henderson, 2011; El-Shenawy *et al*., 2020). At the onset of CO_2 degassing, precipitating carbonates would be close to carbon and oxygen isotopic equilibrium with parent water. However, progressive CO_2 degassing leads to a positive deviation of the precipitating carbonates from the initial carbon and oxygen isotopic equilibria (Dreybrodt and Scholz, 2011). Therefore, a positive correlation between $\delta^{18}O$ and $\delta^{13}C$ values of cave carbonates is a robust indicator of isotopic disequilibria (Hendy, 1971; Mickler *et al*., 2006). The carbonate samples, collected from natural caves in this study, show a significant positive correlation (p-value of ≤ 0.02) between $\delta^{18}O$ and $\delta^{13}C$ values, suggesting that these carbonates formed at isotopic disequilibria with cave water (see their Fig. 1). The calcite rafts from Mexico exhibit a $\delta^{18}O$ - $\delta^{13}C$ covariation with a slope of 0.284 (p-value = 0.008; Figure 3.5). While the farmed calcite plates and the natural speleothem samples from Cueva Bonita (CB) and Cueva de la Puenta (CP) caves in Mexico have slopes of 0.170 (p-value = 0.020) and 0.333 (p-value =

0.0007), respectively (Figure 3.6). This difference in the slopes of the $\delta^{18}O$ - $\delta^{13}C$ covariation indicates a different degree of isotopic equilibria. Note that our regression analyses are undertaken only for the data sets of three or more samples from the same cave system tested in this study.

The slope of $\delta^{18}O$ - $\delta^{13}C$ covariation in carbonates due to CO_2 degassing can be estimated using a Rayleigh Distillation Model (RDM) (Mickler *et al*., 2004; Mickler *et al*., 2009; Scholz *et al*., 2009; El-Shenawy *et al*., 2020). The estimated slopes for calcite which is formed under progressive CO_2 degassing in caves at 0 - 30 ºC range between 0.919 and 1.040, respectively (i.e., Slope≈1). The observed slopes in rafts, natural speleothems, and farmed calcite plates (i.e., 0.284, 0.170 and 0.333) are significantly shallower than their estimated slopes based on RDM (i.e., 0.997, 0.962 and 0.967; Figures 3.5 and 3.6). These shallower slopes can be explained by two potential mechanisms: (A) **OIE**: Oxygen Isotope Exchange between DIC species and water (Beck *et al*., 2005; Dreybrodt and Scholz, 2011; El-Shenawy *et al*., 2020) and (B) **CIE**: Carbon Isotope Exchange between DIC species in water and CO_2 in cave atmosphere (Dreybrodt *et al*., 2016; Hansen *et al*., 2017; El-Shenawy *et al*., 2020). Under complete or partial OIE, ^{16}O depletion (or ^{18}O enrichment) of the DIC species due to CO_2 degassing is typically buffered or minimized by the isotopic exchange with the large oxygen reservoir of cave water, decreasing the slope of the $\delta^{18}O$ - $\delta^{13}C$ covariation in precipitating carbonates (Figure 3.2A). For example, a OIE mechanism would decrease the slope of cave carbonates that grow at a slow rate (e.g., cave carbonates formed in pools under a thick water layer). A relatively slow growth rate of carbonate could thus allow a higher degree of the OIE, which is completed within 24 hours and 9 hours at 15 and 25 ºC, respectively, and also contribute to the lowering of the slope of $\delta^{18}O$ - $\delta^{13}C$ covariation in carbonates (El-Shenawy *et al*., 2020). In contrast, OIE is not expected to significantly contribute to the slope of fast-growing speleothems from a thin water film (Dreybrodt and Romanov, 2016).

On the other hand, a CIE mechanism is active in a ventilated cave where cave air CO_2 is continuously replaced by atmospheric CO_2. The average $\delta^{13}C$ value of cave air CO_2 ranges from -16 ‰ to -22 ‰ that is in carbon isotope equilibrium with DIC species in cave water whereas atmospheric CO_2 has a higher $\delta^{13}C$ value of about -8 ‰. As a result, when the cave air CO_2 is partially or completely replaced by atmospheric CO_2, CIE increases the $\delta^{13}C$ value of the DIC species in cave water and the precipitating carbonates would decrease the slope of $\delta^{18}O$ - $\delta^{13}C$ covariation in carbonates induced by CO_2 degassing. CIE proceeds faster than the OIE (Beck *et al*., 2005; Dreybrodt *et al*., 2016; Hansen *et al*., 2017). El-Shenawy *et al*. (2020) demonstrated that a significant increase in the $\delta^{13}C$ value of stalagmite-like carbonates due to CIE occurred in few hundred seconds (see their Fig. 6a). Therefore, CIE is expected to impact the CO_2 degassing slope in both fast- and slow-growing speleothems in ventilated caves.

The cave rafts from Mexico are rapidly formed at the air-water interface in three proximate caves, which are completely or partially open to the atmosphere, allowing the ventilation of cave air (Kovacs *et al*., 2018). The formation of rafts under these conditions suggests that the CIE mechanism is the most likely cause of their shallower slope of the $\delta^{18}O$ - $\delta^{13}C$ covariation. Likewise, speleothems and farmed calcite from Cueva Bonita cave grew under a seasonal ventilation mode (i.e., low pCO_2 in winter and high pCO_2 in summer; See Fig. S3a in Wright *et al*., 2021), allowing CIE to imprint the carbon isotope composition of these carbonates. However, some of these carbonates exhibit a large spread in their $\delta^{13}C$ values with a more or less constant $\delta^{18}O$ value, suggesting an additional effect of the OIE during carbonate precipitation. The effect of OIE could be due to a relatively thicker water layer on the apex of speleothems and on the glass plate. Cueva de la Puente cave was described as well ventilated and the shallower slope of $\delta^{18}O$-

$\delta^{13}C$ covariation in its farmed calcite samples corroborates this due to the significant impact of CIE with limited/no effect of OIE.

In this study, the regression analysis of the synthetic speleothem samples from the McMaster artificial cave is not possible due to the limited number of samples from each experimental condition (one or two samples). However, the samples from the upper watch glasses (FU samples) were shown to be affected by the CIE whereas the lower watch glass samples were controlled by both the CIE and the OIE (See Fig. 6a, 7 and 8 in El-Shenawy *et al*., 2020). In summary, carbon and oxygen isotope exchange are key mechanisms along with CO_2 degassing in the process of carbonate precipitation in cave environments. However, it is difficult to resolve these effects using bulk stable isotopes alone, thus we look at paired clumped isotope (Δ_{47} and Δ_{48}) analysis to resolve.

3.4.2 Framework for Assessing Cave Carbonate Disequilibria with Dual Clumped Isotopes (Δ_{47} and Δ_{48})

By pairing Δ_{48} and Δ_{47} signatures, we can predict, and model different disequilibria processes. This in turn can augment traditional degassing disequilibria probing techniques, such as linear regression using RDM (Mickler *et al*., 2004, 2006; Mühlinghaus *et al*., 2009) seen in Figure 3.1A. Dual clumped isotopes have been used to correct disequilibria-induced temperature biases through trajectory predictions using the IsoDIC modeling (Fiebig *et al*., 2019; Guo, 2019, 2020; Bajnai *et al*., 2020). However universal application of this approach is somewhat limited due to the complex nature of cave carbonate formation which the IsoDIC model does not fully encompass (Guo *et al.*, 2020). The IsoDIC model represents a major advancement in our understanding of dual clumped isotope disequilibria. In the CO_2 degassing and CO_2 absorption

regime, IsoDIC focuses on speleothem, biogenic carbonates (i.e. corals), and high-pH travertines. However, it is acknowledged to oversimplify speleothem formation and coral calcification processes (Guo *et al.*, 2020), which can affect its universal use in quantitative applications, such as temperature corrections.

Figure 3.1B, is a generic representation of the absorption and degassing process in the $\Delta\Delta_{47}$-$\Delta\Delta_{48}$ space. CO_2 degassing is predicted to originate and propagate in quadrant 2 and 1; and absorption in quadrants 4 and 3. In the case of degassing, quadrant 2, a departure away from equilibria is observed with a rebound moving into quadrant 1. As oxygen isotopes equilibrate, it returns to equilibrium through quadrant 1. A similar cycle occurs with respect to CO_2 absorption disequilibria where an initial migration from the origin propagates into quadrant 4 and return back to equilibrium through quadrant 3. The initial trajectory slopes of departure from the origin in both absorption and degassing disequilibria is what Bajnai *et al.*, (2020) used to successfully correct clumped isotope paleothermometer temperature predictions of warm and cold-water coral (absorption) along with natural and synthetic speleothems (degassing). However, this very simplified correction becomes far more difficult to make when cave carbonates have additional isotopic buffering effects that can remove them from the initial linear regression.

Carbon and oxygen isotope exchange in a homogenous and heterogeneous manner can result in alterations to the isotopic composition of the DIC pool which can affect both Δ_{47} and Δ_{48} signatures. OIE is a homogenous process and based primarily on (de)hydration and (de)hydroxylation reactions 1-2. Homogenous OIE between DIC and H_2O reservoirs within cave water (same phase) can result in isotopic buffering of the ^{18}O enrichment in the DIC pool induced by CO_2 degassing (Beck *et al*., 2005; Mickler *et al*., 2006; Dreybrodt and Scholz, 2011) resulting in migrations from the traditional degassing pathway. CIE is a heterogenous exchange, where

carbon exchange occurs from the DIC and atmospheric CO_2 reservoirs. Heterogeneous CIE between the DIC in cave water and the CO_2 of cave atmosphere (two phases) has been far less studied than OIE, and can result in disequilibrium effects that are inconsistent with degassing (Tremaine *et al*., 2011; Dreybrodt *et al*., 2016; Hansen *et al*., 2017; EL-Shenawy *et al*., 2020). In Figure 3.1A, pure degassing disequilibria is described by the RDM as a 1:1 covariation, or S~1, in the $\delta^{18}O$ and $\delta^{13}C$ space (Mickler *et al*., 2006). This slope is reduced with increasing contributions of OIE and CIE. When S~0, the $\delta^{18}O$ values are at equilibrium. Previous research suggests that well ventilated caves will exhibit greater amounts of CIE (Dreybrodt and Scholz, 2011; Dreybrodt *et al*., 2016; Hansen *et al*., 2017; EL-Shenawy *et al*., 2020).

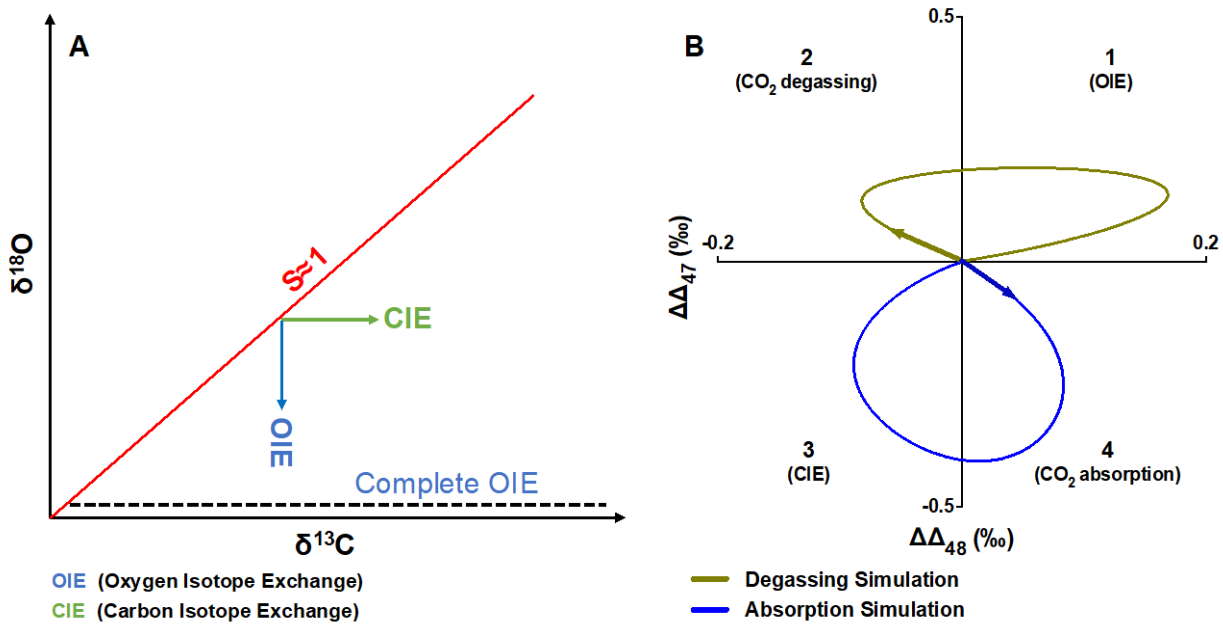

Figure 3.1 Stable isotope ($\delta^{13}C$ and $\delta^{18}O$) and clumped isotope (Δ_{47} and Δ_{48}) model simulations of disequilibria. Panel A simulates degassing disequilibria using the Rayleigh distillation model (RDM). Panel B simulates disequilibria in the degassing (dark yellow) and absorption (blue line) directions using IsoDIC (Guo *et al.*, 2019, 2020) modeling. **A)** $\delta^{13}C$ and $\delta^{18}O$ simulation. A slope value, S, at approximately 1 simulates pure degassing disequilibria. Oxygen Isotope Exchange (OIE) and Carbon Isotope Exchange (CIE) shift the slope to lower values where S<1. Complete OIE results in S≅0 where the $\delta^{18}O$ values are at isotopic equilibrium. **B)** $\Delta\Delta_{47}$ and $\Delta\Delta_{48}$ simulation of disequilibria. Default parameters from Guo *et al.*, (2020) were used for both simulations. Quadrants 1 to 4 are listed and indicate the type of disequilibria we expect to see in each respective quadrant.

3.4.3 Application of Framework for Assessing Cave Carbonate Disequilibria w/ Clumped Isotope (Δ_{47} and Δ_{48})

The dual clumped isotope (Δ_{47} and Δ_{48}) approach allows us to analyze the extent of disequilibria ($\Delta\Delta_{47}$-$\Delta\Delta_{48}$) in each sample, with information provided by both the direction and magnitude of disequilibria. Figures 3.8 and 3.9 show the extent and type of disequilibria associated with each cave carbonate sample. Expanding OIE and CIE into the $\Delta\Delta_{47}$-$\Delta\Delta_{48}$ space, we hypothesize that OIE drives the migration of samples to quadrant 1 and CIE to quadrant 3. In the case of traditional degassing, disequilibria propagate in quadrant 2 with a depletion in Δ_{47} and enrichments in $\delta^{18}O$ (Daëron *et al*., 2011; Kluge and Affek, 2012; Affek and Zaarur, 2014) (Figure 3.2B). This also correlates to an enrichment in Δ_{48} (Fiebig *et al*., 2019; Guo, 2020; Bajnai *et al*., 2020). Increased isotopic equilibration pushes the disequilibria into quadrant 1 through an OIE pathway. In the case of CIE, we hypothesize that this resides in quadrant 3. However, we do not believe samples that fell in quadrant 3 followed an absorption pathway, rather a diffusion pathway. Previously discussed modifications due to CIE could result in a depletion of both Δ_{47} and Δ_{48} values, propagating the disequilibria into quadrant 3. However, thorough confirmation of this phenomenon is still required and could be accomplished through calcium isotopes.

Disequilibria associated with cave rafts recovered by Kovacs *et al.* (2018) appear to migrate away from clumped isotope equilibria in quadrant 3 as indicated by depletions in both $\Delta\Delta_{47}$ and $\Delta\Delta_{48}$ (Figures 3.7 and 3.8). Traditional speleothem and cave samples exhibit a CO_2 degassing disequilibria phenomenon, driven by thin film dynamics and a large pCO_2 gradient between the cave atmosphere and drip water. All cave rafts samples recovered are within or have 1 s.e. within quadrant 3 of Figure 3.9. The thickness of these pools would easily promote greater residence times of DIC in the system allowing for OIE and CIE, corroborating what we see in the

stable isotope analysis. However, within the clumped isotope space we can explicitly resolve the extent of CIE on the cave raft as a function of ventilation. Cenote Feno is considered to have the least ventilation of the three Cenotes, with a small opening to atmosphere. Cenotes Rainbow and Monkey Dust were considered well ventilated with large openings to the atmosphere (Kovacs *et al.*, 2018). Previous research into the CIE affects and their relationship to cave ventilation indicates that this effect is enhanced in well ventilated caves (Dreybrodt *et al*., 2016; Hansen *et al*., 2017; EL-Shenawy *et al*., 2020). We can corroborate this with our three samples in the greatest magnitude of migration from origin to quadrant 3 correlating to greater cave ventilation. Samples (B1, B3, B5) collected from Monkey Dust and Rainbow had large and comparable magnitudes ($\vec{M}$) of departure from origin into quadrant 3 (Monkey Dust = $\overline{\Delta\Delta_{47}}$: -0.032±0.029, $\overline{\Delta\Delta_{48}}$: -0.089±0.036, $\vec{M}$: 0.094; Rainbow = $\overline{\Delta\Delta_{47}}$: -0.022±0.034, $\overline{\Delta\Delta_{48}}$: -0.095±0.032, $\vec{M}$: 0.097), corroborating a well ventilated cave. Samples (F1, F2, F3, F4, F5) from Feno had the smallest magnitude of departure into quadrant 3 ($\overline{\Delta\Delta_{47}}$: -0.007‰±0.032, $\overline{\Delta\Delta_{48}}$: -0.051±0.039, $\vec{M}$: 0.052), corroborating a poorly ventilated cave system relative to the other Cenotes.

Farmed calcite plates and speleothems recovered from Cueva Bonita (Wright *et al.*, 2022) were mostly indistinguishable from equilibrium values (i.e., within 1 s.e. of equilibrium). Temperature predictions from Δ_{47} agree with temperature observations. Stable isotope analysis of the population from this indicates some CIE and/or OIE contributions based on the $\delta^{18}O$-$\delta^{13}C$ covariation slope of 0.170. However, we cannot resolve if CIE or OIE are explicitly causing this through this approach only. Using Figure 3.9, we can see there is a bias towards quadrants 1 and 2 which indicate that there is a preference for degassing and OIE which is present in both speleothem and farmed calcite plate samples. As discussed previously we attribute OIE to thick water layers on farmed calcite plates and potential pooling of water on the tops of the speleothems.

Farmed calcite plates recovered from Cueva de la Puente (Serrato, 2020) have most samples yielding a bias towards quadrants 3 which confirms CIE being the predominant effect with OIE exhibited by sample CP-D3a3 and CP-D2. This corroborates what we see in Figure 3.6 with a slope of 0.333 and $\delta^{13}C$ values shifted to isotopically enriched values.

While the traditional regression analysis approach could not be used to indicate carbon or oxygen isotope exchange in the synthetic speleothems (EL-Shenawy *et al.*, 2020) due to limited population size, we can attempt to resolve this in $\Delta\Delta_{47}$-$\Delta\Delta_{48}$ (Figure 3.9). The sample set from has relatively even distribution with biases in quadrant 2 (degassing) and quadrant 3 (CIE). Samples MIE-25-95-8-FU-Edge and MIE -15-95-9-FU-Edge had the greatest degassing effects and were collected from the upper glasses where the convex nature of the glass plate prevented pooling of the drip water. This is consistent with what we would expect to see with traditional speleothems and associated degassing phenomenon (Fiebig *et al*., 2019; Guo and Zhou, 2019; Guo, 2020; Bajnai *et al*., 2020). However, samples MIE-15-95-9-FL-Center and MIE-32-95-3-FL-Center fall within quadrant 3 which indicates KIE associated with CIE are present. This confirms what EL-Shenawy *et al.*, (2020), reported for their samples collected from the lower watch glass indicating CIE and OIE. However, we only see CIE indicated by our dataset because we analyzed a limited sample set from their study.

While stable isotope regression analysis can only evaluate sample populations of three or more, we can use dual clumped isotopes to examine individual samples collected from each cave locality. Samples GLA and CPY collected from Lilburn Cave (Wortham *et al.*, 2020) exhibited CIE, residing in quadrant 3 of Figure 3.9. Both of these farmed calcite plates were collected from drip sites that were located near the cave entrances with seasonal ventilation variations. Sample TM-D10 collected from Tham Doun Mai (Wang *et al.*, 2019) resides directly in between quadrant

1 and 2, indicating OIE effects or a closed cave. This can be due to increased thickness of water film and pooling of water due to significant rainfall (1200mm) localized during the summer (June-September) monsoon season (Wang *et al.*, 2019). This can also account for what we see with sample TNM collected from Tham Nguen Mai (unpublished), a proximate location to Tham Doun Mai. This sample is a part of unpublished work, so site information is limited, however we can see in Figure 3.9 that it resides in quadrant 1, similar to sample TM-D10, indicating OIE effects driving it back to equilibrium. Speleothem sample MC, collected from the Moaning Cave (Oster *et al.*, 2009) falls within quadrant 3 with a similar magnitude as samples CPY and GLA from Lilburn cave, which are in the same region. Although cave ventilation was not discussed in detail, we can infer that there is ventilation which is driving this sample into quadrant 3. The last batch of speleothem samples were collected from Mechara (Asrat *et al.*, 2008) and Tigray (unpublished) caves on the Ethiopian highlands. All these samples have similar biases towards quadrant 3, within 1 s.e. Samples MM1 and ZA-3 recovered from Tigray cave were collected from areas proximate to the cave entrance which provided good exposure to outside atmospheric CO_2. Sample ASFA collected from Mechara cave is located within 25m of the cave entrance in a vertical orientation. No mention was made on how ventilated the cave was, however, based on the data presented in Figure 3.9B, we infer that it is enough to promote CIE.

3.4.4 Paired clumped isotope analysis as a robust test of isotopic (dis)equilibrium in cave carbonates

One of the most promising applications of the paired-dual clumped isotope space is its ability to test dis/equilibrium isotope conditions in fossil speleothems and therefore its potentiality as a terrestrial paleoclimate archive. Because the paired analysis only relies on the preferential aggregation of heavy isotopes, and does not require information on the drip water isotopic

composition to establish a relationship, we can use this tool to identify samples at equilibrium and use a Δ_{47}-T calibration, or other methods for paleothermometry based on oxygen isotopes (such as fluid inclusion-carbonate mineral thermometry), to determine paleotemperatures.

Most samples (n = 27 out of 44) were at, or within 1 s.e. of both $\Delta\Delta_{47}$ and $\Delta\Delta_{48}$ from the origin (Figure 3.9), consistent with precipitation under equilibrium conditions. The majority of samples that fell in this category had good agreement between predicted Δ_{47} and reported temperature values, seen in Table 3.4. Samples that were outside of 1 s.e. in both $\Delta\Delta_{47}$ and $\Delta\Delta_{48}$ had predicted and temperature profiles that did not match. This indicates that if samples have dual clumped isotope values that exhibit (dis)equilibrium, they can be reliably used to determine if samples can be used for paleothermometer applications.

There were some samples exhibiting disequilibrium in only one of the clumped isotope signatures, Δ_{47} or Δ_{48}, and some of these yielded discrepancies between Δ_{47} predicted and reported temperature values. Samples CB4-12-Wet had only 2 replicates used for analysis due to the limited amount of sample provided resulting in unreliable data. We suggest that samples that exhibit disequilibria in either clumped isotope parameter (Δ_{47} or Δ_{48}) cannot be used confidently for paleothermometry without first exploring the potential origin and nature of kinetic biases by evaluating the potential type(s) and extent of disequilibria.

3.5 Conclusions

We have conducted bulk stable and dual clumped isotope analysis of 44 farmed calcite plates, natural stalagmites, synthetic speleothems and cave rafts from 13 localities, expanding on prior work by other groups. We conducted stable isotope linear regression through RDM and

expanded observations to paired dual clumped (Δ_{47} and Δ_{48}) isotope analysis. And finally, we conducted a thorough evaluation of the paired dual clumped isotope space in its efficacy in identifying (dis)equilibrium and ability to make accurate predictions. More than half the samples examined formed in equilibrium based on paired dual clumped (Δ_{47} and Δ_{48}) measurements and can be used to accurately constrain temperature, suggesting cave carbonates may represent a potentially underutilized archive for Δ_{47}-based temperature reconstructions, and that dual clumped isotopes can be used as a tool for assessing isotopic equilibrium to complement the Hendy test, for samples that are targets for oxygen isotope-based reconstructions.

However, almost half of the samples studied here exhibit kinetic effects in Δ_{47} and/or Δ_{48} can arise in clumped isotopes from carbon and oxygen isotope exchange. Cave carbonate samples that exhibit enrichment in both Δ_{47} and Δ_{48} relative to equilibrium (i.e., fall within quadrant 1 of our schematic of $\Delta\Delta_{47}$-$\Delta\Delta_{48}$) undergo exhibit homogenous oxygen isotope exchange that can occur with longer residence time of DIC in solution due to various conditions such as water layer thickness. We hypothesize cave carbonate samples may exhibit depletion in both Δ_{47} and Δ_{48} relative to equilibrium (i.e., fall within quadrant 3 of the $\Delta\Delta_{47}$-$\Delta\Delta_{48}$ space of our schematic) because of heterogeneous carbon isotope exchange between DIC in cave water and CO_2 in cave atmosphere. This hypothesis is supported by Rayleigh distillation modelling of bulk stable isotopes, and knowledge of cave conditions (i.e. increased ventilation) that indicate conditions conducive to isotope disequilibria. ^{44}Ca isotope measurements could be conducted on samples that fall in quadrant 3 to quantitatively test this hypothesis. Cave rafts examined in this study exhibit evidence for strong CIE as indicated by a flattened slope (0.284) in the RDM linear regression analysis (Figure 3.5) and the strong protrusion of data set into quadrant 3 in the $\Delta\Delta_{47}$-$\Delta\Delta_{48}$ analysis (Figure 3.9). The magnitude of protrusion into quadrant 3 has a correlation to relative cave

ventilation. Most farmed calcite plates and stalagmites examined in this study exhibit some degree of kinetic isotope effects associated with OIE or CIE, with a very limited number exhibiting pure degassing effects as indicated by RDM linear regression analysis (Figures 3.5 and 3.6) and $\Delta\Delta_{47}$-$\Delta\Delta_{48}$ analysis (Figure 3.9). Many of the cave carbonates analyzed in this study that exhibit some degree of kinetic fractionation in Δ_{47} and Δ_{48} due to carbon or oxygen isotope exchange, cannot currently be resolved through existing degassing models used for cave carbonates, but this could be a useful target for future work.

Summary and Future Direction of Research

Research conducted in this dissertation focuses on green chemistry with the goal of addressing topics related to climate change. The first research project focused on creating a next generation of lithium-ion batteries using the redox-active boron cluster scaffold. The second focused on applying a framework for studying dissolved inorganic carbon transformation using dual clumped isotopes at peridotite-associated springs, which represent potential geological sequestration sites. The last project aimed to develop the understanding of terrestrial cave carbonates from a diverse array of sites using dual clumped isotopes as a probe to evaluate the feasibility of their use paleoclimate reconstruction and study kinetic isotope effects.

Chapter 1

Research into additional avenues for energy storage is an important endeavor which must be explored at every level to develop new technology which can help address future energy storage demands. The icosahedral boron cluster platform was explored for potential cathodic applications due to its thermal and chemical stability and the tunable nature of its redox activity. Our research explored the first application of the icosahedral boron cluster for use as a cathode in a lithium-ion cell. It was able to cycle through cyclic voltammetry with a $1e^-$ transfer for 10 cycles in the solid state. However, current degradation and theoretical capacity concerns limited its future application in self sustained lithium-ion battery applications.

Future directions of research aim to address theoretical capacity concerns by reducing the size of ligands attached, using smaller cluster scaffolds, mono-vertex polymerization of clusters, and using redox active metal centers to increase the accessible electrons which can be used for (dis)charging.

Chapter 2

This research contributes to evaluating Δ_{47}-Δ_{48} dual clumped isotopes as a universal approach for determining (dis)equilibria. It builds on prior work from experiments and theory, and using on bulk stable isotopes and Δ_{47} at the Samail ophiolites, and sets up the potential use of the Δ_{47}-Δ_{48} in potential sites of interest for geological sequestration. We analyzed $CaCO_3$ samples collected from springs at The Cedars, located in a peridotite body in Northern California. Our work suggests kinetic biases in dual clumped and bulk stable isotope values arise due to carbonate minerals precipitating out of highly alkaline parent media through a CO_2 absorption-driven disequilibrium pathway. Results are comparable to inorganic lab calcite precipitated at high pH (Lucarelli *et al.*, 2022), with significant KIEs including Δ_{47} enrichments and Δ_{48} depletions relative to equilibrium. We successfully modeled the KIEs associated with a CO_2 absorption-driven disequilibrium process through two different modeling frameworks.

Thus, we have added to an emerging body of work that uses dual clumped isotopes to probe kinetic effects associated with dissolved inorganic carbon transformation, and shows that we can evaluate if samples from such settings can be used for paleoclimate reconstruction. Future research into The Cedars could investigate the carbonates stored in the peridotite veins and evaluate potential kinetic biases, and could evaluate a larger breadth of analogous sites to determine if similar trends are observed. A statistically large dataset would enable the creation of a model which could be used to evaluate geological sequestration sites of interest in a non-invasive, low cost, and and rapid manner. By combining datasets with modeling, timescales of evolution of carbonates can be determined and used to inform us on the feasibility of using these sites for geological CO_2 storage.

Chapter 3

We conducted bulk stable and clumped isotope analysis of 44 cave samples, including farmed calcite plates, natural stalagmites, synthetic speleothems and cave rafts from 17 localities, building on prior work at a small number of sites. We conducted a thorough evaluation of the paired dual clumped isotope space in its efficacy in identifying (dis)equilibrium and as a tool for paleothermometry, and found that more than half of the samples are in quasi-equilibrium and yield accurate estimates of temperature within error of observations. Novel kinetic isotope effects were determined that drive disequilibrium in Δ_{47} and Δ_{48} that we attribute to isotopic buffering, based on comparisons to bulk stable isotopes and Rayleigh distillation modeling. Using $\Delta\Delta_{47}$-$\Delta\Delta_{48}$, we correlated samples that exhibit evidence for carbon isotope exchange with depletions in both Δ_{47} and Δ_{48}, while samples that exhibit evidence for oxygen isotope exchange show enrichment in both Δ_{47} and Δ_{48}.

This work suggest a major future direction for dual clumped isotopes in cave carbonates could be to identify samples that form in equilibrium and use their Δ_{47} and/or other proxy approaches (e.g., oxygen isotope measurements of fluid inclusions and co-occurring carbonates) for paleotemperature analysis. Future research into carbon isotope exchange through a dual clumped isotope (Δ_{47} and Δ_{48}) lens could explore a broader suite of cave carbonates (i.e. stalactites, flow stones, etc.). By creating a database of disequilibria associated with a larger breadth of cave carbonates, we would gain further insights into the processes causing (dis)equilibrium within cave carbonates. In addition, current models such as IsoDIC could be expanded to include kinetic effects associated with oxygen and carbon isotope exchange.

Supplementary Information

S.1 Supporting Information: Synthesis of Novel Dodecaborate Clusters for Lithium-Ion Battery Applications

S.1.1 Synthesis of Precursor Molecules

$Cs_2B_{12}(OH)_{12}$

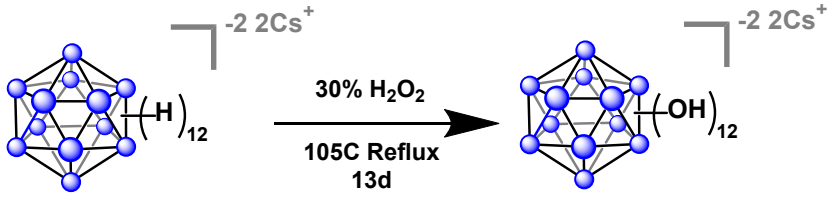

The precursor material $Cs_2B_{12}H_{12}$ was obtained by conducting a cation exchange with 16.00g (46.21 mmol) $TEA_2B_{12}H_{12}$ that was dissolved into 50 mL of MeOH. The addition of CsCl to the solution resulted in the $Cs_2B_{12}H_{12}$ precipitating out of solution. This precipitate was filtered and subjected to recrystallization using hot water. The resulting product was thoroughly dried under high vacuum and 110 ˚C heat overnight.

15.00 g (36.8 mmol) of $Cs_2B_{12}H_{12}$ was added to 30% H_2O_2 (30 mL), and the mixture was heated to 105 ˚C. Five 12 mL portions of H_2O_2 was added over the period of 10 hours and the solution was left to stir for 5 days between a temperature range of 105 – 110 ˚C. ^{11}BNMR of the supernatant mixture was analyzed until after the 5 day period. The reaction mixture was treated with 20 mL of H_2O_2 and subjected to stirring under the same conditions as the previous 5 days. This addition and sample analysis were repeated for 3 additional iterations, until only one signal in the ^{11}BNMR was visible, indicating a complete hydroxylation. The entire procedure took a total of 170 mL of 30% H_2O_2 with approximately 13 days of reaction time. Precipitate begins to form after day 4 and continues to be present upon completion. This solution was left to stir for an additional 5 days after the 13-day hydroxylation while exposed to light to degrade the unreacted

H_2O_2. During this period, the solution was checked daily using potassium iodide starch paper for any residual H_2O_2. The heterogeneous mixture was then concentrated and stored at 4 ˚C overnight. This mixture was then subjected to filtration and vacuum drying. The total yield was 20.9 g, 94.6%. The ^{11}BNMR can be seen in the figure below.

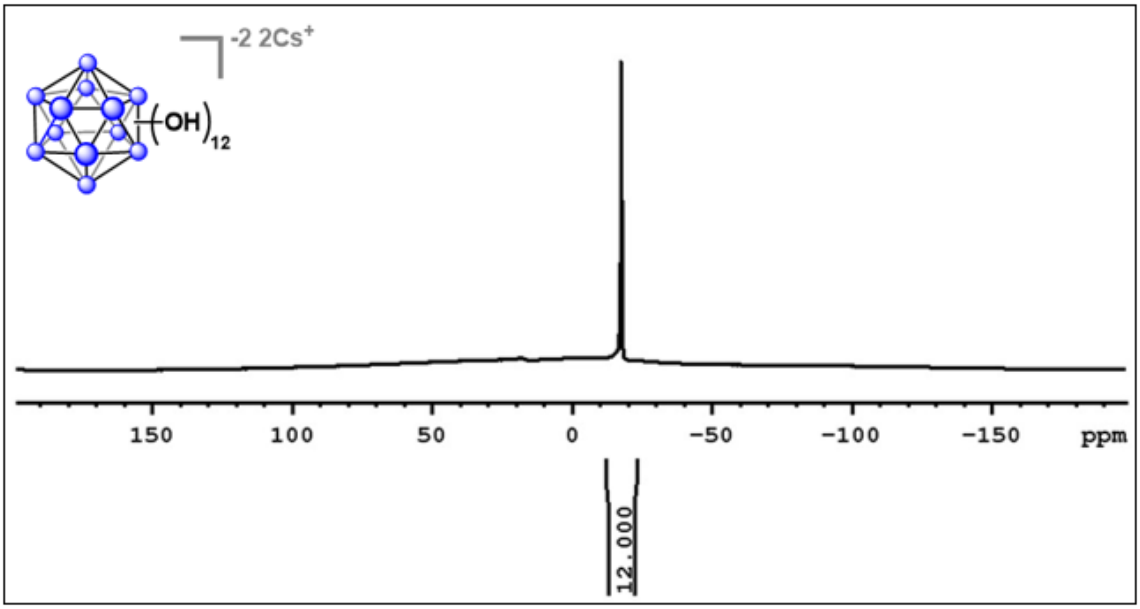

Synthesis of $Cs_2B_{12}H_{11}(NH_3)$

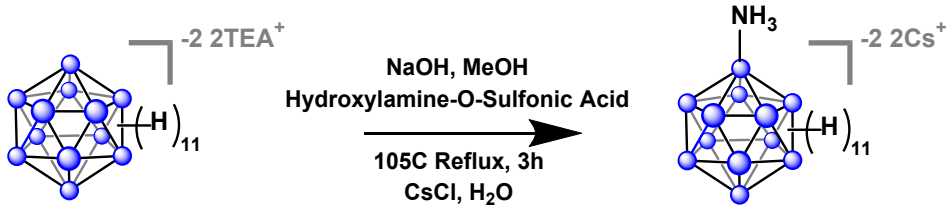

16.00 g (46.21 mmol) of $(TEA)_2B_{12}H_{12}$ was dissolved into 50 mL MeOH. 3.80 g (95.01 mmol) NaOH was dissolved in a separate flask containing 100 mL MeOH and 30 mL H_2O. Both solutions were combined and allowed to mix with stirring at room temperature (25 ˚C). The mixture was then subjected to rotary evaporation to remove the MeOH. 10.45 g (92.40 mmol) of hydroxylamine-O-sulfonic acid was dissolved into 30 mL of H_2O and then added dropwise to the

flask containing the boron cluster. An additional 100 mL of H_2O was added to the resulting mixture and then refluxed at 105 ˚C for 3 hours. 15.56 g (92.42 mmol) of CsCl was added to the solution and left stirring overnight. The solution was then concentrated through rotary evaporation and then stored in a 4 ˚C refrigerator. The precipitate was filtered, washed with H_2O and MeOH and then dried under high vacuum at 130 ˚C for 3 hours.

Synthesis of $TBA_2B_{12}(OH)_{11}(NO_2)$

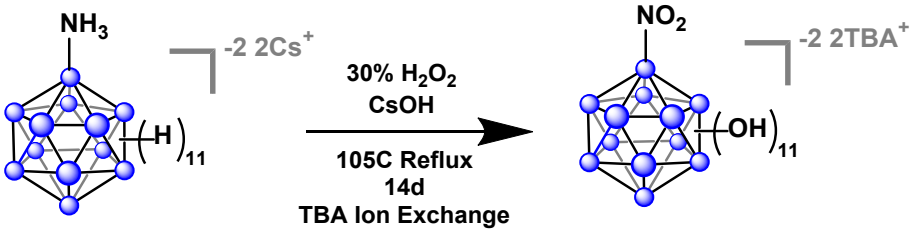

2.25 g (5.30 mmol) of $Cs_2B_{12}H_{11}NH_3$ was added to 50 mL of H_2O_2 and allowed to equilibrate at 105 ˚C under reflux conditions with stirring. An additional 10 mL of H_2O_2 was added approximately 6 hours later. 30 mL of H_2O_2 was added after 3 days along with a 50:50 (H_2O:CsOH), dropwise (approximately 30-40 drops), until the pH of the solution was above 8. The addition of 30 mL of H_2O_2 and 50:50 solution of H_2O:CsOH was repeated every day for a total of 7 days. During this 7-day period, the solution was monitored by insitu ^{11}BNMR to determine if the reaction had gone to completion. After the reaction had completed MeOH was added to the solution to precipitate the final product out of solution. The precipitate was then subjected to filtration and high vacuum at 130 ˚C. 3.98 g (86.8% yield) of product was recovered.

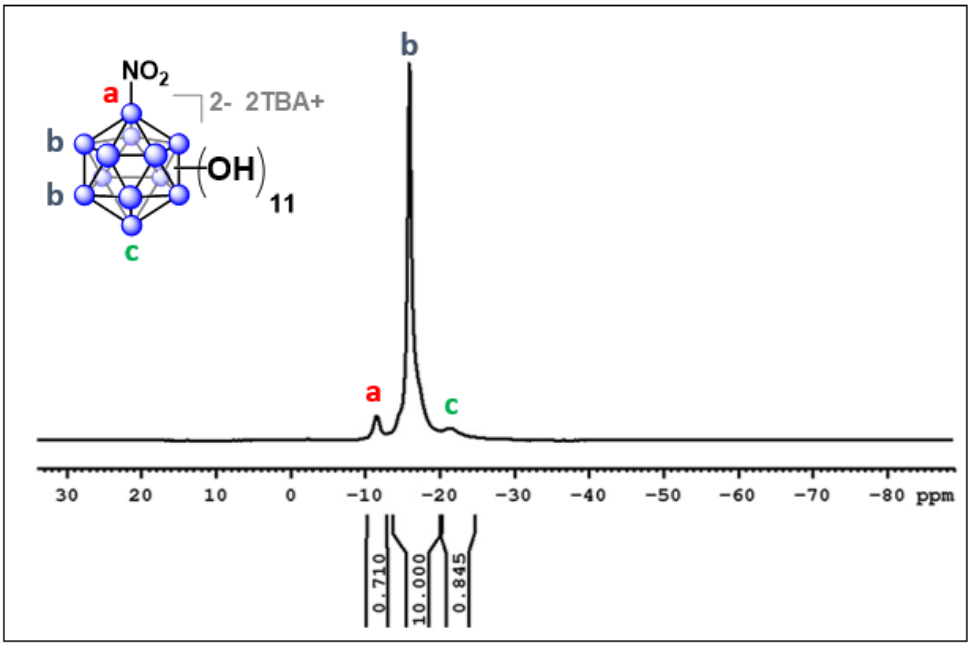
NO2
a
2- 2TBA+
b
b
OH
11
c
b
a
c
30
20
10
0
−10
−20
−30
−40
−50
−60
−70
−80 ppm
0.710
10.000
0.845

S.2 - Paired dual carbonate clumped isotopes (Δ47-Δ48) constrains kinetic effects and timescales in peridotite-associated springs at The Cedars, Northern California

S.2.1 IsoDIC Model Equations

The following numerical values have been assigned to the respective isotopologue: $^{12}C = 2$, $^{13}C = 3$, $^{16}O = 6$, $^{17}O = 7$, $^{18}O = 8$. For example, $H^{12}C^{18}O^{16}O^{17}O^{-}$ = H2867

1. $266 + H_26 \rightleftharpoons H2666 + H^+$
2. $267 + H_26 \rightleftharpoons H2667 + H^+$
3. $268 + H_26 \rightleftharpoons H2668 + H^+$
4. $277 + H_26 \rightleftharpoons H2677 + H^+$
5. $278 + H_26 \rightleftharpoons H2678 + H^+$
6. $288 + H_26 \rightleftharpoons H2688 + H^+$
7. $266 + H_27 \rightleftharpoons H2667 + H^+$
8. $267 + H_27 \rightleftharpoons H2667 + H^+$
9. $267 + H_27 \rightleftharpoons H2678 + H^+$
10. $277 + H_27 \rightleftharpoons H2777 + H^+$
11. $278 + H_27 \rightleftharpoons H2778 + H^+$
12. $288 + H_27 \rightleftharpoons H2788 + H^+$
13. $266 + H_28 \rightleftharpoons H2668 + H^+$
14. $267 + H_28 \rightleftharpoons H2678 + H^+$
15. $268 + H_28 \rightleftharpoons H2688 + H^+$
16. $277 + H_28 \rightleftharpoons H2778 + H^+$
17. $278 + H_28 \rightleftharpoons H2788 + H^+$
18. $288 + H_28 \rightleftharpoons H2888 + H^+$
19. $266 + H_26 \rightleftharpoons H3666 + H^+$
20. $366 + H_26 \rightleftharpoons H3667 + H^+$
21. $377 + H_26 \rightleftharpoons H3668 + H^+$
22. $378 + H_26 \rightleftharpoons H3677 + H^+$
23. $378 + H_26 \rightleftharpoons H3678 + H^+$
24. $388 + H_26 \rightleftharpoons H3688 + H^+$
25. $366 + H_27 \rightleftharpoons H3667 + H^+$
26. $367 + H_27 \rightleftharpoons H3677 + H^+$
27. $368 + H_27 \rightleftharpoons H3678 + H^+$
28. $377 + H_27 \rightleftharpoons H3777 + H^+$
29. $378 + H_27 \rightleftharpoons H3778 + H^+$
30. $388 + H_27 \rightleftharpoons H3788 + H^+$
31. $366 + H_28 \rightleftharpoons H3668 + H^+$
32. $367 + H_28 \rightleftharpoons H3678 + H^+$
33. $368 + H_28 \rightleftharpoons H3688 + H^+$
34. $377 + H_28 \rightleftharpoons H3778 + H^+$
35. $378 + H_28 \rightleftharpoons H3788 + H^+$
36. $388 + H_28 \rightleftharpoons H3888 + H^+$
37. $266 + 6H \rightleftharpoons H2666$
38. $267 + 6H \rightleftharpoons H2667$
39. $268 + 6H \rightleftharpoons H2668$

40. 277 + 6H ⇌ H2677
41. 278 + 6H ⇌ H2678
42. 288 + 6H ⇌ H2688
43. 266 + 7H ⇌ H2667
44. 267 + 7H ⇌ H2677
45. 268 + 7H ⇌ H2678
46. 277 + 7H ⇌ H2777
47. 278 + 7H ⇌ H2778
48. 288 + 8H ⇌ H2788
49. 266 + 8H ⇌ H2668
50. 267 + 8H ⇌ H2678
51. 268 + 8H ⇌ H2688
52. 277 + 8H ⇌ H2778
53. 278 + 8H ⇌ H2788
54. 288 + 8H ⇌ H2888
55. 366 + 6H ⇌ H3666
56. 367 + 6H ⇌ H3667
57. 368 + 6H ⇌ H3668
58. 377 + 6H ⇌ H3677
59. 378 + 6H ⇌ H3678
60. 388 + 6H ⇌ H3688
61. 366 + 7H ⇌ H3667
62. 367 + 7H ⇌ H3677
63. 368 + 7H ⇌ H3678
64. 377 + 7H ⇌ H3777
65. 378 + 7H ⇌ H3778
66. 388 + 7H ⇌ H3788
67. 366 + 8H ⇌ H3668
68. 367 + 8H ⇌ H3678
69. 368 + 8H ⇌ H3688
70. 377 + 8H ⇌ H3778
71. 378 + 8H ⇌ H3788
72. 388 + 8H ⇌ H3888
73 – 152. $H^iC^jO^kO^lO^- + {}^mOH^- \rightleftharpoons {}^iC^jO^kO^lO^2 + H_2{}^mO$
where i = 12, 13, $16 \leq j \leq k \leq l \leq 18$, m = 16, 17, 18
153 – 155. $H_2{}^mO \rightleftharpoons {}^mOH^- + H^+$
where m = 16, 17, 18

The above reactions and their isotope effects were used by Guo *et al.* (2020) calculate intrinsic kinetic clumped isotope fractionation factors associated with CO_2 hydration and hydroxylation and their reverse reactions.

S.2.2 COAD Model Equations

a. Hydration and hydroxylation reactions

1. $266 + H_26 \rightleftharpoons H2666 + H$ (forward = k_{+1}) (reverse = k_{-1})

2. $266 + 6H \leftrightharpoons H2666$ (forward = k_{+4}) (reverse = k_{-4})
3. $366 + H_26 \leftrightharpoons H3666 + H$ (forward = c_{+1}) (reverse = c_{-1})
4. $366 + 6H \leftrightharpoons H3666$ (forward = c_{+4}) (reverse = c_{-4})
5. $266 + H_28 \leftrightharpoons H2866 + H$ (forward = a_{+1}) (reverse = $1/3a_{-1}$)
6. $286 + H_26 \leftrightharpoons H2866 + H$ (forward = b_{+1}) (reverse = $2/3b_{-4}$)
7. $266 + 8H \leftrightharpoons H2866$ (forward = a_{+4}) (reverse = $1/3a_{-4}$)
8. $286 + 6H \leftrightharpoons H2866$ (forward = b_{+4}) (reverse = $2/3b_{-4}$)
9. $366 + H_28 \leftrightharpoons H3866 + H$ (forward = p_{+1}) (reverse = $1/3p_{-1}$)
10. $386 + H_26 \leftrightharpoons H3866 + H$ (forward = s_{+1}) (reverse = $2/3s_{-1}$)
11. $366 + 8H \leftrightharpoons H3866$ (forward = p_{+4}) (reverse = $1/3p_{-4}$)
12. $386 + 6H \leftrightharpoons H3866$ (forward = s_{+4}) (reverse = $2/3s_{-1}$)
13. $286 + H_28 \leftrightharpoons H2886 + H$ (forward = p'_{+1}) (reverse = $2/3p'_{-1}$)
14. $288 + H_26 \leftrightharpoons H2886 + H$ (forward = s'_{+1}) (reverse = $1/3s'_{-1}$)
15. $286 + 8H \leftrightharpoons H2886$ (forward = p'_{+4}) (reverse = $2/3p'_{-4}$)
16. $288 + 6H \leftrightharpoons H2886$ (forward = s'_{+4}) (reverse = $1/3s'_{-4}$)

b. Governing equations for the reaction-diffusion model

17. $\frac{d[266]}{dt} = D_{CO_2} * \frac{d^2[266]}{dz^2} - k_{+1}[266] + k_{-1}[E2666]\chi[H] - k_{+4}[266][6H] + k_{-4}[E2666]\chi$
18. $\frac{d[366]}{dt} = D_{CO_2} * \frac{d^2[366]}{dz^2} - c_{+1}[366] + c_{-1}[E3666]^{13}\chi[H] - c_{+4}[366][6H] + c_{-4}[E3666]^{13}\chi$
19. $\frac{d[286]}{dt} = D_{CO_2} * \frac{d^2[286]}{dz^2} - b_{+1}[286] + \frac{2}{3}b_{-1}[E2866]^{18}X[H] - b_{+4}[286][6H] + \frac{2}{3}b_{-4}[E2866]^{18}X$
20. $\frac{d[386]}{dt} = D_{CO_2} * \frac{d^2[386]}{dz^2} - p_{+1}[386] + \frac{1}{3}p_{-1}[E3866]^{63}X[H] - s_{+4}[386][6H] + \frac{2}{3}s_{-4}[E3866]^{63}X$
21. $\frac{d[288]}{dt} = D_{CO_2} * \frac{d^2[288]}{dz^2} - s'_{+1}[288] + \frac{1}{3}s'_{-1}[E2886]^{64}X[H] - s'_{+4}[288][6H] + \frac{1}{3}s'_{-4}[E2886]^{64}X$
22. $\frac{d[E2666]}{dt} = D_{CO_2} * \frac{d^2[E2666]}{dz^2} + k_{+1}[266] - k_{-1}[E2666]X[H]k_{+4}[266][6H] - k_{-4}[E2666]X - Sp * J_{CaCO_3}$
23. $\frac{d[E3666]}{dt} = D_{CO_2} * \frac{d^2[E3666]}{dz^2} + c_{+1}[366] - c_{-1}[E3666]^{13}X[H]c_{+4}[366][6H] - c_{-4}[E3666]^{13}X - Sp * J_{CaCO_3} * \frac{[E3666]}{[E2666]} *^{13} \alpha_{CaCO_3-EIC}$
24. $\frac{d[E2866]}{dt} = D_{CO_2} * \frac{d^2[E2866]}{dz^2} + a_{+1}[266]r_w - \frac{1}{3}a_{-1}[E2866]^{18}X[H] + a_{+4}[266][8H] - \frac{1}{3}a_{-4}[E2866]^{18}X + b_{+1}[286] - \frac{2}{3}b_{-1}[E2866]^{18}X[H] + b_{+4}[286][6H] - \frac{2}{3}b_{-4}[E2866]^{18}X - Sp * J_{CaCO_3} * \frac{[E2866]}{[E2666]} *^{18} \alpha_{CaCO_3-EIC}$
25. $\frac{d[E3866]}{dt} = D_{CO_2} * \frac{d^2[E3866]}{dz^2} + p_{+1}[366]r_w - \frac{1}{3}p_{-1}[E3866]^{63}X[H] + p_{+4}[266][8H] - \frac{1}{3}p_{-4}[E3866]^{63}X + s_{+1}[386] - \frac{2}{3}s_{-1}[E3866]^{63}X[H] + s_{+4}[386][6H] - \frac{2}{3}s_{-4}[E3866]^{63}X - Sp * J_{CaCO_3} * \frac{[E3866]}{[E2666]} *^{63} \alpha_{CaCO_3-EIC} *^{13} \alpha_{CaCO_3-EIC} *^{18} \alpha_{CaCO_3-EIC}$

26. $\frac{d[E2886]}{dt} = D_{CO_2} * \frac{d^2[E2886]}{dz^2} + p'_{+1}[286]r_w - \frac{2}{3}p'_{-1}[E2886]^{64}X[H] + p'_{+4}[286][8H] - \frac{2}{3}p'_{-4}[E2886]^{64}X + s'_{+1}[288] - \frac{1}{3}s'_{-1}[E2886]^{64}X[H] + s'_{+4}[288][6H] - \frac{1}{3}s'_{-4}[E2886]^{64}X - Sp * J_{CaCO_3} * \frac{[E2886]}{[E2666]} *^{64} \alpha_{CaCO_3-EIC} *^{18} \alpha_{CaCO_3-EIC} *^{18} \alpha_{CaCO_3-EIC}$
27. $\frac{d[Alk]}{dt} = D_{Alk} * \frac{d^2[Alk]}{dz^2} - 2 * Sp * J_{CaCO_3}$
28. $\frac{d[Ca^{2+}]}{dt} = D_{Ca^{2+}} * \frac{d^2[Ca^{2+}]}{dz^2} - Sp * J_{CaCO_3}$

c. Governing equations for the box model

29. $\frac{d[266]}{dt} = -k_{+1}[266] + k_{-1}[E2666]X[H] - k_{+4}[266][6H] + k_{-4}[E2666]X + \frac{F_{spr}}{V_{pool}}([266]_{spr} - [266]) + \frac{F_{cr}}{V_{pool}}([266]_{cr} - [266])$
30. $\frac{d[366]}{dt} = -c_{+1}[366] + c_{-1}[E3666]^{13}X[H] - c_{+4}[366][6H] + c_{-4}[E3666]^{13}X + \frac{F_{spr}}{V_{pool}}([366]_{spr} - [366]) + \frac{F_{cr}}{V_{pool}}([366]_{cr} - [266])$
31. $\frac{d[286]}{dt} = -b_{+1}[286] + \frac{2}{3}b_{-1}[E2866]^{18}X[H] - b_{+4}[286][6H] + \frac{2}{3}b_{-4}[E2866]^{18}X + \frac{F_{spr}}{V_{pool}}([286]_{spr} - [286]) + \frac{F_{cr}}{V_{pool}}([286]_{cr} - [266])$
32. $\frac{d[386]}{dt} = -p_{+1}[386] + \frac{1}{3}p_{-1}[E3866]^{63}X[H] - s_{+4}[386][6H] + \frac{2}{3}s_{-4}[E3866]^{63}X + \frac{F_{spr}}{V_{pool}}([386]_{spr} - [386]) + \frac{F_{cr}}{V_{pool}}([386]_{cr} - [266])$
33. $\frac{d[288]}{dt} = -s'_{+1}[288] + \frac{1}{3}s'_{-1}[E2886]^{64}X[H] - s'_{+4}[288][6H] + \frac{1}{3}s'_{-4}[E2886]^{64}X + \frac{F_{spr}}{V_{pool}}([288]_{spr} - [288]) + \frac{F_{cr}}{V_{pool}}([288]_{cr} - [266])$
34. $\frac{d[E2666]}{dt} = k_{+1}[266] - k_{-1}[E2666]X[H]k_{+4}[266][6H] - k_{-4}[E2666]X + \frac{J_{atm} * SA_{pool}}{V_{pool}} + \frac{F_{spr}}{V_{pool}}([E2666]_{spr} - [E2666]) + \frac{F_{cr}}{V_{pool}}([E2666]_{cr} - [E2666]) - Sp * J_{CaCO_3}$
35. $\frac{d[E3666]}{dt} = c_{+1}[366] - c_{-1}[E3666]^{13}X[H]c_{+4}[366][6H] - c_{-4}[E3666]^{13}X\frac{J_{atm} * SA_{pool}}{V_{pool}} * \left(\frac{[E3666]}{[E2666]}\right)_{hydrox} + \frac{F_{spr}}{V_{pool}}(^{13}R_{EIC_{(spr)}}[EIC]_{spr} - [E3666]) + \frac{F_{cr}}{V_{pool}}([E3666]_{cr} - [E3666]) - Sp * J_{CaCO_3}\frac{[E3666]}{[E2666]} *^{13} \alpha_{CaCO_3-EIC}$
36. $\frac{d[E2866]}{dt} = a_{+1}[266]r_w - \frac{1}{3}a_{-1}[E2866]^{18}X[H] + a_{+4}[266][8H] - \frac{1}{3}a_{-4}[E2866]^{18}X + b_{+1}[286] - \frac{2}{3}b_{-1}[E2866]^{18}X[H] + b_{+4}[286][6H] - \frac{2}{3}b_{-4}[E2866]^{18}X + \frac{J_{atm} * SA_{pool}}{V_{pool}} * (\frac{[E2866]}{[E2666]})_{hydrox} + \frac{F_{spr}}{V_{pool}}([E2866]_{spr} - [E2866]) + \frac{F_{cr}}{V_{pool}}([E2866]_{cr} - [E2866]) - Sp * J_{CaCO_3}\frac{[E2866]}{[E2666]} *^{18} \alpha_{CaCO_3-EIC}$
37. $\frac{d[E3866]}{dt} = p_{+1}[366]r_w - \frac{1}{3}p_{-1}[E3866]^{63}X[H] + p_{+4}[266][8H] - \frac{1}{3}p_{-4}[E3866]^{63}X + s_{+1}[386] - \frac{2}{3}s_{-1}[E3866]^{63}X[H] + s_{+4}[386][6H] - \frac{2}{3}s_{-4}[E3866]^{63}X + \frac{J_{atm} * SA_{pool}}{V_{pool}} * (\frac{[E3866]}{[E2666]})_{hydrox} + \frac{F_{spr}}{V_{pool}}([E3866]_{spr} - [E3866]) + \frac{F_{cr}}{V_{pool}}([E3866]_{cr} - [E3866]) - Sp * J_{CaCO_3}\frac{[E3866]}{[E2666]} *^{63} \alpha_{CaCO_3-EIC} *^{13} \alpha_{CaCO_3-EIC} *^{18} \alpha_{CaCO_3-EIC}$

38. $\frac{d[E2886]}{dt} = p'_{+1}[286]r_w - \frac{2}{3}p'_{-1}[E2886]^{64}X[H] + p'_{+4}[286][8H] - \frac{2}{3}p'_{-4}[E2886]^{64}X + s'_{+1}[288] - \frac{1}{3}s'_{-1}[E2886]^{64}X[H] + s'_{+4}[288][6H] - \frac{1}{3}s'_{-4}[E2886]^{64}X + \frac{J_{atm}*SA_{pool}}{V_{pool}} * (\frac{[E2886]}{[E2666]})_{hydrox} + \frac{F_{spr}}{V_{pool}}([E2886]_{spr} - [E2886]) + \frac{F_{cr}}{V_{pool}}([E2886]_{cr} - [E2886]) - Sp * J_{CaCO_3}\frac{[E2886]}{[E2666]} *^{64} \alpha_{CaCO_3-EIC} *^{18} \alpha_{CaCO_3-EIC} *^{18} \alpha_{CaCO_3-EIC}$
39. $\frac{d[Alk]}{dt} = \frac{F_{spr}}{V_{pool}}([Alk]_{spr} - [Alk]) + \frac{F_{cr}}{V_{pool}}([Alk]_{cr} - [Alk]) - 2 * Sp * J_{CaCO_3}$
40. $\frac{d[Ca^{2+}]}{dt} = \frac{F_{spr}}{V_{pool}}([Ca^{2+}]_{spr} - [Ca^{2+}]) + \frac{F_{cr}}{V_{pool}}([Ca^{2+}]_{cr} - [Ca^{2+}]) - Sp * J_{CaCO_3}$

d. Post-processing: Isotopologue concentrations to isotope ratios

41. $\delta^{13}C(‰) = \left(\frac{^{13}R}{0.0118} - 1\right) * 1000,$
42. $^{13}R = \frac{[3666]}{[2666]}.$
43. $\delta^{18}O(‰) = \left(\frac{3*^{18}R}{0.0020052} - 1\right) * 1000,$
44. $^{18}R = \frac{[2866]}{[2666]}.$
45. $\Delta_{47} = (\frac{^{47}R}{^{47}R} - 1) * 1000,$
46. $\frac{^{47}R}{^{47}R^*} = \frac{[386][266]}{[366][286]},$
47. $\Delta_{63} = \left(\frac{^{63}R}{^{63}R^*} - 1\right) * 1000,$
48. $\frac{^{63}R}{^{63}R^*} = \frac{[3866][2666]}{[3666][2866]}.$
49. $\Delta_{48} = \left(\frac{^{48}R}{^{48}R^*} - 1\right) * 1000,$
50. $\frac{^{48}R}{^{48}R^*} = 4 * \frac{[288][266]}{[286][286]},$
51. $\Delta_{64} = \left(\frac{^{64}R}{^{64}R^*} - 1\right) * 1000,$
52. $\frac{^{64}R}{^{64}R^*} = 3 * \frac{[2886][2666]}{[2866][2866]}$

Table 1: Parameters for conventional isotope ratios.

Symbol	Expression (or value at 25 °C)	Reference/Note
Part I: Chemical parameters		
K_1	$\frac{[\mathrm{H2666}][\mathrm{H}]}{[266][\mathrm{H_26}]}$, $[\mathrm{H_26}] = 1$	$f(T, S)$
K_2	$\frac{[2666][\mathrm{H}]}{[\mathrm{H2666}]}$	$f(T, S)$
K_w	$[6\mathrm{H}][\mathrm{H}]$	$f(T, S)$
k_{+1}	$\ln k_{+1}$=1246.98 - $\frac{61900}{T_\mathrm{K}} - 183.0 \ln T_\mathrm{K}$	Uchikawa and Zeebe (2012)
k_{-1}	$k_{-1}=k_{+1}/K_1$	-
k_{+4}	$\ln k_{+4}$=17.67 - $\frac{2790.47}{T_\mathrm{K}}$	Uchikawa and Zeebe (2012)
k_{-4}	$k_{-4}=k_{+4}\frac{K_w}{K_1}$	-
χ	$\chi = \frac{1}{1+\frac{K_2}{[H^+]}}$	-
Part II: Carbon isotope parameters		
${}^{13}\alpha^{\mathrm{eq}}_{\mathrm{CO_2-HCO_3^-}}$	-9.866 T^{-1} + 1.02412	Zhang et al. (1995)
${}^{13}\alpha^{\mathrm{eq}}_{\mathrm{CO_3^{2-}-HCO_3^-}}$	-0.867 T^{-1} + 1.00252	Zhang et al. (1995)
${}^{13}\alpha^{\mathrm{KFF}}_{c_{+1}}$	0.9872	Yumol et al. (2020)
${}^{13}\alpha^{\mathrm{KFF}}_{c_{+4}}$	0.9814	Christensen et al. (2021)
c_{+1}	$c_{+1} = {}^{13}\alpha^{\mathrm{KFF}}_{c_{+1}} \cdot k_{+1}$	-
c_{-1}	$c_{-1} = c_{+1}/(K_1 \cdot {}^{13}\alpha^{\mathrm{eq}}_{\mathrm{HCO_3-CO_2}})$	-
c_{+4}	$c_{+4} = {}^{13}\alpha^{\mathrm{KFF}}_{c_{+4}} \cdot k_{+4}$	-
c_{-4}	$c_{-4} = c_{+4}/\left(\frac{K_1}{K_w} \cdot {}^{13}\alpha^{\mathrm{eq}}_{\mathrm{HCO_3-CO_2}}\right)$	-
${}^{13}\chi$	${}^{13}\chi = \frac{1}{1+\frac{K_2 \cdot {}^{13}\alpha^{\mathrm{eq}}_{\mathrm{CO_3-HCO_3}}}{[H^+]}}$	-
Part III: Oxygen isotope parameters		
${}^{18}\alpha^{\mathrm{eq}}_{\mathrm{CO_2-H_2O}}$	$\exp(2520\ T_\mathrm{K}^{-2} + 0.01212)$	Beck et al. (2005)
${}^{18}\alpha^{\mathrm{eq}}_{\mathrm{HCO_3^- - H_2O}}$	$\exp(2590\ T_\mathrm{K}^{-2} + 0.00189)$	Beck et al. (2005)
${}^{18}\alpha^{\mathrm{eq}}_{\mathrm{CO_3^{2-} - H_2O}}$	$\exp(2390\ T_\mathrm{K}^{-2}$ - 0.00270)	Beck et al. (2005)
${}^{18}\alpha^{\mathrm{eq}}_{\mathrm{OH^- - H_2O}}$	$5.6676\times10^{-5}\ T_\mathrm{K} + 0.9622$	based on Zeebe (2020)
${}^{18}\alpha^{\mathrm{KFF}}_{a_{+1}}$	1.0000	Yumol et al. (2020)
${}^{18}\alpha^{\mathrm{KFF}}_{b_{+1}}$	0.9812	Yumol et al. (2020)
${}^{18}\alpha^{\mathrm{KFF}}_{a_{+4}}$	0.9988	Christensen et al. (2021)
${}^{18}\alpha^{\mathrm{KFF}}_{b_{+4}}$	1.0000	Christensen et al. (2021)
a_{+1}, b_{+1}	$a_{+1} = {}^{18}\alpha^{\mathrm{KFF}}_{a_{+1}} \cdot k_{+1}$	-
	$b_{+1} = {}^{18}\alpha^{\mathrm{KFF}}_{b_{+1}} \cdot k_{+1}$	-
a_{-1}, b_{-1}	$a_{-1} = a_{+1}/(K_1 \cdot {}^{18}\alpha_{\mathrm{HCO_3-H_2O}})$	-
	$b_{-1} = b_{+1}/(K_1 \cdot {}^{18}\alpha_{\mathrm{HCO_3-CO_2}})$	-
a_{+4}, b_{+4}	$a_{+4} = {}^{18}\alpha^{\mathrm{KFF}}_{a_{+4}} \cdot k_{+4}$	-
	$b_{+1} = {}^{18}\alpha^{\mathrm{KFF}}_{b_{+4}} \cdot k_{+4}$	-
a_{-4}, b_{-4}	$a_{-4} = a_{+4}/\left(\frac{K_1}{K_w}\frac{{}^{18}\alpha_{\mathrm{HCO_3-H_2O}}}{{}^{18}\alpha_{\mathrm{OH-H_2O}}}\right)$	-
	$b_{-4} = b_{+4}/\left(\frac{K_1}{K_w}{}^{18}\alpha_{\mathrm{HCO_3-CO_2}}\right)$	-
${}^{18}\chi$	${}^{18}\chi = \frac{1}{1+\frac{K_2 \cdot {}^{18}\alpha^{\mathrm{eq}}_{\mathrm{CO_3-HCO_3}}}{[H^+]}}$	-

Table 2: Parameters for single-clumped isotopes

Symbol	Value	Reference/Note
Part IV: Single-clumped isotope parameters		
$\Delta^{\mathrm{eq}}_{47,\mathrm{CO_2}}$	$26447/T_{\mathrm{K}}^2 + 285.51/T_{\mathrm{K}} - 0.3004$	Wang et al. (2004)
$\Delta^{\mathrm{eq}}_{63,\mathrm{HCO_3^-}}$	$43655/T_{\mathrm{K}}^2$ - $23.643/T_{\mathrm{K}} - 0.0088$	Hill et al. (2020)
$\Delta^{\mathrm{eq}}_{63,\mathrm{CO_3^{2-}}}$	$43187/T_{\mathrm{K}}^2 + 34.833/T_{\mathrm{K}} + 0.0007$	Hill et al. (2020)
$\left({}^{47}R/{}^{47}R^*\right)^{\mathrm{eq}}_{\mathrm{CO_2}}$	$\Delta^{\mathrm{eq}}_{47,\mathrm{CO_2}}/1000 + 1$	
$\left({}^{63}R/{}^{63}R^*\right)^{\mathrm{eq}}_{\mathrm{HCO_3^-}}$	$\Delta^{\mathrm{eq}}_{63,\mathrm{HCO_3^-}}/1000 + 1$	
$\left({}^{63}R/{}^{63}R^*\right)^{\mathrm{eq}}_{\mathrm{CO_3^{2-}}}$	$\Delta^{\mathrm{eq}}_{63,\mathrm{CO_3^{2-}}}/1000 + 1$	
${}^{63}\alpha^{\mathrm{eq}}_{\mathrm{CO_3^{2-}-HCO_3^-}}$	$\left({}^{63}R/{}^{63}R^*\right)^{\mathrm{eq}}_{\mathrm{CO_3^{2-}}} / \left({}^{63}R/{}^{63}R^*\right)^{\mathrm{eq}}_{\mathrm{HCO_3^-}}$	-
${}^{63}K_2$	${}^{63}\alpha^{\mathrm{eq}}_{\mathrm{CO_3^{2-}-HCO_3^-}} \cdot {}^{13}\alpha^{\mathrm{eq}}_{\mathrm{CO_3^{2-}-HCO_3^-}} \cdot {}^{18}\alpha^{\mathrm{eq}}_{\mathrm{CO_3^{2-}-HCO_3^-}} \cdot K_2$	-
${}^{63}\chi$	$\frac{1}{1+\frac{{}^{63}K_2\,{}^{63}\alpha^{\mathrm{eq}}_{\mathrm{CO_3-HCO_3}}}{[H^+]}}$	-
${}^{13-18}\mathrm{KIE}_{p_{+1}}$	1-0.146/1000	Guo (2020)
${}^{13-18}\mathrm{KIE}_{s_{+1}}$	1-0.219/1000	Guo (2020)
${}^{13-18}\mathrm{KIE}_{p_{+4}}$	1-0.016/1000	Guo (2020)
${}^{13-18}\mathrm{KIE}_{s_{+4}}$	1-0.175/1000	Guo (2020)
p_{+1}, s_{+1}	$p_{+1} = ({}^{13-18}\mathrm{KIE}_{p_{+1}} \cdot c_{+1} \cdot a_{+1})/k_{+1}$	Uchikawa et al. (2021)
	$s_{+1} = ({}^{13-18}\mathrm{KIE}_{s_{+1}} \cdot c_{+1} \cdot b_{+1})/k_{+1}$	Uchikawa et al. (2021)
p_{-1}, s_{-1}	$p_{-1} = p_{+1} / \left[\left({}^{63}R/{}^{63}R^*\right)^{\mathrm{eq}}_{\mathrm{HCO_3^-}} \cdot K_1 \cdot {}^{13}\alpha^{\mathrm{eq}}_{\mathrm{HCO_3^- - H_2O}} \cdot {}^{18}\alpha^{\mathrm{eq}}_{\mathrm{HCO_3^- - H_2O}}\right]$	-
	$s_{-1} = s_{+1} \cdot \left[\left({}^{47}R/{}^{47}R^*\right)^{\mathrm{eq}}_{\mathrm{CO_2}}\right] / \left[\left({}^{63}R/{}^{63}R^*\right)^{\mathrm{eq}}_{\mathrm{HCO_3^-}} \cdot K_1 \cdot {}^{13}\alpha^{\mathrm{eq}}_{\mathrm{HCO_3^- - CO_2}} \cdot {}^{18}\alpha^{\mathrm{eq}}_{\mathrm{HCO_3^- - H_2O}}\right]$	-
p_{+4}, s_{+4}	$p_{+4} = ({}^{13-18}\mathrm{KIE}_{p_{+4}} \cdot c_{+4} \cdot a_{+4})/k_{+4}$	Uchikawa et al. (2021)
	$s_{+4} = ({}^{13-18}\mathrm{KIE}_{s_{+4}} \cdot c_{+4} \cdot b_{+4})/k_{+4}$	Uchikawa et al. (2021)
p_{-4}, s_{-4}	$p_{-4} = p_{+4} / \left[\left({}^{63}R/{}^{63}R^*\right)^{\mathrm{eq}}_{\mathrm{HCO_3^-}} \cdot K_1/K_{\mathrm{w}} \cdot {}^{13}\alpha^{\mathrm{eq}}_{\mathrm{HCO_3^- - CO_2}} \cdot {}^{18}\alpha^{\mathrm{eq}}_{\mathrm{HCO_3^- - OH^-}}\right]$	-
	$s_{-4} = s_{+4} \cdot \left[\left({}^{47}R/{}^{47}R^*\right)^{\mathrm{eq}}_{\mathrm{CO_2}}\right] / \left[\left({}^{63}R/{}^{63}R^*\right)^{\mathrm{eq}}_{\mathrm{HCO_3^-}} \cdot K_1/K_{\mathrm{w}} \cdot {}^{13}\alpha^{\mathrm{eq}}_{\mathrm{HCO_3^- - CO_2}} \cdot {}^{18}\alpha^{\mathrm{eq}}_{\mathrm{HCO_3^- - CO_2}}\right]$	-

Table 3: Parameters for double-clumped isotopes

Symbol	Value	Reference/Note
Part V: Double-clumped isotope parameters		
$\Delta^{\mathrm{eq}}_{48,\mathrm{CO_2}}$	$29306/T_{\mathrm{K}}^2 + 93.885/T_{\mathrm{K}} - 0.2914$	Wang et al. (2004)
$\Delta^{\mathrm{eq}}_{64,\mathrm{HCO_3^-}}$	$21842/T_{\mathrm{K}}^2$ - $50.457/T_{\mathrm{K}} + 0.0291$	Hill et al. (2020)
$\Delta^{\mathrm{eq}}_{64,\mathrm{CO_3^{2-}}}$	$23492/T_{\mathrm{K}}^2$ - $52.842/T_{\mathrm{K}} + 0.0304$	Hill et al. (2020)
$\left({}^{48}R/{}^{48}R^*\right)^{\mathrm{eq}}_{\mathrm{CO_2}}$	$\Delta^{\mathrm{eq}}_{48,\mathrm{CO_2}}/1000 + 1$	-
$\left({}^{64}R/{}^{64}R^*\right)^{\mathrm{eq}}_{\mathrm{HCO_3^-}}$	$\Delta^{\mathrm{eq}}_{64,\mathrm{HCO_3^-}}/1000 + 1$	-
$\left({}^{64}R/{}^{64}R^*\right)^{\mathrm{eq}}_{\mathrm{CO_3^{2-}}}$	$\Delta^{\mathrm{eq}}_{64,\mathrm{CO_3^{2-}}}/1000 + 1$	-
${}^{64}\alpha^{\mathrm{eq}}_{\mathrm{CO_3^{2-}-HCO_3^-}}$	$\left({}^{64}R/{}^{64}R^*\right)^{\mathrm{eq}}_{\mathrm{CO_3^{2-}}} / \left({}^{64}R/{}^{64}R^*\right)^{\mathrm{eq}}_{\mathrm{HCO_3^-}}$	-
${}^{64}K_2$	${}^{64}\alpha^{\mathrm{eq}}_{\mathrm{CO_3^{2-}-HCO_3^-}} \cdot {}^{18}\alpha^{\mathrm{eq}}_{\mathrm{CO_3^{2-}-HCO_3^-}} \cdot {}^{18}\alpha^{\mathrm{eq}}_{\mathrm{CO_3^{2-}-HCO_3^-}} \cdot K_2$	-
${}^{64}\chi$	$\frac{1}{1+\frac{1}{{}^{64}K_2 \cdot {}^{64}\alpha^{\mathrm{eq}}_{\mathrm{CO_3-HCO_3}} \cdot [\mathrm{H^+}]}}$	-
${}^{18-18}\mathrm{KIE}_{p'_{+1}}$	1+0.049/1000	Guo (2020)
${}^{18-18}\mathrm{KIE}_{s'_{+1}}$	1-0.146/1000	Guo (2020)
${}^{18-18}\mathrm{KIE}_{p'_{+4}}$	1-0.144/1000	Guo (2020)
${}^{18-18}\mathrm{KIE}_{s'_{+4}}$	1-0.086/1000	Guo (2020)
p'_{+1}, s'_{+1}	$p'_{+1} = ({}^{18-18}\mathrm{KIE}_{p'_{+1}} \cdot b_{+1} \cdot a_{+1})/k_{+1}$	-
	$s'_{+1} = ({}^{18-18}\mathrm{KIE}_{s'_{+1}} \cdot b_{+1} \cdot b_{+1})/k_{+1}$	-
p'_{-1}, s'_{-1}	$p'_{-1} = p'_{+1} / \left[\left({}^{64}R/{}^{64}R^*\right)^{\mathrm{eq}}_{\mathrm{HCO_3^-}} \cdot K_1 \cdot {}^{18}\alpha^{\mathrm{eq}}_{\mathrm{HCO_3^- -CO_2}} \cdot {}^{18}\alpha^{\mathrm{eq}}_{\mathrm{HCO_3^- -H_2O}} \right]$	-
	$s'_{-1} = s'_{+1} \cdot \left[\left({}^{48}R/{}^{48}R^*\right)^{\mathrm{eq}}_{\mathrm{CO_2}} \right] / \left[\left({}^{64}R/{}^{64}R^*\right)^{\mathrm{eq}}_{\mathrm{HCO_3^-}} \cdot K_1 \cdot {}^{18}\alpha^{\mathrm{eq}}_{\mathrm{HCO_3^- -CO_2}} \cdot {}^{18}\alpha^{\mathrm{eq}}_{\mathrm{HCO_3^- -CO_2}} \right]$	-
p'_{+4}, s'_{+4}	$p'_{+4} = ({}^{18-18}\mathrm{KIE}_{p'_{+4}} \cdot b_{+4} \cdot a_{+4})/k_{+4}$	-
	$s'_{+4} = ({}^{18-18}\mathrm{KIE}_{s'_{+4}} \cdot b_{+4} \cdot b_{+4})/k_{+4}$	-
p'_{-4}, s'_{-4}	$p'_{-4} = p'_{+4} / \left[\left({}^{64}R/{}^{64}R^*\right)^{\mathrm{eq}}_{\mathrm{HCO_3^-}} \cdot K_1/K_{\mathrm{w}} \cdot {}^{18}\alpha^{\mathrm{eq}}_{\mathrm{HCO_3^- -CO_2}} \cdot {}^{18}\alpha^{\mathrm{eq}}_{\mathrm{HCO_3^- -OH^-}} \right]$	-
	$s'_{-4} = s'_{+4} \cdot \left[\left({}^{48}R/{}^{48}R^*\right)^{\mathrm{eq}}_{\mathrm{CO_2}} \right] / \left[\left({}^{64}R/{}^{64}R^*\right)^{\mathrm{eq}}_{\mathrm{HCO_3^-}} \cdot K_1/K_{\mathrm{w}} \cdot {}^{18}\alpha^{\mathrm{eq}}_{\mathrm{HCO_3^- -CO_2}} \cdot {}^{18}\alpha^{\mathrm{eq}}_{\mathrm{HCO_3^- -CO_2}} \right]$	-

Adding double-clumped isotopes to the model

S.2.2.1 Homogeneous reactions and clumped isotope definitions

1. $286 + 286 \rightleftharpoons 288 + 266$
2. ${}^{48}K_{CO_2} = \frac{[288][266]}{[286][286]}$.
3. $\Delta_{48} = \left(\frac{{}^{48}R}{{}^{48}R^*} - 1\right) * 1000$,
4. ${}^{48}R = \frac{[288]}{[266]}$
5. ${}^{48}K_{CO_2} = \frac{[288]}{[266]}\frac{[266]}{[286]}\frac{[266]}{[286]} = {}^{48}R * (2 *^{18} r_{CO_2})^{-1} = \frac{1}{4}(\frac{{}^{48}R}{{}^{48}R^*})^{eq}_{CO_2}$
6. $\frac{[288]}{[266]} = {}^{48}R^* = {}^{18}r^2_{CO_2}$.
7. ${}^{48}K_{CO_2} = \frac{[288][266]}{[286][286]} = \frac{1}{4}\left(\frac{{}^{48}R}{{}^{48}R^*}\right)^{eq}_{CO_2} = \frac{1}{4}(\frac{\Delta^{eq}_{48,CO_2}}{1000} + 1)$
8. $H2866 + H2866 \rightleftharpoons H2886 + H2666$
9. $2866 + 2866 \rightleftharpoons 2886 + 2666$,
10. ${}^{64}K_{HCO_3^-} = \frac{[H2886][H2666]}{[H2866][H2866]} = \frac{1}{3}(\frac{{}^{64}R}{{}^{64}R^*})^{eq}_{HCO_3^-} = \frac{1}{3}(\frac{\Delta^{eq}_{64,HCO_3^-}}{1000} + 1)$
11. ${}^{64}K_{CO_3^{2-}} = \frac{[2886][2666]}{[2866][2866]} = \frac{1}{3}(\frac{{}^{64}R}{{}^{64}R^*})^{eq}_{CO_3^{2-}} = \frac{1}{3}\left(\frac{\Delta^{eq}_{64,CO_3^{2-}}}{1000} + 1\right)$.

S.2.2.2 Heterogeneous reactions involving double-clumped isotopologues

12. $286 + H_28 \underset{2/3p'_{-1}}{\overset{p'_{+1}}{\rightleftharpoons}} H2886^- + H^+$
13. $288 + H_26 \underset{1/3s'_{-1}}{\overset{s'_{+1}}{\rightleftharpoons}} H2886^- + H^+$
14. $286 + 8H^- \underset{2/3p'_{-4}}{\overset{p'_{+4}}{\rightleftharpoons}} H2886^-$
15. $288 + 6H^- \underset{1/3s'_{-4}}{\overset{s'_{+4}}{\rightleftharpoons}} H2886^-$
16. $\frac{d[288]}{dt} = -s'_{+1}[288] + \frac{1}{3}s'_{-1}[E2886]^{64}X[H] - s'_{+4}[288][6H] + \frac{1}{3}s'_{-4}[E2886]^{64}X$
17. $\frac{d[E2886]}{dt} = p'_{+1}[286]r_w - \frac{2}{3}p'_{-1}[E2886]^{64}X[H] + p'_{+4}[286][8H] - \frac{2}{3}p'_{-4}[E2886]^{64}X + s'_{+1}[288] - \frac{1}{3}s'_{-1}[E2886]^{64}X[H] + s'_{+4}[288][6H] - \frac{1}{3}s'_{-4}[E2886]^{64}X$

S.2.3 Δ_{47} and Δ_{48} vs $\delta^{18}O$ IsoDIC Modeling

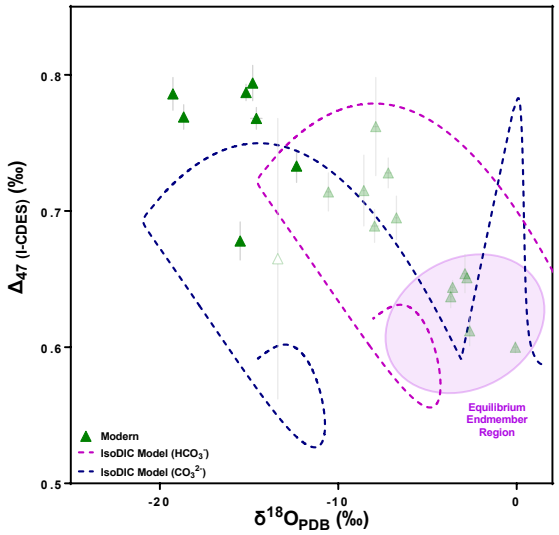

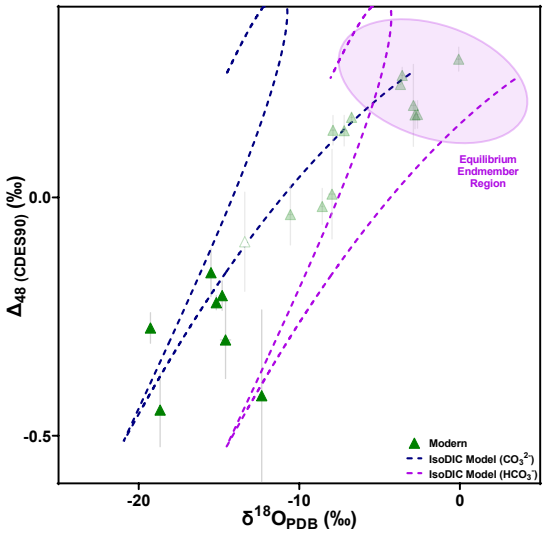

S.3 Paired Δ_{47}-Δ_{48} constrains kinetic effects associated with cave carbonates

S.3.1 IsoDIC Model Equations

The modeling information is the same as that seen in S.2.1.

S.3.2 Additional Site Description Figures

S.2.1 Cenote Rainbow, Feno, and Monkey Dust, Mexico Cave Samples (Kovacs et al., 2018)

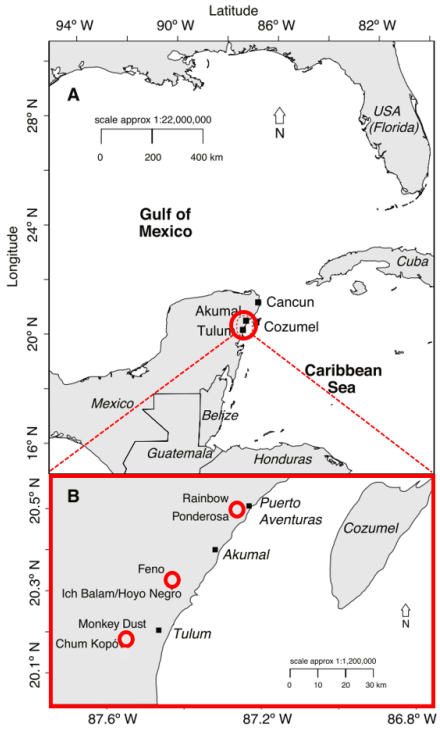

Figure S.3.1 This map was adopted and modified from Kovac *et al* . (Kovacs *et al* ., 2018) **A)** General regional map of Yucatán Peninsula in Mexico highlighting the areas where the cave raft samples were taken from. **B)** Inset with red circles highlighting Rainbow, Feno, and Monkey Dust cave systems where the cave raft samples were recovered from.

S.3.3 Additional Graphs and Charts

S.3.3.1 Extent of Disequilibria Plots (ΔΔ47/ΔΔ48 vs Δδ18O) – All data plotted for farmed calcite plates, speleothems, and cave rafts.

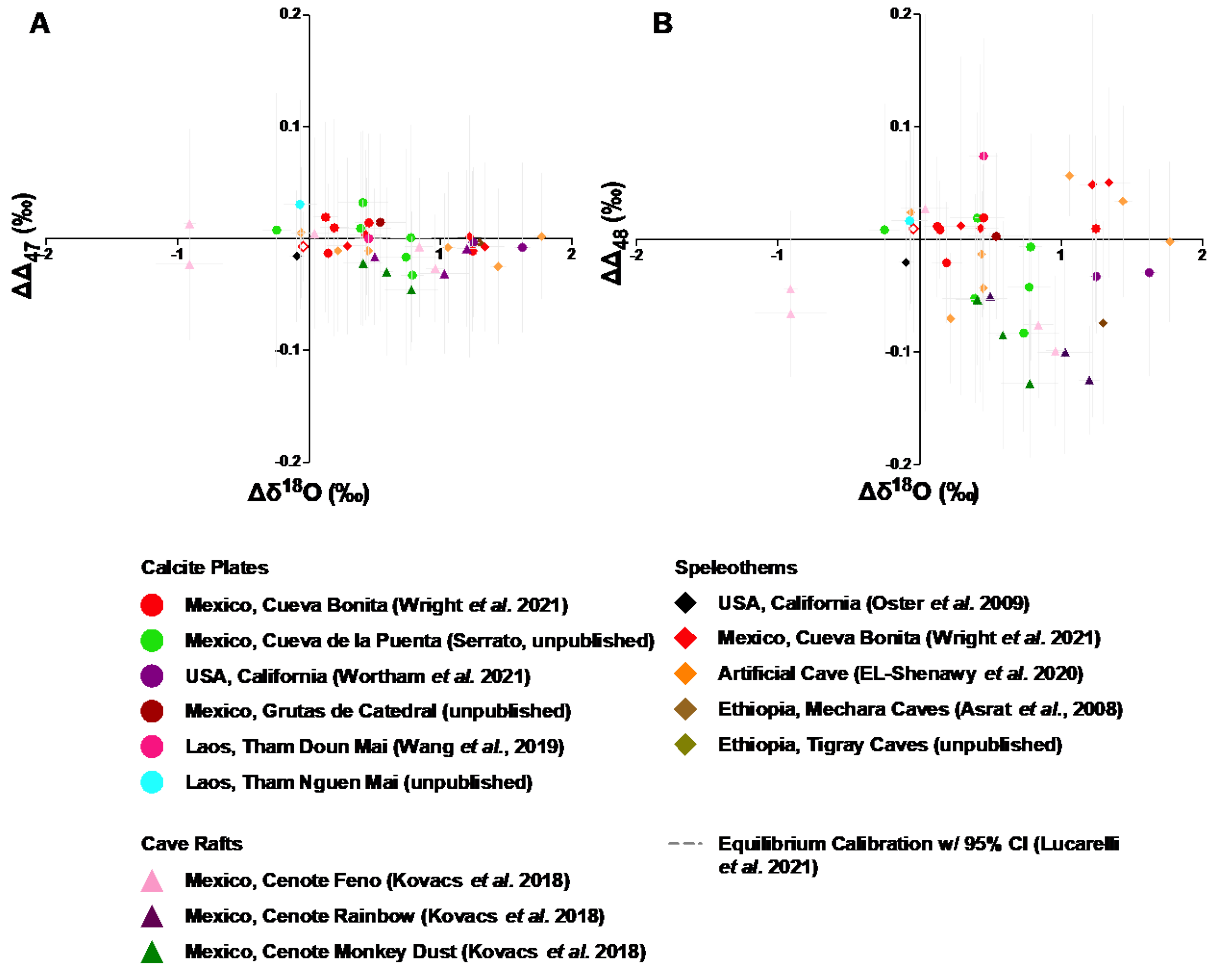

S.3.3.2 $\delta^{18}O$ vs $\delta^{13}C$ plots of farmed calcite plates, speleothems, and cave rafts

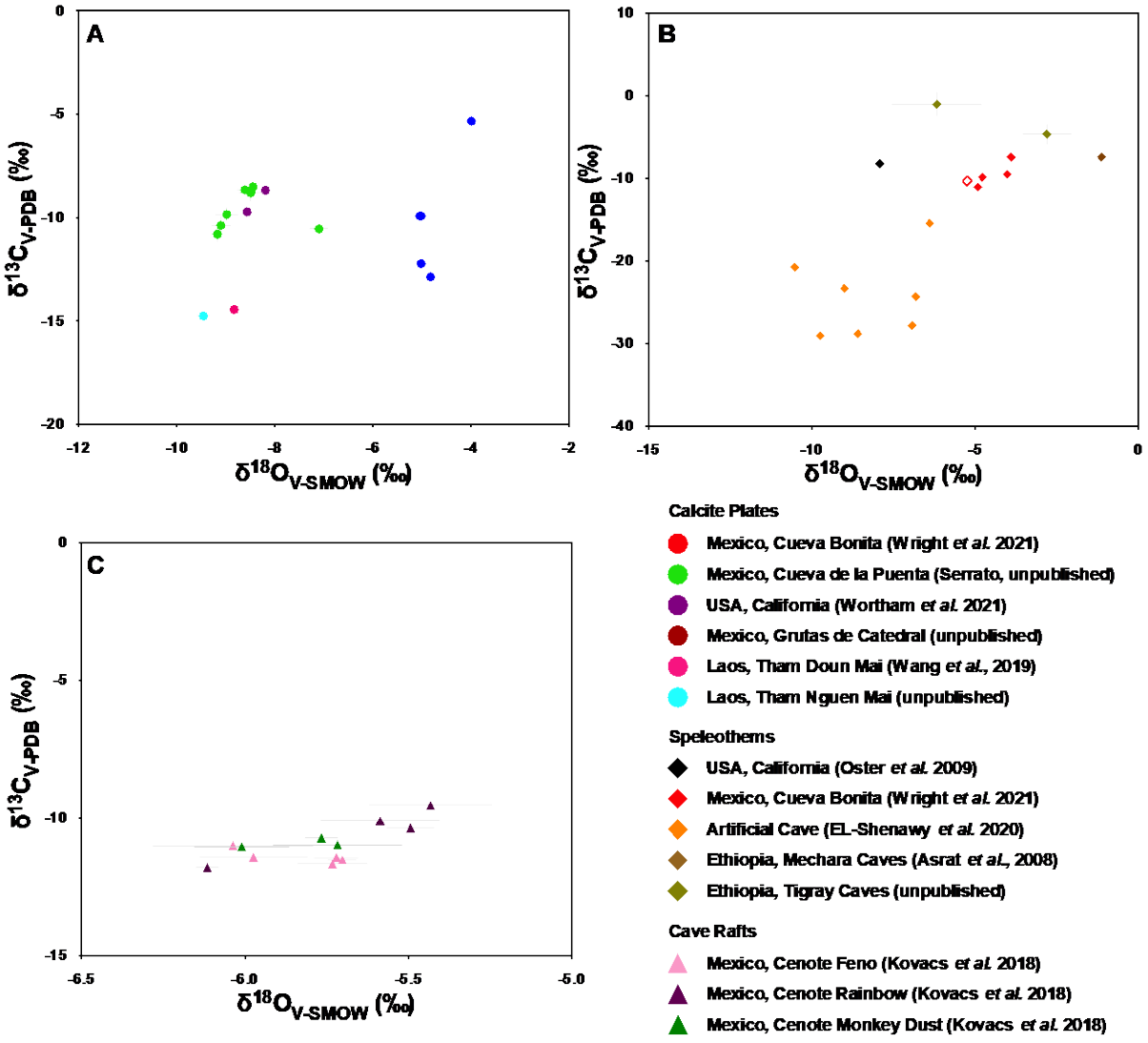

S.3.3.3 $\delta^{18}O$ vs $\delta^{13}C$ plots of farmed calcite plates, speleothems, and cave rafts

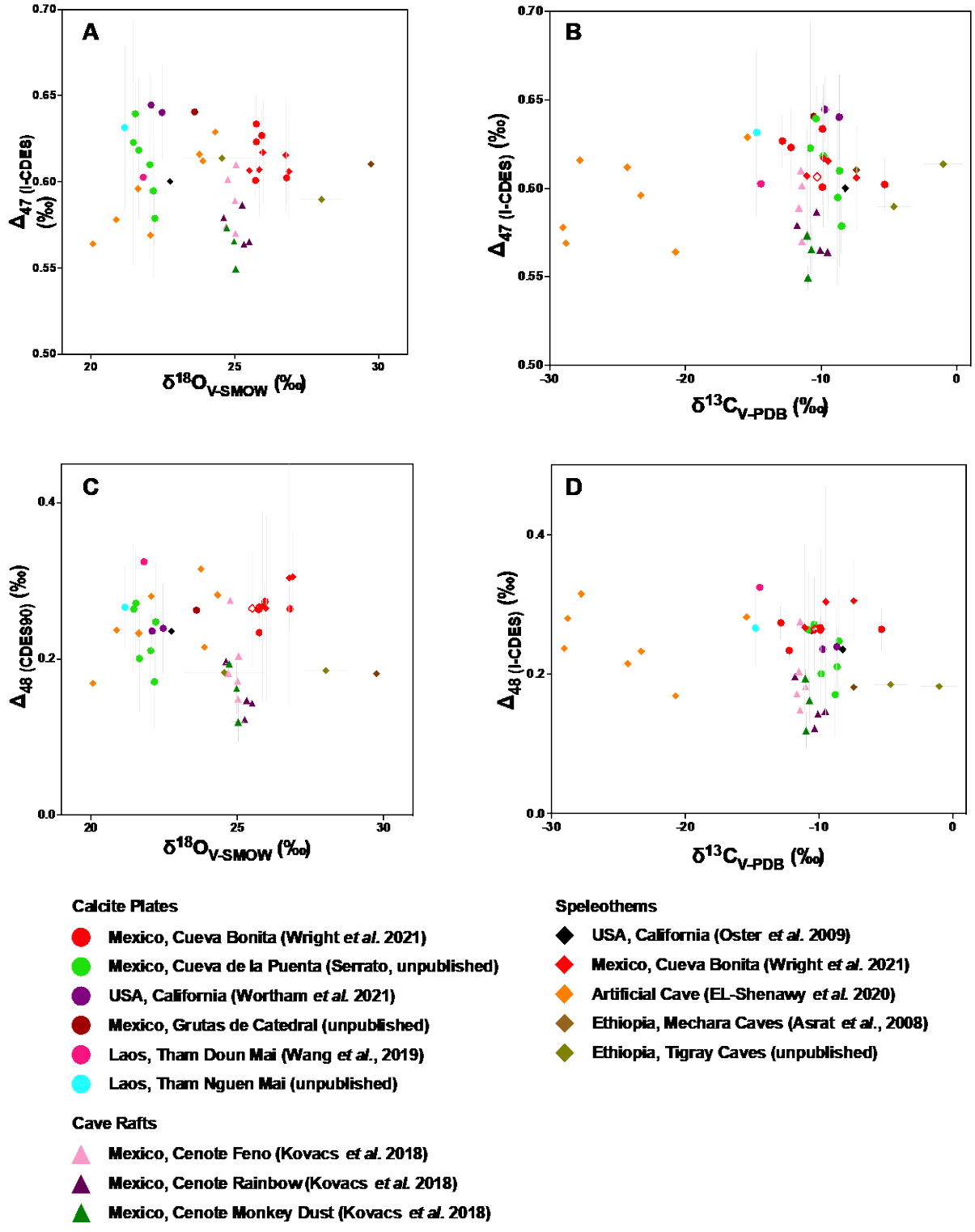

S.3.3.4 Paired clumped isotope (Δ_{47}-Δ_{48}) and extent of disequilibria ($\Delta\Delta_{47}$-$\Delta\Delta_{48}$) analysis

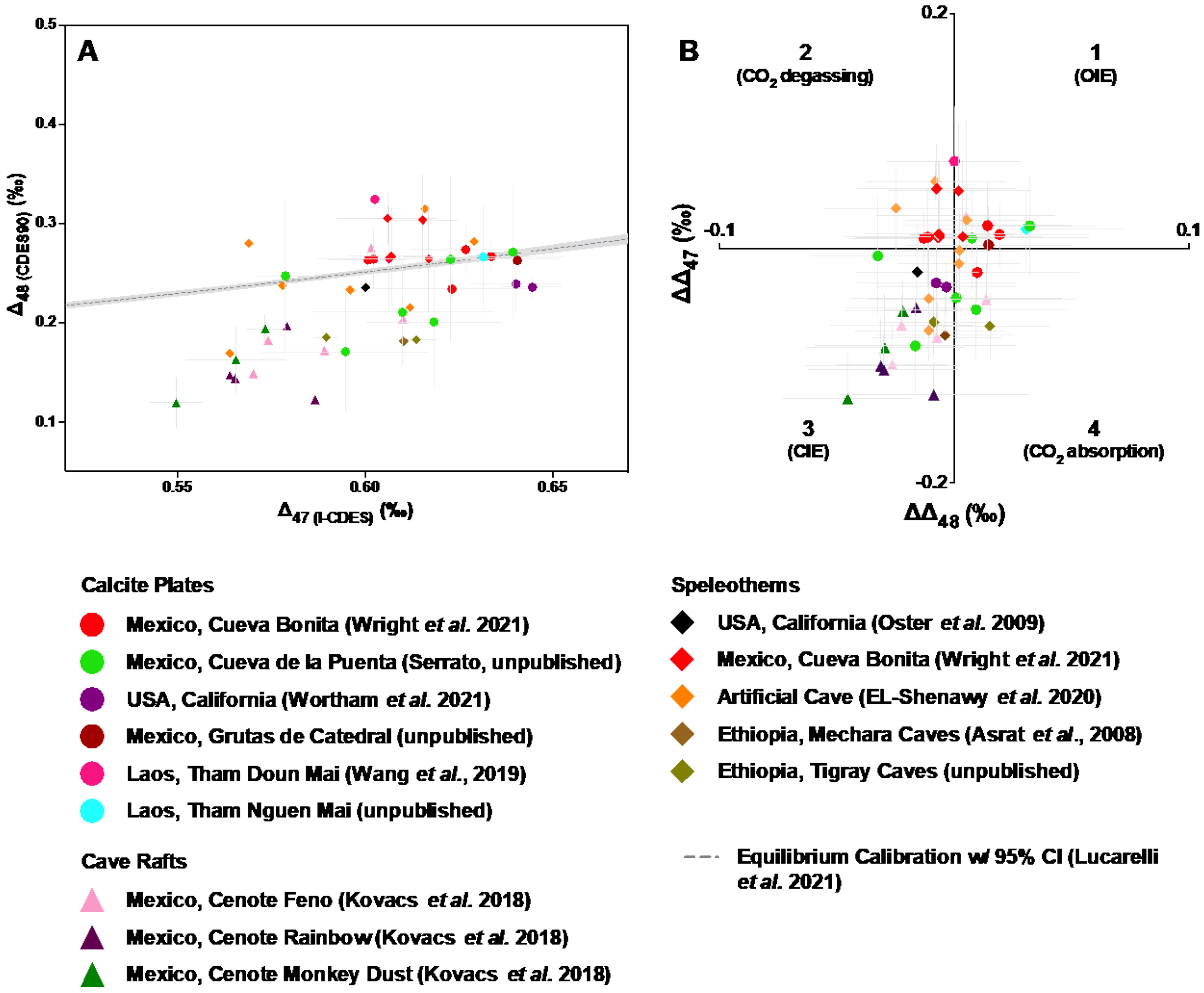

Figure S.3.2 Dual clumped (Δ_{47} and Δ_{48}) isotope plot, panel A, with extent of disequilibria plot, panel B. $\Delta\Delta_{47}$ and $\Delta\Delta_{48}$ were calculated by measuring the difference between the measured clumped isotope signal versus the equilibrium clumped isotope signature, using the temperature-dependent relationship developed by Lucarelli *et al* . (2022). The temperatures varied by the location of recovery and were explicitly measured by collaborators. Panel C was created using IsoDIC (Guo *et al* . 2019, 2020) to simulate disequilibria in the degassing (dark yellow line) and absorption (blue line) pathways **A)** Δ_{47} and Δ_{48} paired dual clumped analysis of cave carbonate samples. **B)** $\Delta\Delta_{47}$ and $\Delta\Delta_{48}$ of cave carbonate samples with disequilibria vectors overlayed. The red vector, labeled as CO_2 exchange, was determined in this study by conducting a linear regression of the entire cave raft sample population (Kovacs *et al.* 2018) yielding -3.06±0.512. Quadrants 1-4 are listed with the general symptom causing disequilibria.

References

Affek H. P., Bar-matthews M., Ayalon A., Matthews A. and Eiler J. M. (2008) Glacial / interglacial temperature variations in Soreq cave speleothems as recorded by 'clumped isotope' thermometry. *Geochimica et Cosmochimica Acta* **72**, 5351–5360.

Affek H. P. and Eiler J. M. (2006) Abundance of mass 47 CO_2 in urban air, car exhaust, and human breath. *Geochimica et Cosmochimica Acta* **70**, 1–12.

Affek H. P. and Zaarur S. (2014) Kinetic isotope effect in CO_2 degassing: Insight from clumped and oxygen isotopes in laboratory precipitation experiments. *Geochimica et Cosmochimica Acta* **143**, 319–330.

Affolter S., Fleitmann D. and Leuenberger M. (2014) New online method for water isotope analysis of speleothem fluid inclusions using laser absorption spectroscopy (WS-CRDS). *Climate of the Past* **10**, 1291–1304.

Almogi-Labin A., Bar-Matthews M., Shriki D., Kolosovsky E., Paterne M., Schilman B., Ayalon A., Aizenshtat Z. and Matthews A. (2009) Climatic variability during the last ~90 ka of the southern and northern Levantine Basin as evident from marine records and speleothems. *Quaternary Science Reviews* **28**, 2882–2896.

Anderson N. T., Kelson J. R., Kele S., Da M., Bonifacie M., Huntington K. W., Bernasconi S. M. and Bergmann K. D. (2021a) A unified clumped isotope thermometer calibration (0.5 – 1100 °C) using carbonate-based standardization., 1–22.

Anon (2018) Accelerating renewables is our most effective climate solution. *IRENA*.

Asrat A., Baker A., Leng M., Gunn J. and Umer M. (2008) Environmental monitoring in the Mechara caves, Southeastern Ethiopia: implications for speleothem palaeoclimate studies. *Int J Speleol* **37**, 207–220.

Axtell Jonathan C, Saleh L. M. A., Qian E. A., Wixtrom A. I. and Spokoyny A. M. (2018) Synthesis and Applications of Perfunctionalized Boron Clusters. *Inorganic Chemistry* **57**, 2333–2350.

Bajnai D., Coplen T. B., Methner K., Löffler N., Krsnik E. and Fiebig J. (2021) Devils Hole Calcite Was Precipitated at ±1°C Stable Aquifer Temperatures During the Last Half Million Years. *Geophysical Research Letters* **48**, 1–10.

Bajnai D., Fiebig J., Tomašových A., Garcia S. M., Rollion- C., Raddatz J., Lö N., Primo-ramos C. and Brand U. (2018) Assessing kinetic fractionation in brachiopod calcite using clumped isotopes., 1–12.

Bajnai D., Guo W., Spötl C., Coplen T. B., Methner K., Löffler N., Krsnik E., Gischler E., Hansen M., Henkel D., Price G. D., Raddatz J., Scholz D. and Fiebig J. (2020a) Dual clumped isotope thermometry resolves kinetic biases in carbonate formation temperatures. *Nature Communications* **11**, 4005.

Bajnai D., Guo W., Spötl C., Coplen T. B., Methner K., Löffler N., Krsnik E., Gischler E., Hansen M., Henkel D., Price G. D., Raddatz J., Scholz D. and Fiebig J. (2020b) Dual clumped isotope thermometry resolves kinetic biases in carbonate formation temperatures. *Nature Communications* **11**, 4005.

Baldini J. U. L., McDermott F. and Fairchild I. J. (2006) Spatial variability in cave drip water hydrochemistry: Implications for stalagmite paleoclimate records. *Chemical Geology* **235**, 390–404.

Baldini J. U. L., McDermott F., Hoffmann D. L., Richards D. A. and Clipson N. (2008) Very high-frequency and seasonal cave atmosphere pCO_2 variability: Implications for stalagmite growth and oxygen isotope-based paleoclimate records. *Earth and Planetary Science Letters* **272**, 118–129.

Bar-Matthews M., Ayalon A., Gilmour M., Matthews A. and Hawkesworth C. J. (2003) Sea - land oxygen isotopic relationships from planktonic foraminifera and speleothems in the Eastern

Mediterranean region and their implication for paleorainfall during interglacial intervals. *Geochimica et Cosmochimica Acta* **67**, 3181–3199.

Bar-Matthews M., Ayalon A. and Kaufman A. (1997) Late Quaternary Paleoclimate in the Eastern Mediterranean Region from Stable Isotope Analysis of Speleothems at Soreq Cave, Israel. *Quaternary Research* **47**, 155–168.

Barnes I. and O'Neil J. (1969) The Relationship between Fluids in Some Fresh Alpine-Type Ultramafics and Possible Modern Serpentinization, Western United States. *Geological Society of America* **80**, 1947–1960.

Barton J. L., Wixtrom A. I., Kowalski J. A., Qian E. A., Jung D., Brushett F. R. and Spokoyny A. M. (2019) Perfunctionalized Dodecaborate Clusters as Stable Metal-Free Active Materials for Charge Storage. *ACS Applied Energy Materials* **2**, 4907–4913.

Beck W. C., Grossman E. L. and Morse J. W. (2005) Experimental studies of oxygen isotope fractionation in the carbonic acid system at 15°, 25°, and 40°C. *Geochimica et Cosmochimica Acta* **69**, 3493–3503.

Benavente J., Vadillo I., Carrasco F., Soler A., Liñán C. and Moral F. (2010) Air Carbon Dioxide Contents in the Vadose Zone of a Mediterranean Karst. *Vadose Zone Journal* **9**, 126.

Berg J., Tymoczko J. and Stryer L. (2002) *Biochemistry*. 5th ed. ed. W. Freeman, New York, NY.

Bernasconi S. M., Daëron M., Bergmann K. D., Bonifacie M., Meckler A. N., Affek H. P., Anderson N., Bajnai D., Barkan E., Beverly E., Blamart D., Burgener L., Calmels D., Chaduteau C., Clog M., Davidheiser-Kroll B., Davies A., Dux F., Eiler J., Elliott B., Fetrow A. C., Fiebig J., Goldberg S., Hermoso M., Huntington K. W., Hyland E., Ingalls M., Jaggi M., John C. M., Jost A. B., Katz S., Kelson J., Kluge T., Kocken I. J., Laskar A., Leutert T. J., Liang D., Lucarelli J., Mackey T. J., Mangenot X., Meinicke N., Modestou S. E., Müller I. A., Murray S., Neary A., Packard N., Passey

B. H., Pelletier E., Petersen S., Piasecki A., Schauer A., Snell K. E., Swart P. K., Tripati A., Upadhyay D., Vennemann T., Winkelstern I., Yarian D., Yoshida N., Zhang N. and Ziegler M. (2021) InterCarb: A Community Effort to Improve Interlaboratory Standardization of the Carbonate Clumped Isotope Thermometer Using Carbonate Standards. *Geochemistry, Geophysics, Geosystems* **22**, 1–25.

Blake M. C., Bailey E. H. and Wentworth C. M. (2012) The Cedars Ultramafic Mass, Sonoma County, California. *USGS Open-File Report* **2012–1164**, 1–16.

Boettger J. D. and Kubicki J. D. (2021) Equilibrium and kinetic isotopic fractionation in the CO_2 hydration and hydroxylation reactions: Analysis of the role of hydrogen-bonding via quantum mechanical calculations. *Geochimica et Cosmochimica Acta* **292**, 37–63.

Brand W. A., Assonov S. S. and Coplen T. B. (2010) Correction for the ^{17}O interference in $\delta^{13}C$ measurements when analyzing CO_2 with stable isotope mass spectrometry (IUPAC Technical Report). *Pure and Applied Chemistry* **82**, 1719–1733.

van Breukelen M. R., Vonhof H. B., Hellstrom J. C., Wester W. C. G. and Kroon D. (2008) Fossil dripwater in stalagmites reveals Holocene temperature and rainfall variation in Amazonia. *Earth and Planetary Science Letters* **275**, 54–60.

Bruni J., Canepa M., Chiodini G., Cioni R., Cipolli F., Longinelli A., Marini L., Ottonello G. and Vetuschi Zuccolini M. (2002) Irreversible water-rock mass transfer accompanying the generation of the neutral, Mg-HCO3 and high-pH, Ca-OC spring waters of the Genova province, Italy. *Applied Geochemistry* **17**, 455–474.

Burns S. J., Fleitmann D., Matter A., Kramers J. and Al-Subbary A. A. (2003) Indian Ocean climate and an absolute chronology over Dansgaard/Oeschger events 9 to 13. *Science (1979)* **301**, 1365–1367.

Carpenter S. and Lohmann K. (1995) $\delta^{18}O$ and $\delta^{13}C$ values of modern brachiopod shells. *Geochimica et Cosmochimica Acta* **59**, 3749–3764.

Chen S., Gagnon A. C. and Adkins J. F. (2018) Carbonic anhydrase, coral calcification and a new model of stable isotope vital effects. *Geochimica et Cosmochimica Acta* **236**, 179–197.

Chen Y., Kang Y., Zhao Y., Wang L., Liu J., Li Y., Liang Z., He X., Li X., Tavajohi N. and Li B. (2021) A review of lithium-ion battery safety concerns: The issues, strategies, and testing standards. *Journal of Energy Chemistry* **59**, 83–99.

Christensen J. N., Watkins J. M., Devriendt L. S., DePaolo D. J., Conrad M. E., Voltolini M., Yang W. and Dong W. (2021) Isotopic fractionation accompanying CO_2 hydroxylation and carbonate precipitation from high pH waters at The Cedars, California, USA. *Geochimica et Cosmochimica Acta* **301**, 91–115.

Cipolli F., Gambardella B., Marini L., Ottonello G. and Zuccolini M. V. (2004) Geochemistry of high-pH waters from serpentinites of the Gruppo di Voltri (Genova, Italy) and reaction path modeling of CO_2 sequestration in serpentinite aquifers. *Applied Geochemistry* **19**, 787–802.

Clark I. D. and Fritz P. (2013) *Environmental isotopes in hydrogeology*., CRC press.

Clark I. D., Fritz P. and Fontes J.-C. (1992) Stable isotope disequilibria in travertine from high pH waters : Laboratory investigations and field observations from Oman. *Geochimica et Cosmochimica Acta* **56**, 2041–2050.

Cohen A. L. and McConnaughey T. A. (2003) Geochemical perspectives on coral mineralization. *Rev. Mineral. Geochem* **54**, 151–187.

Coleman R. G. (2004) Geologic nature of the Jasper Ridge Biological Preserve, San Francisco Peninsula, California. *International Geology Review* **46**, 629–637.

Craig H. and Gordon L. I. (1965) Deuterium and oxygen 18 variations in the ocean and the marine atmosphere.

Daëron M., Blamart D., Peral M. and Affek H. P. (2016) Absolute isotopic abundance ratios and the accuracy of Δ47 measurements. *Chemical Geology* **442**, 83–96.

Daeron M., Drysdale R. N., Peral M., Huyghe D., Blamart D., Coplen T. B., Lartaud F. and Zanchetta G. (2019) Most Earth-surface calcites precipitate out of isotopic equilibrium. *Nature Communications*, 1–7.

Daëron M., Guo W., Eiler J., Genty D., Blamart D., Boch R., Drysdale R., Maire R., Wainer K. and Zanchetta G. (2011) $^{13}C^{18}O$ clumping in speleothems: Observations from natural caves and precipitation experiments. *Geochimica et Cosmochimica Acta* **75**, 3303–3317.

Dansgaard W. (1964) Stable isotopes in precipitation. *Tellus* **16**, 436–468.

Day C. C. and Henderson G. M. (2011) Oxygen isotopes in calcite grown under cave-analogue conditions. *Geochimica et Cosmochimica Acta* **75**, 3956–3972.

Deng D. (2015) Li-ion batteries: Basics, progress, and challenges. *Energy Science and Engineering* **3**, 385–418.

Dennis K. J., Affek H. P., Passey B. H., Schrag D. P. and Eiler J. M. (2011) Defining an absolute reference frame for "clumped" isotope studies of CO_2. *Geochimica et Cosmochimica Acta* **75**, 7117–7131.

Devriendt L. S., Watkins J. M. and McGregor H. V. (2017) Oxygen isotope fractionation in the $CaCO_3$-DIC-H_2O system. *Geochimica et Cosmochimica Acta* **214**, 115–142.

Dorale J. A. and Liu Z. (2009) Limitations of Hendy Test Criteria in Judging the Paleoclimatic Suitability of Speleothems and the Need for Replication. *Journal of Cave and Karst Studies* **71**, 73–80.

Dreybrodt W. (1988) *Processes in Karst Systems: Physics, Chemistry, and Geology*., Springer-Verlag, Berlin, Germany.

Dreybrodt W., Hansen M. and Scholz D. (2016) Processes affecting the stable isotope composition of calcite during precipitation on the surface of stalagmites: Laboratory experiments investigating the isotope exchange between DIC in the solution layer on top of a speleothem and the CO_2 of the cave at. *Geochimica et Cosmochimica Acta* **174**, 247–262.

Dreybrodt W. and Scholz D. (2011) Climatic dependence of stable carbon and oxygen isotope signals recorded in speleothems: From soil water to speleothem calcite. *Geochimica et Cosmochimica Acta* **75**, 734–752.

Dunn B., Kamath H. and Tarascon J.-M. (2011) Electrical Energy Storage for the Grid: A Battery of Choices. *Science (1979)* **334**, 928–935.

Eberhardt W. H., Crawford B. and Lipscomb W. N. (1954) The Valence Structure of the Boron Hydrides. *The Journal of Chemical Physics* **22**, 989–1001.

Eiler J. M. (2007) "Clumped-isotope" geochemistry—The study of naturally-occurring, multiply-substituted isotopologues. *Earth and Planetary Science Letters* **262**, 309–327.

Eiler J. M. (2011) Paleoclimate reconstruction using carbonate clumped isotope thermometry. *Quaternary Science Reviews* **30**, 3575–3588.

Eiler J. M. and Schauble E. A. (2004) $^{18}O^{13}C^{16}O$ in Earth' s atmosphere. *Elsevier* **68**, 4767–4777.

EL-Shenawy M. I., Kim S. T. and Schwarcz H. P. (2020) Carbon and oxygen isotope systematics in cave environments: Lessons from an artificial cave "McMaster Cave." *Geochimica et Cosmochimica Acta* **272**, 137–159.

Faenza N. v., Bruce L., Lebens-Higgins Z. W., Plitz I., Pereira N., Piper L. F. J. and Amatucci G. G. (2017) Editors' Choice—Growth of Ambient Induced Surface Impurity Species on Layered Positive

Electrode Materials and Impact on Electrochemical Performance. *Journal of The Electrochemical Society* **164**, A3727–A3741.

Falk E. S., Guo W., Paukert A. N., Matter J. M., Mervine E. M. and Kelemen P. B. (2016) Controls on the stable isotope compositions of travertine from hyperalkaline springs in Oman: Insights from clumped isotope measurements. *Geochimica et Cosmochimica Acta* **192**, 1–28.

Farha O. K., Julius R. L., Lee M. W., Huertas R. E., Knobler C. B. and Hawthorne M. F. (2005) Synthesis of stable dodecaalkoxy derivatives of hypercloso-B 12H12. *J Am Chem Soc* **127**, 18243–18251.

Fetter C. W. (2018) *Applied hydrogeology*., Waveland Press.

Fiebig J., Bajnai D., Löffler N., Methner K., Krsnik E., Mulch A. and Hofmann S. (2019a) Combined high-precision Δ48 and Δ47 analysis of carbonates. *Chemical Geology* **522**, 186–191.

Fiebig J., Daëron M., Bernecker M., Guo W., Schneider G., Boch R., Bernasconi S. M., Jautzy J. and Dietzel M. (2021) Calibration of the dual clumped isotope thermometer for carbonates. *Geochimica et Cosmochimica Acta* **312**, 235–256.

Fleitmann D., Burns S. J., Mudelsee M., Neff U., Kramers J., Mangini A. and Matter A. (2003) Holocene forcing of the Indian monsoon recorded in a stalagmite from Southern Oman. *Science (1979)* **300**, 1737–1739.

Fones E. M., Colman D. R., Kraus E. A., Nothaft D. B., Poudel S., Rempfert K. R., Spear J. R., Templeton A. S. and Boyd E. S. (2019) Physiological adaptations to serpentinization in the Samail Ophiolite, Oman. *ISME Journal* **13**, 1750–1762.

García del Real P., Maher K., Kluge T., Bird D. K., Brown G. E. and John C. M. (2016) Clumped-isotope thermometry of magnesium carbonates in ultramafic rocks. *Geochimica et Cosmochimica Acta* **193**, 222–250.

Ghadiri E., Vogel N., Brennwald M. S., Maden C., Häuselmann A. D., Fleitmann D., Cheng H. and Kipfer R. (2018) Noble gas based temperature reconstruction on a Swiss stalagmite from the last glacial–interglacial transition and its comparison with other climate records. *Earth and Planetary Science Letters* **495**, 192–201.

Ghosh P., Adkins J., Affek H., Balta B., Guo W., Schauble E. A., Schrag D. and Eiler J. M. (2006) ^{13}C-^{18}O bonds in carbonate minerals: A new kind of paleothermometer. *Geochimica et Cosmochimica Acta* **70**, 1439–1456.

Griffiths M. L., Johnson K. R., Pausata F. S. R., White J. C., Henderson G. M., Wood C. T., Yang H., Ersek V., Conrad C. and Sekhon N. (2020) End of Green Sahara amplified mid- to late Holocene megadroughts in mainland Southeast Asia. *Nature Communications* **11**.

Gu W. and Ozerov O. V. (2011) Exhaustive chlorination of $[B_{12}H_{12}]^{2-}$ without chlorine gas and the use of $[B_{12}Cl_{12}]^{2-}$ as a supporting anion in catalytic hydrodefluorination of aliphatic C-F bonds. *Inorganic Chemistry* **50**, 2726–2728.

Guo W. (2009) Carbonate Clumped Isotope Thermometry: Application to Carbonaecous Chondrites & Effects of Kinetic Isotope Fractionation. California Institute of Technology.

Guo W. (2020) Kinetic clumped isotope fractionation in the DIC-H_2O-CO_2 system: Patterns, controls, and implications. *Geochimica et Cosmochimica Acta* **268**, 230–257.

Guo W. (2019) ScienceDirect Kinetic clumped isotope fractionation in the DIC-H_2O-CO_2 system : Patterns, controls, and implications.

Guo W., Eiler J., Genty D., Blamart D., Boch R., Drysdale R., Maire R., Wainer K. and Zanchetta G. (2011) $^{13}C^{18}O$ clumping in speleothems: Observations from natural caves and precipitation experiments. *Geochimica et Cosmochimica Acta* **75**, 3303–3317.

Guo W. and Zhou C. (2019) Patterns and controls of disequilibrium isotope effects in speleothems: Insights from an isotope-enabled diffusion-reaction model and implications for quantitative thermometry. *Geochimica et Cosmochimica Acta* **267**, 196–226.

Guo W. and Zhou C. (2019a) Triple oxygen isotope fractionation in the DIC-H_2O-CO_2 system: A numerical framework and its implications. *Geochimica et Cosmochimica Acta* **246**, 541–564.

Hansen M., Kluge T. and Scholz D. (2022) Investigation of disequilibrium clumped isotope fractionation in (speleothem) CaCO3 with cave analogous laboratory experiments using thin films of flowing solution. *Geochimica et Cosmochimica Acta* **321**, 244–264.

Hansen M., Scholz D., Froeschmann M. L., Schöne B. R. and Spötl C. (2017) Carbon isotope exchange between gaseous CO_2 and thin solution films: Artificial cave experiments and a complete diffusion-reaction model. *Geochimica et Cosmochimica Acta* **211**, 28–47.

Hansen M., Scholz D., Schöne B. R. and Spötl C. (2019) Simulating speleothem growth in the laboratory: Determination of the stable isotope fractionation ($\delta^{13}C$ and $\delta^{18}O$) between H_2O, DIC and $CaCO_3$. *Chemical Geology* **509**, 20–44.

Hawthorne M. F. (2009) Boron, my favorite element. *Journal of Chemical Education* **86**, 1131.

Hawthorne M. F. (2003) New discoveries at the interface of boron and carbon chemistries. *Pure and Applied Chemistry* **75**, 1157–1164.

Hawthorne M. F. and Pitochelli A. R. (1960) The Isolation of the Icosahedral $B_{12}H_{12}^{-2}$ Ion. *Journal of the American Chemical Society* **82**, 3228–3229.

Hendy C. H. (1971) The isotopic geochemistry of speleothems-I. The calculation of the effects of different modes of formation on the isotopic composition of speleothems and their applicability as palaeoclimatic indicators. *Geochimica et Cosmochimica Acta* **35**, 801–824.

Henkes G. A., Passey B. H., Wanamaker A. D., Grossman E. L., Ambrose W. G. and Carroll M. L. (2013) Carbonate clumped isotope compositions of modern marine mollusk and brachiopod shells. *Geochimica et Cosmochimica Acta* **106**, 307–325.

Hill P. S., Schauble E. A. and Tripati A. (2020) Theoretical constraints on the effects of added cations on clumped, oxygen, and carbon isotope signatures of dissolved inorganic carbon species and minerals. *Geochimica et Cosmochimica Acta* **269**, 496–539.

Hill P. S., Tripati A. K. and Schauble E. A. (2014) Theoretical constraints on the effects of pH, salinity, and temperature on clumped isotope signatures of dissolved inorganic carbon species and precipitating carbonate minerals. *Geochimica et Cosmochimica Acta* **125**, 610–652.

IPCC (2014) *Climate Change 2014: Synthesis Report. Contribution*.,

IPCC (2018) *Global Warming of 1.5°C, Intergovernmental Panel on Climate Change*.,

Ivanov S. V., Miller S. M., Anderson O. P., Solntsev K. A. and Strauss S. H. (2003) Synthesis and stability of reactive salts of dodecafluoro-closo-dodecaborate(2-). *J Am Chem Soc* **125**, 4694–4695.

Jalisatgi, Satish; Kulkarni, Vikas; Tang, Betty; Houston, Zachary; Lee, Mark; Hawthorne F. (2011) A Convenient Route to Diversely Substituted Icosahedral Closomer Nanoscaffolds. *J. Am. Chem. Soc* **133**, 12382–12385.

John Cédric M. and Bowen D. (2016) Community software for challenging isotope analysis: First applications of 'Easotope' to clumped isotopes. *Rapid Communications in Mass Spectrometry* **30**, 2285–2300.

Johnston V. E., Borsato A., Spötl C., Frisia S. and Miorandi R. (2013) Stable isotopes in caves over altitudinal gradients: fractionation behaviors and inferences for speleothem sensitivity to climate change. *Climate of the Past* **9**, 99–118.

Kelemen P. B., Aines R., Bennett E., Benson S. M., Carter E., Coggon J. A., De Obeso J. C., Evans O., Gadikota G., Dipple G. M., Godard M., Harris M., Higgins J. A., Johnson K. T. M., Kourim F., Lafay R., Lambart S., Manning C. E., Matter J. M., Michibayashi K., Morishita T., Noël J., Okazaki K., Renforth P., Robinson B., Savage H., Skarbek R., Spiegelman M. W., Takazawa E., Teagle D., Urai J. L. and Wilcox J. (2018) In situ carbon mineralization in ultramafic rocks: Natural processes and possible engineered methods. *Energy Procedia* **146**, 92–102.

Kelemen P. B., Godard M., Johnson K. T. M., Okazaki K., Manning C. E., Urai J. L., Michibayashi K., Harris M., A. Coggon. J. and Teagle D. A. H. (2017) Peridotite carbonation at the leading edge of the mantle wedge: OmDP Site BT1. *American Geophysical Union*.

Kelemen P. B. and Matter J. (2008a) In situ carbonation of peridotite for CO2 storage. *Proc Natl Acad Sci U S A* **105**, 17295–17300.

Kelemen P., Benson S. M., Pilorgé H., Psarras P. and Wilcox J. (2019) An Overview of the Status and Challenges of CO2 Storage in Minerals and Geological Formations. *Frontiers in Climate* **1**, 1–20.

Kim S. T. and O'Neil J. R. (1997) Equilibrium and nonequilibrium oxygen isotope effects in synthetic carbonates. *Geochimica et Cosmochimica Acta* **61**, 3461–3475.

Kimball J., Eagle R. and Dunbar R. (2016) Carbonate "clumped" isotope signatures in aragonitic scleractinian and calcitic gorgonian deep-sea corals., 6487–6505.

Klimchouk A. B. (2000) The formation of epikarst and its role in vadose speleogenesis. *Speleogenesis: Evolution of karst aquifers*, 91–99.

Kluge T. and Affek H. P. (2012) Quantifying kinetic fractionation in Bunker Cave speleothems using Δ 47. *Quaternary Science Reviews* **49**, 82–94.

Kluge T., Affek H. P., Dublyansky Y. and Spötl C. (2014) Devils Hole paleotemperatures and implications for oxygen isotope equilibrium fractionation. *Earth and Planetary Science Letters* **400**, 251–260.

Kluge T., Affek H. P., Marx T., Aeschbach-Hertig W., Riechelmann D. F. C., Scholz D., Riechelmann S., Immenhauser A., Richter D. K., Fohlmeister J., Wackerbarth A., Mangini A. and Spötl C. (2013) Reconstruction of drip-water $\delta^{18}O$ based on calcite oxygen and clumped isotopes of speleothems from Bunker Cave (Germany). *Climate of the Past* **9**, 377–391.

Kluge T., Marx T., Scholz D., Niggemann S., Mangini A. and Aeschbach-Hertig W. (2008) A new tool for palaeoclimate reconstruction: Noble gas temperatures from fluid inclusions in speleothems. *Earth and Planetary Science Letters* **269**, 408–415.

Knoth W. H., Miller H. C., Muetterties E. L., England D. C. and Parshall G. W. (1962) Derivative Chemistry of B10H10- and B12H12-. *J Am Chem Soc* **84**, 1056–1057.

Korchef A. and Touaibi M. (2008) Effect of pH and temperature on calcium carbonate precipitation by CO_2 removal from iron-rich water., 331–341.

Kovacs S. E., Reinhardt E. G., Werner C., Kim S. T., Devos F. and Le Maillot C. (2018) Seasonal trends in calcite-raft precipitation from cenotes Rainbow, Feno and Monkey Dust, Quintana Roo, Mexico: Implications for paleoenvironmental studies. *Palaeogeography, Palaeoclimatology, Palaeoecology* **497**, 157–167.

Krüger Y., Marti D., Staub R. H., Fleitmann D. and Frenz M. (2011) Liquid-vapour homogenisation of fluid inclusions in stalagmites: Evaluation of a new thermometer for palaeoclimate research. *Chemical Geology* **289**, 39–47.

Lachniet Matthew S. (2009) Climatic and environmental controls on speleothem oxygen-isotope values. *Quaternary Science Reviews* **28**, 412–432.

Lackner K. S., Wendt C. H., Butt D. P., Joyce E. L. and Sharp D. H. (1995) Carbon dioxide disposal in carbonate minerals. *Energy* **20**, 1153–1170.

Lee M. W., Farha O. K., Hawthorne M. F. and Hansch C. H. (2007) Alkoxy Derivatives of Dodecaborate: Discrete Nanomolecular Ions with Tunable Pseudometallic Properties. *Angewandte Chemie International Edition* **46**, 3018–3022.

Lerman A. and Stumm W. (1989) CO2 storage and alkalinity trends in lakes. *Water Research* **23**, 139–146.

Lewis N. S. (2016) Research opportunities to advance solar energy utilization. *Science (1979)* **351**, aad1920.

Lívanský K. (1982) Effect of temperature and pH on absorption of carbon dioxide by a free level of mixed solutions of some buffers. *Folia Microbiologica* **27**, 55–59.

Longuet-Higgins H. C., Roberts M. D. v and Emeleus H. J. (1955) The electronic structure of an icosahedron of boron atoms. *Proceedings of the Royal Society of London. Series A. Mathematical and Physical Sciences* **230**, 110–119.

Lowenstam H. (1961) Mineralogy, O18/O16 Ratios, and Strontium and Magnesium Contents of Recent and Fossil Brachiopods and Their Bearing on the History of the Ocean. *The Journal of Geology* **69**.

Lucarelli J., Hannah C., Ben E., Tyler C., Eagle R. and Tripati A. (2021) Equilibrated gas and carbonate standard-derived paired clumped isotope (D47 and D48) values on the absolute reference frame. *Rapid Communications in Mass Spectrometry*, 3–29.

Lucarelli J., Purgstaller B., Parvez Z., Watkins J. M., Eagle R. A., Dietzel M., Tripati A. and Angeles L. (2022) Paired Δ_{47} and Δ_{48} analyses and model calculations constrain equilibrium, experimentally-manipulated kinetic isotope effects, and mixing effects in calcite. *Geochimica et Cosmochimica Acta*.

Maderna A., Knobler C. B. and Hawthorne M. F. (2001) hedral core Ð12(12)-closomers are obtained by total esterification of $[B_{12}(OH)_{12}]^{-2}$. **12**, 1661–1664.

Malamud-Roam F. P., Lynn Ingram B., Hughes M. and Florsheim J. L. (2006) Holocene paleoclimate records from a large California estuarine system and its watershed region: linking watershed climate and bay conditions. *Quaternary Science Reviews* **25**, 1570–1598.

Marques J. M., Carreira P. M., Carvalho M. R., Matias M. J., Goff F. E., Basto M. J., Graça R. C., Aires-Barros L. and Rocha L. (2008) Origins of high pH mineral waters from ultramafic rocks, Central Portugal. *Applied Geochemistry* **23**, 3278–3289.

Mattey D., Lowry D., Duffet J., Fisher R., Hodge E. and Frisia S. (2008) A 53 year seasonally resolved oxygen and carbon isotope record from a modern Gibraltar speleothem: Reconstructed drip water and relationship to local precipitation. *Earth and Planetary Science Letters* **269**, 80–95.

McCollum D. L., Zhou W., Bertram C., De Boer H. S., Bosetti V., Busch S., Després J., Drouet L., Emmerling J., Fay M., Fricko O., Fujimori S., Gidden M., Harmsen M., Huppmann D., Iyer G., Krey V., Kriegler E., Nicolas C., Pachauri S., Parkinson S., Poblete-Cazenave M., Rafaj P., Rao N., Rozenberg J., Schmitz A., Schoepp W., Van Vuuren D. and Riahi K. (2018) Energy investment needs for fulfilling the Paris Agreement and achieving the Sustainable Development Goals. *Nature Energy* **3**, 589–599.

McConnaughey T. (1989) ^{13}C and ^{18}O isotopic disequilibrium in biological carbonates: I. Patterns. *Geochimica et Cosmochimica Acta* **53**, 151–162.

McDermott F. (2004) Palaeo-climate reconstruction from stable isotope variations in speleothems: A review. *Quaternary Science Reviews* **23**, 901–918.

Mcdermott F., Atkinson T. C., Fairchild I. J., Baldini L. M. and Mattey D. P. (2011) A first evaluation of the spatial gradients in $\delta^{18}O$ recorded by European Holocene speleothems. *Global and Planetary Change* **79**, 275–287.

McDermott F., Schwarcz H. and Rowe P. J. (2006) Isotopes in Speleothems. In *Isotopes in Palaeoenvironmental Research* (ed. M. J. Leng). Springer Netherlands, Dordrecht. pp. 185–225.

Meckler A. N., Affolter S., Dublyansky Y. V., Krüger Y., Vogel N., Bernasconi S. M., Frenz M., Kipfer R., Leuenberger M., Spötl C., Carolin S., Cobb K. M., Moerman J., Adkins J. F. and Fleitmann D. (2015) Glacial-interglacial temperature change in the tropical West Pacific: A comparison of stalagmite-based paleo-thermometers. *Quaternary Science Reviews* **127**, 90–116.

Mickler P. J., Banner J. L., Stern L., Asmerom Y., Edwards R. L. and Ito E. (2004) Stable isotope variations in modern tropical speleothems: Evaluating equilibrium vs. kinetic isotope effects. *Geochimica et Cosmochimica Acta* **68**, 4381–4393.

Mickler P. J., Stern L. A. and Banner J. L. (2006) Large kinetic isotope effects in modern speleothems. *Bulletin of the Geological Society of America* **118**, 65–81.

Mizushima K., Jones P. C., Wiseman P. J. and Goodenough J. B. (1981) *Li_xCoO_2 ($0 < x \sim< 1$): A NEW CATHODE MATERIAL FOR BATTERIES OF HIGH ENERGY DENSITY*., North-Holland Publishing Company.

Morrill P. L., Kuenen J. G., Johnson O. J., Suzuki S., Rietze A., Sessions A. L., Fogel M. L. and Nealson K. H. (2013) Geochemistry and geobiology of a present-day serpentinization site in California: The Cedars. *Geochimica et Cosmochimica Acta* **109**, 222–240.

Muetterties E. L., Balthis J. H., Chia Y. T., Knoth W. H. and Miller H. C. (1964) Chemistry of Boranes. VIII. Salts and Acids of $B_{10}H_{10}^{-2}$ and $B_{12}H_{12}^{-2}$. *Inorganic Chemistry* **3**, 444–451.

Mühlinghaus C., Scholz D. and Mangini A. (2009) Modelling fractionation of stable isotopes in stalagmites. *Geochimica et Cosmochimica Acta* **73**, 7275–7289.

de Obeso J. C. and Kelemen P. B. (2018) Fluid rock interactions on residual mantle peridotites overlain by shallow oceanic limestones: Insights from Wadi Fins, Sultanate of Oman. *Chemical Geology* **498**, 139–149.

de Obeso J. C., Kelemen P. B., Manning C. E., Michibayashi K. and Harris M. (2017) Listvenite formation from peridotite: Insights from Oman Drilling Project hole BT1B and preliminary reaction path model approach. *American Geophysical Union*.

Opiyo N. (2016) Energy storage systems for PV-based communal grids. *Journal of Energy Storage* **7**, 1–12.

Oster J. L., Montañez I. P., Sharp W. D. and Cooper K. M. (2009) Late Pleistocene California droughts during deglaciation and Arctic warming. *Earth and Planetary Science Letters* **288**, 434–443.

Owen R. A., Day C. C., Hu C. Y., Liu Y. H., Pointing M. D., Blättler C. L. and Henderson G. M. (2016) Calcium isotopes in caves as a proxy for aridity: Modern calibration and application to the 8.2 kyr event. *Earth and Planetary Science Letters* **443**, 129–138.

Ozawa K. (1994) *Lithium-ion rechargeable batteries with $LiCoO_2$ and carbon electrodes: the $LiCoO_2$/C system*.,

Pacala S., Al-Kaisi M., Brteau M., Erica B., Benson S., Birdsey R., Boysen D., Duren R., Hopkinson C., Jones C., Kelemen P., Levasseur A., Paustian K., Tang J., Troxler T., Wara M. and Wilcox J. (2019) *Negative Emissions Techonologies and Reliable Sequesteration: A Research Agenda*., National Academy of Science, Washington, DC.

Paukert A. N., Matter J. M., Kelemen P. B., Shock E. L. and Havig J. R. (2012) Reaction path modeling of enhanced in situ CO 2 mineralization for carbon sequestration in the peridotite of the Samail Ophiolite, Sultanate of Oman. *Chemical Geology* **330–331**, 86–100.

Peryshkov D. V., Popov A. A. and Strauss S. H. (2009) Direct perfluorination of $K_2B_{12}H_{12}$ in acetonitrile occurs at the gas bubble-solution interface and is inhibited by HF. Experimental and DFT study of inhibition by protic acids and soft, polarizable anions. *J Am Chem Soc* **131**, 18393–18403.

Peymann T., Herzog A., Knobler C. B. and Hawthorne M. F. (1999) Oxidation of icosahedral These [a]inorganic sugars" are. *Group (New York)*, 1061–1064.

Polyakov V. B., Horita J. and Cole D. R. (2005) Isotopic Self-Exchange Reactions of Water: Evaluation of the Rule of the Geometric Mean in Liquid - Vapor Isotope Partitioning., 8642–8645.

Poulson T. and White W. (1969) The Cave Environment. *Science (1979)* **165**, 3897.

Powers L. A., Werne J. P., Johnson T. C., Hopmans E. C., Damsté J. S. S. and Schouten S. (2004) Crenarchaeotal membrane lipids in lake sediments: A new paleotemperature proxy continental paleoclimate reconstruction? *Geology* **32**, 613–616.

R.G. Coleman (2000) *Ophiolites and Oceanic Crust: New Insights from Field Studies and the Ocean Drilling Program*., Geological Society of America, Boulder, Colorodo.

Richards D. A. and Dorale J. A. (2003) Uranium-series Chronology and Environmental Applications of Speleothems. *Reviews in Mineralogy and Geochemistry* **52**, 407–460.

Rollion-bard C., Blamart D., Cuif J. and Dauphin Y. (2010) In situ measurements of oxygen isotopic composition in deep-sea coral , Lophelia pertusa : Re-examination of the current geochemical models of biomineralization. *Geochimica et Cosmochimica Acta* **74**, 1338–1349.

Rollion-Bard C., Garcia S., Burckel P., Angiolini L., Jurikova H., Tomasovych A. and Henkel D. (2019) Assessing the biomineralization processes in the shell layers of modern brachiopods from oxygen

isotopic composition and elemental ratios: Implications for their use as paleoenvironmental proxies. *Chemical Geology* **524**, 49–66.

Saenger C., Affek H. P., Felis T., Thiagarajan N., Lough J. M. and Holcomb M. (2012a) Carbonate clumped isotope variability in shallow water corals : Temperature dependence and growth-related vital effects. *Geochimica et Cosmochimica Acta* **99**, 224–242.

Saylik D., Horvath M. J., Elmes P. S., Jackson W. R., Lovel C. G. and Moody K. (1999) Preparation of isocyanates from primary amines and carbon dioxide using Mitsunobu chemistry. *Journal of Organic Chemistry* **64**, 3940–3946.

Schauble E. A., Ghosh P. and Eiler J. M. (2006) Preferential formation of ^{13}C-^{18}O bonds in carbonate minerals, estimated using first-principles lattice dynamics. *Geochimica et Cosmochimica Acta* **70**, 2510–2529.

Scheidegger Y., Brennwald M. S., Fleitmann D., Jeannin P. Y., Wieler R. and Kipfer R. (2011) Determination of Holocene cave temperatures from Kr and Xe concentrations in stalagmite fluid inclusions. *Chemical Geology* **288**, 61–66.

Scholz D. and Hoffmann D. (2008) 230Th/U-dating of fossil corals and speleothems. *E and G Quaternary Science Journal* **57**, 52–76.

Serrato G. (2020) Investigating Mexican Paleoclimate with Precisely Dated Speleothems. Dissertation , MIT.

Sleep N. H., Meibom A., Fridriksson T., Coleman R. G. and Bird D. K. (2004) H2-rich fluids from serpentinization: Geochemical and biotic implications. *Proc Natl Acad Sci U S A* **101**, 12818–12823.

Smith A. (2021) *Climate change and batteries: the search for future power storage solutions (Briefing 6)*.,

Spooner P. T., Guo W., Robinson L. F., Thiagarajan N., Hendry K. R., Rosenheim B. E. and Leng M. J. (2016a) ScienceDirect Clumped isotope composition of cold-water corals : A role for vital effects ? *Geochimica et Cosmochimica Acta* **179**, 123–141.

Spötl C., Fairchild I. J. and Tooth A. F. (2005) Cave air control on dripwater geochemistry, Obir Caves (Austria): Implications for speleothem deposition in dynamically ventilated caves. *Geochimica et Cosmochimica Acta* **69**, 2451–2468.

Stauber J. M., Schwan J., Zhang X., Axtell J. C., Jung D., McNicholas B. J., Oyala P. H., Martinolich A. J., Winkler J. R., See K. A., Miller T. F., Gray H. B. and Spokoyny A. M. (2020) A Super-Oxidized Radical Cationic Icosahedral Boron Cluster. *J Am Chem Soc* **142**, 12948–12953.

Suzuki S., Ishii S., Hoshino T., Rietze A., Tenney A., Morrill P. L., Inagaki F., Kuenen J. G. and Nealson K. H. (2017) Unusual metabolic diversity of hyperalkaliphilic microbial communities associated with subterranean serpentinization at the Cedars. *ISME Journal* **11**, 2584–2598.

Tang J., Dietzel M., Fernandez A., Tripati A. K. and Rosenheim B. E. (2014) Evaluation of kinetic effects on clumped isotope fractionation (Δ_{47}) during inorganic calcite precipitation. *Geochimica et Cosmochimica Acta* **134**, 120–136.

Tang J., Köhler S. J. and Dietzel M. (2008) Sr^{2+}/Ca^{2+} and $^{44}Ca/^{40}Ca$ fractionation during inorganic calcite formation: I. Sr incorporation. *Geochimica et Cosmochimica Acta* **72**, 3718–3732.

Tang K. and Feng X. (2001) The effect of soil hydrology on the oxygen and hydrologen isotopic compositions of plants' source water. *Earth and Planetary Science Letters* **185**, 355–367.

Thiagarajan N., Adkins J. and Eiler J. (2011) Carbonate clumped isotope thermometry of deep-sea corals and implications for vital effects. *Geochimica et Cosmochimica Acta* **75**, 4416–4425.

Tierney J. E., Russell J. M., Huang Y., Sinninghe Damsté J. S., Hopmans E. C. and Cohen A. S. (2008) Northern hemisphere controls on tropical southeast African climate during the past 60,000 years. *Science (1979)* **322**, 252–255.

Treble P. C., Chappell J., Gagan M. K., McKeegan K. D. and Harrison T. M. (2005) In situ measurement of seasonal $\delta^{18}O$ variations and analysis of isotopic trends in a modern speleothem from southwest Australia. *Earth and Planetary Science Letters* **233**, 17–32.

Tremaine Darrel M., Froelich P. N. and Wang Y. (2011) Speleothem calcite farmed in situ: Modern calibration of $\delta^{18}O$ and $\delta^{13}C$ paleoclimate proxies in a continuously-monitored natural cave system. *Geochimica et Cosmochimica Acta* **75**, 4929–4950.

Tripati A. K., Hill P. S., Eagle R. A., Mosenfelder J. L., Tang J., Schauble E. A., Eiler J. M., Zeebe R. E., Uchikawa J., Coplen T. B., Ries J. B. and Henry D. (2015) Beyond temperature: Clumped isotope signatures in dissolved inorganic carbon species and the influence of solution chemistry on carbonate mineral composition. *Geochimica et Cosmochimica Acta* **166**, 344–371.

Uchikawa J., Chen S., Eiler J. M., Adkins J. F. and Zeebe R. E. (2021) Trajectory and timescale of oxygen and clumped isotope equilibration in the dissolved carbonate system under normal and enzymatically-catalyzed conditions at 25 °C. *Geochimica et Cosmochimica Acta* **314**, 313–333.

Uchikawa J. and Zeebe R. E. (2012a) The effect of carbonic anhydrase on the kinetics and equilibrium of the oxygen isotope exchange in the CO_2-H_2O system: Implications for $\delta^{18}O$ vital effects in biogenic carbonates. *Geochimica et Cosmochimica Acta* **95**, 15–34.

UNEP (2017) *The Emissions Gap Report 2017 - A UN Environment Synthesis Report*.,

Upadhyay D., Lucarelli J., Arnold A., Flores R., Bricker H., Ulrich R. N., Jesmok G., Santi L., Defliese W., Eagle R. A., Carroll H. M., Bateman J. B., Petryshyn V., Loyd S. J., Tang J., Priyadarshi A., Elliott B. and Tripati A. (2021) Carbonate clumped isotope analysis (Δ_{47}) of 21 carbonate standards

determined via gas-source isotope-ratio mass spectrometry on four instrumental configurations using carbonate-based standardization and multiyear data sets. *Rapid Communications in Mass Spectrometry* **35**.

Usdowski E., Michaelis J., Bottcher M. E. and Hoefs J. (1991) Factors for the oxygen isotope equilibrium fractionation between aqueous and gaseous CO2, carbonic acid, bicarbonate, carbonate, and water. *Z. Phys. Chem.* **170**, 237–249.

Vinet L. and Zhedanov A. (2011) A "missing" family of classical orthogonal polynomials. *Journal of Physics A: Mathematical and Theoretical* **44**, 1947–1960.

W Seifritz (1990) CO_2 disposal by means of silicates. *Nature* **345**, 486.

Wainer K., Genty D., Blamart D., Daëron M., Bar-matthews M., Vonhof H. and Dublyansky Y. (2011) Speleothem record of the last 180 ka in Villars cave (SW France): Investigation of a large $\delta^{18}O$ shift between MIS6 and MIS5. *Quaternary Science Reviews* **30**, 130–146.

Wang J. K., Johnson K. R., Borsato A., Amaya D. J., Griffiths M. L., Henderson G. M., Frisia S. and Mason A. (2019) Hydroclimatic variability in Southeast Asia over the past two millennia. *Earth and Planetary Science Letters* **525**.

Wang X., Auler A. S., Edwards L. L., Cheng H., Cristalli P. S., Smart P. L., Richards D. A. and Shen C. C. (2004) Wet periods in northeastern Brazil over the past 210 kyr linked to distant climate anomalies. *Nature* **432**, 740–743.

Wang Y. J., Cheng H., Edwards R. L., An Z. S., Wu J. Y., Shen C. C. and Dorale J. A. (2001) A high-resolution absolute-dated late pleistocene monsoon record from Hulu Cave, China. *Science (1979)* **294**, 2345–2348.

Wang Y., Liu C., Pan R. and Chen Z. (2017) Modeling and state-of-charge prediction of lithium-ion battery and ultracapacitor hybrids with a co-estimator. *Energy* **121**, 739–750.

Wang Z., Schauble E. A. and Eiler J. M. (2004) Equilibrium thermodynamics of multiply substituted isotopologues of molecular gases. *Geochimica et Cosmochimica Acta* **68**, 4779–4797.

Watkins J. M. and Devriendt L. S. (2021) A generalizable box model for kinetic clumped isotope effects in the CaCO3-DIC-H2O system. *Geochimica et Cosmochimica Acta*.

Watkins J. M. and Hunt J. D. (2015) A process-based model for non-equilibrium clumped isotope effects in carbonates. *Earth and Planetary Science Letters* **432**, 152–165.

Weise A. and Kluge T. (2020) Isotope exchange rates in dissolved inorganic carbon between 40 °C and 90 °C. *Geochimica et Cosmochimica Acta* **268**, 56–72.

Whittingham M. S. (2004) Lithium Batteries and Cathode Materials. *Chemical Reviews* **104**, 4271–4302.

Wiersema R. J. and Middaugh R. L. (1969) Electrochemical preparation and halogenation of 1,1′-μ-Hydro-bis(undecahydro-closo-dodecaborate)(3-), B24H233-1. *Inorganic Chemistry* **8**, 2074–2079.

Williams P. W. (2008) The role of the epikarst in karst and cave hydrogeology: A review. *Int J Speleol* **37**, 1–10.

Wixtrom A. I., Parvez Z. A., Savage M. D., Qian E. A., Jung D., Khan S. I., Rheingold A. L. and Spokoyny A. M. (2018) Tuning the electrochemical potential of perfunctionalized dodecaborate clusters through vertex differentiation. *Chemical Communications* **54**, 5867–5870.

Wixtrom Alex I, Shao Y., Jung D., Machan C. W., Kevork S. N., Qian E. A., Axtell J. C., Khan S. I., Kubiak C. P. and Spokoyny A. M. (2016) Rapid synthesis of redox-active dodecaborane $B_{12}(OR)_{12}$ clusters under ambient conditions. *Inorganic Chemistry Frontiers* **3**, 711–717.

Wortham B. E., Montañez I. P., Bowman K., Kuta D., Contreras N. S., Brummage E., Pang A., Tinsley J. and Roemer-Baer G. (2021) Monitoring of Sierra Nevada Caves Reveals the Potential for Stalagmites to Archive Seasonal Variability. *Frontiers in Earth Science* **9**, 1–13.

Wright K. T., Johnson K. R., Bhattacharya T. and Marks G. S. (2022) Precipitation in Northeast Mexico Primarily Controlled by the Relative Warming of Atlantic SSTs.

Yonge C. J., Ford D. C., Gray J. and Schwarcz H. P. (1985) Stable isotope studies of cave seepage water. *Chemical Geology: Isotope Geoscience Section* **58**, 97–105.

Zeebe R. E. and Wolf-Gladrow D. A. (2001) *CO_2 in seawater: Equilibrium, Kinerics,Isotopes*. 1st ed. ed. D. Halpern, Elsevier, Amsterdam, Netherlands.

Zhang S. and DePaolo D. J. (2017) Rates of CO_2 Mineralization in Geological Carbon Storage. *Accounts of Chemical Research* **50**, 2075–2084.